RADIATION FROM ADVANCED SOLID ROCKET MOTOR PLUMES

Contract No. NAS8-39370
Final Report

Prepared for:

National Aeronautics & Space Administration
George C. Marshall Space Flight Center
Marshall Space Flight Center, AL 35812

By:

Richard C. Farmer
Sheldon D. Smith
Brian L. Myruski

SECA, Inc.
3313 Bob Wallace Avenue
Suite 202
Huntsville, AL 35805

December, 1994

NATIONAL AERONAUTICS AND SPACE ADMINISTRATION
SBIR PHASE II FINAL REPORT

PROJECT SUMMARY

CONTRACT NO.: NAS8-39370

PROJECT TITLE: Radiation from Advanced Solid Rocket Motor Plumes

---

PURPOSE: The overall objective of this study was to develop an understanding of solid rocket motor (SRM) plumes in sufficient detail to accurately explain the majority of plume radiation test data. Improved flowfield and radiation analysis codes were to be developed to accurately and efficiently account for all the factors which effect radiation heating from rocket plumes. These codes were to be verified by comparing predicted plume behavior with measured test data. Extensive radiation data were provided by the NASA/MSFC test programs conducted to support the design of the ASRM.

RESEARCH COMPLETED: Upon conducting a thorough review of the current state-of-the-art of SRM plume flowfield and radiation prediction methodology and the pertainent experimental data base, the following analyses were developed for future design use.
- The NOZZRAD code was developed for preliminary base heating design and Al_2O_3 particle optical property data evaluation using a generalized two-flux solution to the radiative transfer equation.
- The IDARAD code was developed for rapid evaluation of plume radiation effects using the spherical harmonics method of differential approximation to the radiative transfer equation.
- The FDNS CFD code with fully coupled Euler-Lagrange particle tracking was validated by comparison to predictions made with the industry standard RAMP code for SRM nozzle flowfield analysis. The FDNS code provides the ability to analyze not only rocket nozzle flow, but also axisymmetric and three-dimensional plume flowfields with state-of-the-art CFD methodology.
- Procedures for conducting meaningful thermo-vision camera studies were developed.
- The final report on this study provides user's manuals for the codes developed, and the source codes were delivered to NASA for their use.

RESULTS: The NOZZRAD code was validated for preliminary base heating design use. The FDNS code was validated for SRM nozzle analysis. The potential of the IDARAD code was identified for future use. New treatments of Al_2O_3 optical property data base were recommended for making better use of existing test data.

POTENTIAL APPLICATIONS: The radiation analyses methods developed in this study are useful for predcicting and understanding thermal environments of launch vehicles and launch stand facilities, of missile infrared missiles, and of decoy designs to defeat heat seeking missiles. The methodology is also appropriate to furnace design and the thermal loads produced within gas turbine and diesel engines.

NAME AND ADDRESS OF CONTRACTOR:

SECA, INC.
3313 Bob Wallace Avenue
Suite 202
Huntsville, AL 35805

PRINCIPAL INVESTIGATOR:

Richard C. Farmer

Foreword

The document presents the results of a phase II SBIR study performed by SECA, Inc. to investigate Radiation from Advanced Solid Rocket Motor Plumes. The study was performed for NASA Marshall Space Flight Center under Contract NAS8-39370. The NASA/MSFC technical monitor for the study is Mr. Peter R. Sulyma.

TABLE OF CONTENTS

1.0 INTRODUCTION

An investigation was conducted to develop an understanding of solid rocket motor (SRM) plumes which was sufficiently accurate to explain the majority of plume radiation test data. The goal of this study was to produce methodology which can be used as a design tool for predicting the radiation environment created by the plumes of a launch vehicle. Considering the vast expenditures of many government agencies on experimental studies of SRM plume related problems, the successful completion of this investigation offers a significant potential cost savings.

Historically, SRM plume radiation has been underpredicted by existing analytical methods. This was attributed to unrealistically low values of the imaginary part of the index of refraction of Al_2O_3 and the neglect of the searchlight effect which redistributes interior motor radiation into the plume. Grumman's shock tube experiments to obtain better Al_2O_3 optical property data (Ref. 1.1) and Remtech's development of a Monte Carlo code to include the searchlight effect (Ref. 1.2) allowed significant improvement in plume radiation predictions. However, several additional factors which affect particle size and temperature and the need for a more efficient radiation prediction code required more study. This investigation was designed to provide these improvements. However, several concurrent researches , namely: (1) the continued improvement of optical property data (Ref. 1.3), the development of a new heat transfer analysis to account for particle/gas heat exchange (Ref. 1.4), extensive measurements of particle size distribution in SRM plumes (Ref. 1.5), and recent access to Russian data on plume radiation (Ref. 1.6), greatly influenced the final outcome of this study. One of the more significant concurrent studies that helped improve the radiation base heating predictions was the development of the improved Cycle 2.0 solid rocket motor flowfield methdology which incorporates the results of these recent studies into the heating analysis (Ref. 1.7).

This investigation addressed: the evaluation of particle and gas radiation data, the development of a computationally efficient radiation analysis, and the prediction of the two-phase flowfield. Finally, predictions and comparisons to other methodology of specific test data will be presented to evaluate the utility and contribution made by this study.

2.0 PLUME RADIATION PROPERTIES

Radiation properties of the optically active plume species and the method of analyzing the radiative transfer process control the accuracy of predicted plume radiation. These subjects are described in Sections 2.1, 2.2 and 2.3.

2.1 Radiation Properties

SRM plume radiation heating is predominately from Al_2O_3 particles and is augmented by gaseous radiation from combustion products, namely: CO_2, H_2O, CO, and HCl. Soot particles may also contribute to the radiation, but an accurate measure of such radiation has not yet been established. Exhaust products from liquid rocket motors (LRM), which utilize RP-1, H_2, and O_2 as propellants, comprise a subset of these radiating species, hence an analysis which is acceptable for SRM's will also be appropriate for most launch vehicle design purposes. These plume constituents radiate in the following manner in the near infrared region of the spectrum which controls radiation heating:

1. Al_2O_3 and, perhaps, soot particles are large enough that they emit, absorb, and scatter radiation in a continuous frequency spectrum. The real and imaginary parts of the index of refraction are obtained from experiments, and Mie theory is usually used to convert from index of refraction values to absorption and scattering coefficients.

2. Gaseous radiation in the infrared is non-continuous, non-luminous molecular radiation associated mainly with rotational and vibrational energy modes.

Radiation predictions involve solving the radiative transfer equation (RTE), an energy balance on radiation, which requires specification of absorption and scattering coefficients. This section addresses the evaluation of such coefficients.

2.1.1 Particle Radiation

Thermal radiation from SRM plumes occurs between 0.5 and 8.0 μm, as shown by a typical SRM spectral signature in Fig. 2.1. The spectral data shown in this figure were taken by Sverdrup Technology personnel (Ref. 2.1) for MNASA-6, a subscale ASRM test motor. The spectrometer sees a 6-inch circle at the plume centerline about 24 inches downstream of the nozzle exit. The spectrometer was located 340 feet from the nozzle at an elevation of 10 feet. The nozzle exhausted upward from an elevation of 17 feet. The radiation peaks in the 1-2 μm wavelength region, and absorption by cool combustion gases along the plume boundary and by the atmosphere between the plume and the detector cause the dips in the radiance at the band centers. Al_2O_3 optical properties are authoritatively described by Reed, et al (Ref. 2.2) and indicate that liquid alumina has an imaginary index of refraction (N_2) of:

$$N_2 = 4.66E\text{-}4 \ \lambda^{1.33} \ T^{1.5} \ \exp\{-29420/T\}$$

independent of impurities in the alumina. For solid, crystalline alumina, the state, whether α or γ, and impurity levels have a strong effect on N_2. Particle samples taken from the centerline of an SRM plume, designated Rocket 1, and from the edge of the plume, Rocket 2, were measured by Grumman (Ref. 2.3). The Rocket 1 particles were found to have less impurities than the Rocket 2 particles and to have lower values of N_2 but still higher than pure alumina. Rocket 2 particles in the solid phase had an N_2 which was essentially that of the liquid at the melt point. Recently, the use of argon as a carrier gas in these shock tube experiments has been questioned (Ref. 2.2). When a CO/CO_2 carrier gas was used, lower values of N_2 were measured for pure alumina liquid particles. Sufficient experiments to fully qualify this observation with respect to particles collected from SRM plumes have not yet been performed. The effect of γ to α phase transformations will be considered subsequently. For the present, the current Grumman shock tube data for alumina particles will be used as the best available data for N_2 (Ref. 2.2).

Fig. 2.1 Spectral Radiance from the MNASA6 SRM
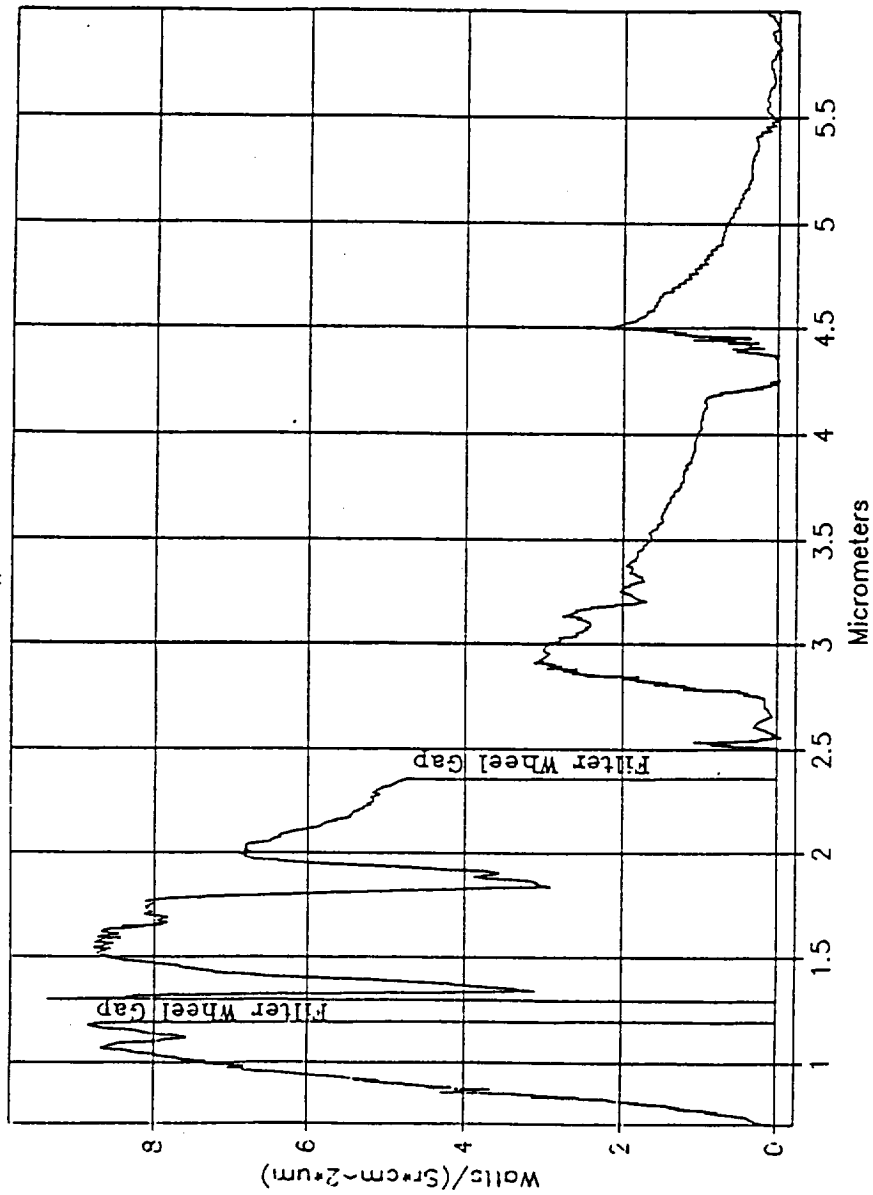
FILE: REDNASA6.SPC

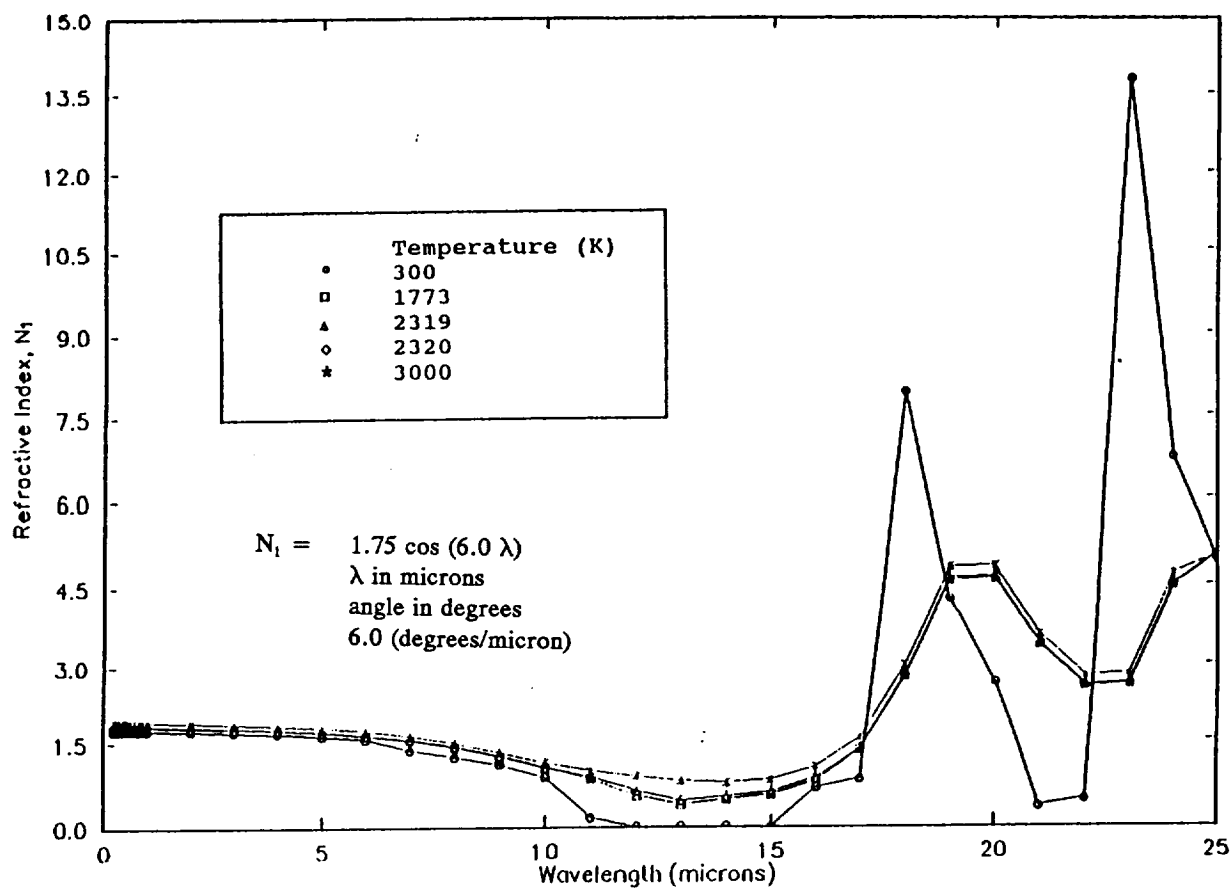IRIG time = 19:29:53.609

Gain = 2.07

The real part of the index of refraction, N_1, is insensitive to impurities and to temperature. In the spectral interval of interest, it varies slightly with wavelength, and is well represented by:

$$N_1 = 1.75 \cos\{6\lambda\}$$
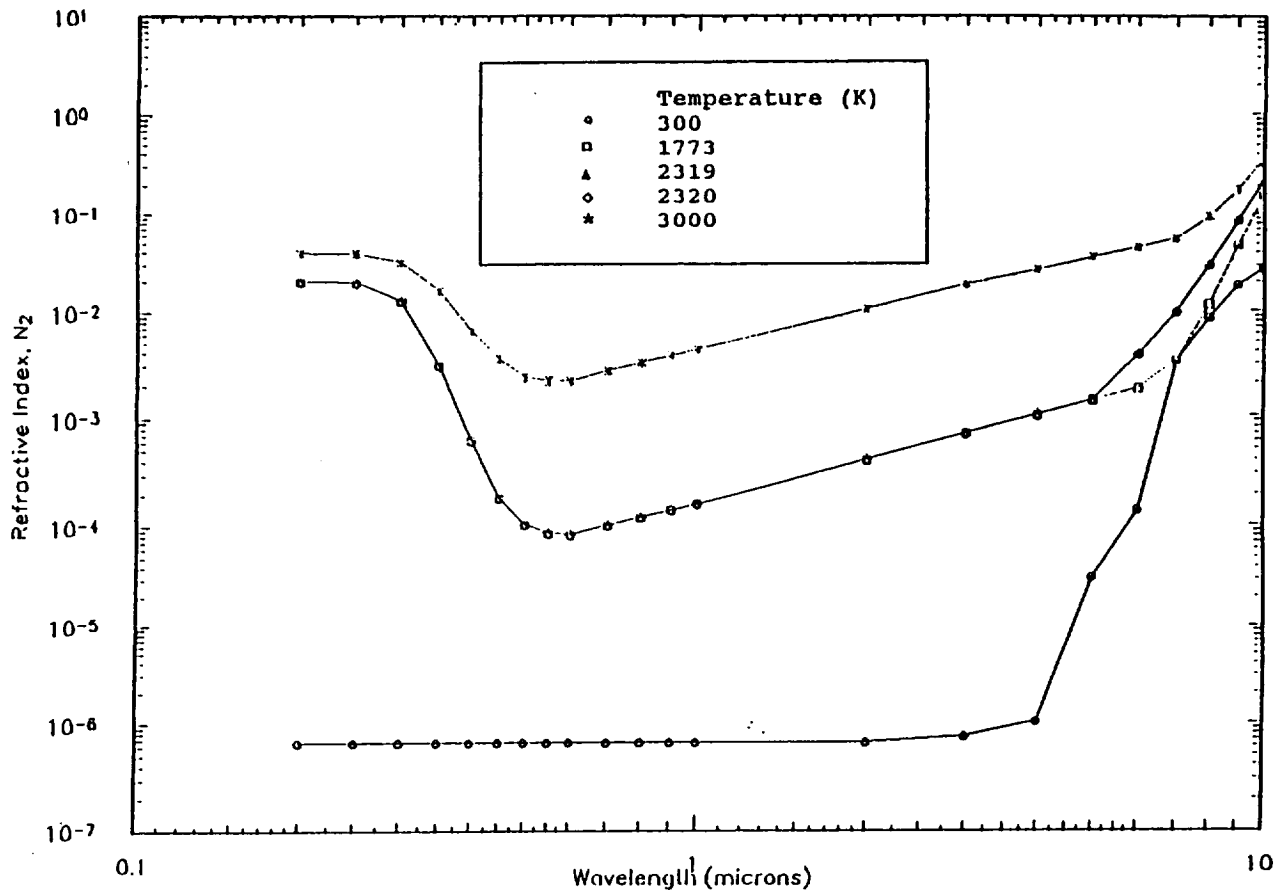
where the 6 has units of degrees/micron.

Optical properties for Al_2O_3 were obtained from Grumman's OPTROCK data (Ref. 2.4). Plots of the refractive index N_1 and the absorptive index N_2 are given in Figs. 2.2 and 2.3. These data were transformed to radiation properties by a MIE scattering code (Ref. 2.5) which determines absorption and scattering cross-sections as well as phase functions. The OPTROCK data includes wavelengths ranging from 0.2 to 25 μm. Notice that between 0.5 and 8 μm there are much less variation in the data. Additional work has been reported (Ref. 2.2) to provide the previously mentioned curve-fits of the absorptive index for the liquid Al_2O_3 optical property data. Since Al_2O_3 radiation is continuum in the region of interest, no problem exists with respect to defining a meaningful spectral average for a given wavelength.

Scattering angle dependence on the diffractive, reflective and absorptive processes are determined through the phase function, P, as illustrated in Fig. 2.4. Note that a specific value of $\log_{10} P$ is computed for each scattering angle COS (Θ). These figures indicate that as the size parameter ($X = \pi D/\lambda$) increases, forward scattering increases. The smoothing effect of using a particle size distribution is not illustrated by Fig. 2.4, but it is expected. It is known that Mie scattering theory is a good approximation for forward scattering for large non-spherical particles. Since extinction is dominated by scattering in the forward direction (as seen in these figures), then scattering is not very sensitive to particle shape. This justifies using the Mie theory. The OPTROCK data for N_1 and N_2 were used to create the data tables for σ_e, albedo, and the backscattering fraction in SIRRM (Ref. 2.6). SECA's MIE code is used to predict σ_s, σ_a, and the backscattering function. Using both SIRRM and the MIE code results in the radiation predictions for a homogeneous slab shown in Fig. 2.5. Data at temperatures of 2300 and 3000 °K are in the tables; the intermediate temperatures of 2500 and 2800 °K are not. Obviously,

N_1 as a function of λ and temperature
— Grumman's "OPTROCK" Data

The chart shows Refractive Index, N_1 (y-axis, 0.0 to 15.0) versus Wavelength (microns) (x-axis, 0 to 25).

Legend — Temperature (K):
- • 300
- □ 1773
- ▲ 2319
- ◊ 2320
- ∗ 3000

$$N_1 = 1.75 \cos (6.0\ \lambda)$$
λ in microns
angle in degrees
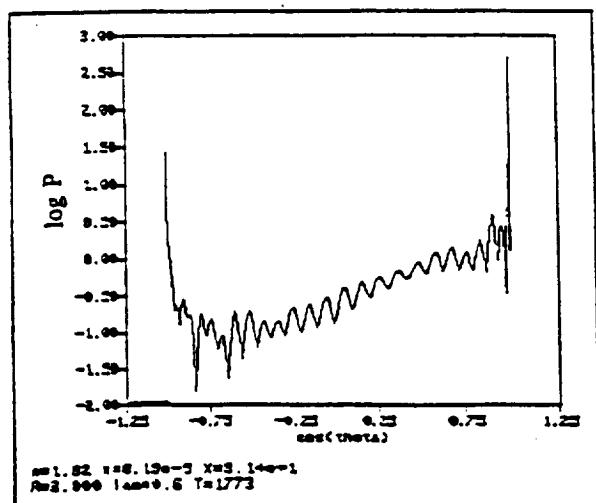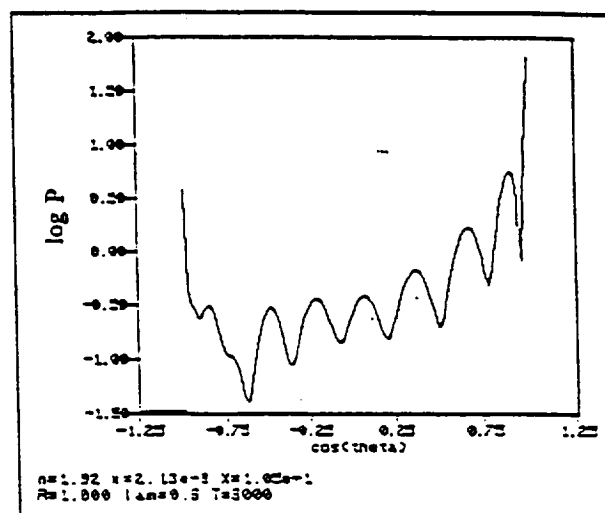6.0 (degrees/micron)

Fig. 2.2

N_2 as a function of λ and temperature
— Grumman's "OPTROCK" Data

Fig. 2.3
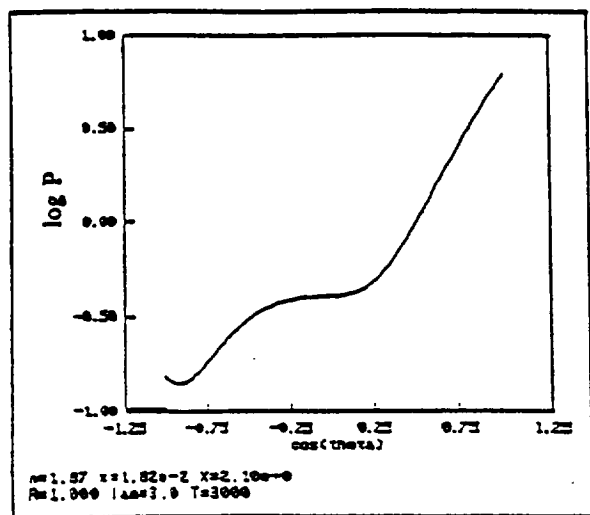
**PHASE FUNCTION AS
DETERMINED BY
MIE THEORY
CALCULATION**

Optical properties: n,κ
Particle Radius: R
Wavelength: lam
Temperature: T
Particle Size
  Parameter: X=2πR/λ

Fig. 2.4
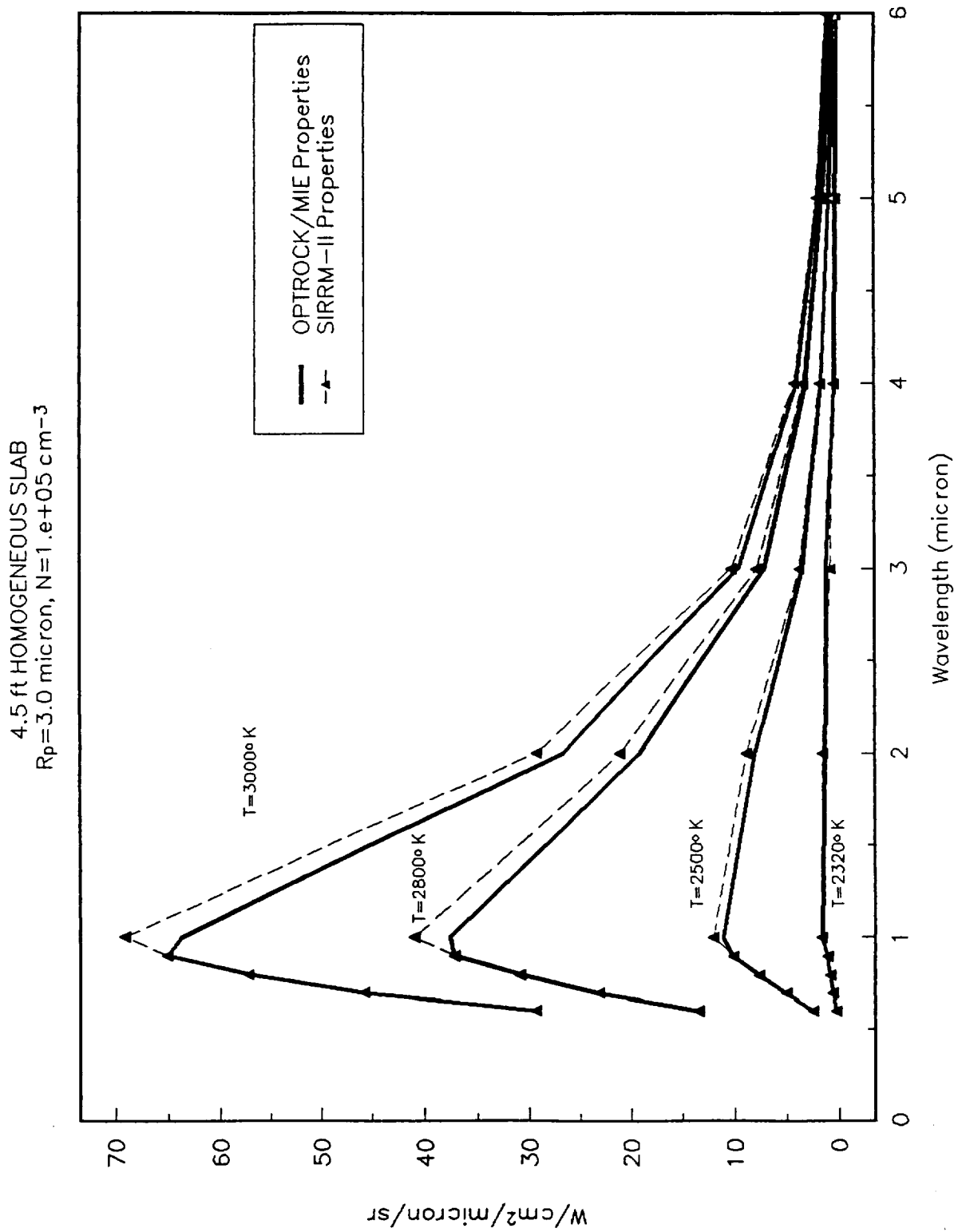
Fig. 2.5 SIRRM and Mie Code Comparison for an Isothermal Slab

differences in the interpolation schemes for the MIE and SIRRM codes exist; methods of reducing these differences will be discussed later in this section.

Several investigators have postulated that rapid quenching of molten Al_2O_3 particles leaves them in a γ state rather than the more usual α state and that this state exhibits greatly different radiative properties. Russian investigators (Ref. 2.7) made a study of this effect with both laboratory and flight experiments, but the investigation was limited to small wavelengths, such that IR heating could not be evaluated. The Russian investigators experimentally demonstrated the importance of alumina impurities and γ/α phase transitions, but offered no general purpose models for predicting these effects. The largest wavelength observed was $1.1\mu m$ where at most a 20% increase in radiance was observed. PSI investigators (Ref. 2.8) observed high emissivities of pure alumina solid particles which were rapidly cooled in a shock tube, which substantiates the Russian experiments. However, most of the plume radiance data which are difficult to evaluate are for conditions where the particles are molten as they leave the nozzle in the plume where the radiance was measured. Sverdrup investigators (Ref. 2.9) predicted particle states for a specified phase transition kinetics rate; no optical data were presented to support this analysis. Other Sverdrup investigators (Ref. 2.10) sampled rocket plumes and determined the ratio of α/γ crystals in the particles and used these data to deduce a kinetics expression for the phase transition. As mentioned previously, impurities in the Al_2O_3 dominate the solid phase optical properties, and none of the phase transition studies have yet addressed the effects of impurities on observed optical properties.

The data shown for N_2 of solid Al_2O_3 in Fig. 2.3 suggest that using properties for solid particles at the melting temperature is valid at all temperatures; since the room temperature data are for pure Al_2O_3. This idea has not yet been evaluated with a radiation heating analysis, but it should be.

Although several questions concerning Al_2O_3 optical property data have not yet been satisfactorily answered, available Grumman data are believed to be sufficiently reliable to be

used for plume radiation analysis. This is especially true for the purpose of making validation predictions for available rocket plume test data.

Absorption coefficient data for soot are found in the radiation handbook (Ref. 2.9) and complex index of refraction values are found in documentation for SIRRM (Ref. 2.6). Other data sources for soot are not considered sufficient for consideration. Optical properties for soot are reasonably well known; the problem is that the accurate predictions of particle size and number density for the soot particles cannot yet be made.

2.1.2 Gaseous Radiation

To solve the RTE for gaseous (molecular) radiators, a value of the absorption coefficient (κ_λ) must be provided. For monochromatic radiation this is possible, but too many individual lines must be considered to make a practical heat transfer analysis by simply summing the lines. Three alternatives have been proposed in the literature: (1) the use of narrow band models (Refs. 2.6 and 2.11), the use of wide-band models (Refs. 2.12 and 2.13), and the use of a total emissivity (Ref. 2.14). It should be noted that linear absorption coefficients (κ_λ) are required to solve the RTE; hence, if mass $(\kappa_{\rho\lambda})$ or pressure $(\kappa_{p\lambda})$ absorption coefficients are taken from correlation equations, they must be converted before they are used. Both the narrow and wide band models involve spatial averaging along a line-of-sight (LOS) before spectral averaging over a spectral interval can be accomplished. Unless this procedure is reversed, severe restrictions on the method of solving the RTE result. Theoretically, the narrow band models involve summations over many narrow spectral intervals, whereas the wide band models treat an entire band at one time. However, the entire band modeling procedure has not yet been developed to the point that a rigorous method of inverting the spatial/spectral integration is available. The total emissivity method has only been studied for the CO_2/H_2O system, is completely empirical, and is not practical for the several plume species with strong temperature, concentration, and pressure gradients in the flowfields of interest.

The extensive radiation data developed by MSFC in support of the Saturn program (Ref. 2.11) provides the narrow band (NB) absorption coefficients for plume gases for many SRM and LRM. Inhomogeneous optical paths are treated with the modified Curtis-Godson approximation to allow spatial integration along a LOS. Remtech's Monte Carlo (Ref. 2.15) and GASRAD (Ref. 2.16) codes and the SIRRM two-flux and six-flux radiation models use these narrow band models for evaluating plume radiation (Ref. 2.17). Integrations along specific LOS are performed for spectral intervals of 100 to 400 cm^{-1} wave numbers. The narrow spectral intervals require lengthy computation times to evaluate radiative heating. Furthermore, local absorption coefficients are not provided by the narrow band model which are useful for obtaining solutions to the RTE by more general and economical methods. Such absorption coefficient evaluation methods could be developed, but the narrow spectral interval integrations would still be required.

Since the radiation model developed by this study was to be designed to be fast and economical to use, the exponential wide band (EWB) model (Ref. 2.12) was investigated for use in solving the RTE. This model was developed to describe radiation from a LOS with constant temperature, pressure, and composition for each major band of the optically active species present. In general, the test data that the EWB model is based upon were taken at higher pressures than the NB model data previously mentioned, but still at pressures much lower than typical rocket motor combustion chamber pressure. Correlation parameters for this model are given in Table 2.1 for the following thermally important bands for H_2O, CO_2, and CO:

$$\lambda_{H2O} = 1.38, 1.87, 2.7, \text{ and } 6.3 \ \mu m$$
$$\lambda_{CO2} = 2.0, 2.7, 4.3, 9.4, \text{ and } 10.4 \ \mu m$$
$$\kappa_{CO} = 2.35 \text{ and } 4.7 \ \mu m$$

Table 2.1 Wide band model correlation parameters for various gases

Band Location		Pressure Parameters		Correlation Parameters		
λ [μm]	(δ_k)	n	b	α_0 [cm^{-1}/(g/m^2)]	γ_0	ω_0 [cm^{-1}]
H$_2$O m = 3 , η_1 = 3652 cm^{-1}, η_2 = 1595 cm^{-1}, η_3 = 3756cm^{-1}, g$_k$ = (1, 1, 1)						
6.3μm	η_c = 1600 cm^{-1} (0,1,0)	1	8.6 (T$_0$/T)$^{0.5}$ +0.5	41.2	0.09427	56.4
2.7μm	η_c = 3760 cm^{-1} (0,2,0) (1,0,0) (0,0,1)	1	8.6 (T$_0$/T)$^{0.5}$ +0.5	0.2 2.3 23.4	1.03219	60.0
1.87μm	η_c = 5350 cm^{-1} (0,1,1)	1	8.6 (T$_0$/T)$^{1.5}$ +1.5	3.0	0.08169	43.1
1.38μm	η_c = 7250 cm^{-1} (1,0,1)	1	8.6 (T$_0$/T)$^{1.5}$ +1.5	2.5	0.11628	32.0
CO$_2$ m = 3, η_1 = 1351cm^{-1}, η_2 = 666 cm^{-1}, η_3 = 2396^{-1}, g$_k$ = (1,2.1)						
10.4μm	η_c = 960 cm^{-1} (-1,0,1)	0.8	1.3	2.47X10^{-9}	0.04017	13.4
9.4μm	η_c = 1060 cm^{-1} (0,-2,1)	0.8	1.3	2.48X10^{-9}	0.11888	10.1
4.3μm	η_c = 2410 cm^{-1} (0,0,1)	0.8	1.3	110.0	0.24723	11.2
2.7μm	η_c = 3660 cm^{-1} (1,0,1)	0.65	1.3	4.0	0.13341	23.5
2.0μm	η_c = 5200 cm^{-1} (2,0,1)	0.65	1.3	0.060	0.39305	34.5
CO m = 1, η_1 = 2143 cm^{-1}, g$_1$ = 1						
4.7μm	η_c = 2143 cm^{-1} (1)	0.8	1.1	20.9	0.07506	25.5
2.35μm	η_c = 4260 cm^{-1} (2)	0.8	1.0	0.14	0.16758	20.0

Methods to average the EWB model for inhomogeneous path lengths, simply average the temperature and species over a finite length (Ref. 2.18). This is not an appropriate method for obtaining local values of the absorption coefficient. Modest devised a method for defining local coefficients by using an optically thin and a mean beam length to define the two variables: absorption coefficient and effective band-width (Ref. 2.19). Even though the accuracy of such a method has not yet been established, this method was used by Modest in conjunction with a first order ordinary differential approximation. SECA used the same EWB model in the ordinary and improved differential approximation methods which are described in the next Section.

Ultimately, both particle and gaseous radiation must be described. Figure 2.6 shows a LOS calculation for a particle gas mixture which was made with the narrow band models in SIRRM (Ref. 2.6). This example was taken from a slice out of a SRM plume. The radiation looks like an averaged absorption coefficient for the Al_2O_3 particle gas mixture was used. However, gas/particle radiation interaction can look quite different, depending on specific concentration and temperature variations along the LOS.

The narrow band models, such as those used in the JANNAF standard plume radiation code, SIRRM, are the most accurate molecular radiation models currently available. However, the spectral integration required to use such models is too computationally intensive for economical use and probably prohibitive for practical use in a fully coupled solution. Therefore, an evaluation of the EWB model was made in this investigation.

2.2 Solution of the RTE by Using Differential Approximations

The radiation analysis developed for this study is uncoupled, in the sense that the flowfield is first calculated then the radiation resulting from the predicted temperature distribution is calculated. Such a treatment assumes that the energy lost by radiation is small compared to the energy in the flowfield. The plume's of SRM's emit, scatter, and absorb, so
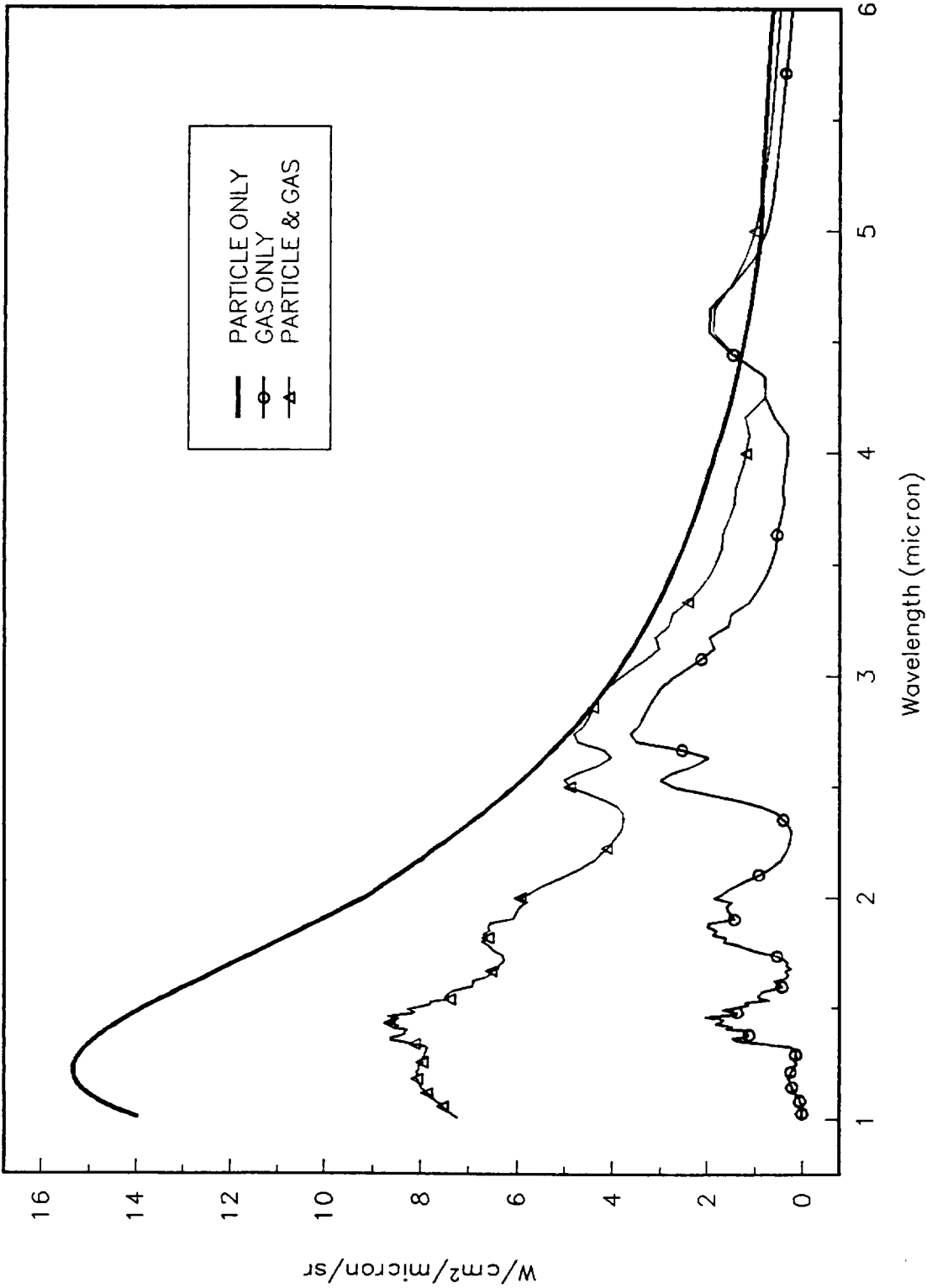
Fig. 2.6 Gas/Particle Radiation Interaction

that a solution to the general radiative transfer equation (RTE) is needed for the intensity, I_λ. Hence the intensity obtained from the RTE given below must be integrated in wavelength to obtain heating rates.

$$\vec{\Omega} \cdot \nabla I_\lambda\{\vec{r}, \vec{\Omega}\} = \kappa_\lambda I_{\lambda b}\{T\} - (\kappa_\lambda + \sigma_\lambda) I_\lambda\{\vec{r}, \vec{\Omega}\}$$

$$+ \frac{\sigma_\lambda}{4\pi} \int_{4\pi} P\{\vec{r}, \vec{\Omega}' - \vec{\Omega}\} I_\lambda\{\vec{r}, \vec{\Omega}'\} d\Omega' \tag{1}$$

The RTE may be formally integrated over space to obtain:

$$I\{\vec{r}, \vec{\Omega}\} = I\{\vec{r}', \vec{\Omega}\} e^{-\tau}$$

$$+ \int_0^\tau e^{\kappa t} \left[\kappa I_b\{\vec{r}\} + \frac{\sigma}{4\pi} \int_{4\pi} I\{\vec{r}, \vec{\Omega}\} P\{\vec{r}, \vec{\Omega}' - \vec{\Omega}\} d\vec{\Omega}' \right] dt \tag{2}$$

The subscript λ is suppressed in this and subsequent equations for clarity, but it must be remembered that the intensities are appropriately averaged monochromatic values. Direct numerical solutions to the integrated RTE have been reported by Tan (Ref. 2.20) and Tan and Howell (Ref. 2.21). These methods are quite interesting, but such solutions have not been performed for problems as complex as those found in rocket plumes. To provide efficient solutions to the RTE, a variation of a differential approximation and a generalized two-flux model were chosen for further development in this study. Details of these methods are described in the remainder of this Section. Of course, the Monte-Carlo method (Ref. 2.15) could have been used for solving the RTE, but this method was not deemed to be sufficiently fast for exploratory studies or for routine use.

2.2.1 The ODA Method

The method of spherical harmonics (a type of differential approximation) was developed for solving the RTE. The method of spherical harmonics is implemented by expressing the phase function and intensity as Legendre polynomials as shown in Chart 2.1. The result of these transformations is to replace the integro-partial differential equation with partial differential

Chart 2.1

SOLUTIONS TO THE RTE USING SPHERICAL HARMONICS

(P_N - Approximation)

<u>The P_1 - Approximation</u> (ODA) requires solutions of PDE's to evaluate the integrated form of the RTE rather than integral equations:

1. Express the intensity as a generalized Fourier Series using Legendre Polynomials.

2. Express the Phase Function with Legendre Polynominals

$$P\{\vec{r}, \ \vec{\Omega}' - \vec{\Omega}\} = 1 + A_1 \vec{r} \cdot (\vec{\Omega}' - \vec{\Omega})$$

<u>Requires solution to:</u>

$$\nabla_\tau \cdot \left(\frac{1}{(1 - A_1 \omega/3)} \nabla_\tau G \right) = -3(1 - \omega)(4\pi I_b - G)$$

If $A_1 \omega$ is constant, this is an elliptic PDE. When solved,

$$\vec{q} = - \left(\frac{1}{3 - A_1 \omega} \right) \nabla_\tau G$$

G is incident radiation at a point

$$G\{r\} = \int_{4\pi} I\{\vec{r}, \ \vec{\Omega}'\} \, d\Omega'$$

$$I\{\vec{r}, \ \vec{\Omega}\} = \frac{1}{4\pi} [G\{\vec{r}\} + 3\vec{q}\{\vec{r}\} \cdot \vec{\Omega}]$$

Limitation: For N=1 or 3, accurate for only optically thick media.

equations (PDE). The P_1 approximation or the ordinary differential approximation (ODA) is shown along with the one PDE which must be solved, but this method is accurate only for optically thick media. Higher order P_N approximations may be used, but the accuracy increases slowly with the order of the solution whereas the number of partial differential equations required for a solution increases dramatically. For the P_3 approximation 4 simultaneous PDE must be solved. Modest (Ref. 2.19) has suggested the Modified Differential Approximation (MDA) and the Improved Differential Approximation (IDA) as shown in Charts 2.2 and 2.3, respectively. The IDA is simpler to use, and it has the advantage of starting from the P_1 solution. Hence, if the media is optically thick, i.e. inside the motor, only this part of the analysis is required. Having the P_1 solution, the J, G, and $\bar{q}$ terms shown in Chart 2.3 must be evaluated for each point where a solution is desired, i.e. at each grid point in the flowfield.

To obtain the P_1 solution, the RTE will be written explicitly in terms of cylindrical coordinates (Ref. 2.22) as

$$\frac{1}{\sigma}\left[\cos(\phi-\phi_r)\sin\theta\frac{\partial}{\partial r} + \sin(\phi-\phi_r)\frac{\sin\theta}{r}\frac{\partial}{\partial\phi_r} + \cos\theta\frac{\partial}{\partial z}\right]I_v(r,\phi_r,z;\theta,\phi)$$
$$+ I_v(r,\phi_r,z;\theta,\phi) = (1-\omega)I_{b_v}$$
$$+ \frac{\omega}{4\pi}\int_o^{2\pi}\int_{-1}^{1}I_v(r,\phi_r,z;\theta',\phi')P(\theta,\phi;\theta',\phi')d\cos\theta'd\phi'$$

$$(3)$$

To transfer Eq. 3 to the P_1-approximation, the phase function is defined by:

$$P(\vec{\Omega},\vec{\Omega}') = \sum_{l=o}^{N}\sum_{m=-l}^{l}\rho_l Y_l^m(\vec{\Omega})Y_l^{m*}(\vec{\Omega}')$$

$$(4)$$

Likewise, I, is expanded in spherical harmonics. Next, the first moment of the reformulated RTE is made, and after the same manipulation the P_1-approximation in cylindrical coordinates results in a Helmholtz equation for $I_{o,}$:

Chart 2.2

THE MODIFIED DIFFERENTIAL APPROXIMATION

The MDA generalizes P_1 solution to treat arbitrary optical thickness.

Let surface & media contribute to intensity:

$$I\{\vec{r}, \vec{s}\} = I_w\{\vec{r}, \vec{s}\} + I_m\{\vec{r}, \vec{s}\}$$

Solution requires evolution of:

$$G_w\{\vec{r}\} = \frac{1}{\pi} \int_{4\pi} J_w\{\vec{r}_w\}\, e^{-\tau_s}\, d\Omega$$

$$\vec{q}_w\{\vec{r}\} = \frac{1}{\pi} \int_{4\pi} J_w\{\vec{r}_w\}\, e^{-\tau_s}\, \vec{s}\, d\Omega$$

$$J_i = \epsilon_i\, \pi I_{bi} + (1-\epsilon_i) \sum_{j=1}^{N} J_i\, e^{-\tau_{ij}} F_{i-j}$$

$$\nabla_\tau\, G_m = A_1\, \omega\, (\vec{q}_w + \vec{q}_m) - 3\, \vec{q}_m$$

$$\nabla_\tau \cdot \vec{q}_m = (1-\omega) 4\pi I_b + \omega\, (G_w + G_m) - G_m$$

Chart 2.3

THE IMPROVED DIFFERENTIAL APPROXIMATION

The IDA has the same solution features as the MDA but is more computationally efficient.

Solution requires:

The ODA, i.e. the P_1 solution, and also:

$$J_w\{\vec{r}\} = \epsilon \pi I_{bw}\{\vec{r}\}$$

$$+ (1-\epsilon)\int\int_A \left[J_w\{\vec{r}'\}e^{-\tau_s} + \pi S^*\{\vec{r}-s_o\hat{s},\ \hat{s}\}(1-e^{-\tau_s})\right] \frac{\cos\theta \cos\theta'}{\pi S^2}\, dA$$

$$G\{\vec{r}\} = \int_A [J_w\{\vec{r}'\}e^{-\tau_s} + \pi S^*\{\vec{r}-s_o\hat{s},\ \hat{s}\}(1-e^{-\tau_s}) \frac{\cos\theta'\, dA}{\pi S^2}$$

$$\vec{q}\{\vec{r}\} = \int_A [J_w\{\vec{r}'\}e^{-\tau_s} + \pi S^*\{\vec{r}-s_o\hat{s},\ \hat{s}\}(1-e^{-\tau_s})]\,\hat{s}\, \frac{\cos\theta'\, dA}{\pi S^2}$$

$$\frac{1}{r}\frac{\partial}{\partial r}\left(r\frac{\partial I_{ov}}{\partial r}\right) + \frac{1}{r^2}\frac{\partial^2 I_{ov}}{\partial \phi^2} + \frac{\partial^2 I_{ov}}{\partial Z^2} - \Lambda^2 I_{ov} = -\Lambda^2 I_{bv}\{T\} \qquad (5)$$

For an axisymmetric system, the ϕ term is zero.

$$\Lambda^2 = 3\gamma_o\,\gamma_1\,\sigma_{ext}^2$$

$$\gamma_o = 1 - \omega\rho_o$$

$$\gamma_1 = 1 - \omega\rho_1/3$$

(for isotropic scattering, $\rho_o = 1$, $\rho_1 = 0$)

I_{ov} is the first moment of the scattering integral defined by:

$$I_{ov} = \int_0^{2\pi}\int_0^{\pi} I_v\,\sin\theta\,d\theta\,d\phi \qquad (6)$$

The radiation intensity in Eq. 6 is a function of position and direction. However, the evaluation of the Helmholtz equation above for the P_1-approximation eliminates the need to resolve the complicated angle dependencies within the integral. The azimuthal angle ϕ was eliminated from the original RTE by integration over all directions. In other words, when the first moment of the RTE is taken to derive the P_1-approximations, the ϕ term becomes:

$$\frac{1}{r}\frac{\partial I_{ov}}{\partial \phi_r}\int_0^{2\pi}\int_0^{\pi}\sin(\phi-\phi_r)\,\sin^2\theta\,d\theta\,d\phi$$

$$= \frac{1}{r}\frac{\partial I}{\partial \phi_r}(0) = 0 \qquad (7)$$

Equation 5 has been written in a discretized form suitable for computer simulation. The procedure for solving Eq. 4 proceeds from a successive-line overrelaxation (SLOR) method. Rewriting Eq. 5 with a source term defined by R_{Iov},

$$\nabla_c^2 I_{ov} = \Lambda^2 (I_{ov} - I_{bv}) = R_{I_{ov}} \tag{8}$$

∇_c^2 is the cylindrical operator corresponding to the differential terms on the left-hand side of Eq. 5.

Terms in Eq. 8 have been normalized with respect to reference values and will not be discussed further.

Boundary conditions for Eq. 5 are:

$$\begin{aligned}
\frac{\partial I_{ov}}{\partial r} &= 0 && (symmetry) \quad r=r, \\
\frac{\partial I_{ov}}{\partial Z} \pm h I_{ov} &= 0 && (inlet) \quad Z=Z_1(-) \\
& && (exit) \quad Z=Z_2(+)
\end{aligned} \tag{9}$$

where $h = 1.5\sigma_{ext} \gamma_1$. At the plume boundary there is no incoming radiation.

Once the P_1 solution is obtained, the IDA analysis can be accomplished. Since this radiation analysis is to be uncoupled, provision for using either SPF/2 and FDNS flowfield solutions will be provided as input for the plume radiation analysis.

2.2.2 The IDA Method

Since the ODA is not valid for optically thin regions, it was extended to accommodate all optical thicknesses through the IDA. The logic which allows the ODA to be transformed to the IDA lies in the linear approximation of the radiative source term s*, which is itself a function of the ODA results. Also, the radiation intensity at any point (i, j) in the medium is written as the sum of wall and medium contributions. Transmissivity of wall radiosities to the medium point are obtained from extinction coefficients that are evaluated from a Mie scattering code. The medium contribution includes an adjusted source term which is not evaluated at the medium point (i, j), but at an adjusted point. Instead of evaluating the derivative of s* at (i, j),

it is easier to evaluate S at a point τ_0 away from (i, j). This is accomplished by the following procedure.

A Taylor series representation for s can be written at a point (i, j) or $\overline{r} = \overline{r}_w + s_w\hat{s}$ in the medium by assuming that s varies linearly from $\overline{r}$ to $\overline{r}_w$ in the direction (-$\hat{s}$) by:

$$s^*(\overline{r}_w + s_w\hat{s}, \hat{s}) = s^*(\overline{r}, \hat{s}) - (\tau_s - \tau_{s_v})\frac{ds^*}{d\tau_s}(\overline{r}, \hat{s}) \qquad (10)$$

τ_s is the optical depth along a path length from (i, j) to $\overline{r}_w$, the star refers to values based upon ODA results, and subscript w corresponds to the wall. S_w is the magnitude of the vector $\hat{s}$ from the wall to $\overline{r}_w$. The radiative intensity in the medium is determined by straight-forward integration of:

$$I_m = \int_0^{\tau_s} s^*(\overline{r}_w + s_w\hat{s}, \hat{s}) e^{-(\tau_s - \tau_s')} d\tau_s'$$

$$(11)$$

$$= s^*(\overline{r}, \hat{s})(1 - e^{-\tau_s}) - \frac{ds^*(\overline{r}, s)}{d\tau_s}[1 - (1 + \tau_s)e^{-\tau_s}]$$

To eliminate the derivative in Eq. 11, the method is to take the assumed linearity of s in reverse order, transforming an integral to an unknown Taylor series. The procedure is to determine the Taylor series, call it L, that produces the RHS of Eq. 11:

$$L = RHS(2) \qquad (12)$$

Rearranging terms in Eq. 12 leads to

$$\frac{L}{1 - e^{\tau_s}} = s^*(\overline{r}, \hat{s}) - \left(1 - \frac{\tau_s e^{-\tau_s}}{1 - e^{-\tau_s}}\right)\frac{ds^*}{d\tau_s}(\overline{r}, \hat{s}) \qquad (13)$$

Comparison on Eqs. 10 and 13 gives the following correspondences:

$$\left(1 - \frac{\tau_s e^{-\tau_s}}{1-e^{-\tau_s}}\right) \leftrightarrow (\tau_s - \tau_{s_w})$$

$$\left(\frac{L}{1-e^{-\tau_s}}\right) \leftrightarrow S^*(\vec{r}_w + s_w \hat{s}, \hat{s})$$

In this way, $(\gamma_s - \gamma_{sw})$ is replaced by γ_o, where

$$\tau_o = 1 - \frac{\tau_s e^{-\tau_s}}{1-e^{-\tau_s}} \tag{14}$$

Then $(s_w \hat{s})$ is replaced by $(-s_o \hat{s})$ since the series is taken in reverse order, so that the radiative source term becomes $s^*(\vec{r}_w - s_o \hat{s}, \hat{s})$, and s_o is backed out from

$$\tau_o = \int_0^{s_o} \sigma_{ext}(\vec{r} - s'' \hat{s}) \, ds'' \tag{15}$$

Finally, from

$$\frac{L}{1-e^{-\tau_s}} = s^*(\vec{r}_w - s_o \hat{s}, \hat{s})$$

we obtain the result

$$I_m = L = \int_0^{\tau_s} s^*(\vec{r}_w + s_{w_o} \hat{s}, \hat{s}) e^{-(\tau_s - \tau_s')} d\tau_s' \tag{16}$$

$$\approx s^*(\vec{r}_w - s_o \hat{s}, \hat{s}) (1-e^{-\tau_s})$$

s_o is the physical distance across the LOS into the plume, and

$$S^*\{\vec{r}_w - s_o \vec{s}, \vec{s}\} = (1-\omega)I^*_b\{\vec{r}_w - s_o \vec{s}\} + (\omega/4\pi)[G^*\{\vec{r}_w - s_o \vec{s}\} + A_1 \vec{q}^*\{\vec{r}_w - s_o \vec{s}\} \bullet \vec{s}] \tag{17}$$

2-23

Eq. 16 replaces Eq. 10 and does not require an evaluation of a derivative, but the value for s_o must be found along each line-of-sight according to Eq. 15. The radiative source contribution at (i, j) is transformed to evaluating a radiative source a distance s_o from point (i, j) in the direction toward the wall.

The IDA modules were coded for accepting FDNS or SPF/2 flowfields as input. Briefly, the IDA modules are set up to allow the user to choose the number of wall points deemed important for radiosity computations; a reduction in CPU requirements will result if fewer wall points are chosen. A view factor code then evaluates view factors between wall segments, after which the optical distance between wall points and between medium and wall points are determined. Adjusted source terms, wall radiosities, and wall and medium contributions to the incident radiation are then evaluated.

Analyses for gaseous radiation based upon the exponential wide band (EWB) model for the absorption coefficients of H_2O and CO_2 was included in the ODA and IDA codes. The rocket fuels of interest create aluminum oxide particles and soot in the combustion process and other gases, primarily CO and HCl. Using the FDNS-EL code, two-phase flowfield predictions can be post-processed through a SIRRM map module that determines the particle density, gas phase species concentrations, pressure, and temperature as a function of position. Combining the Mie code with the optical property data for Al_2O_3 to get absorption and scattering coefficients, along with the SIRRM map, particle radiation computations can be made. This procedure has been implemented for the ODA where the scattering integral is now accounted for through the albedo and an isotropically scattering phase function. Multiple solutions of the RTE equation are used to predict monochromatic or band averaged intensities; these intensities are then summed to obtain total radiative transfer.

A similar procedure was used for the IDA. The only remaining step for the IDA gas/particle radiation method was the development of an optical path procedure between two points so that surface radiosity and source effects can be determined. Since the ODA method

2-24

is valid only in optically dense regions and can be substantially in error when surface emission dominates over medium emission, it was extended to include arbitrary optical densities through the IDA method. This is especially necessary for plume regions where the optical thickness is relatively small. The main concept in the IDA is to bring in the wall or geometric influence to the radiation calculation at all flowfield points. In the ODA methodology, the Legendre Polynomial Series expansion for the radiation intensity and the phase function were sufficient to account for an optically dense region. But in optically thin cases, the influence of radiation from one point to another requires extending the optical path farther out. The IDA procedure accomplishes this by incorporating the wall effects into the formulation. It is therefore important to be able to choose, for each flowfield node, a sufficient number of lines-of-sight to the wall surfaces to properly account for the radiosity effects. To simplify the logic, the radiation intensity is split into two terms, one for the wall and one for the medium. The three steps to an IDA solution are: 1) ODA solution for the flowfield node source term, 2) surface integrals for wall radiosities, and 3) surface integrals for flowfield node incident radiation.

An important part of the surface integral, the geometric component, requires the evaluation of the view factors between two wall points and of the solid angles between a wall and a flowfield node. An existing code, RAVFAC (Ref. 2.23) was incorporated into the IDA solver, along with a preprocessor code that initializes RAVFAC with surface data for a nozzle configuration. The coordinates of the nozzle wall are obtained from a grid file, and then the line connecting two neighboring wall boundaries are described as either a circular disk (inlet), a cylinder (combustor wall) or a cone (converging and diverging nozzle sections). Other input variables describe the local coordinate system of each surface shape to allow the evaluation of unit normals and the determination of whether a surface is shaded by another surface. The accuracy in describing view factors between wall surfaces can be chosen relative to the number of angular planes desired. This can range from a single 360-degree circumferential surface, resulting in circular band or hoop shapes, to any portion of 360 degrees, which results in a much larger number of wall-to-wall combinations. In addition, code was provided to allow the

calculation of the solid angles between wall points and flowfield points, which is needed for the evaluation of the incident radiation.

Another important aspect of the IDA requires the evaluation of source terms and optical distances along various lines-of-sight. As mentioned previously, the flowfield influence to the IDA equations includes the source term S^* from the ODA as part of its solution. Instead of using S^* at a particular flowfield point, however, an adjusted S^* is required. A module that determines the optical length along a chosen line-of-sight was added to the IDA code, along with the logic that determines the adjusted S^*. Lines-of-sight are chosen to extend from the axisymmetric plane, where the flowfield solution is known, to other circumferential planes. The line-of-sight module evaluates the product of the extinction coefficient and a differential distance, for each increment along a line-of-sight from a flowfield node to a wall node, and sums these values for a total optical depth τ_s. An adjusted source location $S_\emptyset$ along the line-of-sight is backed out from $\tau_\emptyset = \mathrm{fn}\,(\tau_s)$. Once the value of $S_\emptyset$ is determined, its coordinates are extended back to the axisymmetric plane, from which the new S^* can be interpolated. The surface integrals for radiosity, J_w, and incident radiation, G, then follow from the variables described above. An inversion routine for J_w that is efficient in inverting a matrix with non-zero entries in almost every location (the entries have a zero value where the view factors between surface nodes are zero) was also included. Specifically, the equation for the wall radiosity can be written as:

$$[A]\ [J_w] = [R] \tag{18}$$

where the elements of matrix A are

$$a_{ii} = 1 - (1 - \epsilon_i)\, e^{-\tau_{ii}}\, F_{ii} \tag{19}$$

and the right-hand-side is

$$a_{ij} = -(1 - \epsilon_i)\, e^{-\tau_{ij}}\, F_{ij} \tag{20}$$

and the right-hand-side is

$$R_i = \epsilon_i \pi I_{bi} + (1-\epsilon_i) \sum_j S_{ij}^* (1-e^{-\tau_{ij}}) F_{ij} \tag{21}$$

The F_{ij} is the view factor from surface node i to surface node j. This matrix differs from the usual equation for J_w by the addition of the adjusted ODA source term S^*.

The discussion to this point has focused on the radiation solution within a region enclosed by solid walls, an inlet and an exit. The method was extended to plume regions where radiation heating to a rocket base region must be determined. To accomplish this task appropriate boundary conditions must be specified on the boundaries for the initial ODA solution. In particular, if the plume region is solved independently from the nozzle flowfield (after the nozzle solution is obtained), the nozzle exit can be prescribed with the following condition:

$$I = \frac{\alpha \epsilon \sigma T_{exit}^4}{\pi} \tag{22}$$

with the percent of radiation crossing the exit plane specified by α (Ref. 2.24), and with an emissivity specific to the gas and particle mixture at each exit point. For the other boundaries, a constant radiation intensity can be specified as above. Lines-of-sight from the rocket base region to any point within the plume can be accomplished as was done within the nozzle.

Initially, the ODA equations were solved for a specified wavelength, where the wavelengths corresponded to those of the gas or particles. The ODA equations were then solved for each wavelength without regard for gas/particle overlap. Logic was added to extend this procedure by taking into account the fact that gas band radiation is modified by the presence of the overlapping particle bands. Specifically, the gas band absorption coefficient was augmented by the extinction coefficient of the particle background (Ref. 2.19). A set of subroutines was developed to separate the particle-only bands or windows from the gas/particle overlap bands. The option to run a single wavelength for purposes of getting an initial solution is available as well, along with the option of running a monochromatic solution with a mean absorption coefficient for H_2O and CO_2.

A listing of the types of options available in IDA is given below in Table 2.2, followed by a brief description of the subroutines and a flow chart of the code, which are shown in Table 2.3 and Chart 2.4, respectively. The BLKDAT subroutine contains all of the radiation parameter options necessary to make an ODA or IDA computation. The 9 major options shown in Table 2.2 must be chosen to initiate the radiation computation.

2.2.3 Description and Use of IDARAD Code

The overall architecture of the IDARAD radiation code evolved as a result of using a version of the computational fluid dynamics (CFD) code, FDNS (Ref. 2.25), that was developed under a previous NASA phase I SBIR study (Ref. 2.26) to examine the coupling of the radiation and fluid mechanics that can occur in high temperature, high pressure rocket exhausts. Input and use of the resultant radiation code is somewhat more cumbersome than would otherwise have resulted if the code had been written from scratch. However, a large advantage of using the FDNS code is the ability to incorporate the ODA and IDA methodologies in a coupled CFD code so that at some future date, a fully coupled radiation/fluids code could be more easily developed.

A flow chart of the program elements that make up the IDARAD radiation code along with the data files and transfer of information between the various codes is shown in Chart 2.5. The code generates the grid (fort.12), and flowfield property (fort.13) and mapped particle-gas property (fort.61) files. The RAD0 program generates initial guesses for the radiant intensities of the individual gas and particle bands (fort.15 and fort.16) at each of the grid locations. Following the execution of these codes, the IDARAD code is executed to calculate the heat fluxes at the boundaries. Details of preparing the user specified input files and preparing the codes for execution is found in Section 2.2.3.1.

Table 2.2 IDA Code Options

1.	Radiation wavelength input:
	  ● gas species type
	  ● particle type (presently Al_2O_3)
	  ● values of wavelengths of interest for gas and particle species

2.	IDA switch
3.	View factor and solid angle switch
4.	Wall and inlet plane gas emissivity
5.	Spectral or mean absorption coefficient switch for H_2O/CO_2 mixture

6.	Absorption coefficient and band width model:
	  ● exponential wide band
	  ● picket fence
	  ● box model
	  ● block model

7.	Mean beam length for cylinder, function of:
	  ● average distance between neighboring grid points
	  ● diameter at given axial location
	  ● radius and length
	  ● radius and optical depth at band head

8.	Boundary conditions at inlets and wall:
	  ● spectral diffuse emitting and reflecting wall
	  ● diffuse emitting and reflecting BC with pseudo-black inlet

9.	Gas/particle radiation procedure:
	  ● gas only
	  ● particle only
	  ● gas + non-overlapping particle
	  ● gas/particle overlap

Table 2.3 Description of IDA Code Subroutines
(in alphabetical order)

ASTAR	Dimensionless band absorption for H_2O and CO_2
BLKDAT	Radiation parameter options
CELLIJ	Determines cell in which adjusted IDA source term lies
ECOEFG	Extinction coefficient for H_2O and CO_2
ECOEFP	Extinction coefficient for Al_2O_3
EXTINC	Driver for extinction coefficient
GMEDUM	Driver for medium surface integrals
GWALL	Driver for wall surface integrals
HTRAD	Radiative heating
IDA	Driver for IDA method
IDABC	Determines incident radiation on radiating boundaries
INRAD	IDA value for incident radiation and radiative heat flux
INTRP1	Interpolation of incident radiation from IDA grid to total flowfield grid
INTRP2	Interpolation of SIRRM properties along a line-of-sight
INTRP3	Log $1\emptyset$ interpolation of adjusted IDA source term within a cell
JWALL	Sets up matrix elements for radiosity
LININR	Linear interpolation of refractive index as function of temperature
LININT	Double linear interpolation of particle size and temperature for the absorption coefficient
LOGINT	Double log $1\emptyset$ interpolation of particle size and temperature for the scattering coefficient
LSIGHT	Determines coordinates on a line-of-sight through a 2D axisymmetric geometry
MONCHR	Monochromatic values for absorption and extinction coefficients, albedo and Planck function
ODA	Driver for ODA method
ODABC	Boundary condition module for ODA incident radiation

Table 2.3 Description of IDA Code Subroutines (Continued)
(in alphabetical order)

OPDIST	Driver for optical depth along a line-of-sight
OVRLAP	Interpolation for particle absorption and scattering coefficients within a gas band
PATH	Path length used for gas extinction coefficient
PBAND	Particle band widths
PLANKF	Planck blackbody function
RADØ	Driver for radiation code
RADINØ	Driver for radiative transfer equation
RAVFAC_SA	Solid angle routine
RAVFAC_VF	View factor routine
RDOSTY	Radiosity matrix inversion routine
REFRAC	Reads in particle refractive index (used in evaluation of Planck function)
REFRIN	Driver for refractive index interpolation
RSIRRM	Reads in SIRRM map
SIGACL	Reads in particle absorption coefficient data file
SIGSCL	Reads in particle scattering coefficient data file
SIGAV	Driver for particle absorption and scattering coefficient interpolation
SRCIDA	Driver for IDA (source terms adjusted for transmissivity and absorptivity)
SUMMA1 and SUMMA2	Wide band model summation - function of vibrational quantum number
TAUDR	Determines optical depth at single position on a line-of-sight
TRDIAG	Tridiagonal solver for ODA
VFINIT	Initializes RAVFAC input file for a nozzle
WIDEBM	Wide band model for H_2O and CO_2

RADØ

BLKDAT
PATH
RSIRRM
SIGACL
SIGSCL
REFRIN
VFINIT
RAVFAC_VF
RAVFAC_SA

RADINØ

HTRAD

Monochromatic:
MONCHR

Gas:
ECOEFG ———— WIDEBM ———— SUMMA1
                              SUMMA2
                              ASTAR

Particles:
REFRAC ———— LININR

Spectral:

EXTINC ———— PBAND ———— OVRLAP ———— SIGAV ———— LOGINT
                       ECOEFP   LININT

                       PLANKF ———— TRDIAG
                       ODA   ODABC

                       SIGAV ———— LOGINT
                                   LININT

PLANKF ———— ECOEFP

ODA ———— OVRLAP

TRDIAG
ODABC

IDA

GWALL ———— OPDIST ———— LSIGHT
            RDOSTY   INTRP2
                        TAUDR
                        SRCIDA ———— CELLIJ
                        JWALL   INTRP3

GMEDUM ———— OPDIST ———— LSIGHT
             IDABC   INTRP2
             INTRP1   TAUDR
                         SRCIDA ———— CELLIJ
                         INRAD   INTRP3

Chart 2.4 Subroutine Sequence For IDA Code

Chart 2.5 Flowchart of IDARAD Program Elements

```
                            ┌─────────────┐
                           /  SIRRM.MAP  /
                          └─────────────┘
                                 │
                                 ▼
                          ┌─────────────┐
                          │    GRID     │
                          │   Program   │
                          └─────────────┘
              ┌──────────────────┼──────────────────┐
              ▼                  ▼                  ▼
       ┌───────────┐      ┌───────────┐      ┌───────────┐
       │  fort.12  │      │  fort.13  │      │  fort.61  │
       │  (grid)   │      │(flowfield)│      │(sirrm map)│
       └───────────┘      └───────────┘      └───────────┘
   ┌──────────────┐
  / koch2.prn    /
 / SIGACL.DAT   /
/ SIGSCL.DAT   /
└──────────────┘
                          ┌─────────────┐
                          │    RAD0      │
                          │   Program   │
                          └─────────────┘
              ┌──────────────────┼──────────────────┐
              ▼                  ▼                  ▼
       ┌───────────┐      ┌───────────┐      ┌───────────┐
       │  fort.11  │      │  fort.15  │      │  fort.16  │
       └───────────┘      └───────────┘      └───────────┘
                          ┌─────────────┐
                          │   IDARAD    │      ┌──────────────┐
                          │   Program   │◄─── / NOZZRAD.INP  /
                          └─────────────┘      └──────────────┘
              ┌──────────────────┼──────────────────┐
              ▼                  ▼                  ▼
       ┌───────────┐      ┌───────────┐      ┌───────────┐
       │  fort.6   │      │  fort.36  │      │  fort.67  │
       └───────────┘      └───────────┘      └───────────┘
```
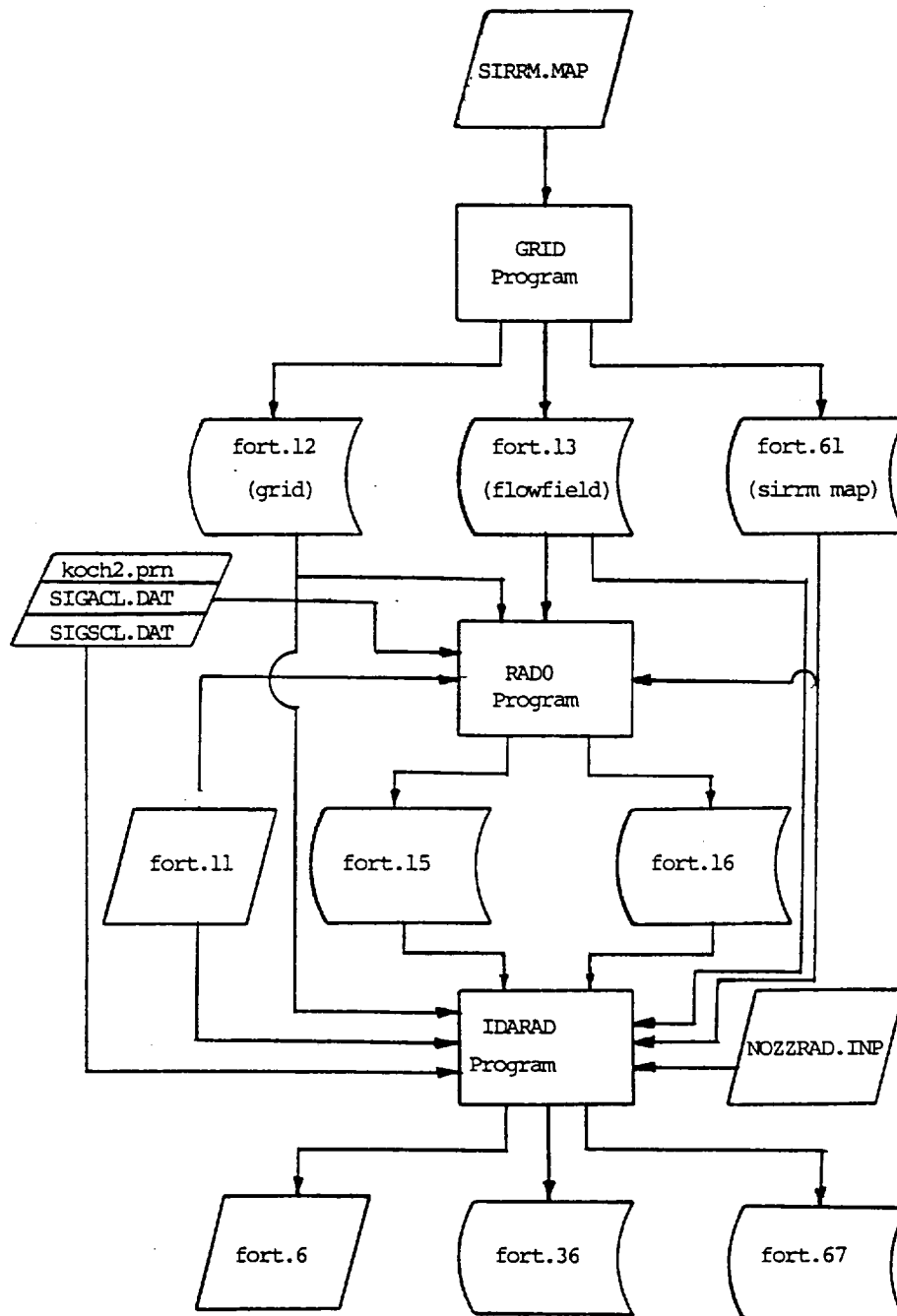
Table 2.4 Description of fort.12 Grid File

Record 1: (Free Format)
IZON Number of grid zones

Record(s) 2: (Free Format)

IZT(IZ)	Number of i stations (x direction) for zone IZ
JZT(IZ)	Number of j points (y direction) at each station for zone IZ
KZT(IZ)	Number of k points (z direction) at each station for zone IZ

Record(s) 3: Format: 5(1PE16.8)
These records input the axial(x) locations of each grid point.
(X(I,J,K), I=1, IZT(IZ)), J=1, JZT(IZ)), K=1, KZT(IZ))
The X values are non dimensional values based on XREF input in fort.11 file.

Record(s) 4: Format: 5(1PE16.8)
These records input the radial (Y) location of each grid point.
(Y(I,J,K), I=1, IZT(IZ)), J=1, JZT(IZ)), K=1, KZT(IZ))
The Y values are non-dimensional values based on XREF input in fort.11 file.

Record(s) 5: Format: 5(1PE16.8)
These records input the Z direction location of each grid point. Set = 1.0 if asymmetric case is being run.
(Z(I,J,K), I=1, IZT(IZ)), J=1, JZT(IZ)), K=1, KZT(IZ))
The Z values are non-dimensional values based on XREF input in fort.11 file.

Notes: If multi-zone cases are being input, input all records 2 first followed by records 3,4, and 5 for each zone. The radiation code is limited to one zone while FDNS can be run using several zones.

Table 2.5 Description of fort.13 Flowfield File for Radiation Code

Record 1: Format: 8I5

Variable	Column	Value
INSO(1)	5	1
INSO(4)	10	1
INSO(5)	15	1
INSOFM	20	1
NGAS	24-25	12

The variables input on Record 1 control the input for the flowfield properties that are input to the radiation code. The radiation code assumes that the gas specie set consists of 12 species in the order specified on the example fort.11 file shown in Table 2.6.

Record(s) 3: Format (5(1PE16.8) Gas Density
These records input the gas density at each grid location
(((DEN(I,J,K), I=1, IZT(IZ)), J=1, JZT(IZ)), K=1, KZT(IZ))
Densities are input in non-dimensional values based on DENREF input in fort.11 file.

Record(s) 4: Format (5(1PE26.8))
These records input the component of velocity in the i (x) direction at each grid location
(((U(I,J,K), I=1, IZT(IZ)), J=1, JZT(IZ)), K=1, KZT(IZ))
Velocity is input in non-dimension values based on UREF input in fort.11.

Record(s) 5: Format 5(1PE16.8)
These records input the component of velocity in the j (y) direction at each grid location
(((V(I,J,K), I=1, IZT(IZ)),J=1, JZT(IZ)), K=1, KZT(IZ))
Velocity is input in non-dimensional values based on UREF input in fort.11 file.

Record(s) 6: Format 5(1PE16.8)
These records input the component of velocity in the k(z) direction at each grid location
(((W(I,J,K), I=1, IZT(IZ), J=1, JZT(IZ)), K=1, KZT(IZ))
Velocity is input in non-dimensional values based on UREF input in fort.11 file

Table 2.5 Description of fort.13 Flowfield File for Radiation Code (Continued)

Record(s) 7: Format 5(1PE16.8)
These records input the static pressure at each grid location
(((P(I,J,K), I=1, IZT(IZ), J=1, JZT(IZ)), K=1, KZT(IZ))
Pressure is input in non-dimensional values based on the product DENREF*UREF**2 input in fort.11 file

Record(s) 8: Format 5(1PE16.8)
These records input the temperature at each grid location
(((TM(I,J,K), I=1, IZT(IZ), J=1, JZT(IZ)), K=1, KZT(IZ))
Temperature is input in non-dimensional values based on the reference temperature-TREF input in fort.11 file.

Record(s) 9: Format 5(1PE16.8)
The records input the turbulent kinetic energy at each grid point. Record 9 is input only if INSO(5) = 1
(((DK(I,J,K),I=1, IZT(IZ)), J=1, JZT(IZ)), K=1, KZT(IZ))
Turbulent kinetic energy is input in non-dimensional values based on the reference velocity squared (UREF**2) input in fort.11 file.

Record(s) 10:   Format 5(1PE16.8)
These records input the turbulent dissipation at each grid location, Record 10 is input only if INSO(5)=1.
(((DE(I,J,K), I=1, IZT(IZ)), J=1, JZT(IZ)), K=1, KZT(JZ))
Turbulent dissipation is input in non-dimensional values based on the product UREF**3/XREF input in fort.11 file.

Record(s) 11:   Format 5(1PE16.8)
These records input the Mach number at each grid location
(AP(I,J,K), I=1, IZT(IZ)), J=1, JZT(IZ)), K=1, KZT(IZ))
Mach number is input in non-dimensional values based on AMC input in fort.11.

Record(s) 13:   Format 5(1PE16.8)
Records 13 are input only if NGAS>0 from fort.11 file. Records 13 input the mass fractions for each gas specie in the same order the species are input in fort.11.
(((FM(I,J,K,L), I=1, IZT(IZ)), J=1, JZT(IZ)), K=1, KZT(IZ)), L=1, NGAS)

Table 2.5 Description of fort.13 Flowfield File for Radiation Code (Continued)

Record(s) 14:* Format 5(1PE16.8)

These records input particle temperature for each grid location in dimensional values (Deg K)

(((TMPP(I,J,K), I=1, IZT(IZ)), J=1, JZT(IZ)), K=1, KZT(IZ))

Record(s) 15:* Format 5(1PE16.8)

These records input particle number density at each flowfield point in dimensional values (#/CM**3)

(((DNPP(I,J,K), I=1, IZT(IZ)), J=1, JZT(IZ)), K=1, KZT(IZ))

Note:* Records 14 and 15 are input only for uncoupled radiation cases (IFL13 > 0). For each particle group (size) records 14 and 15 are input followed by records 14 and 15 for each size group until all sizes have been input. The uncoupled radiation code assumes that 5 particle groups are always used.

The starting point for the radiation analysis is a precomputed flowfield file in a standard JANNAF SIRRM (Ref. 2.16) format. The SIRRM map describes the spatial variation of gas pressure, temperature and species as well as particle temperatures and number densities.

The basic FDNS code requires 3 input files. Unit fort.11 is the input data file that controls the operation of the FDNS or radiation code. Section 2.2.3.1 describes the generation of, and variables input into this file. The other two files are the grid file (fort.12) and the flowfield file (fort.13). The format of these two files are shown in Tables 2.4 and 2.5, respectively.

The FDNS code uses grid systems that follow the right hand rule for the i(X), j(Y) and k(Z) line orientations. The basic FDNS code can handle two-dimensional (axisymmetric) or three-dimensional grids having several zones. However, the radiation code developed under this contract is limited to axisymmetric single zone grids. The grid must be represented by i axial stations with j radial points at each station. Z values must be set to one. It is not necessary to have a large number of grid points. A typical mesh for a sea level plume (out to 10 exit radii) would be 20-30 i stations with 20 j points per station. Results for radiation at the boundary of this size grid versus a grid having 30 times as many grid points are basically the same. Run times for an IDA solution for a 400 grid problem of this type are on the order of 6 minutes of CPU time on an IBM 320 RISC system.

The flowfield file (fort.13) described in Table 2.5 provides the gaseous and particulate properties at each grid point. All variables except the particle temperatures and number densities are input non-dimensionally based on the reference values prescribed in fort.11 (Table 2.6). The only variables that are actually used by the radiation code are gas pressure, gas temperature, specie mass fractions, particle temperature, and number density. All other variables can be set to 1.0.

The user must also input a SIRRM.MAP file corresponding to the same grid as the

fort.12 and fort.13 files. This is really redundant, but due to how the code was developed and coded, makes it necessary to input this file. SIRRM maps from typical flowfield codes such as SPF/2 (Ref. 2.27) have non-uniform (not equal number) of radial points as well as having too many points. A preprocessing code called GRID has been written that uses the SIRRM flowfield the user supplies to generate the fort.12, fort.13 and SIRRM flowfield (fort.61) that is input to the radiation code.

The GRID code allows the user to specify how many radial (j) grid points to use for the grid and how many axial stations to skip between i stations for the grid. Thus, a number of SIRRM map points can be eliminated when generating the grid (fort.12), flowfield (fort.13) and map (fort.61) files. This is a interactive code that requires the user to have the input SIRRM map file named as SIRRM.MAP. The user must respond to inquiries by the GRID code as to how many radial points are desired (as well as whether the points should be evenly spaced or compressed toward the outer part of the flowfield), the station at which to begin the grid, the station to end the grid and reference values of length, density, velocity and temperature. These values are used to non-dimensionalize values of the grid and flowfield files and must be the same that are specified on fort.11. The GRID code assumes that there are 12 species in the same order as is specified on the sample fort.11 file shown in Table 2.6 (i.e. H_2O, O_2, H_2, O, H, OH, CO, CO_2, Cl, Cl_2, HCl and N_2). If any other set of gas species are input on fort.11, the data statement for the specie names in GRID.f must be changed. The source code for GRID and the SIRRM map for the MNASA48 ASRM contoured nozzle Cycle 2.0 plume are contained on the MS-DOS disk, DISC.

2.2.3.1 Preparation of Input Files, Subroutines and Steps Necessary to Run IDARAD

Each time IDARAD is executed for a new case, several steps must be performed prior to execution. In addition to preparing the grid (fort.12), flowfield (fort.13) and SIRRM map files (fort.61), which was described in Section 2.2.3, the following steps must be performed:

(1)   Generate the input data file fort.11. A description of the fort.11 file is contained in Table 2.6. This table describes the fort.11 input for both IDARAD as well as the FDNS code, which was used to produce the FDNS results presented in Section 3 of this report. FORTRAN unit 11 (fort.11) inputs to FDNSEL and IDARAD are slightly different and are noted in Table 2.6. Further explanation of these inputs can be found in Ref. 2.25. A sample input file for radiation predictions inside a solid rocket motor using the IDA method can be found in Table 2.7.

(2)   The second file that must be generated is the NOZZRAD.INP file. This file is necessary only if running the IDA model. Table 2.8 presents a discussion of the input variables contained in NOZZRAD.INP. Table 2.9 presents a listing of the NOZZRAD.INP file that corresponds to the fort.11 file shown in Table 2.7.

(3)   Modify the rad01 include file for both the IDARAD and RAD0 programs. Table 2.10 describes the variables that are contained in rad01. These variables set array sizes inside the codes.

(4)   Modify the BLKDAT_U.f (IDARAD) and BLKDAT_0.f(RAD0) subroutines to set the proper input parameters that are specified by these routines. Table 2.11 provides a description of the variables contained in the BLKDAT_*.f files.

(5)   Recompile IDARAD and RAD0 if either BLKDAT_*.f or rad01 were changed from previous runs. If rad01 was changed, recompile the entire program since the rad01 file is an 'include' file called by numerous subroutines.

Table 2.6 Description of FDNS and IDARAD
(fort. 11) Input Data File

Record Group #1: Gives the case title and identifies whether the problem is 2-D or 3-D.
Format:
IDIM, (put title of the problem here -- maximum 60 characters)
< ----------(one data line)

Definition:
IDIM = 2 for 2-dimensional flow problems
     = 3 for 3-dimensional flow problems

Record Group #2: Specifies zonal information and number of flow and wall boundaries.
Format:
IZON, IZFACE, IBND, ID, ISNGL   (FDNS)
IZON, IBND, ID, IRAD, IDRW, IFL13   (IDARAD)
< ----------(one data line)

Definition:

IZON	number of zones or mesh blocks
IZFACE	number of patched interfaces
IBND	number of flow boundaries (e.g. inlet, outlet or symmetry planes)
ID	number of wall elements (blocks)
ISNGL	number of singularity lines
IRAD	radiation control parameter

            0: No radiation: > 0:   Radiation

            1:     Gas rad only

            2:     Particle rad only

            3:     Gas and particle radiation separately (with no gas/solid overlap regions)

            4:     Gas and particle radiation with overlap (with at least one gas/solid overlap region). Treats the overlapping particle band with the same band width as the overlapping gas band width

                a.   Does not account for overlap of adjacent gas band and points

                b.   Does not account for gas overlap at particle band endpoints

IDRW	Number of radiating boundaries in axisymmetric plane (for IDA method) (eg, can be solid wall or inlet)
IFL13	0 Do not input particle properties on Unit 13 file
	1 Input particle properties on Unit 13 file

* Each card group has a header card of whether the record is used or not. See Table 2.7 for examples for IDARAD and Table 3.1 for FDNS.

Record Group #3: Specifies zonal grid size and zonal rotational/translational speeds
Format:
IZT, JZT, KZT, CBGX, CBGY, CBGZ, CBVX, CBVY, CBVZ
$$<\text{----------}(IZ = 1,IZON)(FDNS)$$
IZT,JZT,KZT (IDARAD)

Definition:
IZT(IZ)	I-max in zone IZ
JZT(IZ)	J-max in zone IZ
KZT(IZ)	K-max in zone IZ
CBGX(IZ)	rotational speed ($R\Omega_x/U_{ref}$) of zone IZ about X-axis
CBGY(IZ)	rotational speed ($R\Omega_y/U_{ref}$) of zone IZ about Y-axis
CBGZ(IZ)	rotational speed ($R\Omega_z/U_{ref}$) of zone IZ about Z-axis
CBVX(IZ)	translational speed of zone IZ in X-axis direction
CBVY(IZ)	translational speed of zone IZ in Y-axis direction
CBVZ(IZ)	translational speed of zone IZ in Z-axis direction

Record Group #4: Identifies the zonal interface matching indices. (This group input for FDNS only, not radiation code.)
Format:
NNBC, IZB1, IZF1, IJZ1, IJZ2, JKZ1, JKZ2,
     IZB2, IZF2, IJZ1, IJZ2, JKZ1, JKZ2,
$$<\text{----------}(2*IZFACE\ data\ lines)$$
Definition:
NNB IZFACE counter (not used in the code)
IZB1 zonal index of interface plane #1
IZF1 interface plane identifier for plane #1
    1: I = I-max (or East)
    2: I = 1 (or West)
    3: J = J-max (or North)
    4: J = 1 (or South)
    5: K = K-max (or Top)
    6: K = 1 (or Bottom)
IZB2 zonal index of interface plane #2
IZF2 interface plane identifier for plane #2
IJZ1 the starting point of the first running index on the interface plane
IJZ2 the ending point of the first running index on the interface plane
JKZ1 the starting point of the second running index on the interface plane
Example: If IZF1 or IZF2 is either 1 or 2 then IJZ1 and IJZ2 are the indices in J-direction and JKZ1 and JKZ2 are the indices in K-direction. If IZF1 or IZF2 is either 3 or 4 then IJZ1 and IJZ2 are the indices in I-direction and JKZ1 and JKZ2 are the indices in K-direction. If IZF1 or IZF2 is either 5 or 6 then IJZ1 and IJZ2 are

the indices in I-direction and JKZ1 and JKZ2 are the indices in J-direction.

Notice: The interface patching surface indices for planes #1 and #2 (i.e. IJZ1, IJZ2, JKZ1, JKZ2) must have consistent running order.

Record Group #5: Specifies flow boundaries (inlet, outlet, symmetry).
Format:
IBCZON, IDBC, ITYBC, IJBB, IJBS, IJBT, IKBS, IKBT,

<------------(IBND data lines)

Definition:

IBCZON	zonal index for the flow boundary
IDBC	boundary facing index

      1: I = I-max (or East)
      2: I = 1 (or West)
      3: J = J-max (or North)
      4: J = 1 (or South)
      5: K = K-max (or Top)
      6: K = 1 (or Bottom)

ITYBC   identifies boundary type

   -2:   inlet fixing everything except pressure
   -1:   inlet fixing mass flow rates (e.g. solid fuel blowing surfaces)
    0:   inlet fixing everything (e.g. supersonic)
    1:   inlet fixing total pressure (compressible flow only)
    2:   outlet boundary
    3:   symmetry plane (can also be used for slip wall boundary conditions)

IJBB   I, J or K location (depends on IDBC) of the boundary
IJBS, IJBT boundary starting and ending indices (for I or J)
JKBS, JKBT boundary starting and ending indices (for J or K)

      1: I = I-max (or East)
      2: I = 1 (or West)
      3: J = J-max (or North)
      4: J = 1 (or South)
      5: K = K-max (or Top)
      6: K = 1 (or Bottom)

ITYBC   identifies boundary type

   -2:   inlet fixing everything except pressure
   -1:   inlet fixing mass flow rates (e.g. solid fuel blowing surfaces)
    0:   inlet fixing everything (e.g. supersonic)
    1:   inlet fixing total pressure (compressible flow only)
    2:   outlet boundary

> 3: symmetry plane (can also be used for slip wall boundary conditions)

IJBB — I, J or K location (depends on IDBC) of the boundary

IJBS,IJBT — boundary starting and ending indices (for I or J)

JKBS,JKBT — boundary starting and ending indices (for J or K)

Record Group #6: Specifies wall block indices.

Format:

IWBZON,L1,L2,M1,M2,N1,N2,IWTM,HQDOX,IWALL,DENNX,VISWX (FDNS)

IWBZON, L1,L2,M1,M2,N1,N2 (IDARAD)

<----------(ID data lines)

Definition:

IWBZON — zonal index for the wall block

L1, L2 — starting and ending indices in the I-direction

M1, M2 — starting and ending indices in the J-direction

N1, N2 — starting and ending indices in the K-direction

IWTM — solid-wall thermal boundary condition options
- -1: for fixed wall-temperature
- 1: for heat-flux (=HQDOX) b.c.

HQDOX — non-dimensional wall heat flux when IWTM=1, positive from wall to fluid. Normalization for $\dot{Q}$:

SI Units $= \dot{Q} / (\rho_{ref} U_{ref} Cp_{ref} T_{ref})$

English Units $= \dot{Q} / (32.174 \rho_{refl} U_{refl} Cp_{refl} T_{refl})$

IWALL — solid wall heat conduction option

0: to deactivate;   1: to activate

DENNX — non-dimensional solid wall density
= (wall-density)/(den-ref)

VISWX — non-dimensional solid wall thermal conductivity
= k/(x-ref)/(den-ref)/(u-ref)/(Cp-ref)

Record Group #7: Specifies the singularity lines. (FDNS only)

Format:

ISNZON, ISNBC, ISNAX, ISNBS, ISNBT,

<----------(ISNGL data lines)

Definition:

ISNZON — zonal index for the singularity lines

ISNBC — singularity line boundary facing index
- 1: I = I-max (or East)
- 2: I = 1 (or West)
- 3: J = J-max (or North)
- 4: J = 1 (or South)
- 5: K = K-max (or Top)
- 6: K = 1 (or bottom)

*When IWALL = 1 is selected, the program will set IWTM = -1, since this is a correct combination.

ISNAX   orientation of the singularity line axis for example:

on I-J plane (ISNBC = 5 or 6)
     ISNAX = 1 for I-axis
     ISNAX = 2 for J-axis
on J-K plane (ISNBC = 1 or 2)
     ISNAX = 1 for J-axis
     ISNAX = 2 for K-axis
on K-I plane (ISNBC = 3 or 4)
     ISNAX = 1 for I-axis
     ISNAX = 2 for K-axis

ISNBS, ISNBT   starting and ending indices along ISNAX

Record Group #8:   I/O parameters and problem control parameters. (FDNS only)

Format:

IDATA, IGEO, ITT, ITPNT, ICOUP, NLIMT, IAX, ICYC,

                                <----------(one data line)

Definition:

IDATA   restart options

IDATA = 1 for regular restart runs. Restart grid and flow files fort.12 and fort.13 must be made available.

IDATA = 2 for example start run. Initial grid and flow data must be made available in the fexmp01 include file.

IGEO   geometry parameter (for user applications)

IGEO = 1 is specifically for problems without inlets and outlets (e.g. cavity flows)

IGEO = 9 is reserved for 3-D pump or turbine type applications (with ICYC=3)

IGEO = 19 is reserved for linear cascades applications

ITT   number of time steps limit

ITPNT   the frequency on printing out solutions (through files fort.22, fort.23, fort.91, fort.92 and fort.93)

ICOUP   number of pressure correctors (typically 1 for steady-state applications and 3-6 for transient or rough initial start applications)

NLIMT   typically 1;

     0:      for printing out the initial or restart files without going through solution procedures

IAX   1:   for 2-D planar or 3-D flows

     2:      for 2-D axisymmetric flow problems

ICYC   cyclic or periodic boundary conditions identifier

Currently, only ICYC = 3 is active for turbomachinery applications.

Record Group #9: Time-step size, upwind schemes and time-marching scheme selections (FDNS only).
Format:
DTT, IREC, REC, THETA, BETAP, IEXX, PRAT,

<---------(one data line)

Definition:
DTT non-dimensional time step size, DT*Uref/Xref
IREC selects upwind scheme options
    0: for second-order upwind scheme
    1: for third-order upwind scheme
    2: for second-order central scheme
REC upwind damping parameter (0.1 recommended)
    0.0 for second-order accuracy
    1.0: for first-order upwind scheme
THETA time-marching scheme Θ parameter
    1.0: for steady-state applications
    .99: for implicit-Euler transient applications
    0.5: for Crank-Nicholson second-order accurate transient applications
BETAP pressure updating under-relaxation parameter typically 1.0; small values can be used to reduce the amount on pressure corrections for rough start initial runs
IEXX outlet extrapolation parameter for scalar quantities
    1: for zero-gradient extrapolation
    2: for linear extrapolation
PRAT specifies outlet boundary condition options
    -1.0: for supersonic outlet b. c.
    0.0: for outlet mass conservation b. c.
    >0.0: for outlet fix pressure b. c. The outlet pressure reference point (IPEX, JPEX) is used here. Pressure at this point is maintained at a value of PRAT*PPCN. Where PPCN = $1/\gamma M^2$

Record Group #10: Specifies inlet, outlet pressure points and data monitoring point (FDNS only).
Format:
IPC, JPC, IPEX, JPEX, IMN, JMN,

<---------(one data line)

Definition:
IPC, JPC flowfield reference point
    IPC: local grid index in zone JPC (not the global grid index)

IPEX, JPEX outlet pressure reference point (same way of indexing as IPC, JPC)

IMN, JMN solution monitoring point (same way of indexing as IPC, JPC)

Record Group #11: Gives reference viscosity, Mach number and options of turbulence models (FDNS only).
Format:
VISC, IG, ITURB, AMC, GAMA CBE, CBH, EREXT,

$\qquad\qquad\qquad\qquad\qquad\qquad$ <----------(one data line)

Definition:

VISC non-dimensional fluid viscosity = 1/(Reynolds number)
= vis-ref/(den-ref)/u-ref)/(x-ref)

IG = 1: for laminar flow option
= 2: for turbulent flow option

ITURB for turbulence model selection
1: for standard high-Re k-ϵ model
2: for extended high-Re k-ϵ model
3: for L-B low-Re k-ϵ model
4: for H-G low-Re k-ϵ model

AMC reference Mach number, = (u-ref)/(ref.sound speed)

GAMA reference specific heat ratio

CBE non-dimensional buoyancy force parameter = Gr/Re**2, where Gr stands for the Grashoff number and Re is the flow Reynolds number

CBH used to activate compressibility corrections for the k-ϵ turbulence models
= -1.0: for k-corrected model
= -2.0: for ϵ-corrected model
< -3.0: for t-corrected model where $C_3(T/T_{ref})^\gamma$. $\gamma = (3-CBH)$

EREXT convergence criterion (typically 5.0E-04 for steady-state solutions)

Record Group #12: Specifies number of zonal iterations in the matrix solver when INFACE is used for overlaid grid zonal interface interpolations and indicates orthogonal or non-orthogonal grid options (FDNS only).
Format:
ISWU, ISWP, ISWK, ISKEW,

$\qquad\qquad\qquad\qquad\qquad\qquad$ <----------(one data line)

Definition:

ISWU number of iterations for the overlaid zonal boundaries for the momentum and energy equations
ISWU $\leq$ 90: using point implicit matrix solver,

ISWU > 90: using conjugate gradient matrix solver with a convergence criteria that the residual has to be reduced by (ISWU-90) order

ISWP number of iterations for the overlaid zonal boundaries for the pressure correction equations

ISWP ≤ 90: using point implicit matrix solver,

ISWP > 90: using conjugate gradient matrix solver with a convergence criteria that the residual has to be reduced by (ISWU-90) order

ISWK number of iterations for the overlaid zonal boundaries for the scalar equations

ISWK ≤ 90: using point implicit matrix solver,

ISWK > 90: using conjugate gradient matrix solver with a convergence criteria that the residual has to be reduced by (ISWU-90) order

ISKEW non-orthogonal grid viscous flux option

0: for orthogonal grid

1: for non-orthogonal grid

Record Group #13: Specifies which equations are to be solved (FDNS only.)

Format:

INSO(IEQ):

U, V, W, TM, DK, DE, 7, 8, 9, VS, FM, SP,

<------------(one data line)

Definition: (0 to deactivate; 1 to activate)

U, V, W   for the momentum equations

TM   for the energy equation

DK, DE   for the turbulence model

7, 8, 9   not used

VS   for updating the turbulence eddy viscosity

FM   for the species mass-fraction equations

SP   for calculating the gas thermal properties, and selecting various treatment for species production term.

= 1   explicit chemistry model (penalty function)

= 11 or 12   implicit chemistry model (1st or 2nd-order) with psudo-time step size

= 21 or 22   implicit chemistry model (1st or 2nd-order) with real time step size

= 31 or 32   implicit chemistry model (1st or 2nd-order) with time integration to flow time step size

= 33   4th-order PARASOL

> 100   equilibrium plus (SP-100) global finite rate chemistry models

Record Group #14: Specifies wall radiosity data for IDA method. Input only for IDA method. (IDARAD only) Input as many Record 14's as IDRW.
IORDR, IDBR, IRADW

IORDER	indicates wall order from which radiosity is to be calculated (coincides with ityp order in RAVFAC input file: NOZZRAD.INP)
IDBR	= 1 for an IDBC (open) boundary (input, output or symmetry);
	= 2 for an ID (solid) boundary
IRADW	boundary index (1:east-I; 2:west-I; 3:north-J; 4:south-J; 5:top-I; 6:bottom-K)

Record Group #15: Specifies number of gas species and reactions, and gives the reference conditions
Format:
NGAS, NREACT, IUNIT, DENREF, UREF, TREF, XREF, (FDNS)
NGAS,IUNIT,DENREF,UREF,TREF,XREF (IDARAD)

$<$----------(one data line)

Definition:

NGAS	number of gas species CEC tables to be read
	= 0: for ideal gas run
	>0: for CEC real gas run
	=-1: for LOX NBS-table property option **(Check subroutine INIT for hard-wired LOX initial conditions)**
NREACT	number on reaction steps to be used
	= 0: for non-reacting flow
	>0: for finite-rate reacting flow
IUNIT	= 1: for SI-unit reference conditions
	= 2: for English-unit reference conditions
DENREF	reference density (in kg/m^3 or $slug/ft^3$)
UREF	reference velocity (m/sec or ft/sec)
TREF	reference temperature (°K or °R)
XREF	reference length (m or ft)

Record Group #16: Include the CEC thermodynamics data here
Format:
Name, Molecular Weight, Coefficients (7 x 2)

$<$----------(4*NGAS lines)

FDNS reads in the data in CEC format.

Record Group #17: Specifies the finite-rate reacting steps (FDNS only)
Format:
REACTING: Species Names, N = 1, NGAS (this is a title line)
IREACT, A, B, E/RT, ITHIRD, IGLOB
(STOCEF(N, IREACT), N=1,NGAS)
(STOCEG(N, IREACT), N=1,NGAS) ---- If IGLOB = 2
$\qquad\qquad\qquad\qquad\qquad\qquad\qquad\qquad$ <----------(NREACT sets)

Definition:
IREACT   reaction step counter
A   reaction rate leading constant
B   reaction rate temperature exponent
E/RT   reaction rate activation energy constant
ITHIRD   third-body reaction indicator
         0:      deactivated
         N: for using the N-th species as third body
         999:      for global (every species) third-body

Record Group #18: provides particle input control
Format:
IDPTCL, IPREAD

$\qquad\qquad\qquad\qquad\qquad\qquad\qquad\qquad$ <----------(1 data line)

Definition:
IDPTCL   number on particle sizes initial condition input lines
         0:      to deactivate particulate phase option
IPREAD   1 for reading in particle data (fort.14) from upstream domain (this allows transferring the outlet particle data from the upstream domaine solutions to the inlet boundary for succeeding domain computations --especially useful for multi-phase rocket plume simulations)

Record Group #19: for reading in particle initial conditions (for steady-state runs only) (FDNS only)

Format:

IPTZON,IDBCPT,LPTCL1,LPTCL2,MPTCL1,MPTCL2,NPTCL1,NPTCL2,
ITPTCL,DDPTCL,DNPTCL,WDMASS,UUPTCL,HTPTCL

<----------(2*IDPTCL data lines)

Definition:

IPTZON   zonal index for the particle initial position

IDBCPT   I-, J- or K-plane identifier

        1:    for I-plane (plane normal to I lines)

        2:    for J-plane (plane normal to J lines)

        3:    for K-plane (plane normal to K lines)

LPTCL1,LPTCL2 I-interval for the particle initial position

MPTCL1,MPTCL2 J-interval for the particle initial position

NPTCL1,NPTCL2 K-interval for the particle initial position

ITPTCL   number of particle groups (trajectories) starting from each grid cell

DDPTCL   particle diameter in μm

DNPTCL   particle density in lbm/ft**3

WDMASS   particle mass flow rate for the current particle group

UUPTCL   particle/gas velocity ratio at the initial positions

HTPTCL   particle initial enthalpy in ft**2/sec**2

(6) Execute the RAD0 program. This code generates the fort.15 and fort.16 initial guesses for radiant intensities for the gas and particles at each flowfield point for each of the gas and particle bands that are specified by the user in the BLKDAT_*.f routine.

(7) Execute the IDARAD program. Output of the code consists of a fort.6 file that tracks the progress of the code through each of the bands (gas and particle) as the program executes and can provide the user information necessary to correct any errors that are encountered during execution. The actual radiation output in the form radiation heat fluxes at each wall (or boundary point) are found in fort.37 and fort.67. Fort.37 gives the location of the wall point along with the difference in incident radiation to the point and radiation intensity at the point due to the medium at the point. Fort.67 provides the axial location of the point and the incident radiation at the point (wall or boundary). For ODA cases, the radiation intensities (BTU/ft^2/sec) are output for all wall points. In the case of an IDA calculation, only those points that are specified as radiating boundary points have non-zero heat fluxes.

Three data files that must reside in the directory in which the IDARAD and RAD0 codes are being executed in are: SIGACL.DAT, SIGSCL.DAT and koch2.prn. SIGACL.DAT contains the absorption coefficient data for Al_2O_3. SIGSCL.DAT contains the scattering coefficient data for Al_2O_3 and koch2.prn contains the extinction coefficients for Al_2O_3. Particulates other than Al_2O_3 would require regeneration of the files to describe the properties of the particular particulate.

Additional notes on the options available to the IDARAD code are shown in Table 2.12.

Table 2.7 Listing of fort.11 IDARAD Sample Input File

```
IDIM, (2-D asrm48-5 nozzle, PARTICULATE TWO-PHASE FLOW)
    2,
 IZON,   IBND,    ID,   IRAD,    IDRW,     IFL13
    1,     3,     1,      4,      4,        1
  IZT,   JZT,   KZT,
  179,    81,    1,
IBCZON,  IDBC,  ITYBC,  IJBB,   IJBS,   IJBT,   IKBS,   IKBT,
    1,     1,     2,     179,     1,      81,     1,      1,
    1,     2,     1,       1,     1,      81,     1,      1,
    1,     4,     3,       1,     1,     179,     1,      1,
IWBZON,   L1,    L2,     M1,     M2,     N1,     N2,
    1,     1,    179,     81,     81,     1,      1,
IORDER,  IDBR,  IRADW,
    1,     1,     2,    !rad segment 1, boundary 1, west boundary
    2,     1,     2,    !rad segment 2, boundary 1, west boundary
    3,     2,     3,    !rad segment 1, boundary 2, north boundary
    4,     2,     3,    !rad segment 2, boundary 2, north boundary
----NGAS, IUNIT, DREF(SLG), UREF(F/S), TREF(R), XREF  (FT),
   12,    2,5.2991E-03, 116.68630, 6319.80, 1.00000000,
H2O                                              300.000  5000.000     18.01520
 0.26340654E+01 0.31121899E-02-0.90278451E-06 0.12673054E-09-0.69164734E-14
-0.29876258E+05 0.70823874E+01 0.41675563E+01-0.18106868E-02 0.59450877E-05
-0.48670872E-08 0.15284144E-11-0.30289547E+05-0.73087996E+00
O2                                               300.000  5000.000     31.99880
 0.36122139E+01 0.74853166E-03-0.19820646E-06 0.33749007E-10-0.23907374E-14
-0.11978151E+04 0.36703308E+01 0.37837136E+01-0.30233634E-02 0.99492754E-05
-0.98189101E-08 0.33031826E-11-0.10638107E+04 0.36416345E+01
H2                                               300.000  5000.000      2.01580
 0.30558124E+01 0.59740403E-03-0.16747471E-08-0.21247544E-10 0.25195486E-14
-0.86168475E+03-0.17207073E+01 0.29432328E+01 0.34815508E-02-0.77713821E-05
 0.74997493E-08-0.25203379E-11-0.97695410E+03-0.18186136E+01
O                                                300.000  5000.000     15.99940
 0.25342960E+01-0.12478170E-04 0.12562724E-07 0.69029860E-11-0.63797098E-15
 0.29231107E+05 0.49628592E+01 0.30309401E+01-0.22525853E-02 0.39824540E-05
-0.32604921E-08 0.10152035E-11 0.29136525E+05 0.26099341E+01
H                                                300.000  5000.000      1.00790
 0.25000000E+01 0.00000000E+00 0.00000000E+00 0.00000000E+00 0.00000000E+00
 0.25474391E+05-0.45989841E+00 0.25000000E+01 0.00000000E+00 0.00000000E+00
 0.00000000E+00 0.00000000E+00 0.25474391E+05-0.45989841E+00
OH                                               300.000  5000.000     17.00730
 0.28897815E+01 0.10005879E-02-0.22048808E-06 0.20191288E-10-0.39409830E-15
 0.38857041E+04 0.55566425E+01 0.38737299E+01-0.13393773E-02 0.16348351E-05
-0.52133636E-09 0.41826975E-13 0.35802349E+04 0.34202406E+00
CO                                               300.000  5000.000     28.01040
 0.29840696E+01 0.14891390E-02-0.57899683E-06 0.10364577E-09-0.69353550E-14
-0.14245228E+05 0.63479156E+01 0.37100928E+01-0.16190964E-02 0.36923593E-05
-0.20319675E-08 0.23953344E-12-0.14356310E+05 0.29555352E+01
CO2                                              300.000  5000.000     44.00980
 0.44608040E+01 0.30981719E-02-0.12392571E-05 0.22741325E-09-0.15525955E-13
-0.48961441E+05-0.98635983E+00 0.24007797E+01 0.87350961E-02-0.66070879E-05
 0.20021862E-08 0.63274039E-15-0.48377527E+05 0.96951456E+01
CL???                                            300.000  5000.000     35.45300
 0.29537796E+01-0.40792712E-03 0.15288342E-06-0.26384345E-10 0.17206581E-14
 0.13695677E+05 0.30667325E+01 0.20774281E+01 0.29487169E-02-0.43919732E-05
 0.24499776E-08-0.41007685E-12 0.13871928E+05 0.73136343E+01
CL2??                                            300.000  5000.000     70.90600
 0.43077814E+01 0.31182816E-03-0.16310807E-06 0.44511913E-10-0.43057753E-14
-0.13458251E+04 0.20666684E+01 0.31316886E+01 0.48997877E-02-0.69411463E-05
 0.44785641E-08-0.10621859E-11-0.10979696E+04 0.77833424E+01
HCL??                                            300.000  5000.000     36.46100
 0.27665884E+01 0.14381883E-02-0.46993000E-06 0.73499408E-10-0.43731106E-14
-0.11917468E+05 0.64583540E+01 0.35248171E+01 0.29984862E-04-0.86221891E-06
 0.20979721E-08-0.98658191E-12-0.12150509E+05 0.23957713E+01
N2                                               300.000  5000.000     28.01340
 0.28532898E+01 0.16022128E-02-0.62936891E-06 0.11441022E-09-0.78057466E-14
-0.89008093E+03 0.63964896E+01 0.37044177E+01-0.14218753E-02 0.28670393E-05
-0.12028885E-08-0.13954677E-13-0.10640795E+04 0.22336285E+01
```

Table 2.8 Description of IDA Input File NOZZRAD.INP*

Record 1:   Header   Format:: 80A1

<u>Variable</u>   <u>Column</u>

HEAD   I-80   Problem description

Record 2:   Format: Free
                nstart, nt, nvfcal, norm, rmax, nprt, nfe, nfs, ntvf

<u>Variable</u>	<u>Value</u>	<u>Description</u>
nstart	1	Restart control flag
nt	0	Output tape for restart
nvfcal	1	View factor calculation technique option (also used to calculate solid angles). The solid angle computations are coded for the finite difference technique only. Therefore, nvfcal is set to 1 in the ravfac_sa subroutine.
norm	0	View factor normalization option
rmax	0.0	Maximum area-to-distance ratio
nprt	0	Immediate output control
nfe	0	Element override option
nfs	0	Shading override option
ntvf	1	View factor output tape

Record 2:   Format: Free
                IPLANE

<u>Variable</u>	<u>Value</u>	<u>Description</u>
IPLANE	N	Number of 3D planes (suggest 2)

Record 4:   Format: Free
                IDRW

<u>Variable</u>	<u>Value</u>	<u>Description</u>
IDRW	N	Number of radiating boundary segments

*Each input record has a header card associated with it. See Table 2.9 for sample case.

Table 2.8 Description of IDA Input File NOZZRAD.INP (Continued)

Record 5:   Format: Free
ITYPE(1),ITYPE(2),......, ITYPE(IDRW)

Variable	Value	Description
(ITYPE (I),I=1,IDRW)	2	Circular plane
	5	Cone

This record specifies the geometry used to describe each IDRW segment. A negative sign ahead of the variable is used to specify an outside surface.

Record(s) 6:   Format: Free
ILV1, ILV2, LQ, MV1, MV2, MV3

Record 6 is input for each IDRW surface which describes the flowfield grid indices that describe the inlet and wall joints that are to be treated as radiating surfaces.

Variable	Value	Description
ILV1	N	Beginning i index
ILV2	N	Ending i index
LQ	N	i increment
MV1	N	Beginning j index
MV2	N	Ending j index
MV3	N	j increment

Record 7:   Format: Free
ILOOP, INDIV, INRB

This record inputs the number of radiation source flowfield segments or points for each of three input variables.

Variable	Value	Description
ILOOP	N	number of do loops used to input flowfield points
INDIV	N	number of individual points to input as flowfield points
INRB	N	number of non-radiating boundary flowfield do loop's

Table 2.8 Description of IDA Input File NOZZRAD.INP (Continued)

Record(s) 8:   Format: Free
                               IN1, IN2, INQ, JN1, JN2, JNQ

Input one record 8 for each ILOOP zones

Variable	Value	Description
IN1	N	Beginning i index for iloop flowfield zones
IN2	N	Ending i index for iloop flowfield zones
INQ	N	i increment
JN1	N	Beginning j index for iloop flowfield zones
JN2	N	Ending j index for iloop flowfield zones
JNQ	N	j increment

Record(s) 9:   Format: Free
                               IXNODE, IYNODE

Input one record 9 for each specified INDIV flowfield point

Variable	Value	Description
IXNODE	N	i point index
IYNODE	N	j point index

Record(s) 10:   Format: Free
                               IN1, IN2, JN1, JN2, JNQ

Input one record 10 for each non-radiating boundary point (INRB) loop

Variable	Value	Description
IN1	N	Beginning i index for points
IN2	N	Ending i index for points
INQ	N	i increment
JN1	N	Beginning j index for points
JN2	N	Ending j index for points
JNQ	N	j increment

Table 2.8 Description of IDA Input File NOZZRAD.INP (Continued)

General notes on inputting NOZZRAD.INP

The input files contain headers for each input record. The headers must be input as shown in the sample input case (Table 2.9).

Two ranges of interpolation domains are required in the input (inlets/walls and flowfield.)

User must make sure that the corner and edge points of each interpolation domain are specified as either radiating boundary points or flowfield points. This ensures that interpolation of unknown incident radiation points in INTRP.f will be bounded by known values. These points are indicated in the input file 'NOZZRAD.INP'.

a. The radiating boundary points must be bounded by known values. This is accounted for by providing the node values associated with (1v1,1v2,1q;mv1,mv2,mq), and must include the endpoints and corner points of the radiating boundaries.

b. The flowfield points (not including radiating boundary points) must be bounded by known values. This is accounted for by providing the node values associated with iloop, indiv and inrb. The limits of the incident radiation nodes should extend one point off the radiation boundary nodes.

Incident RAD or flow nodes:

Do not input overlapping or duplicate points; i.e., each point specified through the iloop, indiv and inrb (non-radiating boundary) parameters must be unique (see subroutine VFINIT.f for more description).

Radiating boundary nodes:

Boundary points specified through (1v1,1v2,1q;mv1,mv2,mq) can overlap, especially when merging two segments together.

Can input segments in any order. Must specify at least two points per radiating boundary segment (can specify open flow (IDBC) boundaries as radiating boundaries).

Do not overlap radiating boundary points with incident flow points - this will result in incorrect calculation of interpolation indices in SORT.f.

It is important that the incident radiation source flow nodes input in NOZZRAD.INP bound all of the interior nodes, not including the radiating boundaries (no error message is generated if this procedure is not followed).

Table 2.8 Description of IDA Input File NOZZRAD.INP (Continued)

If iloop range, including step values, does not extend to all non-radiating boundaries, must include points via indiv or inrb input regions. Otherwise, SORT.f will not run correctly.

When running the IDA case within a portion of the total grid domain, the rule stated above must be followed (for 2D); user must supply radiating boundary such that all corner and edge points are specified, and incident radiation points such that all corner and edge points are specified; all of the corner and edge points together must form a square region.

Interpolation indices are determined only for J-lines that have more than one known point.

To get the best interpolation between known IDA points, and to avoid interpolation within skewed cells, place the radiating boundary points in the same J-line as the flowfield node points. Otherwise, there may result only one point in a given J-line (that corresponding to the radiating wall point).

When splitting a radiating boundary into more than one segment (1v1,1v2,lq;mv1,mv2,mq), user needs to group together all segments associated with the same wall in the RAD wall input portion of the NOZZRAD.INP file.

The differential increments along a line-of-sight in the Z (DSZ) and R (DSR) directions are currently set at 0.1 ft in subroutine OPDIST.f.

Zones
>   The radiation coding is written for a single grid zone only (IZON=1). However, there can be more than one radiation zone (IRADZN) through the inputs corresponding to iloop, indiv and inrb in file NOZZRAD.INP.

Wall Boundary
>   The radiation portion of code assumes following wall boundary location: A single nozzle wall located on north boundary.

VFINIT.f notes

Initializes the RAVFAC input file for a nozzle

Can choose a number of radiating wall points through the increment in the axial (LQ) and radial (MQ) directions (required input for view factor and solid angle runs)

Can also choose a number of flowfield grid nodes (required input for solid angle run)

Table 2.8 Description of IDA Input File NOZZRAD.INP (Continued)

The order of accuracy in calculating the view factors and the solid angles at each point can also be adjusted through the factor   ibe(# of elements in beta dir) and
ige(# of elements in gamma dir).

vfinit reads in NOZZRAD.INP and generates the file:

A.   IN.DAT_VF when iflow = 0
        View Factor Pre-processor -
                view factor computations from wall point to wall point:
                used in determining radiosity RADOSW in IDA method.

B.   IN.DAT_SA when iflow > 0
        Solid Angle Pre-processor -
                solid angle computations from wall point to flowfield node
                used in determining incident radiation RIO in IDA method.

iloop -   number of do-loop input 'zones'
indiv -   number of individual point input 'zones'
inrb -   number of non-radiating boundaries

1.   iflow is set to 1 for wall points to flowfield points by inputting through a do-loop (iloop > 0).
        The order of input is: do loop for radial dir.
                                    do loop for axial dir.
        This will result in 2 grid regions if all flowfield nodes are chosen:
                FDNS flowfield grid, IDA grid = SIRRM grid,
        or in 3 grid regions if some flowfield nodes are chosen:
                FDNS flowfield grid, SIRRM grid and IDA grid.

To get incident radiation at all points in flowfield with IDA method, program user must supply some nodes on all boundaries in the input (through iloop, indiv and/or inrb). This will provide values on all boundaries so that interpolation can be effective.

If a do-loop (*iloop > 0) with an increment in the i-node does not allow the max i-node to end on a boundary, then must input some boundary points individually or must specify points on a non-radiating boundary.
        (If iflow "ge" 1, points chosen lie in axisymmetric plane)

iplane -   number of planes within total angle (g2-g1)

        The circumferential extent of the wall surfaces is taken into account by the angle parameters g1 and g2.

Table 2.9 Listing of NOZZRAD.INP Sample Case

```
                    NOZZLE VIEW FACTORS
nstart nt nvfacl norm rmax nprt nfe nsf ntvf (nvfacl must = 1)
   1    0   1     0   0.   0    0   0    1
# of planes in 360 degrees (iplane)
2
--RADIATING WALL OR RADIOSITY POINTS--
   number of radiating walls (idrw)
   4
   type of wall (ityp)  [2=circular plate, 5=cone; (-) for outside surface]
    2    2   -5   -5
   indices for radiating wall 1 (lv1,lv2,lq;mv1,mv2,mq)
    1    1    1       1   77   19
   indices for radiating wall 2 (lv1,lv2,lq;mv1,mv2,mq)
    1    1    1      77   81    4
   indices for radiating wall 3 (lv1,lv2,lq;mv1,mv2,mq)
    1  177   44      81   81    1
   indices for radiating wall 4 (lv1,lv2,lq;mv1,mv2,mq)
  177  179    2      81   81    1
--RADIATION SOURCE FLOWFIELD OR INCIDENT RADIATION POINTS--
   # of do-loop zones (iloop), individual points (indiv),
   and non-rad boundaries (inrb)
   2    2    2
 a.  do-loop points: in1,in2,inq; jn1,jn2,jnq
   45  177   44       1   77   19
   45  177   44      80   80    1
 b.  ixnode, iynode indices for flowfield points:
    2   80
  179   80
 c.  non-radiating boundary points: in1,in2,inq; jn1,jn2,jnq
    2    2    1       1   77   19
  179  179    1       1   77   19
```

(5) *
(2)
(5)
(2)

(20) **
(4)
(1)
(1)
(5)
(5)

* The variable IWR (# of radiating boundary points) in BLKDAT_*.f must be set based on the wall points selected in this input file which is 14 for this case.

** The variable IWN (# of radiating flowfield points) in BLKDAT__*.f must be set based on the flowfield points selected in this input file which is 36 for this case.

Table 2.10 Description of rad01 Include File

PARAMETER   (IIQMAX = 14500, IWP = 201)
                    !max grid points and max wall points in 2D

PARAMETER   (NSPM = 12, ISPMAX = IIQMAX)
                    !max species and switch that lets code know that every point in domain requires species calculations (set ispmax to 1 otherwise)

PARAMETER   (NPMAX = 1, IJKPMX = IIQMAX)
                    !number types of particles and switch that lets code know that every point in domain requires particle calculations (set ijkpmx to 1 otherwise)

PARAMETER   (IMAP = 60)
                    !60 SIRRM map input nodes (for particle radiation)

PARAMETER   (IPLMAX = 2, IDRWMX = 4, IDRNMX = 6)
                    !Two 3D revolved planes for IDA radiation

PARAMETER   (IWR = 14, IWN = 36)
                    !number of radiating boundary points and incident radiation nodal points in interior for IDA)

PARAMETER   (NGBAND = 4, NPBAND = 5)
                    !max number of gas and particle bands or windows (choice of npband is tricky when irad=4 since the number of particle band segments the code chooses may not be evident. Choose a reasonable value for this variable).

PARAMETER   (IWRP = IWR*IPLMAX, NTBAND = NGBAND+NPBAND)

Notes on setting variables in RAD01

Change IIQMAX and IWP in RAD01 for appropriate dimensions. (for multi-species problems set NSWPM = number of species and ISPMAX = IIQMAX. Note: Do not change other parameters.)

Set IMAP to the larger of the following values:
         IXSTA (number of x-stations in SIRRM map file)
         IYSTA (number of y-stations in SIRRM map file)

Set IPLMAX to the number of 3D planes required for radiosity calculations.

Set IDRWMX to the maximum number of radiating walls in the axisymmetric plane, and IDRNMX to the maximum number of radiating source zones in the axisymmetric plane (see NOZZRAD.INP file).

Set IWR to the maximum number of radiating boundary points on any boundary for IDA in the axisymmetric plane (if two boundary corners have overlapping point, must count as 2 points).

Table 2.10 Description of rad01 Include File (Continued)

Set IWN to the maximum number of flowfield node points for IDA incident radiation in the axisymmetric plane. (IWR and IWN must be equal to the values in NOZZRAD.INP that correspond to the number of radiating wall or radiosity points (lv1, lv2, lq:mv1,mv2,mq) and to the number of radiating source or incident radiation points (iloop;indiv;inrb), respectively).

Set NGBAND to the dimension of the total number of gas bands, summed over all gas species.

Set NPBAND to the dimension of the total number of particle bands (or particle window bands for IRAD=4), summed over all particle species. For IRAD=4, make NPBAND a little larger. This is required since the number of particle bands may be split into additional band segments due to gas/particle overlap.

(ex.1:

for IRAD=3,	NGBAND=11	for all gas bands of H_2O and CO_2;
	NPBAND=12	for all particle bands from 0.5 to 6.0 microns.)

(ex2:

for IRAD=4	NGBAND=11	for all gas bands of H_2O and CO_2;
	NPBAND=18	for all particle bands from 0.5 to 6.0 microns, where the 18 bands are associated with the particle window regions (those regions that are not associated with the gas/particle overlap regions.))

Table 2.11 Notes in Setting BLKDAT_*.f Variables

There are several options to choose to run a radiation case, as described in the following fortran files:

BLKDAT_0.f (radiation initializing),
BLKDAT_U.f (uncoupled radiation code)

NOTE: The BLKDAT_*.x files differ in the amount of data required to run the specific code in their respective subdirectories. Make sure that any data changes made to BLKDAT_0.f is likewise made in BLKDAT_U.f. Also, recompile the code when BLKDAT_*.f has been modified.

However, most of the values in the block data files above can be left as the default values.

The most common values which must be changed are the following:

1. IAP:

=	1:	ODA (optically thick region only)
=	2:	Defunct
=	3:	IDA (all optical thicknesses)

2. For gas cases:

NSPMS, NSPME -   The starting and ending indices for the gas species
NLAMGS,NLAMGE -   The corresponding wavelength indices as listed in The ALAMG data statement

3. For particle cases:

NPMAXS,NPMAXE -   The starting and ending indices for the particle species
NLAMPS,NLAMPE -   The corresponding wavelength indices as listed in The ALAMP data statement.

4. IDSPG   Indices corresponding to the gas species number as input in the CEC section of fort.11 (those corresponding to H_2O and or CO_2)

Example: To run an IDA case with gas/particle overlap
NSPM = 1 (starts with H_2O)
NSPME = 2 (ends with CO_2)
NLAMGS(1) = 3 (starts with 2.7 microns for H_2O)
NLAMGS(1) = 4 (ends with 1.87 microns for H_2O)
NLAMGS(2) = 4 (starts with 4.3 microns for CO_2)
NLAMGS(2) = 5 (ends with 2.7 microns for CO_2)
NPMAXS = 1 (starts with Al_2O_3)
NPMAXE = 1 (ends with Al_2O_3)
NLAMPS(1) = 7 (starts with 1.0 micron for Al_2O_3)
NLAMPS(1) = 9 (ends with 3.0 microns for Al_2O_3)

SET   IVIEW = 0 for ODA cases and
IVIEW = 1 for IDA cases

Additional notes on the variables set in BLKDAT*.f can be found in comments contained in BLKDAT*.f

Table 2.12 Additional Notes on the Options Available in IDARAD

Number of gas-only bands: NOLAMG
Number of particle-only bands: NOLAMP

Wavelength sequence (ILT) for ISPECL > 0:
    IRAD=1 (gas-only):
    ILT sequence corresponds to descending wavelength order

```
        ILT = 0
        DO ISP=NSPMS,NSPME                       (outer loop)
        DO IWV=NLAMGS(ISP),NLAMGE(ISP)           (inner loop)
            ILT = ILT+1
        END DO
```

  IRAD=2 (particle-only):
  ILT sequence corresponds to ascending wavelength order

```
        ILT = 0
        DO IPA=NPMAXS,NPMAXE                     (outer loop)
        DO IWV+NLAMPS(IPA),NLAMPE(IPA)           (inner loop)
            ILT = ILT+1
        END DO
```

  IRAD=3 (non overlapping gas and particles):
    Determines ILT according to IRAD=1 first, then continues ILT according to IRAD=2.

IRAD=4   *   gas-only bands
         *   Overlapping gas and particles within the total particle band width DLAMP (continuum width DLAMP chosen by the user),
         *   The remaining particle bands that fall within DLAMP
         *   The DLAMP bands that have no overlapping gas bands (referred to as windows):

a: Determines gas-only and gas/particle overlap sequencing first by ranging through the loops as in IRAD=1. The wavelengths are in descending order, consistent with the input order for ALAMG above. (This descending order must be adhered to as the gas band widths in WIDEMB.f are calculated accordingly).

b.   Continues ILT sequencing by finding the remaining particle bands that do not overlap with any gas band (window region). These particle wavelengths are in ascending order, with the particle band widths calculated as described in i and ii below. (Gas wavelength parameters are computed in subroutine RADO(1) so that they are in ascending wavelength order, making it more convenient to check for gas/particle overlapping with the ascending wavelength of the particles, and separating out the remaining particle bands from the gas bands).

i.   If there are overlapping gas bands, the total particle band width (DLAMP) is split into a number of smaller particle bands (reduced particle band width) which lie between the two DLAMP endpoints ALPEND. The particle bands extend from ALPEND to the nearest gas band endpoint, and/or between gas band endpoints.

Table 2.12 Additional Notes on the Options Available in IDARAD (Continued)

ii.   If there are no overlapping gas bands within the particle width DLAMP, the particle band corresponding to ILT is ALAMP.

NOTE: The number of particle-only band 'centers' (ILT sequencing) may not equal the number of particle-only band widths. For example, when a gas band overlaps or extends past the ALPEND boundary (gas band width varies as the temp., pressure and species mass fraction varies), the reduced particle band width would equal zero since there would be no particle gap (See coding in PBAND.f).

NOTE: For IRAD 4

a.   The portion of the particle band that overlaps with a gas band is accounted for. The effect of overlapping particle bands are not subtracted.

b.   If two neighboring particle band widths overlap, there will be a discrepancy in the value of NOLAMP (should be decreased by 1). For different press and temp states, NOLAMP could feasibly fluctuate. The code requires a constant value for NOLAMP. Until a method is devised that computes a single P1 equation for all of the particle-only bands together (which would automatically take the varying band width total into account), NOLAMP must remain constant. Therefore, if two particle bands overlap, the value for DLAMG is set to zero.

c.   Band widths which extend beyond the input values for ALAMP are necessarily cut off at the band end points (ALPEND) of the band centers (ALAMP). This shortcut reduces the coding complexity. The result is an increase in the total particle-only bands, which may be somewhat erroneous. However, the gas band widths are accounted for without shortcuts, since the actual value for the gas band widths are used. If this causes concern, the remedy is to choose new (initial) values for ALAMP (and corresponding values for ALPEND) which bypass this problem. For example, if the 1.38 band of H_2O has a width that extends beyond the 1.5 particle band end point, the value 1.5 could be changed to 1.7 to allow the 1.38 band width to fall within the particle band search region; or, the value of ALAMP could be kept as is, but ALPEND could be adjusted.

d.   For more than one type of solid species (eg, Al_2O_3, C(S), etc), the loop (IPA in subroutine RADIN0) would have to be extended to the other species, in addition to a single species.

    eg.:   DO IS = 1,NSPEC

                DO N=1, IRP

This would be required when choosing the option IRAD=4, where the extinction coefficient (averaged over all particle sizes) at a gas band center would be a summation of the SIGEXT of the gas band plus the overlapping particle bands. No provision is made in the code for this at present; only a single solid species type (Al_2O_3) is allowed (SIGEXT = SIGABS_gas + SIGEXT_Al_2O_3)

Wall Emissivity

    The code is presently set up to allow the same wall emissivity value at every wall point. Also, the black wall option, IBLAKW, must be set to 0 for IDA cases, since the black wall boundary condition case is not coded.

ODA Case

    If a larger number of ODA iterations is required for additional convergence, along with a tighter tolerance on the two convergence criteria, these values can be changed in subroutine ODA.f:

        IODAIT = # of iterations (default = 1500)

        TOL1 = Tolerance for average residual (default = 1.E-9)

        TOL2 = Tolerance for maximum residual (default = 1.E-6)

Additional description can be found in read.me_rad_u_1, read.me_rad_u_2 (uncoupled radiation code)

2.2.3.2 Installation of IDARAD

IDARAD was developed and checked out on a UNIX based IBM RISC work station. There is no system specific coding so that the program can be readily compiled on any system that has a fortran compiler and sufficient storage. The core storage requirements are dependent on the problem being run (i.e., dimensions set in rad01). The radiation initiation code (RAD0) and the actual IDARAD code (RAD) should be loaded in separate directories. The RAD0 initialization code is contained on the MS-DOS disk RAD1. The IDARAD code is contained on MS-DOS disk RAD2. Table 2.13 lists the make file that contains the compilation and links instructions for the flow initialization code (RAD0), using an IBM AIX XL/6000 fortran compiler. Table 2.14 contains a listing of the make file for the IDARAD code. Table 2.15 contains a listing of the functional subroutines and include files that make up the IDARAD code.

The most efficient way to use the initialization and IDARAD codes is to execute them in a separate directory for each problem. In addition to fort.11, fort.12, fort.13, fort.61 and NOZZRAD.INP files that are set up by the user, the optical properties files; koch2.prn, SIGACL.DAT and SIGSCL.DAT must also be contained in the working directory. The MS-DOS disc RAD3 contains sample case input data files and the optical properties files for running the cases whose results are presented in the next section. The fort.11 files are fort.11_ODA and fort.11_IDA for the ODA and IDA cases.

2.2.4 IDA and ODA Results

The experiment selected to check out the IDARAD code was the MNASA 48 inch contoured ASRM nozzle plume radiation test. A Cycle 2.0 SIRRM map was converted into fort.12, fort.13 and fort.61 grid, flowfield and SIRRM mapped files for a 20 x 21 grid. The fort.11, fort.12, fort.13, fort.61 and NOZZRAD.INP files are contained on the MS-DOS disk RAD2. ODA and IDA results consist of emissive power at the boundary as a function of axial

Table 2.13 Listing of the makefile File For Compiling and Linking the Radiation Initializing Program (RAD0)

```
rad_0 : rad_init.o r1.o r2.o r3.o BLKDAT_0.o TRANF.o
        xlf rad_init.o r1.o r2.o r3.o BLKDAT_0.o TRANF.o  -o rad_0
rad_init.o : rad_init.f
        xlf -c -v -g -qcheck -qflttrap -qdpc=e -qhssngl -qautodbl=dblpad -I. -NQ20000 rad_init.f
r1.o : r1.f
        xlf -c -v -g -qcheck -qflttrap -qdpc=e -qhssngl -qautodbl=dblpad -I. -NQ20000 r1.f
r2.o : r2.f
        xlf -c -v -g -qcheck -qflttrap -qdpc=e -qhssngl -qautodbl=dblpad -I. -NQ20000 r2.f
r3.o : r3.f
        xlf -c -v -g -qcheck -qflttrap -qdpc=e -qhssngl -qautodbl=dblpad -I. -NQ20000 r3.f
BLKDAT_0.o : BLKDAT_0.f
        xlf -c -v -g -qcheck -qflttrap -qdpc=e -qhssngl -qautodbl=dblpad -I. -NQ20000 BLKDAT_0.f
TRANF.o : TRANF.f
        xlf -c -v -g -qcheck -qflttrap -qdpc=e -qhssngl -qautodbl=dblpad -I. -NQ20000 TRANF.f
```

Table 2.14 Listing of the makefile File For Compiling and Linking the IDARAD Program

```
rad : radpl.o r2.o r1.o WIDERM.o VFINIT.o TRANF.o TRDIAG.o TAUDR.o SUMMA1.o SRCIDA.o SORT.o SIGSCL.o SIGAV.o SIGACL.o RSIRRM.o
REFRIN.o REFRAC.o RDOSTY.o RAVFAC.o RADIN0.o RAD0.o PLANKF.o PLANKB.o FBAND.o PATHL.o OVRLAP.o OPDIST.o ODABC.o ODA.o MONCHR.o L
SIGHT.o LOGINT.o LININR.o LININT.o JWALL.o INVERT.o INTRF3.o INTRF2.o INTRF1.o INTRF0.o INRAD.o IDABC.o IDA.o HTRAD.o GMEDUM.o E
XTINC.o ECOEFP.o ECOEFG.o DLAMB.o CELLIJ.o BLKDAT_U.o ASTAR.o
	xlf radpl.o r2.o r1.o WIDERM.o VFINIT.o TRANF.o TRDIAG.o TAUDR.o SUMMA1.o SRCIDA.o SORT.o SIGSCL.o SIGAV.o SIGACL.o RSI
RRM.o REFRIN.o REFRAC.o RDOSTY.o RAVFAC.o RADING.o RAD0.o PLANKF.o FLANKB.o PBAND.o FATHL.o OVRLAP.o OPDIST.o ODABC.o ODA.o MONC
HR.o LSIGHT.o LOGINT.o LININT.o LININR.o JWALL.o INVERT.o INTRF3.o INTRF2.o INTRF1.o INTRF0.o INRAD.o IDABC.o IDA.o HTRAD.o GWALL.o GMED
UM.o EXTINC.o ECOEFP.o ECOEFG.o DLAMB.o CELLIJ.o BLKDAT_U.o ASTAR.o -bloadmap:error -o rad

ASTAR.o : ASTAR.f
	xlf -c -v -O3 -qcheck -qflttrap -qdpc=e -qhssngl -qautodbl=dblpad -I. -NQ20000 ASTAR.f
BLKDAT_U.o : BLKDAT_U.f
	xlf -c -v -O3 -qcheck -qflttrap -qdpc=e -qhssngl -qautodbl=dblpad -I. -NQ20000 BLKDAT_U.f
CELLIJ.o : CELLIJ.f
	xlf -c -v -O3 -qcheck -qflttrap -qdpc=e -qhssngl -qautodbl=dblpad -I. -NQ20000 CELLIJ.f
DLAMB.o : DLAMB.f
	xlf -c -v -O3 -qcheck -qflttrap -qdpc=e -qhssngl -qautodbl=dblpad -I. -NQ20000 DLAMB.f
ECOEFG.o : ECOEFG.f
	xlf -c -v -O3 -qcheck -qflttrap -qdpc=e -qhssngl -qautodbl=dblpad -I. -NQ20000 ECOEFG.f
ECOEFP.o : ECOEFP.f
	xlf -c -v -O3 -qcheck -qflttrap -qdpc=e -qhssngl -qautodbl=dblpad -I. -NQ20000 ECOEFP.f
EXTINC.o : EXTINC.f
	xlf -c -v -O3 -qcheck -qflttrap -qdpc=e -qhssngl -qautodbl=dblpad -I. -NQ20000 EXTINC.f
GMEDUM.o : GMEDUM.f
	xlf -c -v -O3 -qcheck -qflttrap -qdpc=e -qhssngl -qautodbl=dblpad -I. -NQ20000 GMEDUM.f
GWALL.o : GWALL.f
	xlf -c -v -O3 -qcheck -qflttrap -qdpc=e -qhssngl -qautodbl=dblpad -I. -NQ20000 GWALL.f
HTRAD.o : HTRAD.f
	xlf -c -v -O3 -qcheck -qflttrap -qdpc=e -qhssngl -qautodbl=dblpad -I. -NQ20000 HTRAD.f
IDA.o : IDA.f
	xlf -c -v -O3 -qcheck -qflttrap -qdpc=e -qhssngl -qautodbl=dblpad -I. -NQ20000 IDA.f
IDABC.o : IDABC.f
	xlf -c -v -O3 -qcheck -qflttrap -qdpc=e -qhssngl -qautodbl=dblpad -I. -NQ20000 IDABC.f
INRAD.o : INRAD.f
	xlf -c -v -O3 -qcheck -qflttrap -qdpc=e -qhssngl -qautodbl=dblpad -I. -NQ20000 INRAD.f
INTRF0.o : INTRF0.f
	xlf -c -v -O3 -qcheck -qflttrap -qdpc=e -qhssngl -qautodbl=dblpad -I. -NQ20000 INTRF0.f
INTRF1.o : INTRF1.f
	xlf -c -v -O3 -qcheck -qflttrap -qdpc=e -qhssngl -qautodbl=dblpad -I. -NQ20000 INTRF1.f
INTRF2.o : INTRF2.f
	xlf -c -v -O3 -qcheck -qflttrap -qdpc=e -qhssngl -qautodbl=dblpad -I. -NQ20000 INTRF2.f
INTRF3.o : INTRF3.f
	xlf -c -v -O3 -qcheck -qflttrap -qdpc=e -qhssngl -qautodbl=dblpad -I. -NQ20000 INTRF3.f
INVERT.o : INVERT.f
	xlf -c -v -O3 -qcheck -qflttrap -qdpc=e -qhssngl -qautodbl=dblpad -I. -NQ20000 INVERT.f
JWALL.o : JWALL.f
	xlf -c -v -O3 -qcheck -qflttrap -qdpc=e -qhssngl -qautodbl=dblpad -I. -NQ20000 JWALL.f
LININR.o : LININR.f
	xlf -c -v -O3 -qcheck -qflttrap -qdpc=e -qhssngl -qautodbl=dblpad -I. -NQ20000 LININR.f
LININT.o : LININT.f
	xlf -c -v -O3 -qcheck -qflttrap -qdpc=e -qhssngl -qautodbl=dblpad -I. -NQ20000 LININT.f
LOGINT.o : LOGINT.f
	xlf -c -v -O3 -qcheck -qflttrap -qdpc=e -qhssngl -qautodbl=dblpad -I. -NQ20000 LOGINT.f
LSIGHT.o : LSIGHT.f
	xlf -c -v -O3 -qcheck -qflttrap -qdpc=e -qhssngl -qautodbl=dblpad -I. -NQ20000 LSIGHT.f
MONCHR.o : MONCHR.f
	xlf -c -v -O3 -qcheck -qflttrap -qdpc=e -qhssngl -qautodbl=dblpad -I. -NQ20000 MONCHR.f
ODA.o : ODA.f
	xlf -c -v -O3 -qcheck -qflttrap -qdpc=e -qhssngl -qautodbl=dblpad -I. -NQ20000 ODA.f
ODABC.o : ODABC.f
	xlf -c -v -O3 -qcheck -qflttrap -qdpc=e -qhssngl -qautodbl=dblpad -I. -NQ20000 ODABC.f
```

Table 2.14 Listing of the makefile File For Compiling and Linking the IDARAD Program (Continued)

```
OPDIST.o : OPDIST.f
    xlf -c -v -O3 -qcheck -qflttrap -qdpc=e -qhssngl -qautodbl=dblpad -I. -NQ20000 OPDIST.f
OVRLAP.o : OVRLAP.f
    xlf -c -v -O3 -qcheck -qflttrap -qdpc=e -qhssngl -qautodbl=dblpad -I. -NQ20000 OVRLAP.f
PATHD.o : PATHD.f
    xlf -c -v -O3 -qcheck -qflttrap -qdpc=e -qhssngl -qautodbl=dblpad -I. -NQ20000 PATHD.f
PATHL.o : PATHL.f
    xlf -c -v -O3 -qcheck -qflttrap -qdpc=e -qhssngl -qautodbl=dblpad -I. -NQ20000 PATHL.f
PBAND.o : PBAND.f
    xlf -c -v -O3 -qcheck -qflttrap -qdpc=e -qhssngl -qautodbl=dblpad -I. -NQ20000 PBAND.f
PLANKB.o : PLANKB.f
    xlf -c -v -O3 -qcheck -qflttrap -qdpc=e -qhssngl -qautodbl=dblpad -I. -NQ20000 PLANKB.f
PLANKF.o : PLANKF.f
    xlf -c -v -O3 -qcheck -qflttrap -qdpc=e -qhssngl -qautodbl=dblpad -I. -NQ20000 PLANKF.f
RAD0.o : RAD0.f
    xlf -c -v -O3 -qcheck -qflttrap -qdpc=e -qhssngl -qautodbl=dblpad -I. -NQ20000 RAD0.f
RADIN0.o : RADIN0.f
    xlf -c -v -O3 -qcheck -qflttrap -qdpc=e -qhssngl -qautodbl=dblpad -I. -NQ20000 RADIN0.f
RAVFAC.o : RAVFAC.f
    xlf -c -v -O3 -qcheck -qflttrap -qdpc=e -qhssngl -qautodbl=dblpad -I. -NQ20000 RAVFAC.f
RDOSTY.o : RDOSTY.f
    xlf -c -v -O3 -qcheck -qflttrap -qdpc=e -qhssngl -qautodbl=dblpad -I. -NQ20000 RDOSTY.f
REFRAC.o : REFRAC.f
    xlf -c -v -O3 -qcheck -qflttrap -qdpc=e -qhssngl -qautodbl=dblpad -I. -NQ20000 REFRAC.f
REFRIN.o : REFRIN.f
    xlf -c -v -O3 -qcheck -qflttrap -qdpc=e -qhssngl -qautodbl=dblpad -I. -NQ20000 REFRIN.f
RSIRRM.o : RSIRRM.f
    xlf -c -v -O3 -qcheck -qflttrap -qdpc=e -qhssngl -qautodbl=dblpad -I. -NQ20000 RSIRRM.f
SIGACL.o : SIGACL.f
    xlf -c -v -O3 -qcheck -qflttrap -qdpc=e -qhssngl -qautodbl=dblpad -I. -NQ20000 SIGACL.f
SIGAV.o : SIGAV.f
    xlf -c -v -O3 -qcheck -qflttrap -qdpc=e -qhssngl -qautodbl=dblpad -I. -NQ20000 SIGAV.f
SIGSCL.o : SIGSCL.f
    xlf -c -v -O3 -qcheck -qflttrap -qdpc=e -qhssngl -qautodbl=dblpad -I. -NQ20000 SIGSCL.f
SORT.o : SORT.f
    xlf -c -v -O3 -qcheck -qflttrap -qdpc=e -qhssngl -qautodbl=dblpad -I. -NQ20000 SORT.f
SRCIDA.o : SRCIDA.f
    xlf -c -v -O3 -qcheck -qflttrap -qdpc=e -qhssngl -qautodbl=dblpad -I. -NQ20000 SRCIDA.f
SUMMA1.o : SUMMA1.f
    xlf -c -v -O3 -qcheck -qflttrap -qdpc=e -qhssngl -qautodbl=dblpad -I. -NQ20000 SUMMA1.f
SUMMA2.o : SUMMA2.f
    xlf -c -v -O3 -qcheck -qflttrap -qdpc=e -qhssngl -qautodbl=dblpad -I. -NQ20000 SUMMA2.f
TAUDR.o : TAUDR.f
    xlf -c -v -O3 -qcheck -qflttrap -qdpc=e -qhssngl -qautodbl=dblpad -I. -NQ20000 TAUDR.f
TRANF.o : TRANF.f
    xlf -c -v -O3 -qcheck -qflttrap -qdpc=e -qhssngl -qautodbl=dblpad -I. -NQ20000 TRANF.f
TRDIAG.o : TRDIAG.f
    xlf -c -v -O3 -qcheck -qflttrap -qdpc=e -qhssngl -qautodbl=dblpad -I. -NQ20000 TRDIAG.f
VFINIT.o : VFINIT.f
    xlf -c -v -O3 -qcheck -qflttrap -qdpc=e -qhssngl -qautodbl=dblpad -I. -NQ20000 VFINIT.f
WIDEBM.o : WIDEBM.f
    xlf -c -v -O3 -qcheck -qflttrap -qdpc=e -qhssngl -qautodbl=dblpad -I. -NQ20000 WIDEBM.f
r2.o : r2.f
    xlf -c -v -O3 -qcheck -qflttrap -qdpc=e -qhssngl -qautodbl=dblpad -I. -NQ20000 r2.f
r1.o : r1.f
    xlf -c -v -O3 -qcheck -qflttrap -qdpc=e -qhssngl -qautodbl=dblpad -I. -NQ20000 r1.f
radpl.o : radpl.f
    xlf -c -v -O3 -qcheck -qflttrap -qdpc=e -qhssngl -qautodbl=dblpad -I. -NQ20000 radpl.f
```

Table 2.15 Listing of Fortran and Includes Files for the IDARAD Program

```
FORTRAN FILES:
* rinit.f = initialization files
  VFINIT.f RAVFAC.f PATHD.f  PATHL.f
  r1.f r2.f radp1.f
* rprop.f = particle input files
  SIGACL.f SIGSCL.f REFRIN.f
* rgas.f = gas property files
  ECOEFG.f WIDEBM.f SUMMA1.f SUMMA2.f ASTAR.f
* rprtcl.f = particle property files
  ECOEFP.f SIGAV.f  REFRAC.f FBAND.f  OVRLAP.f
* radint.f = radiation driver files
  RADIN0.f MONCHR.f EXTINC.f PLANKF.f HTRAD.f
* roda.f = oda files
  ODA.f     TRDIAG.f ODABC.f  DLAMB.f  PLANKB.f
* rida.f = ida files
  IDA.f    GWALL.f  GMEDUM.f OPDIST.f IDABC.f
  INRAD.f
* rlos.f = line-of-sight files
  LSIGHT.f TAUDR.f  SRCIDA.f
* rwall.f = radiosity files
  RDOSTY.f JWALL.f  INVERT.f
* rintrp.f = interpolation files
  LOGINT.f LININT.f LININR.f CELLIJ.f SORT.f
  INTRP0.f INTRP1.f INTRP2.f INTRP3.f
* BLKDAT_U.f = block data file


INCLUDE FILES:
  common block files -
                 rad01, rad02,...,rad24,
             and alumox.inc, rad1.inc
  fortran code include files -
                 rad2.inc - error statement check
                 init.inc - sets additional radiation parameters
                 dataio1.inc - reads in radiation files
                         fort.15 and fort.16
                 dataio2.inc - outputs radiation files
                         fort.25 and fort.26
                 widebm1.inc & widebm2.inc -
                         additional fortran code for
                         wide band model (WIDEBM.f)
                 h2o.inc - fortran code for determining
                         wide band parameters for h2o
                 co2.inc - fortran code for determining
                         wide band parameters for co2
                 print_u.inc - heating rate driver
```
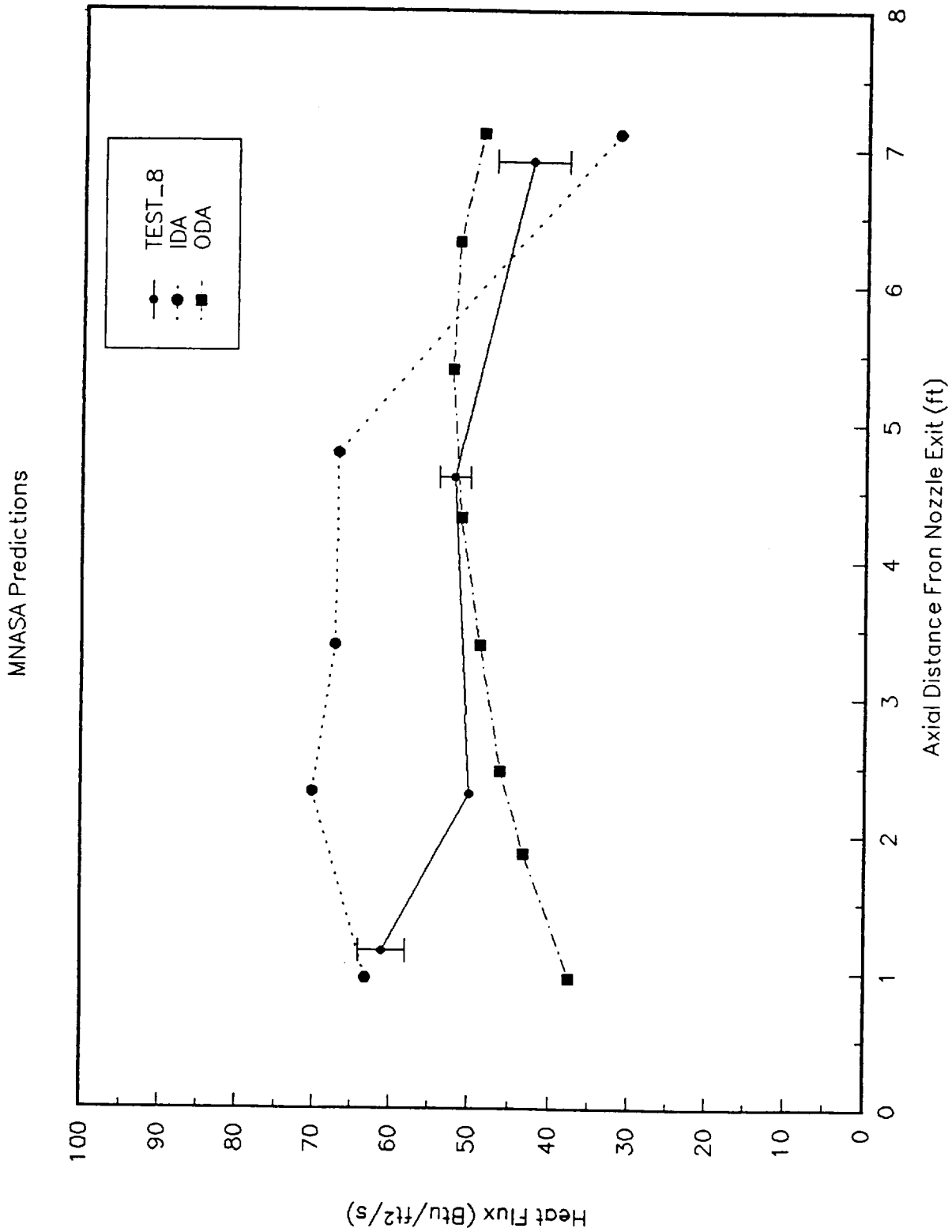
MNASA Predictions

Fig. 2.7   Comparison of ODA and IDA Prediction of Plume Emissive Power Distributions
for the MNASA48 inch Contoured ASRM Nozzle

distance from the nozzle exit plane. Figure 2.7 presents the IDA and ODA results compared with the measured data.

The ODA methodology tends to underpredict the measurements in the near field of the plume. The flowfield that was used for these calculations started at the exit plane. Subsequent calculations that included the nozzle flowfield, as well as the plume, better predict the observed trends in the measurements. These calculations reproduce the test data beyond 2 feet and are 20% low at 1 foot. The IDA results generally overpredict the data (up to 25-30%). It is possible that the boundary conditions that are used at the plume boundary are not appropriate for this application (although they are very good for radiation to the internal portions of nozzles). Further, research is required to investigate the potential effects on the IDA results due to boundary condition treatment. In view of the limited amount of validation that was performed with the IDARAD code as compared to the SIRRM and REMCAR codes, the results are encouraging.

2.3 Other Solution Methods for the RTE, Including Two-Flux Models

Although the method of spherical harmonics discussed in previous section appeared to be an attractive approach to predicting radiation heating from SRM plumes, it had not been applied to this problem prior to this study. Therefore, several radiation analysis codes from the literature were considered for use in this study. The SIRRM-II code (Ref. 2.6) contains an extensive data base for gaseous narrow band models and particle radiation, and two-flux and six-flux radiation models. However, the SIRRM flux models are written for fore, aft, and side-on radiation analysis only, so they are of little direct value for base heating analysis. The REMCAR code (Ref. 2.15) is the reverse Monte Carlo code written by REMTECH; it is very general and useful, but it is also slow because of the extensive calculations required. The GASRAD code (Ref. 2.16) describes gaseous emission and absorption from H_2O, CO_2, CO, and soot for axisymmetric or three-dimensional flowfield input by integrating along multiple lines of sight. Among the other solution methods for the RTE considered was the method of

discrete coordinates (Ref. 2.19). This method has been used extensively and successfully for describing furnace operation. Furthermore, the first-order discrete coordinate solution is the two-flux model which forms the basis of the JANNAF SIRRM code (Ref. 2.6) and has been used in early work for SRM plume heating analysis. Therefore, a parallel study was made to determine the utility of the two-flux as an alternative analysis for SRM plume radiation evaluation. This two-flux study also provided a convenient tool for utilizing the extensive radiation property data base which already exists in the SIRRM code. The NOZZRAD code (Ref. 2.27) utilizes a two-flux model to describe emitting/absorbing/scattering media for an axisymmetric flowfield input. Gas and particle radiation are treated independently, not simultaneously in the NOZZRAD code. Both the NOZZRAD and GASRAD codes were used for sooty plumes. After the GASRAD or NOZZRAD code is used to establish the directional emissivities at the plume boundaries, the RAVFAC code (Ref. 2.23) is used to calculate radiation to points outside the plume. When RAVFAC is used to determine base heating, the view factors predicted with this code account for shading of vehicle components along the various lines-of-sight. Detailed descriptions of all of the codes mentioned in this paragraph are described in the cited references, except for the NOZZRAD code which is described herein.

For emitting/absorbing media, integrations along lines-of-sight can be performed to predict radiation, as is done in the GASRAD code. If the media also scatters the radiation, the entire radiating volume must be considered at one time. If the volume consists of plane layers, each of which have constant properties, the radiative transport becomes essentially one-dimensional and the two-flux radiation analysis applies. Since the two-flux model resembles the gas only analysis, the same type of one-dimensional beam analysis can be applied to emitting/absorbing/scattering media if the following assumption is made. If the radiation field is assumed to be represented by a series of plane uniform layers which overlap and vary along each line-of-sight, multiple two-flux analyses can be performed to evaluate the local directional emission from the radiating volume. This procedure was used in the Aeronutronic work (Ref. 2.28) and in the SIRRM code for field-of-view calculations. In SECA's launch stand design studies (Ref. 2.27), the two-flux model analysis for slabs of varying temperature and particle

properties was updated and issued as the NOZZRAD code. In this study, the NOZZRAD code was extended to use an axisymmetric plume or motor analysis as input and perform one-dimensional beam analyses along selected lines-of-sight to provide directional emissivities from the plume. The resulting NOZZRAD predictions could then be used with RAVFAC to provide plume heating analyses. Thus, an analysis analogous to the GASRAD/RAVFAC predictions for gas plumes can now be performed for SRM plumes. The NOZZRAD analysis is developed as follows.

2.3.1 The Two-Flux Model for Particle Flows

The equation of radiative transfer along a line of sight:

$$dI_\lambda\{s,\mu,\phi\}/ds = -(\sigma_a+\sigma_s) I_\lambda\{s,\mu,\phi\} + \sigma_a I_{\lambda b} + (\sigma_s/4\pi) \int_0^{2\pi} \int_0^\pi$$
$$I_\lambda\{s,\mu,\phi\} P \{\mu,\phi;\mu,'\phi'\} \sin \Theta' d\Theta'd\phi' \qquad (23)$$

A beam of light which traverses an inhomogeneous medium is attenuated, a process called extinction, both by scattering of the light into other directions and by absorption. At a distance R from the scattering particle the scattered light has the character of a spherical wave. The direction of the scattered light is characterized by the angle θ with the direction of the incident beam, and by the azimuthal angle ϕ. The scattered intensity may be written as:

$$I = I_o P\{\theta,\phi\}/k^2 R^2 \qquad (24)$$

where $k = 2\pi/\lambda$ is the wave number, F is the scattering function. If the total energy scattered is equated to the energy incident on an effective area σ_s, it follows that:

$$\sigma_s = (1/k^2) \int P\{\theta,\phi\}d\omega \qquad (25)$$

where $d\omega = \sin\theta d\theta d\phi$ and the integration is performed over all directions. The energy absorbed by the particle is set equal to the energy incident on the area σ_a, and the total energy is set equal to the energy removed by the area σ_e. Therefore:

$$\sigma_e = \sigma_s + \sigma_a \tag{26}$$

At a given wavelength, the scattering and absorption cross sections of a spherical, homogeneous particle depend on only two parameters: the ratio of particle circumference to wavelength $X = 2\pi r_p/\lambda$, and the complex index of refraction $m = n_1 - in_2$. For spherical particles of arbitrary size, all three of these cross sections can be determined by Mie theory. Since the scattering function is also determined by the Mie theory, the fraction of light scattered in a backward direction b is also determined. Tabulated values of n_1 and n_2 as a function of particle temperature T_p, r_p, and λ are provided to a Mie code to yield σ_s, σ_a, and Eq. (29a). In fact, fractions of scattered radiation in any angle can be determined; for a six-flux radiation calculation fractions in the backward, forward, and sideways directions are so determined.

Average values of σ_a and σ_s over a particle size distribution are used, where $\sigma_i = \Sigma N_p \sigma_{i,p}/N_t$ and the summation is on the particle size classes p. N_t is the total number density of particles. Let $ds = dz/\mu$, where $\mu = \cos\Theta$.

$$\mu \, dI_\lambda/dz = -N_t (\sigma_a + \sigma_s) I_\lambda + N_t \sigma_a I_{\lambda b}$$

$$+ (N_t \sigma_s/4\pi) \int_0^{2\pi} I_\lambda P \, d\mu \, d\phi \tag{27}$$

Eliminate the phase function, P, using the "one-dimensional beam" approximation.

$$dI_\lambda^+/dz = -N_t(\sigma_a + b\sigma_s)I_\lambda^+ + N_t\sigma_a I_{\lambda b} + bN_t\sigma_s I_\lambda^- \tag{28}$$

$$-dI_\lambda^-/dz = -N_t(\sigma_a + b\sigma_s)I_\lambda^- + N_t\sigma_a I_{\lambda b} + bN_t\sigma_s I_\lambda^+ \tag{29}$$

where $b = \Sigma [N_p \, \sigma_{s,p} \, b_p]/(\sigma_s \, N_t)$ and $\qquad$ (29a)

$$I_{\lambda b} = \Sigma [N_p \, \sigma_{a,p} \, I_{\lambda b}\{T_p\}]/(\sigma_a \, N_t)$$

Introduce the Optical Depth, τ:

$$dI_\lambda^+/N_t(\sigma_a+\sigma_s)dz = -I_\lambda^+ + [(1-b)\sigma_s/(\sigma_a+\sigma_s)]I_\lambda^+ \qquad (30)$$

$$+[\sigma_a/(\sigma_a+\sigma_s)]I_{\lambda b} + [b\sigma_s/(\sigma_a+\sigma_s)]I_\lambda^-$$

b = fraction back scattered radiation = $1-f$

f = fraction forward scattered radiation

$d\tau = N_t(\sigma_a+\sigma_s)dz$, the differential optical depth

where $a_\lambda = [\sigma_s/(\sigma_s+\sigma_a)]$, the albedo

$$1- a_\lambda = [\sigma_a/(\sigma_a+\sigma_s)]$$

Wavelength dependence of f & b will not be indicated.

$$+dI_\lambda^+/d\tau = -I_\lambda^+ + (1-b)a_\lambda I_\lambda^+ + (1-a_\lambda)I_{\lambda b} + ba_\lambda I_\lambda^- \qquad (31)$$

$$+dI_\lambda^+/d\tau = -I_\lambda^+ + a_\lambda(fI_\lambda^+ + bI_\lambda^-) + (1-a_\lambda)I_{\lambda b} \qquad (32)$$

$$-dI_\lambda^-/N_t(\sigma_a+\sigma_s)dz = -I_\lambda^- + (1-b)\sigma_s I_\lambda^-/(\sigma_a+\sigma_s) \qquad (33)$$

$$+b\sigma_s I_\lambda^+/(\sigma_a+\sigma_s) \qquad + \sigma_a I_{\lambda b}/(\sigma_a+\sigma_s)$$

$$-dI_\lambda^-/d\tau = -I_\lambda^- + a_\lambda(fI_\lambda^- + bI_\lambda^+) + (1-a_\lambda)I_{\lambda b} \tag{34}$$

Assuming all intensities and optical properties are monochromatic λ will be omitted from here on.

$$+dI^+/d\tau = -I^+ + a(fI^+ + bI^-) + (1-a)I_b \tag{35}$$

$$+dI^-/d\tau = +I^- - a(fI^- + bI^+) - (1-a)I_b \tag{36}$$

Let $m = \sigma_a/(\sigma_a + \sigma_s) = (1-a)$ or $a = 1-m$

$$k = [m(2b(1-m)+m)]^{0.5} \tag{37}$$
$$k = m[(2b(1-m)/m)+1]^{0.5}$$
$$(k/m)^2 = [(2b/m)(1-m)+1]$$

$$dI^+/d\tau = -0.5[(k^2/m)+m]I + 0.5[(k^2/m)-m]I^- + mI_b \tag{38}$$

$$dI^-/d\tau = +0.5[(k^2/m)+m]J - 0.5[(k^2/m)-m]I^+ - mI_b \tag{39}$$

The solution of the equation of transfer for a single isothermal slab is:

$$I^+ = 0.5A[(k/m)+1]e^{-k\tau} + 0.5C[(k/m)-1]e^{k\tau} + I_b \tag{40}$$

$$I^- = 0.5A[(k/m)-1]e^{-k\tau} + 0.5C[(k/m)+1]e^{k\tau} + I_b \tag{41}$$

This solution for several isothermal slabs is obtained by imposing the interface boundary conditions:

$$I^+_{m-1}\{\tau_i\} = I^+_m\{\tau_i\} \quad \& \quad I^-_{m-1}\{\tau_i\} = I^-_m\{\tau_i\} \tag{42}$$

If the interface position, i, and nearest slab, m-1, are numbered the same, say p, and if the next slab out is numbered q, these conditions become:

$$I^+_p\{\tau_p\} = I^+_q\{\tau_p\} \quad \& \quad I^-_p\{\tau_p\} = I^-_q\{\tau_p\} \tag{43}$$

Surface boundary conditions:

$$I^+_o\{\tau_o\} = \epsilon_o\, I_b\{\tau_o\} + r_o\, I^-_o\{\tau_o\} \tag{44}$$

$$I^-_n\{\tau_n\} = \epsilon_n\, I_b\{\tau_n\} + r_n\, I^+_n\{\tau_n\} \tag{45}$$

where the emissivity, ϵ, and reflectivity, r, are for the environments of the slabs.

With these boundary and interface conditions, the solution for several isothermal slabs is given by:

$$I^+_o = 0.5A_1[(k/m)+1]_1 + 0.5C_1[(k/m)-1]_1 + I_{b1} \tag{46}$$

$$I^+_p\{\tau_p\} = 0.5A_p[(k/m)+1]_p e^{-k_p\,\tau_p} + 0.5C_p[(k/m)-1]_p e^{k_p\,\tau_p} + I_{bp} \tag{47}$$

$$I^+_q\{\tau_p\} = 0.5A_q[(k/m)+1]_q e^{-k_q\,\tau_p} + 0.5C_q[(k/m)-1]_q e^{k_q\,\tau_p} + I_{bq} \tag{48}$$

$$I^-_p\{\tau_p\} = 0.5A_p[(k/m)-1]_p e^{-k_p\,\tau_p} + 0.5C_p[(k/m)+1]_p e^{k_p\,\tau_p} + I_{bp} \tag{49}$$

$$I^-_q\{\tau_p\} = 0.5A_q[(k/m)-1]_q e^{-k_q\,\tau_p} + 0.5C_q[(k/m)+1]_q e^{k_q\,\tau_p} + I_{bq} \tag{50}$$

$$I^-_n = 0.5A_n[(k/m)-1]_n e^{-k_n\,\tau_n} + 0.5C_n[(k/m)+1]_n e^{k_n\,\tau_n} + I_{bn} \tag{51}$$

If the I^+'s and I's at the interfaces are eliminated, there are sufficient equations to evaluate the A's and C's. The solution of these equations is provided by the NOZZRAD code.

2.3.2 The NOZZRAD Code

NOZZRAD was developed by SECA to predict radiation heat transfer to a point on a nozzle wall or plume boundary. NOZZRAD has also been set up to be used in conjunction with the RAVFAC (Ref. 2.23) code for prediction of radiation heat rates to surfaces outside the flowfield boundaries.

Flowfield data for NOZZRAD is supplied in an input file of the same format used in SIRRM (Ref. 2.16) and must be axisymmetric. The nozzle wall or plume boundary is assumed to be the outer boundary of this flowfield map. Lines-of-sight (LOS), from a specified point on the nozzle wall or plume boundary, are drawn across the flowfield at evenly spaced angular intervals. Flowfield properties are obtained at specified distances along each specific LOS creating one-dimensional slabs from which specific intensity is calculated from the two-flux method described in Section 2.31. The specific intensities for each LOS are appropriately integrated to calculate the total and average radiation intensity to the specific point.

NOZZRAD has the capability to calculate radiation from either Al_2O_3 or carbon/soot particles and the gaseous species of H_2O and CO_2. Particle and gas calculations are treated separately. Two options for the gaseous radiation calculations are included. The first option treats the gas as one isothermal, homogeneous slab by averaging the points along the LOS. The second option treats the composition and temperature across the LOS as a summation of isothermal slabs.

Al_2O_3 particle optical properties are read from the files **SIGSCL01.DAT, SIGACL01.DAT,** and **BETACL01.DAT.** Carbon/soot particle optical properties are read from the files **SIGSCL02.DAT, SIGACL02.DAT,** and **BETACL02.DAT.** These files contain

scattering and absorption cross-sections and back scatter efficiencies assuming a spherical shape as a function of 10 particle sizes, 5 particle temperatures, and 37 wavelengths. More information on these files can be found in Section 2.1.

Flowfield properties are read into NOZZRAD via a file named **SIRRM.DAT**. This file is a standard SIRRM flowfield map which is generated by the Standard Plume Flowfield Code (SPF/2) (Ref. 2.29) with five gaseous species in the following order: H_2O, CO_2, HCl, CO, OH. More information on this flowfield data file can be found in Section 2.1.

User inputs are read into NOZZRAD via a file named **NOZZRAD.INP**. This file controls all of the user options available for NOZZRAD. These options include:

1) Case or NOZZRAD Run Description
2) Type of Particle or Gas Radiation Calculation
3) Number of Angular Intervals
4) Thickness of Slabs along a LOS
5) Fields of View
6) Angles of Orientation .

An example **NOZZRAD.INP** is given in Table 2.16. The format of **NOZZRAD.INP** along with the descriptions of each input variable is given in Table 2.17. The source code for NOZZRAD, along with the required data files and sample input files, are contained on the MS-DOS disk, RAD7.

Table 2.16 Example of Input File - **NOZZRAD.INP**

```
 EXAMPLE OF NOZZRAD USER INPUT
IOPT-flow type option,1 = AL2O3 particle,2 = Soot particle,3 = gas 4 = gas avg
1
M -number of LOS intervals
5
DDD -LOS INTERVAL (ft)
 .0500
K-wall boundary: 1 = wall perpendicular to axis, 2 = radial wall
2
Number of J-POINTs to evaluate and number of the J-POINT
9
4,7,12,15,4,5,6,14,9
FOV -Field of View (deg.)
0.,0.,0.,0.,0.,0.,0.,0.,0.,0.,0.,0.,0.,0.,0.,0.,0.,0.,0.,0.
Orientation option: 1 = user defined,0 = perpendicular to wall or plume boundary
 1
SLP  -User defined orientation ( + deg)
0.,0.,0.,0.,240.,30.,60.,30.,60.,
```

Table 2.17 Format and Description of NOZZRAD.INP

Record	Variable	Description
1	TITLE	Case or Run Description
2	dummy	Dummy variable to describe next input.
3	IOPT	Particle/Gas Radiation Calculation Option 0 = Particle Radiation Calculations for AL_2O_3 1 = Particle Radiation Calculations for Carbon/Soot 3 = H_2O & CO_2 Gaseous Radiation Calculations -One Slab, Average Properties 4 = H_2O & CO_2 Gaseous Radiation Calculations -Multiple Slab
4	dummy	Dummy variable to describe next input.
5	M	1/2 the number of angular subintervals to be used in the composite numerical integration scheme (Simpson's Rule). Radiation intensities for $(2M+1)^2$ lines of sight will be calculated. (MAX = 100)
6	dummy	Dummy variable to describe next input.
7	DDD	Distance between points along the line of sight where flowfield properties are "looked up". For particle radiation, this distance can also be thought of as the thickness for the slabs in the radiation calculations.
8	dummy	Dummy variable to describe next input.
9	K	Wall Type Option 1 = Inlet Wall (Nozzles) or Exit Plane (Plumes) 2 = Nozzle Radial Wall or Plume Radial Boundary (See Figure 1.)
10	dummy	Dummy variable to describe next input.
11	NL	Number of wall points for which radiation calculations will be made.
12	J	Wall Identity (J-POINT) Identity of each wall point. These are integer values corresponding to the boundary points in the flowfield data file, SIRRM.DAT
13	dummy	Dummy variable to describe next input.
14	FOV	Field of View Full field of view seen by each wall point. Corresponds to the same order of the J-POINT wall identification. (See Figure 1)
15	dummy	Dummy variable to describe next input.
16	ISLP	User Defined Orientation Option 0 = Field of View is oriented normal to the specified wall. 1 = Field of View is oriented as defined by user.
17	dummy	Dummy variable to describe next input.
18	SLP	User Defined Orientation Angles Orientation angles for each specified wall point if ISLP=1. Corresponds to the same order of the J-POINT wall identification. (See Figure 1)

The RAVFAC (Ref. 2.23) code can be used in conjunction with NOZZRAD for the calculation of radiative heat flux to surfaces outside a rocket plume boundary. RAVFAC is essentially a view factor code which represents a rocket plume as a geometrical surface with specific emissive intensities. With the proper input, NOZZRAD will generate all RAVFAC input files associated with the plume surface. These files can be run with the original RAVFAC code which assumes diffuse surface radiation or with a modified version of the RAVFAC code which accounts for variations in directional intensities. The modified RAVFAC code reads and properly evaluates directional intensity data stored on an additional file called **SPECINT.DAT** which is generated by NOZZRAD. The diffuse surface radiation assumption should predict conservative answers in relatively short NOZZRAD run times. Directional considerations should be more accurate; but, they require more time for NOZZRAD to calculate. Table 2.18 provides the user with a guide for setting up the appropriate geometrical inputs to NOZZRAD.INP to generate inputs for the original RAVFAC code (diffuse emission). Table 2.19 provides the user with a guide for setting up NOZZRAD.INP to generate inputs for the modified RAVFAC code (directional emission).

The output file named **RWALL.DAT** provides the user with the total radiation heat flux and average radiation intensities as calculated for each user specified boundary point. The total radiation heat flux prediction accounts for the normal surface to LOS angle difference to provide predictions which are comparable to radiometer values. Intensities are averaged over the user specified field of view. An example of **RWALL.DAT** is given in Table 2.20.

Table 2.18 NOZZRAD Input for use with RAVFAC (diffuse emission)

Variable	Description
K	USE 2
NL	The number of boundary points (J-Points) in the axial direction needed for the accurate description of the plume surface and emissivity. Generally the user should use the total number of axial points described in SIRRM.DAT.
J	Identity of axial boundary point. For the proper generation of the plume surface description these must be in consecutive order.
FOV	USE 0 for each J
ISLP	USE 0 (LOS normal to plume surface)

Table 2.19 NOZZRAD Input for use with modified RAVFAC (directional emission)

Variable	Description
M	User should chose this variable based on the angular increment which is desired between directional intensities. The suggested value of 11 will provide a maximum angular increment of 18°.
K	USE 2
NL	Number of boundary points (J-Points) in the axial direction needed for the accurate description of the plume surface and emissivity. Generally the user should use the total number of axial points described in SIRRM.DAT.
J	Identity of axial boundary point. For the proper generation of the plume surface file, these must be in consecutive order.
FOV	USE 180 for each J
ISLP	USE 0 (LOS normal to plume surface)

Table 2.20 Example of the Output File **RWALL.DAT**

```
************************************************************************
                              SECA"S NOZZRAD
----------------------------------------------------------------------
                     AL2O3 PARTICLE RADIATION CALCULATIONS
                     M-INTERVAL = 5
                     K-WALL     = 2
                     J-POINTS   =   4,  7, 12, 15,  4
                                    5,  6, 14,  9,
                     LOS INCREMENT = 0.5000E-01 (ft)
************************************************************************
                       EXAMPLE OF  NOZZRAD OUTPUT


              RADIATION HEAT RATE TO WALL or PLUME BOUNDARY
    ------------------------------------------------------------------
                              (BTU/ft2/s)
      X (ft)    R (ft)   RADIATION HEAT RATE  AVG. INTENSITY   FOV (deg)  S (deg)
      ------    ------   -------------------  --------------   ---------  -------
    0.9537E+00 0.1353E+01    0.70772E+02         0.22893E+02      .00      .00
```

The output files **PLUME.DAT**, **ICS.DAT**, and **RAD.DAT** are standard input for the radiation view factor code RAVFAC (Ref. 2.23). The output file named **SPECINT.DAT** is a data file with the specific intensities of every calculated line of sight. This file provides the directional intensities for the modified version of RAVFAC described previously.

2.3.3 Results of the NOZZRAD Analysis

Results of the MNASA Test Measurements along with comparisons to SIRRM-II and Monte-Carlo based predictions were used to validate the NOZZRAD methodology. The plume flowfield which was used for the SIRRM-II, Monte-Carlo, and NOZZRAD predictions was generated with SPF/2 and is discussed in detail in Ref. 2.29. The MNASA test setup is illustrated in Fig. 2.8. Radiometer instrument numbers 1-9 are small field of view instruments. Radiometers 17-21 are full field of view instruments. Table 2.21 shows the experimental results for radiometers 1-9 along with the predictions made from SIRRM-II, Monte-Carlo and NOZZRAD. NOZZRAD was run in these cases for Al_2O_3 particle radiation with one line- of-
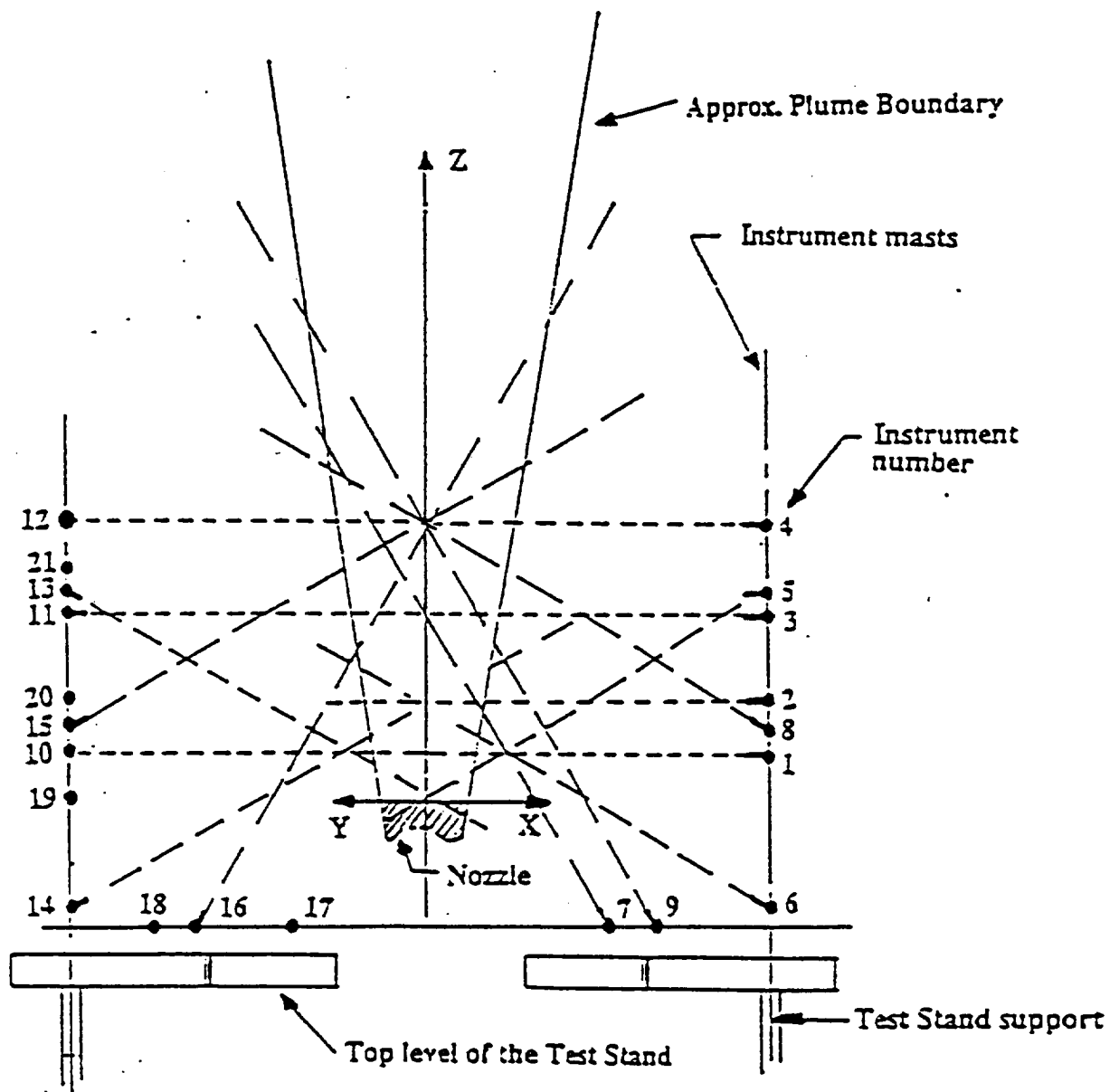
Fig. 2.8 Radiometer Orientations for the MNASA Tests

(Ref. REMTECH RTN 213-18)

sight. Both SIRRM-II and NOZZRAD intensity values were multiplied by the cosine of the angle between the surface of the plume and the radiometer to provide the correct view factor. The MONTE-CARLO predictions were taken from (Ref. 2.30). With the exception of Radiometer #5 the results obtained from NOZZRAD were reasonable.

Table 2.21   Comparison of MNASA Test Measurements for Small Field of View Radiometers with MONTE-CARLO, SIRRM-II, and NOZZRAD Predictions

INSTRUMENT NUMBER	TEST (Btu/ft²/s)				MONTE-CARLO (Btu/ft²/s)	SIRRM-II (Btu/ft²/s)	NOZZRAD AL₂O₃ Particle (Btu/ft²/s)
	3	6	8	11			
1	55-56	55-57	58-64	-	67.1	64.8	66.7
2	44	46	50	43-48	52.8	40.1	45.5
3	38-43	46-48	50-54	-	57.4	47.2	56.9
4	10-29	36-46	38-47	29-30	58.1	45.7	55.2
5	66-67	51-56	59-60	-	99.5	60.8	87.4
6	50-53	47-49	56-57	-	54.2	53.7	50.0
7	43	38	38	-	48.6	58.2	54.2
8	35	41	43	-	60.0	46.6	57.8
9	38-43	34-39	37-42	-	54.5	35.3	49.2

Since gaseous and particle radiation is treated separately in NOZZRAD, similar predictions were made with SIRRM-II where gaseous and particle radiation was separated by altering the flowfield input. Gas partial pressures were set to zero for Al_2O_3 particle radiation predictions and particle number densities were set to zero for gaseous radiation calculations. These calculations were made for a single line-of-sight for each of the Radiometers numbers 1-4 of the MNASA tests. Results for the gaseous radiation predictions are shown in Table 2.22. Results for the particle radiation calculations are shown in Table 2.23. Good agreement is shown for the gaseous results but the particle radiation results show relatively large differences even after the regular NOZZRAD properties were replaced by the same properties used in SIRRM-II. Further investigation revealed that these differences are due to the differences in the optical property interpolation schemes used by the two codes. Figure 2.5 showed the spectral emissive power of a 4.5 ft thick homogeneous slab of Al_2O_3 particles with radius of 3 microns

and 100,000 cm^{-3} in number density. Particle temperatures were varied between the tabulated values of 3000°K and 2320°K. At the tabulated values there is excellent agreement; but, NOZZRAD predicts higher values at temperatures in between the tabulated temperatures. It is believed that similar differences will be present as a function of particle size but specific calculations in this regard have not been made. No inferences should be made from Fig. 2.5 concerning the conservative predictions made by NOZZRAD. Non-homogeneous slab configurations can be combined to produce NOZZRAD predictions which are lower than SIRRM-II predictions as evident from Table 2.23. The reason that the particles only SIRRM solution is higher than the particles, plus gas, is shown in Fig. 2.6 and is due to the assumed gas particle radiation interaction coded in SIRRM. This effect is very large for this case. More consideration of the gas/particle interaction and of the interpolation method used to obtain optical properties of the particles is evidently needed to reconcile these large differences in these prediction methods.

Table 2.22 Comparison of SIRRM-II and NOZZRAD for Gaseous Radiation Predictions

INSTRUMENT #	SIRRM-II (Btu/ft^2/s)	NOZZRAD Multiple Slab (Btu/ft^2/s)	NOZZRAD One Averaged Slab (Btu/ft^2/s)
1	10.1	10.3	8.6
2	12.98	13.0	10.6
3	19.7	17.9	13.2
4	16.7	16.9	11.8

Table 2.23 Comparison of SIRRM-II and NOZZRAD for AL$_2$O$_3$ Particle Radiation Predictions

INSTRUMENT #	SIRRM-II (Btu/ft^2/s)	NOZZRAD (Btu/ft^2/s	NOZZRAD SIRRM Properties
1	69.2	66.7	70.8
2	64.2	45.5	48.2
3	73.8	56.9	60.3
4	71.8	55.2	58.5

In order to predict radiation heat flux to surfaces outside the plume boundary with large fields of view, NOZZRAD should be used in conjunction with the RAVFAC code. The results of this methodology as applied to the MNASA test data are shown in Table 2.24. NOZZRAD was run according to the guides provided in Tables 2.18 and 2.19 for Al_2O_3 particle radiation. As expected the diffuse assumption provided conservative answers. Radiometers 17 and 18 were much more sensitive to directional considerations due to their orientation with respect to the plume surface (see Fig. 2.8). The fields of view for these radiometers see intensities with angular directions far from the normal of the plume surface.

Table 2.24 Comparison of MNASA Test Measurements for Full Field of View Radiometers
with RAVFAC/NOZZRAD methodology

INSTRUMENT NUMBER	TEST ($Btu/ft^2/s$)				RAVFAC DIFFUSE ($Btu/ft^2/s$)	RAVFAC DIRECTIONAL ($Btu/ft^2/s$)
	3	6	8	11		
17	2.80	2.66	2.75	2.83	4.63	2.77
18	3.11	3.00	3.07	-	4.25	2.99
19	5.47	5.27	5.39	-	6.22	5.21
20	7.12	6.99	7.21	-	8.46	7.30
21	9.73	9.30	9.54	-	11.15	9.99

Other general comments on the use of NOZZRAD:

1) The number of slabs for a particular LOS is limited to 200.

2) Numerical integration errors for the total radiation heat
   flux calculations may arise if the number of angular increments
   which is chosen is too low. This problem occurs to a greater
   extent as the field of view angle becomes smaller. For field of view
   angles < 30° it is suggested that the user assume diffuse radiation
   and chose an FOV of 0°.

NOZZRAD has been validated with some comparisons to SIRRM (Ref. 2.6) and general isothermal slab solutions as well as some experimental data, however; until NOZZRAD has been used more extensively caution should be exercised with the use of the results.

2.3.3 Radiation from Sooty Plumes

Current NASA interest in hybrid motors and RP-1 fuel has prompted including soot radiation in this study. Soot radiation can be predicted with either NOZZRAD or the GASRAD code (Ref. 2.16). Soot particles in plumes are believed to be small enough that they do not scatter radiation. This assumption is made in the GASRAD program. However, the required mole fraction of soot is a difficult variable to evaluate. Not only must the chemistry of the sooting combustion be described, but the molecular weight of the soot must be specified. Such predictions are not within the scope of the current investigation; therefore, soot was approximated as a specified fraction of the carbon in the fuel with the thermodynamic properties of graphite.

Preliminary analysis of radiation heating rates has been performed on a hybrid motor using SPF/2 predicted plume with 2% carbon. Radiation heating rates were calculated using NOZZRAD and GASRAD for a full field of view at various points downstream along the plume boundary. Figure 2.9 illustrates the positions and calculated heat rates from NOZZRAD using a particle size of 0.1 micrometer. The radiation heating rates calculated by GASRAD for the same points were negligible. When GASRAD was run without the cool outer layers of the plume, the radiation heat rates which were calculated were comparable to NOZZRAD. Apparently, the assumed carbon content in the low temperature shear layer absorbed most of the radiation from the high temperature portions of the plume. The discrepancies in the answers from NOZZRAD and GASRAD can be attributed to particle size. GASRAD assumes the carbon particles are so small that no scattering effects are present. Since radiation heating rates which are shown in Fig. 2.9 are reasonable in comparison with data from similar engines, this initial investigation indicates that scattering for the soot particles should be considered for the assumed carbon distribution used in the SPF/2 plume flowfield prediction. However, the real problem is to accurately predict the soot concentrations and particle size distributions.

C'-2
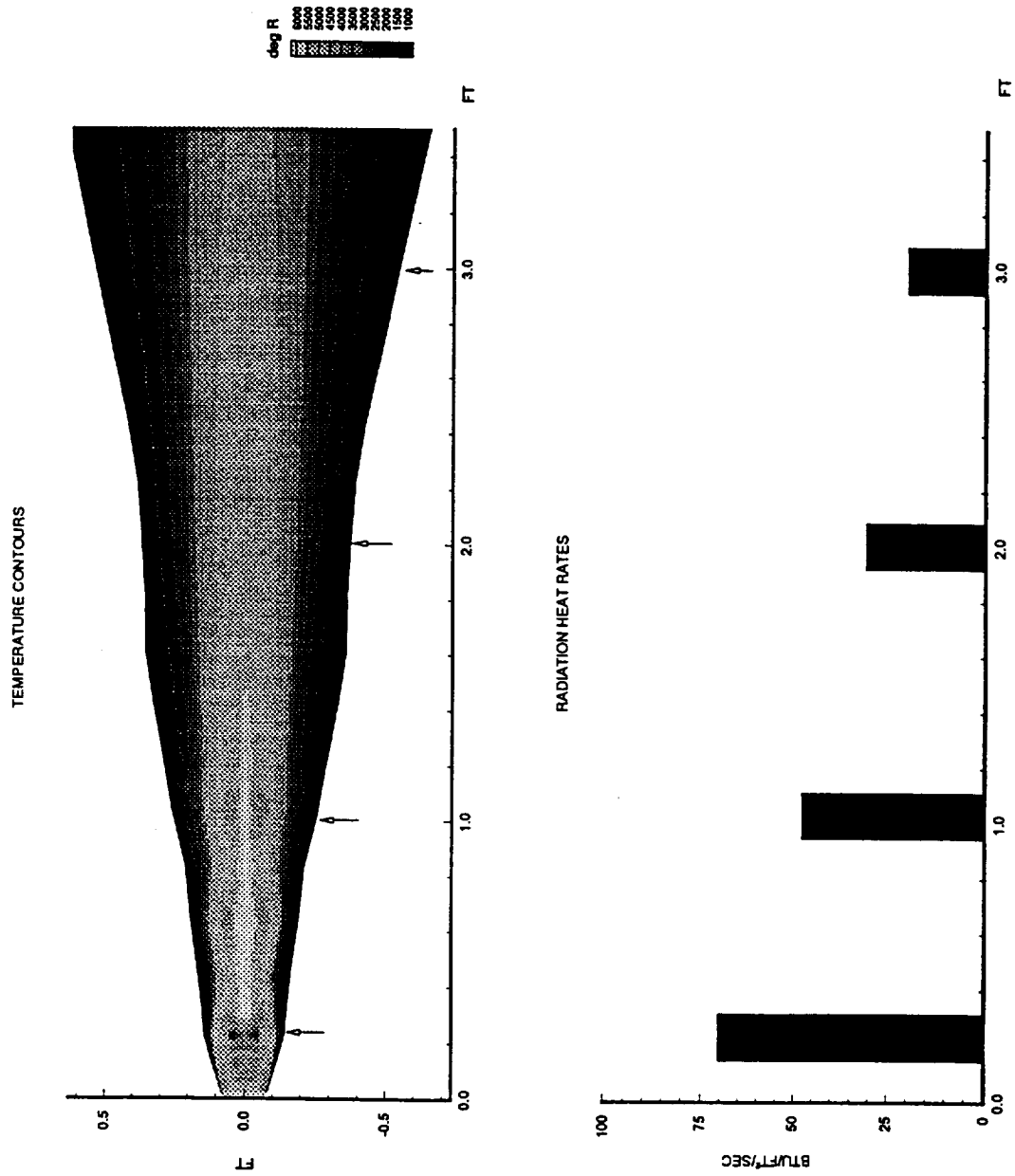
Fig. 2.9 Plume Radiation from Soot

3.0 TWO-PHASE FLOW MODELING FOR
SOLID ROCKET MOTOR RADIATION PREDICTIONS

The spatial characterization of gas and particulate properties of solid rocket motor nozzle and exhaust plume properties is more important than the radiation models which are used to determine the radiation fluxes that are emitted from the flowfields. Even if the radiative model exactly models all the radiation processes of the gas and particulates, it is impossible to perform a radiation prediction if the flowfield is improperly characterized. Thus an important part of the investigation of new techniques for solid rocket motor radiation predictions was the investigation of the adequacy and accuracy of the existing models which are available to predict solid rocket motor flowfields. This section of the report describes the results of the evaluation of solid rocket motor flowfield models. In addition to the actual flowfields models, submodels such as particle size models (Section 3.3), and soot (Section 2.3.3) were investigated relative to the importance of the submodels used by the flowfield codes in predicting radiation.

3.1 Conventional Solid Motor Flowfield Prediction Methodology

The most commonly utilized model for calculating solid rocket motor flowfields for low altitude solid rocket motors is the JANNAF sponsored Standard Plume Flowfield Model. The older versions of the SPF code (Ref. 3.1) (SPF1 and SPF2) required that the combustion chamber-nozzle flowfield be calculated with another code and passed to the SPF code in the form of exit plane distributions of gas and particle flow properties. A typical code used to supply exit plane properties to SPF is the RAMP2 code (Ref. 3.2).

The RAMP2 code has been continuously improved under NASA funding since the mid 70's. This code was originally developed to support the Space Shuttle design studies for the low to mid altitude flight regions. In the early 80's the capabilities of the code were extended so that

vacuum plumes could be treated for in orbit spacecraft design applications. The code calculates an inviscid flowfield and is limited to flows which contain no imbedded subsonic regions.

Rocket exhaust flowfields are very complicated and are governed by many phenomena. Many simplifying assumptions are made to enable one to compute exhaust flows. However, many of these simplifying assumptions can compromise and invalidate the results, depending on the application for which the flowfield is intended. Numerous inviscid codes are available that treat many of the governing phenomena, but no single code is available that treats reacting single- and multi-phase flows including boundary-layer effects as an integral part of the solution. Thus, previously it was necessary to use a multitude of codes to treat inviscid nozzle/plume flow in detail. It is therefore desirable from both computational and economic standpoints to have a single code that can treat all the dominant phenomena in a rocket nozzle/plume flowfield. Additionally, it is possible to perform calculations which may range from the most simple (as for preliminary design studies) to the most complex as required for final design.

The basic RAMP2 code employs modular construction and has the following capabilities: (1) Two-phase with a two-phase transonic solution, (2) Two-phase, reacting gas (chemical equilibrium, reaction kinetics), supersonic inviscid nozzle/plume solution, and is (3) Operational for inviscid solutions at both high and low altitudes, (4) Direct interface with the JANNAF SPF code, (5) Shock capturing finite difference numerical operator, (6) Two-phase, equilibrium/frozen, boundary-layer analysis, (7) Variable oxidizer-to-fuel ratio transonic solution, (8) Improved two-phase transonic solution, (9) Two-phase real gas semi-empirical nozzle boundary layer expansion, (10) Continuum limit criteria, and (11) Sudden freeze free molecular calculation beyond the continuum limit.

Most of the above capabilities already exist in other computer codes. These codes were incorporated into the RAMP code to enhance its usefulness.

The three programs which make up the RAMP2 code (TRAN72-Ref. 3.3), RAMP2F,

and (BLIMPJ-Ref. 3.4) have been modified so as to interact as if they were a single code even though they are executed separately due to computer storage restrictions.

In general, in order to solve a high altitude plume the following steps are required. First, the TRAN72 program input data is prepared and executed to generate a data file describing the thermodynamic characteristics of the post-combustion gases. Next, the RAMP2F flowfield data are prepared and the nozzle flowfield is solved using the TRAN72 program data file as input. Then, in order to adequately describe the nozzle boundary layer, the BLIMPJ code is executed using an input data file and the flowfield file generated by the RAMP2F nozzle solution. Finally the exhaust plume is calculated by using the nozzle solution and boundary layer solution to generate an exit plane start line that is used to initiate the plume solution. Thus, the generation of a high altitude plume can require up to four different executions of programs (TRAN72, RAMP2F, BLIMPJ, and RAMP2F) for the specification of the most detailed and accurate results. Physical input data are required only for the TRAN72 and first RAMP2F execution. All data required for the BLIMPJ code and second RAMP2F execution are generated internal to the program and/or communicated via data tapes or temporary files. Depending on the application, the problem, or the level of sophistication required in the plume results, it may not be necessary to run the TRAN72 or BLIMPJ codes. It is possible that a single RAMP2F calculation may be adequate, such as in the case for a low altitude plume, which is what was done in this study to support the ASRM flowfield modeling. For low altitude cases the RAMP2 code was used to generate the exit plane start line which is used by SPF/2 to initiate the plume solution.

The Joint-Army-Navy-NASA-Air Force (JANNAF) Standard Plume Flowfield (SPF) Model is a modular computer program which has been under development several years by Science Applications International Corporation (SAIC) of Wayne, PA. The development of this program has been sponsored by the U. S. Army Missile Command, (AMICOM) at Huntsville, AL, NASA at Langley Research Center, VA, and Arnold Engineering Development Center (AEDC) at Tullahoma, Tennessee. The program has undergone three stages (SPF/1, SPF/2, and

SPF/3) in its development.

The version of the SPF Program that was used in this study to investigate all flowfields is the SPF/2 version. In SPF/2 the input is supplied both from the user and from the data bank component. The data bank contains JANNAF thermodynamic data from about 95 chemical species and chemical reaction data from about 107 chemical reactions. This input data then goes to the processor component, PRC2 of the program. The output from PRC2 serves as input to the inviscid component, SCP2 (provided a 2-D startline is desired). The output from SCP2 is then used as input to the plume mixing layer component, BOT2. If a 1-D startline is desired, no inviscid calculation will be obtained, and the output from PRC2 will go directly to BOT2.

The SPF/2 Program has the capability of treating the following six chemical systems: 1) H/O, 2) C/H/O, 3) C/H/O/Cl, 4) C/H/O/Cl/F, 5) H/O/B, and 6) H/O/B/Cl/F. In addition, another system may be used in which the user specifies the chemical species.

For a 2-D input across the exit plane (or separation plane) the input was obtained from the output of the RAMP2 program with a distribution of the gas temperature, pressure, axial and radial velocity; particle density, velocity and temperature at each radial point on the startline. The chemical species are frozen across the exit plane and for the entire length of the inviscid plume.

The plume flowfield generated by SPF/2 is calculated by SCP2 for the internal inviscid core (hyperbolic solution). The outer annulus or plume mixing layer (parabolic solution) is computed by BOT2.

The SPF/2 program is used primarily at the lower altitudes where the Mach disc is an important contribution to the overall base radiation flux and where mixing and afterburning along the plume boundary play an important role in the base environment.

RAMP2 and SPF2 codes have been extensively used to perform solid rocket motor flowfield predictions that were subsequently used by radiation codes to predict radiation fluxes to vehicle structure. The RAMP2 and SPF2 codes have been improved (Ref. 3.5) to the point that along with the NASA funded REMCAR (Ref. 3.6) radiation code accurate prediction of radiation loads to launch vehicles and missiles are now possible. These improvements in RAMP2 and SPF2 are referred to as the Cycle 2.0 methodology.

3.2 Two-Phase Navier Stokes Flowfield Modeling

Navier Stokes flow solvers have reached a level of maturity that potentially could result in two-phase flowfields which could be utilized to perform radiation predictions of launch vehicle plume induced radiation heating. Under a previous NASA funded study (Ref. 3.7), a particulate two-phase model was incorporated into an existing, gas only, Navier-Stokes Computation Fluid Dynamics code (CFD). The code which was used as the basis of the new code was the FDNS code (Refs. 3.8, 3.9 and 3.10).

The FDNS code solves a set of nonlinear and coupled transport equations, the Navier-Stokes equations, energy equation, two-equation turbulence models and chemical species continuity equations in non-dimensional form. Finite difference approximations are employed to discretize the transport equations on non-staggered grid mesh systems. High-order (second- or third-order) upwind or central differencing schemes plus adaptive second-order and fourth-order dissipation terms are used to approximate the convective terms of the transport equations. Second-order central differencing schemes are used for the viscous and source terms of the governing equations. To insure positive numbers for some scaler quantities such as turbulence kinetic energy and species mass fractions, a first-order upwind scheme is employed for the convection process. A pressure based predictor/multi-corrector solution procedure is employed in the FDNS code to enhance velocity-pressure coupling and mass-conserved flowfield solutions at the end of each time step. This pressure based method is suitable for all speed flow computations. A time-centered Crank-Nicholson time-marching scheme is used for the temporal

discretization for time-accurate solutions. For steady-state flows, an implicit Euler time-marking scheme can be used for better computational efficiency. The selection of time marching scheme can be used for better computational efficiency. The selection of time-marching schemes is controlled through input data.

In the current version of the FDNS code (Ref. 3.11), incompressible or compressible, standard or extended, k-ϵ turbulence models with wall function or direct integration to the wall (low-Reynolds number turbulence model) options are included. Turbulence model options are selected through input data. Chemical kinetics and species thermodynamics data are required to be prepared in the input data file.

For particulate two-phase flow simulations, a Lagrangian method using an implicit particle trajectory integration scheme is used. In the present version of FDNS, called FDNSEL, only steady state (not time-varying) solutions of two-phase flow is possible. This section of the report describes: theories that are incorporated in FDNS (3.2.1), the history and validation of FDNS two-phase flow version (3.2.2), FDNS input instructions and sample cases for two-phase nozzle analysis (3.2.3) and the possible influence of combustion chamber geometry on predicted radiation (3.2.4).

3.2.1 FDNS Theories

This subsection describes some of the basic theories that are incorporated into FDNS. More detailed descriptions of the theories and basic code description can be found in Ref. 3.11.

Governing Equations. The gas-phase governing equations of the FDNS module are the Reynolds-averaged Navier-Stokes equations with the addition of particle drag forces and heat fluxes in the momentum equations and the energy equation, respectively. Due to the effect of large density differences between the particles and the surrounding gas, the drag force was considered to be the primary contribution to the inter-phase momentum exchange. The gas-

phase governing equations are written as:

$$J^{-1}(\partial \rho q/\partial t) = \partial[-\rho U_i q + \mu_{eff} G_{ij}(\partial q/\partial \xi_j)]/\partial \xi_i + S_q$$

where $q = 1$, u, v, w, h, k, ϵ and α_i for the continuity, momentum, energy, turbulence model and chemical species transport equations respectively. And, the transformation parameters and effective viscosity, μ_{eff}, are given as:

$$J = \partial(\xi,\eta,\zeta)/\partial(x,y,z)$$

$$U_i = (u_j/J)(\partial \xi_i/\partial x_j)$$

$$G_{ij} = (\partial \xi_i/\partial x_k)(\partial \xi_j/\partial x_k)/J$$

$$\mu_{eff} = (\mu + \mu_t)/\sigma_q$$

The source terms in the governing equations, S_q, are given as:

$$S_q = J^{-1} \begin{bmatrix} 0 \\ -P_x + \nabla[\mu_{eff}(u_j)_x] - (2/3)(\mu_{eff}\nabla u)_x + D_x \\ -P_y + \nabla[\mu_{eff}(u_j)_y] - (2/3)(\mu_{eff}\nabla u)_y + D_y \\ -P_z + \nabla[\mu_{eff}(u_j)_z] - (2/3)(\mu_{eff}\nabla u)_z + D_z \\ DP/DT + h_v + H_p - u_p D_x - v_p D_y - w_p D_z \\ \rho(P_r - \epsilon) \\ \rho(\epsilon/k)[(C_1 + C_3 P_r/\epsilon)P_r - C_2\epsilon] \\ \omega_i \end{bmatrix}$$

where Dx, Dy and Dz represent the drag forces and c takes on values between 1 and N (number of gas species). u_p, v_p and w_p are the particle velocity components. H_p is the rate of heat transfer per unit volume to the gas phase. h_v stands for the viscous heat flux of the gas phase. P_r stands for the turbulence kinetic energy production rate and is written as:

$$P_r = (\mu_t/\rho)[(\partial u_j/\partial x_i + \partial u_i/\partial x_j)^2/2 - 2(\partial u_k/\partial x_k)^2/3]$$

An equation of state, $\rho = p/(RT/M_w)$, is used to close the above system of equations. Turbulent Schmidt and Prandtl numbers, σ_q, for the governing equations and other turbulence model constants given, are taken from Refs. 3.12, 3.13 and 3.14.

Finite Rate Chemistry Model. For gas-phase chemical reaction modeling, a general system of chemical reactions is written in terms of the stoichiometric coefficients (ν_{ij} and ν_{ij}') and the i-th chemical species name (M_i) of the j-th reaction as

$$\sum_i \nu_{ij} M_i = \sum_i \nu_{ij}' M_i'$$

The net rate of change in the molar concentration of species i due to reactions j, X_{ij}, is written as:

$$X_{ij} = (\nu_{ij}'-\nu_{ij}) [K_{fj}\Pi(\rho\alpha_i/M_{Wi})^{r_{ij}} - K_{bj}\Pi(\rho\alpha_i/M_{Wi})^{r_{ij}'}]$$

and the species production rate, ω_i , (in terms of mass fraction) is calculated by summing over all reactions.

$$\omega_i = M_{wi} \sum_j X_{ij}$$

where
    M_{wi} = molecular weight of species i
    α_i = mass fraction of species i
    ρ = fluid density
    K_{fj} = forward rate of reaction j
    K_{bj} = backward rate of reaction j = K_{fj}/K_{ej}
    K_{ej} = equilibrium constant = $(1/RT)^{\Sigma(r_{ij}'-r_{ij})} \exp\{\Sigma(f_i'\nu_{ij}' - f_i\nu_{ij})\}$
    f_i = Gibbs free energy of species i
    K_f = $A\ T^B \exp\{-E/RT\}$

Finally, the species continuity equations are written as:

$$\rho\ D_t\alpha_i - \nabla[(\mu_{eff}/\sigma_\alpha)\nabla\alpha_i] = \omega_i$$

where σ_α (assumed to be 0.9) represents the Schmidt number for turbulent diffusion. Either a penalty function or an implicit integration is employed to ensure the basic element conservation

constraints at the end of every time marching step. This is a crucial requirement for the numerical stability and accuracy of a CFD combustion model. The penalty function calculation is accomplished by limiting the allowable changes in species concentrations, which are the solutions of the species continuity equations, for each time step such that the species mass fractions are well bounded within physical limits. The resulting limited changes are adjusted so that they are proportional to the species source terms. A similar chemistry approach and detailed turbulence submodels were reported previously (Ref. 3.15).

Particulate-Phase Equations. A Eulerian-Lagrangian particle tracking method is employed in FDNS to provide effects of momentum and energy exchanges between the gas phase and the particle phase. The particle trajectories are calculated using an efficient implicit time integration method for several groups of particle sizes by which the drag forces and heat fluxes are then coupled with the gas phase equations. The equations that constitute the particle trajectory and temperature history are written as:

$$DV_i/Dt = (U_i - V_i)/t_d$$
$$Dh_p/Dt = C_{pc} (T_{aw} - T_p)/t_H - 6 \, \sigma \epsilon f \, T_p^4/(\rho_p \, d_p)$$

where U_i = Gas Velocity

$\quad$ V_i = Particle Velocity

$\quad$ t_d = Particle Dynamic Relaxation Time = $4 \, \rho_p \, d_p/(3 \, C_d \, \rho_c \, |U_i - V_i|)$

$\quad$ h_p = Particle Enthalpy

$\quad$ C_{pc} = Particle Heat Capacity

$\quad$ T_p = Particle Temperature

$\quad$ T_{aw} = Gas Recovery Temperature

$\quad$ t_H = Particle Thermal-Equilibrium Time = $(\rho_p \, d_p)/[12 \, Nu \, \mu/(Pr \, d_p)]$

$\quad$ σ = Stefan-Boltzmann Constant = 4.76E-13 BTU/FT²-SR

$\quad$ ϵ = Particle Emissivity = 0.20 -- 0.31

$\quad$ f = Radiation Interchange Factor

d_p = Particle Diameter

ρ_p = Particle Density

C_d and Nu stand for drag coefficient and Nusselt number for heat transfer which are functions of Reynolds number and relative Mach number. Typical correlations are given in Refs. 3.16 and 3.17. Carlson and Hoglund's correlation (Ref. 3.16) is written as:

$$C_d = (24/Re)\ (1\ +\ 0.15\ Re^{0.687})\ (1\ +\ e^{-a})/$$
$$[1\ +\ M\ (3.82\ +\ 1.28\ e^{-1.25Re/M})/Re]$$

$$Nu\ =\ (1\ +\ 0.2295\ Re^{0.55})/\ [1\ +\ 3.42\ M\ (2\ +\ 0.459\ Re^{0.55})/Re]$$

where $a = 0.427/M^{4.63} + 3.0/Re^{0.88}$. A more accurate but more complicated correlation for the drag coefficient is provided by Henderson (Ref. 3.17). That is, for Mach $\geq$ 1,

$$C_d = 24\ [Re\ +\ S\ \{4.33\ +\ exp(-0.247\ Re/S)\ (3.65\ -\ 1.53\ T_w/T)$$
$$/(1\ +\ 0.353\ T_w/T)\}]^{-1}$$
$$+\ exp(-0.5*M/Re^{1/2})[0.1M^2\ +\ 0.2M^8\ +\ (4.5\ +\ 0.38a)$$
$$/(1\ +\ a)]\ +\ 0.6\ S\ [1\ -\ exp(-M/Re)]$$

where $S = M(\gamma/2)^{1.2}$ is the molecular speed ratio. $a = 0.03\ Re\ +\ 0.48\ Re^{1/2}$. For Mach $\geq$ 1.75,

$$C_d = [0.9\ +\ 0.34/M^2\ +\ 1.86(M/Re)^{1/2}\ \{2\ +\ 2/S^2$$
$$+\ 1.058\ (T_w/T)^{1/2}/S\ -\ 1/S^4\}]\ /\ [1\ +\ 1.86\ (M/Re)^{1/2}]$$

And, for 1 < Mach < 1.75,

$$C_d = C_{d\ M=1}\ +\ (4/3)\ (M\ -\ 1)\ (C_{d\ M=1.75}\ -\ C_{d\ M=1})$$

3-10

which assumes a linear variation between M = 1 and M = 1.75.

While the Henderson drag law has been found to give slightly better motor performance predictions, the differences in results using the Carlson-Hogland and Henderson method are slight. The Henderson method was used in the Cycle 2 RAMP/SPF2 (Ref. 3.5) model and can easily be incorporated into FDNS. All FDNS calculations presented in this report used the Carlson-Hogland model. The Nusselt number correlation of Drake (Ref. 3.18) which corresponds to the Cycle 1.0 methodology was used for all FDNS calculations. It is recommended that the heat transfer model of Moylan (Ref. 3.19), which was developed for the Cycle 2.0 plume methodology, be incorporated into FDNS.

Details of the Particle Solution Method. In the present two-phase flow model, an independent module was employed for the calculation of particle drag forces and heat flux contributions to the gas flow field. Subroutines for locating the particles and integrating their trajectories are called for each particle size group. The drag forces and heat fluxes are then saved for every grid point. These forces and fluxes are then used to evaluate the particle source terms in the gas-phase governing equations. In the present FDNS flow solver, either of two forms of the energy equation (i.e. static enthalpy form or total enthalpy form) can be selected. It has been found that although either form of energy equation usually gives similar solutions, the static enthalpy equation provides better definition of the liquid rocket plume shear layers, as shown by extensive solutions made for the SSME. The energy equation presented previously under the governing equations section is the total enthalpy form. The static enthalpy option (see Section 3.2.2) should be used for two-phase flow solutions.

Particle wall-boundary conditions are treated by using a specified fraction of the colliding particles which stick to the wall. Particles which stick result in a decreased particle velocity normal to the wall for that particle size fraction. Therefore, for the particle size fraction which locally collides with the wall, part of the particles stick and the other part is turned parallel to

the wall. Energy exchange is assumed to be due only to the particles which stick. This model of particle wall interaction can be improved, but new experimental test data must become available in order to do so.

In the 2-D version of the FDNS flow solver, a fourth-order Runge-Kutta method was employed to integrate the particle trajectories. After a thorough test of the integration routine, it was found that the explicit scheme sometimes results in divergent particle solutions when the source terms become large. Therefore, an implicit integration scheme was employed in the present model. For convenience, consider the X-component of the particle equation of motion. That is,

$$dX_p/dt = U_p$$

$$dU_p/dt = A (U_c - U_p)$$

where $A = 1/t_d$

U_c = gas velocity

U_p = particle velocity

X_p = particle location

In finite difference form the above equations can be written as:

$$X_p^{(n+1)} - X_p^{(n)} = (\Delta t/2) [U_p^{(n+1)} + U_p^{(n)}]$$

$$U_p^{(n+1)} - U_p^{(n)} = \Delta t A [U_c - U_p^{(n+1)}]$$

or

$$X_p^{(n+1)} = X_p^{(n)} + \Delta t/2 [U_p^{(n+1)} + U_p^{(n)}]$$

$$U_p^{(n+1)} = [U_p^{(n)} + \Delta t A U_c]/(1+\Delta t A)$$

These two equations are unconditionally stable despite the magnitude of the source terms. To provide better time resolution, a variable time step size is chosen so that a particle would take at least 4 time steps to go across a grid cell.

3.2.2 History and Validation of the FDNSEL Navier Stokes Two-Phase Code

The two-phase flow capability was added under a previous NASA study (Ref. 3.7) to support the development of a solid rocket motor plume impingement model for predicting launch stand environments. Checkout cases for the previous study focused on modeling the flowfield of a 20% scale model of the Space Shuttle solid rocket motor combustion chamber/nozzle flowfield. Results of the FDNS calculation for this motor were then compared with a RAMP2 nozzle solution for the same case. While the results of these comparisons were for the most part qualitatively acceptable, quantitatively there were enough differences in the results that the application of an FDNS flowfield for radiation predictions was not recommended. One of the reasons that the results were not absolutely comparable was the geometry which is used in the combustion chamber. The combustion chamber for the FDNS calculation was simulated as shown in Fig. 3.1 which corresponds to a simulation of the grain geometry late in the burn of the motor. The RAMP2 transonic module assumes an infinite sink at an inlet angle corresponding to the inlet angle to the throat. The FDNS code was also run for turbulent reacting flow while RAMP2 was run using laminar equilibrium chemistry. For these reasons it was not possible to absolutely check out the FDNS solution during the previous study.

At the onset of this study, validation of the FDNS code continued using the same check case as was used previously with little improvement in the comparative results. However, instead of the radical geometry used in the previous comparison, a more regular geometry as is shown in Fig. 3.2 was used. This corresponded to an early burn time. All other variables that dictate the solution were identical, i.e.:

- Frozen chemistry
- Prandtl number = .7
- Viscosity and viscosity exponent (.6 laminar)
- Particle-gas heat transfer model (Drake)
- Drag law - Carlson-Hogland
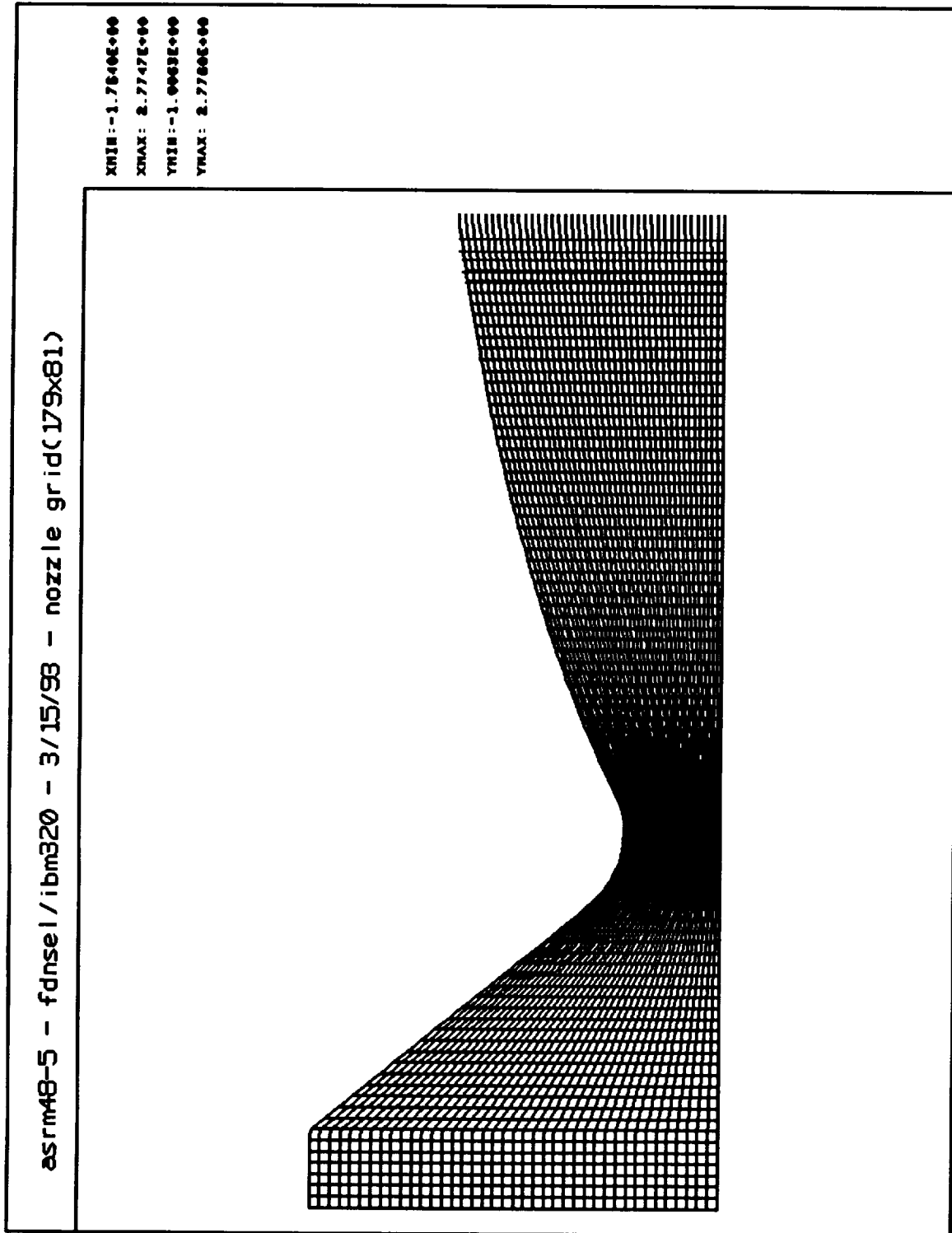
Figure 3.1 FDNSEL MNASA08/ASRM48-5 Nozzle Flowfield Grid (179 x 81)

XMIN:-1.6344E+00
XMAX: 2.7716E+00
YMIN:-1.2590E+00
YMAX: 2.4127E+00
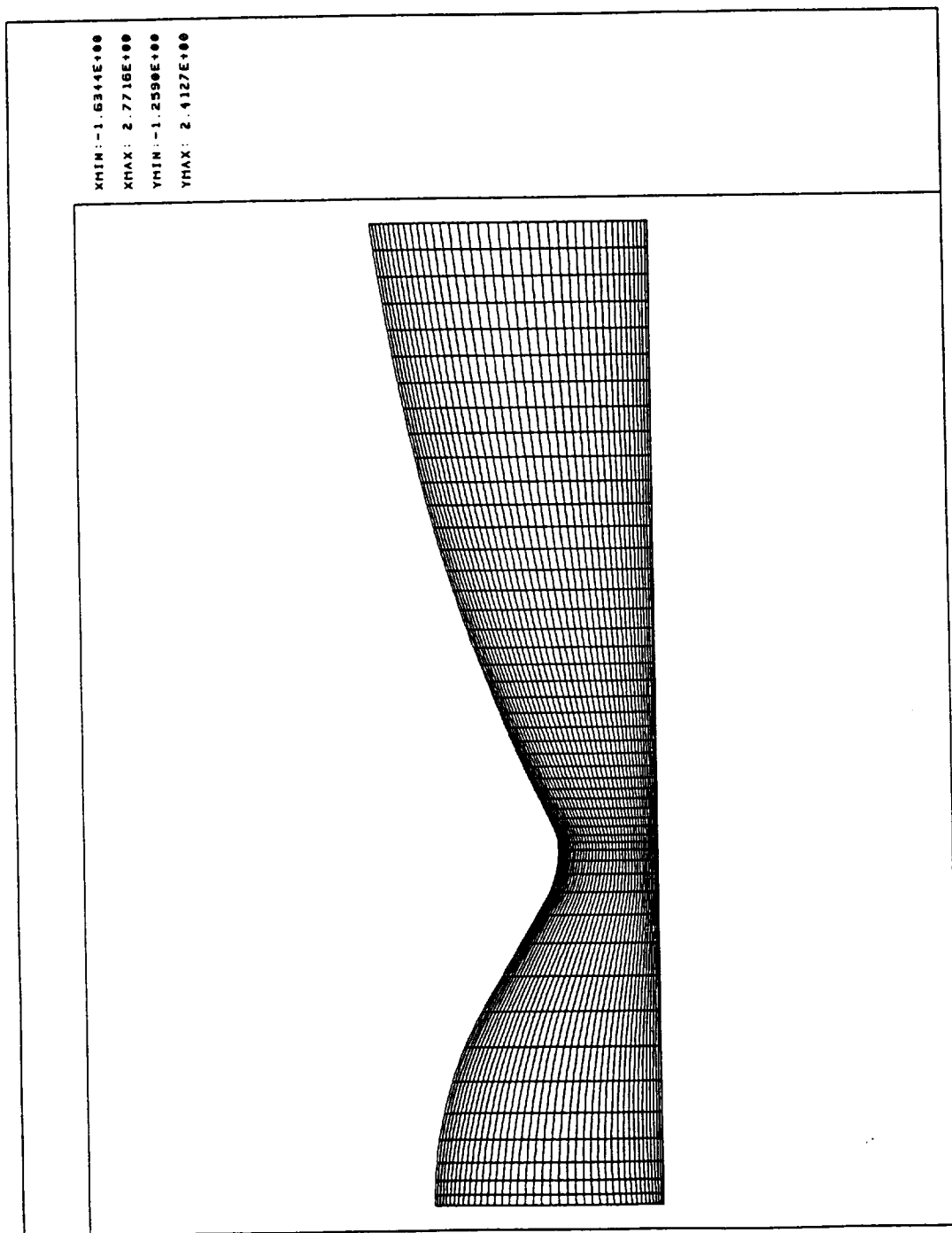
Fig. 3.2 FDNSEL MNASA08 ASRM Contoured Nozzle Grid (201 x 41) Simulating Early Burn Time

Results of RAMP2 and FDNS calculations are shown in Figs. 3.3 and 3.4. These figures show a comparison of Mach number and temperature distributions at the exit plane of the motor. The results are significantly different. It is apparent that the majority of the particles are contained in a smaller area of the exit for the FDNS solution. This is evident by observing the peak in temperature at .9 ft radius while the RAMP solution peaks at 1.05 ft. This effect could be attributed to the difference in the combustion chamber geometry used for FDNS versus that used by the RAMP transonic module. Also, notice the spike in temperature that FDNS predicts near the axis. This was traced to predicted particle number densities on and near the axis. The FDNS calculation used a single particle trajectory at each grid point to perform the Lagrangian tracking. This, compounded with the tight grid near the axis, led to numerical problems with the code that resulted in a poor distribution of particle number densities. This could have been corrected by using more trajectories in each cell and changing the grid; but even then the results of the RAMP and FDNS calculations would be different enough that any conclusions about the accuracy of FDNS would not be possible. At this stage of the validation, it was decided to eliminate combustion chamber geometry effects and concentrate on validating the equations which are solved by FDNS for two-phase flow.

A 15 degree source flow case was set up for RAMP and FDNS. Identical start lines were input to both codes consisting of the following conditions:

- Mach number - 2.0
- Gas temperature - 6000
- Gas velocity - 6500 ft/sec
- Molecular weight - 20
- Pressure - 500 psi
- Particle size - 4 micron radius
- Particle/gas flow rate ratio - .5
- Particle temperature - 6500 °R
- Particle velocity - 6000 ft/sec
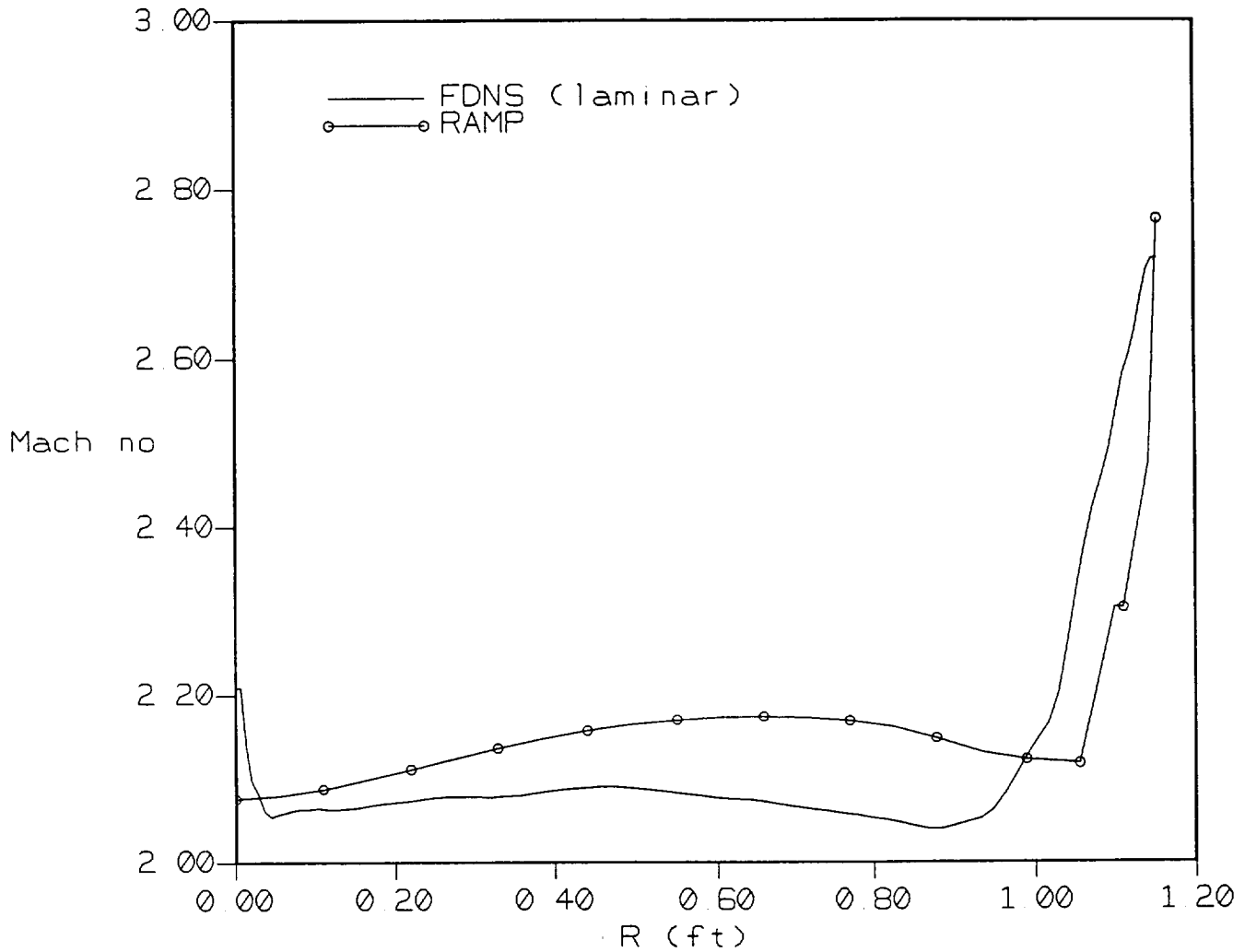
Fig. 3.3   Mach Number Profile at the MNASA ASRM Contoured Nozzle Exit
(Slip Wall, Two-phase, Frozen Chemistry)
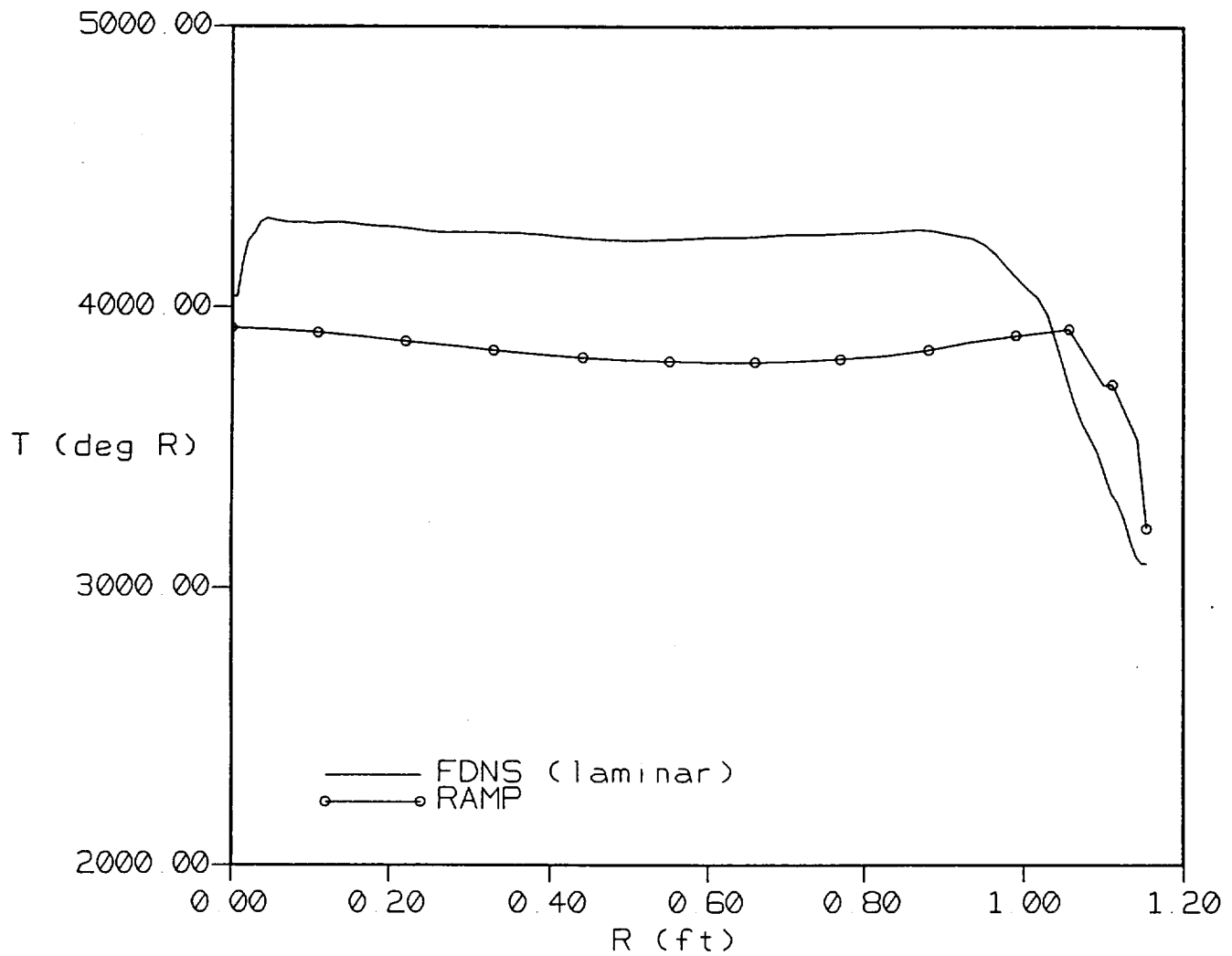
Fig. 3.4   Temperature Profile at the MNASA ASRM Contoured Nozzle Exit
(Slip Wall, Two-phase, Frozen Chemistry)

Calculations using FDNS resulted in the flow going subsonic downstream of the start line while RAMP had a slight decrease in Mach number near the start line followed by a gradual acceleration of the flow.

First, it was thought that the initial guess for the flowfield was the problem. To check this out the initial flowfield was set to exactly what RAMP calculated. The flow still went subsonic. Next, the calculated drag and heat transfer terms were compared to those calculated by RAMP. They were found to be the same. By examining the trend in the results, evidence pointed toward the gas energy equation since far too much energy was transferred to the gas which caused the flow to heat up and decelerate. Upon looking at the terms in the static form of the energy equation, it was found that the sign and magnitude of the work loss portion of equation was incorrect. Instead of multiplying the difference in gas and particle velocity by the drag force, the code was multiplying the absolute particle velocity by the drag force (which is the total energy form of the equation). The energy equation was modified and the calculation rerun. Figures 3.5 and 3.6 show a comparison of RAMP and FDNS for pressure and temperature distributions along any given gas streamline. The results are almost exactly the same. To further verify the energy equation, several axisymmetric constant area duct flow cases were set up for RAMP and FDNS.

Constant area, duct flow, two-phase cases eliminate particle trajectory effects since the particle streamlines remain straight and particle number density is only affected by the change in particle velocity. Several cases were run making various assumptions on particle and gas temperature and velocity lags. The results of three of these cases are shown in Figs. 3.7 thru 3.12. All cases assumed a particle/gas flow rate ratio of 0.5 and a static pressure of 500 psi. Case 1 assumed that the particle and gas velocities were 6500 ft/sec, the particle temperature was 5500°R and the gas temperature was 5000°R. Figure 3.7 presents a comparison of the gas and particle temperature distributions down the duct for FDNS and RAMP. The results are almost identical. Differences in RAMP and FDNS at the beginning of the duct are due to differences in step size and the fact that FDNS uses gas properties corresponding to the flow
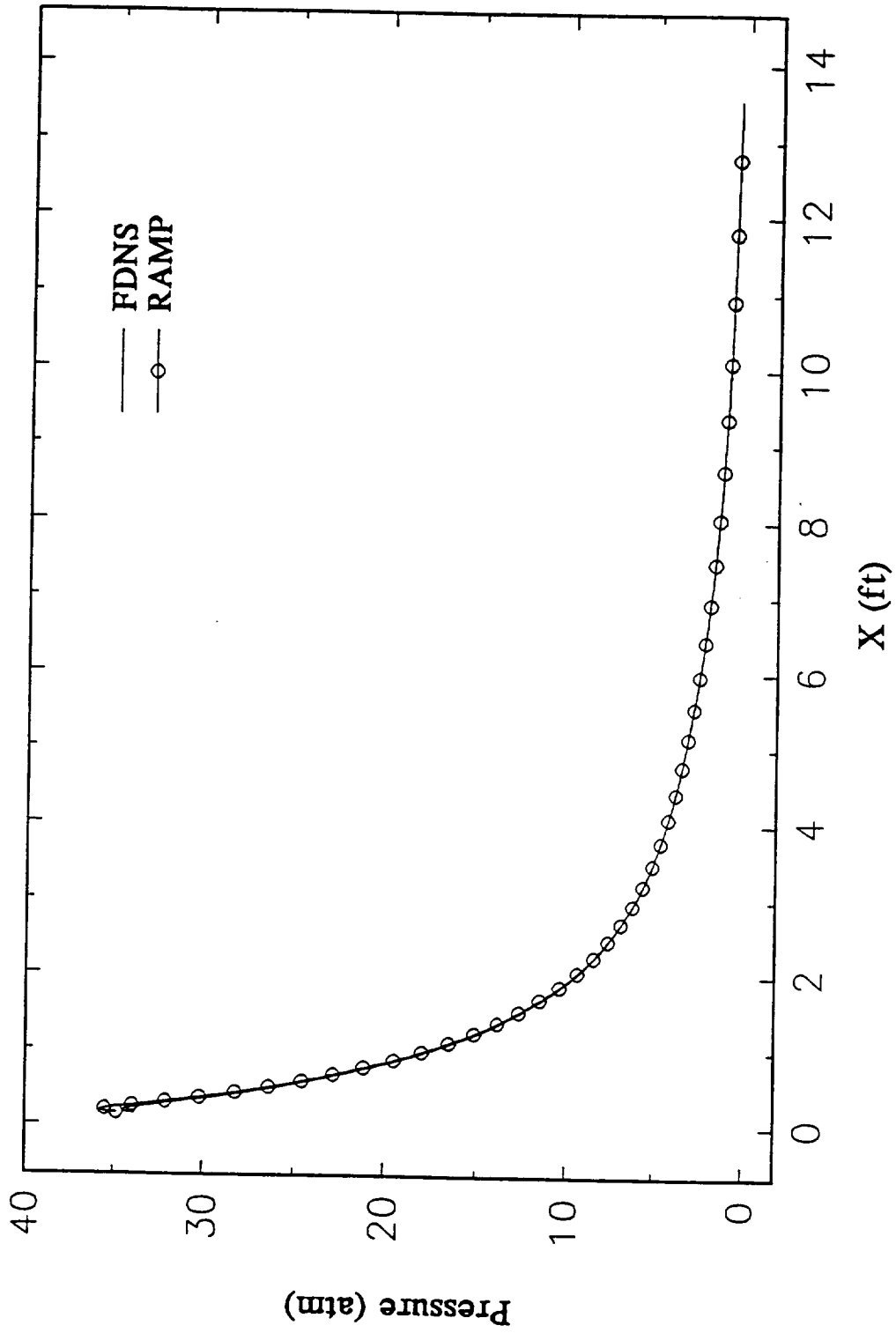
Fig. 3.5   Pressure Distribution Along a Streamline of a Nozzle Source Flow (Two-phase, Frozen Chemistry, Laminar)
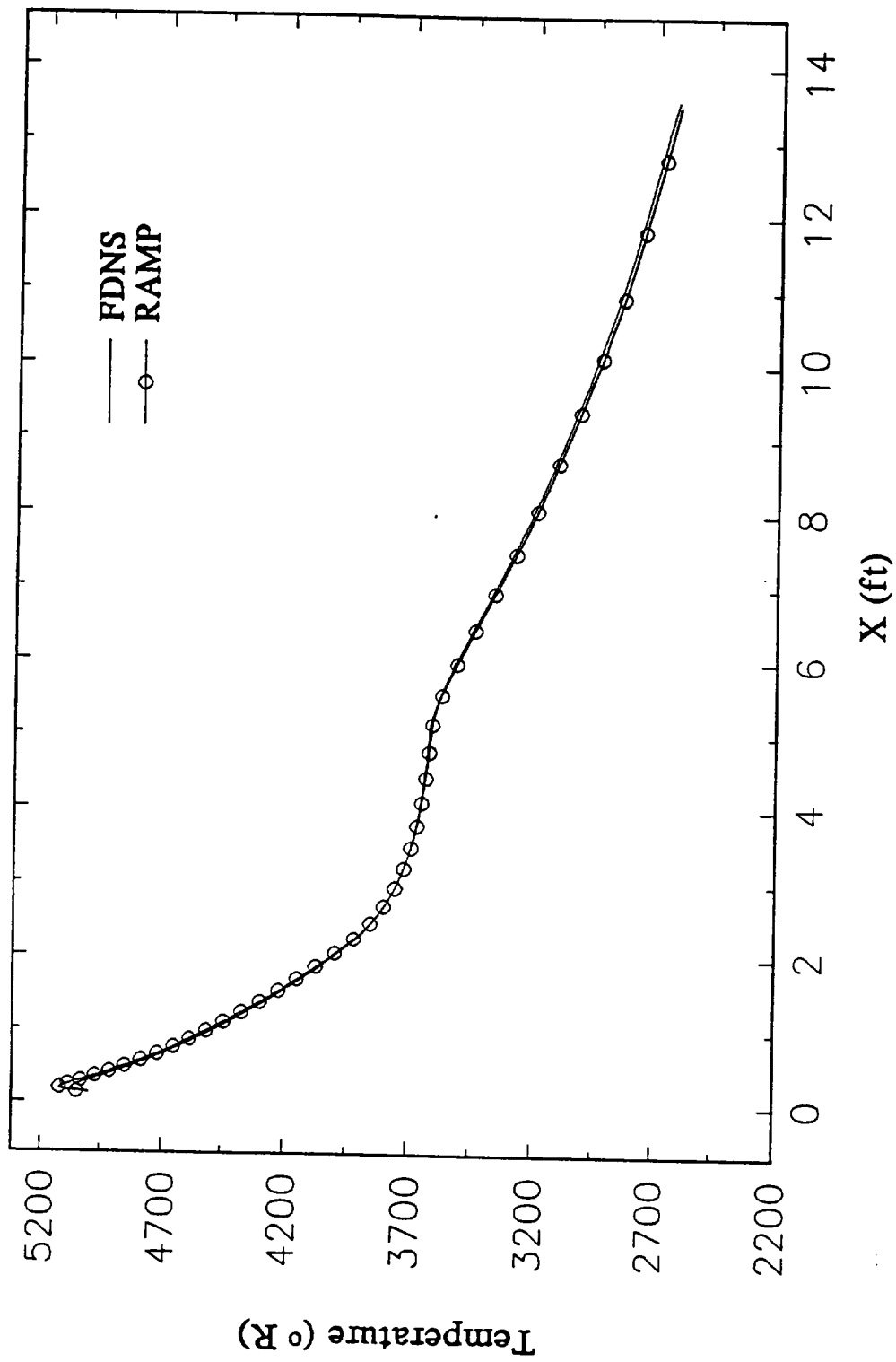
Fig. 3.6   Temperature Distribution Along a Streamline of a Nozzle Source Flow (Two-phase, Frozen Chemistry, Laminar)
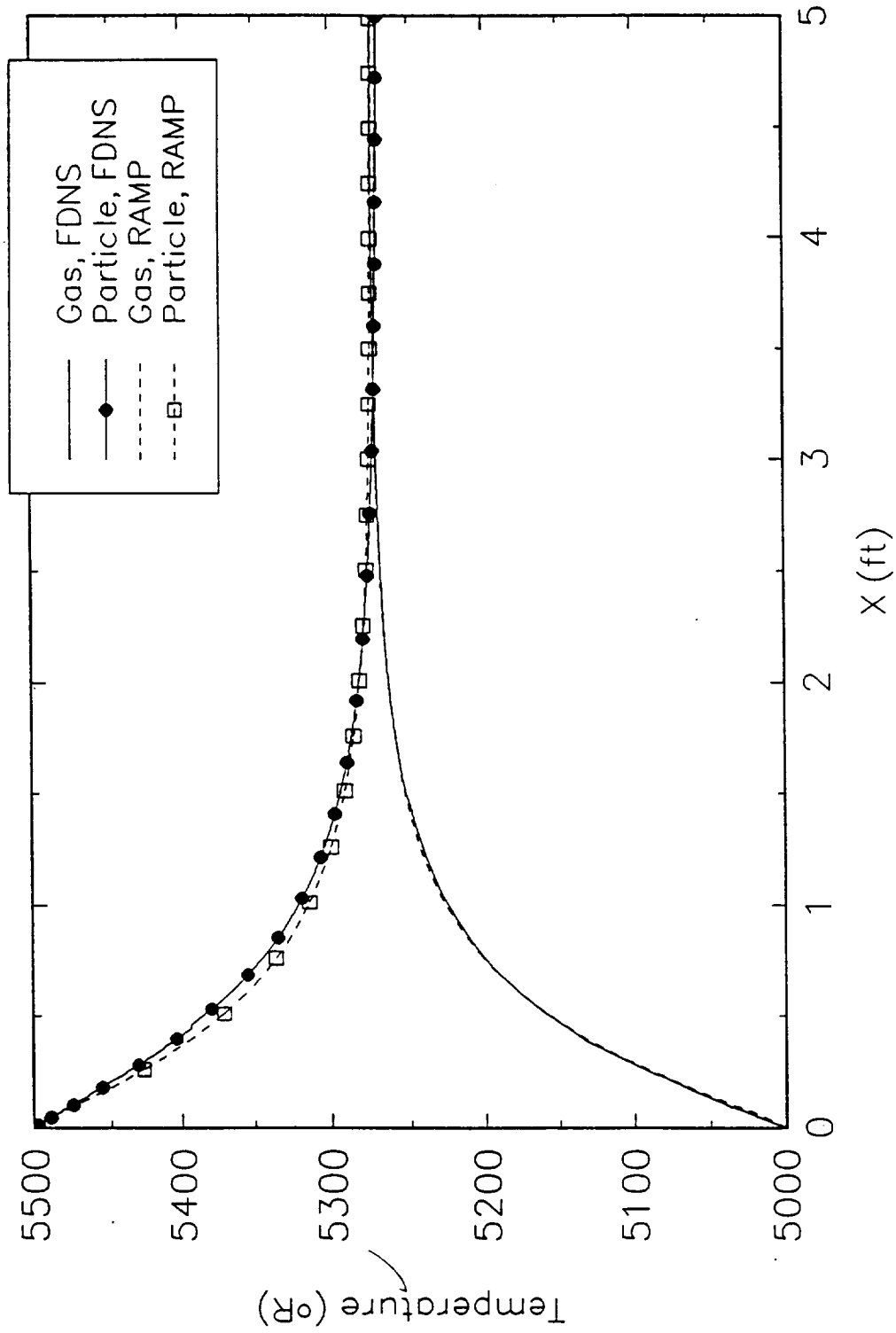
Fig. 3.7 Temperature Distribution Along a Two-phase Supersonic Stream Tube
Test Case #1

properties at the beginning of each particle trajectory step while RAMP uses average gas properties. Figure 3.8 presents velocity distributions for Case 1. Case 2 is the same as Case 1 except the particle velocity is 5500 ft/sec and the gas velocity if 6500 ft/sec. Again, the temperature (Fig. 3.9) and velocity (Fig. 3.10) distributions are almost identical. Case 3 is the same as Case 1 except the particle velocity is 7500 ft/sec while the gas velocity is 6500 ft/sec. Figure 3.11 presents a comparison of the temperature distribution and Fig. 3.12 presents the axial distribution of particle and gas velocity. Additional cases making various other assumptions on gas and particle temperature and velocity lags were calculated with similar results. These results confirm that the momentum and energy transfer between the particles and gas are now properly described by the FDNS governing equations.

It now appears that FDNS is solving the proper set of equations. In order to determine the effect and the difference in treatment of the transonic region by FDNS and RAMP, the nozzle case was rerun using the corrected version of FDNS for the geometry shown in Fig. 3.2 as well as a new geometry corresponding to a later burn time which is shown in Fig. 3.13.

Results of the two FDNS and RAMP calculations are presented in Figs. 3.14 thru 3.17. Figures 3.14 and 3.15 present centerline distributions of Mach number and temperature, respectively. The centerline Mach number distributions presented in Fig. 3.14 show that FDNS allows the flow to accelerate more along the centerline of the motor than does RAMP. Inlet geometry effects predicted by RAMP shows that for the case where the grain has burned back (which results in a steeper effective inlet angle) the flow does not accelerate as much as the initial burn case. FDNS results for the two cases show an opposite trend. Centerline temperature distributions shown in Fig. 3.15 indicate similar trends with RAMP having higher centerline temperatures than FDNS, as well as opposite trends with burnback geometry changes. Figures 3.16 and 3.17 present exit plane Mach number and temperature distributions for the two FDNS and RAMP cases. In Fig. 3.16, RAMP predicts less acceleration of the flow except near the outer portion of the flow where the particle limiting streamlines are located. The overall trends of flow acceleration of the two RAMP cases versus the FDNS cases are again reversed
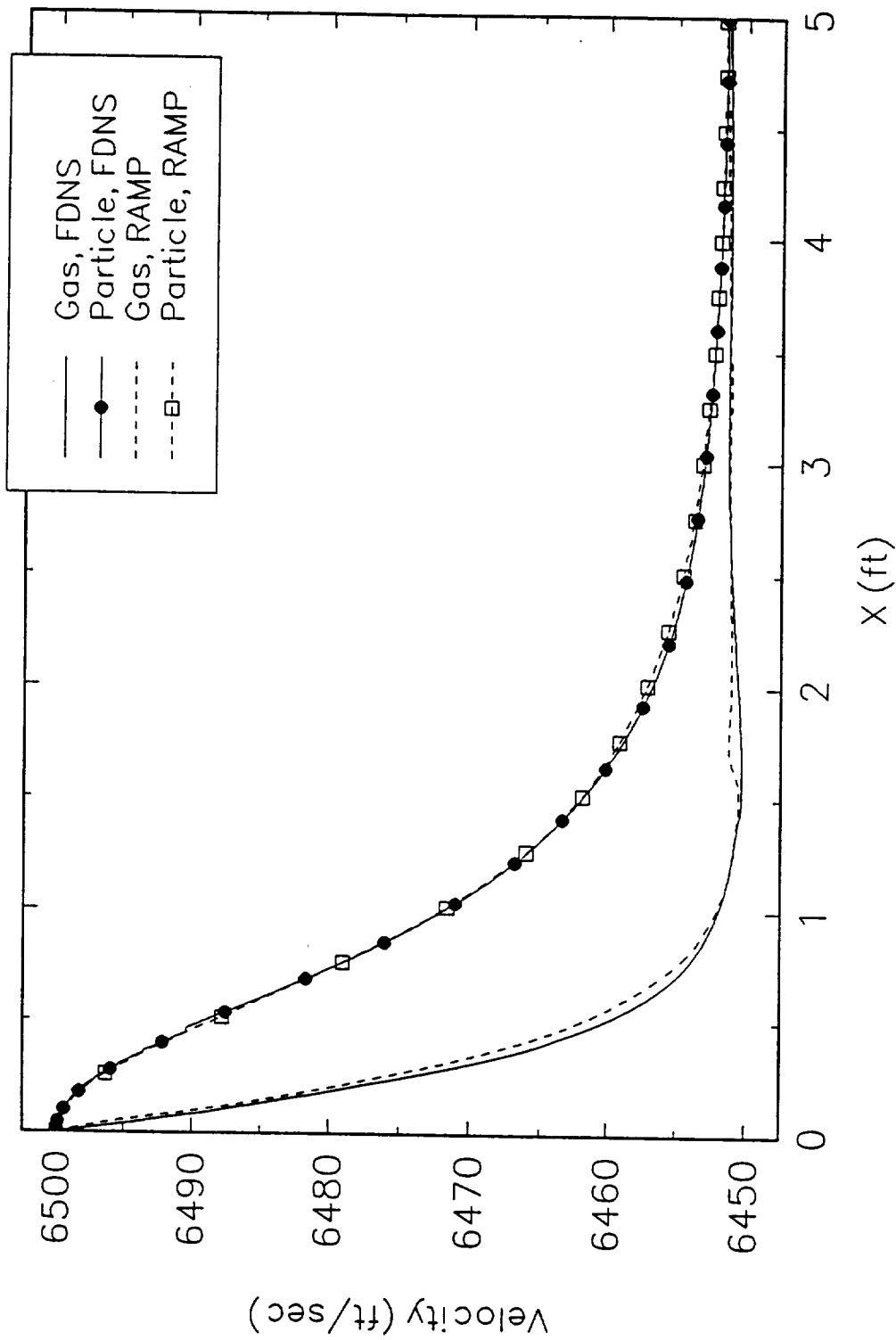
Fig. 3.8 Velocity Distribution Along a Two-Phase Supersonic Stream Tube
Test Case #1
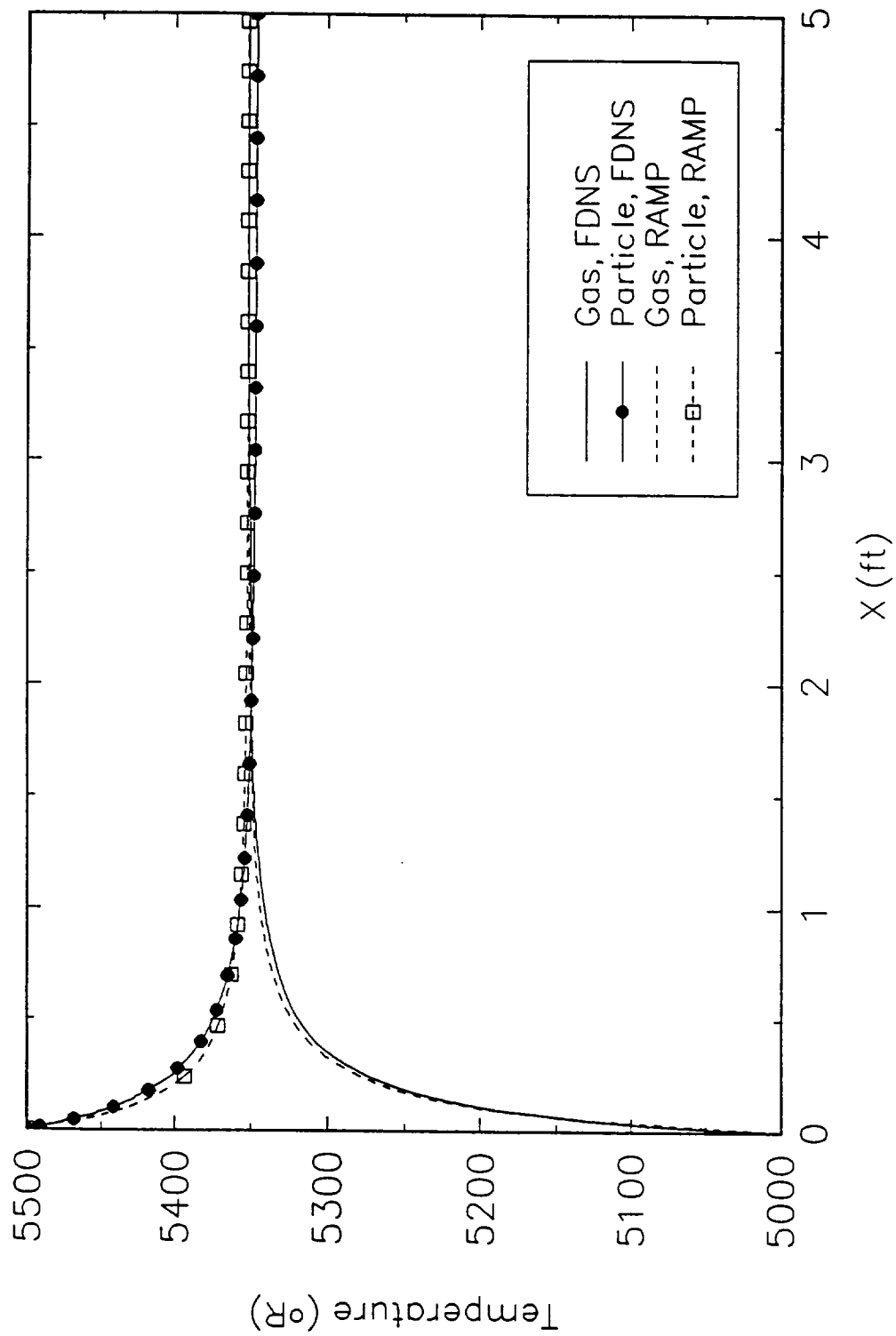
Fig. 3.9 Temperature Distribution Along a Two-Phase Supersonic Stream Tube
Test Case #2
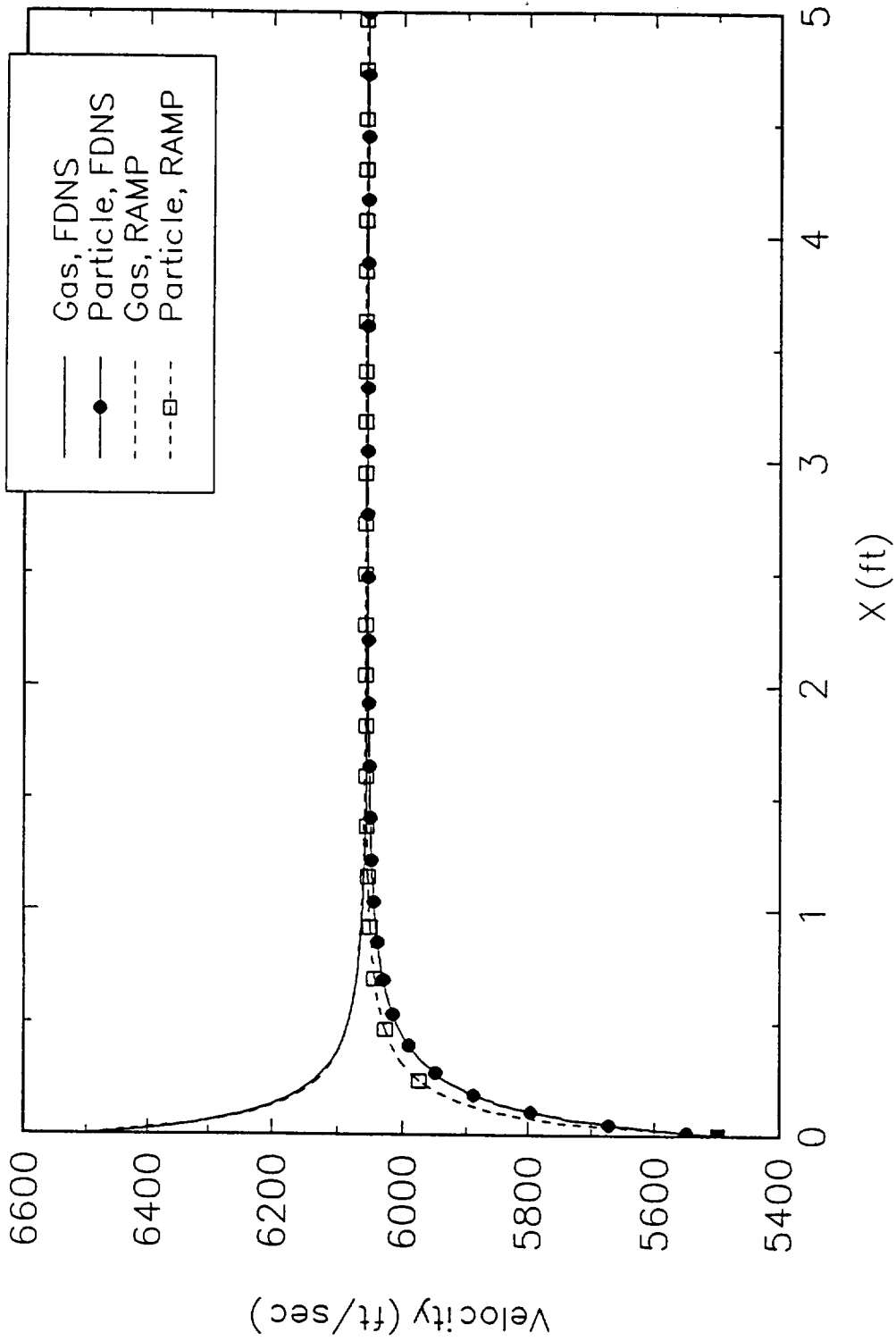
Fig. 3.10 Velocity Distribution Along a Two-Phase Supersonic Stream Tube
Test Case #2
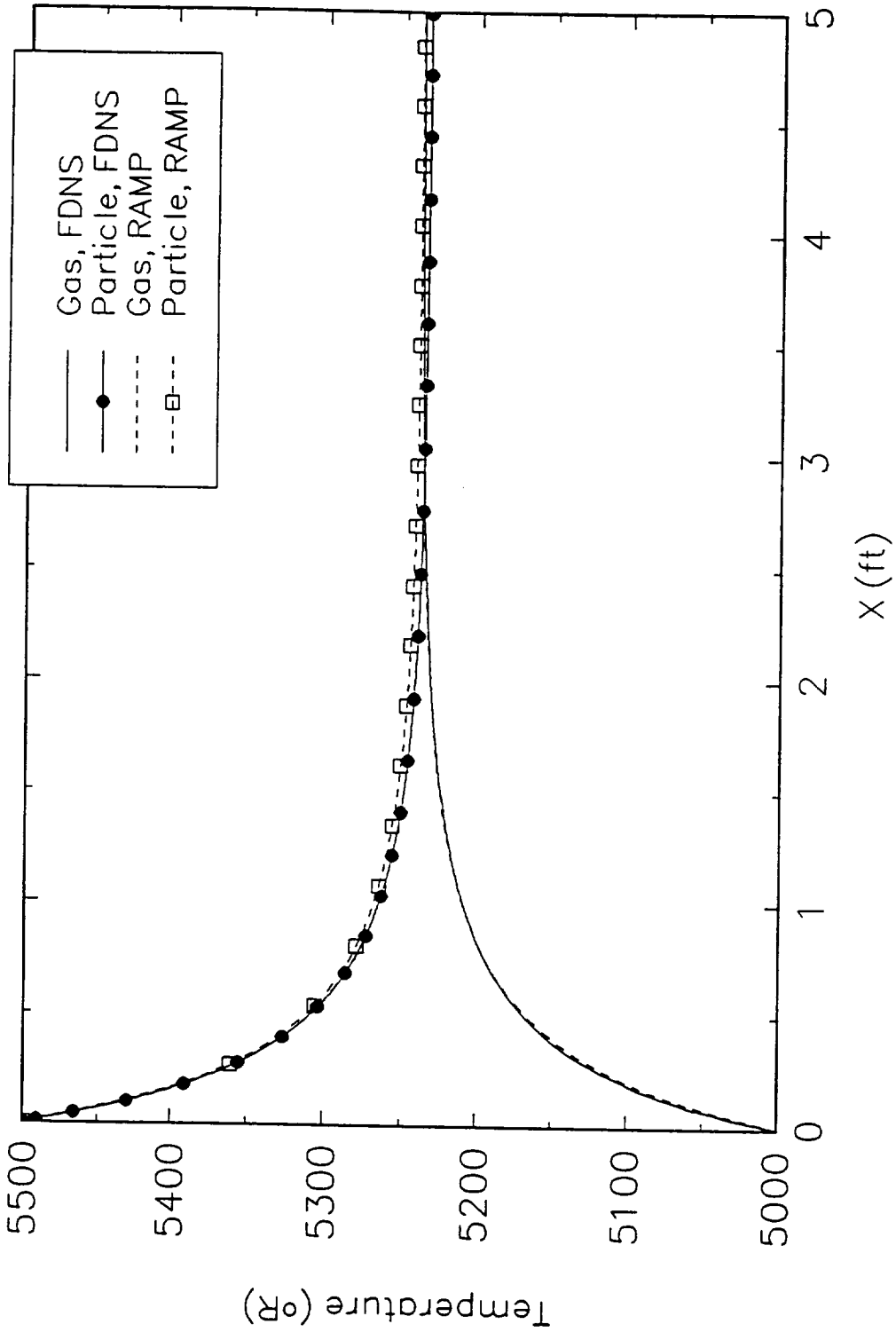
Fig. 3.11 Temperature Distribution Along a Two-Phase Supersonic Stream Tube
Test Case #3
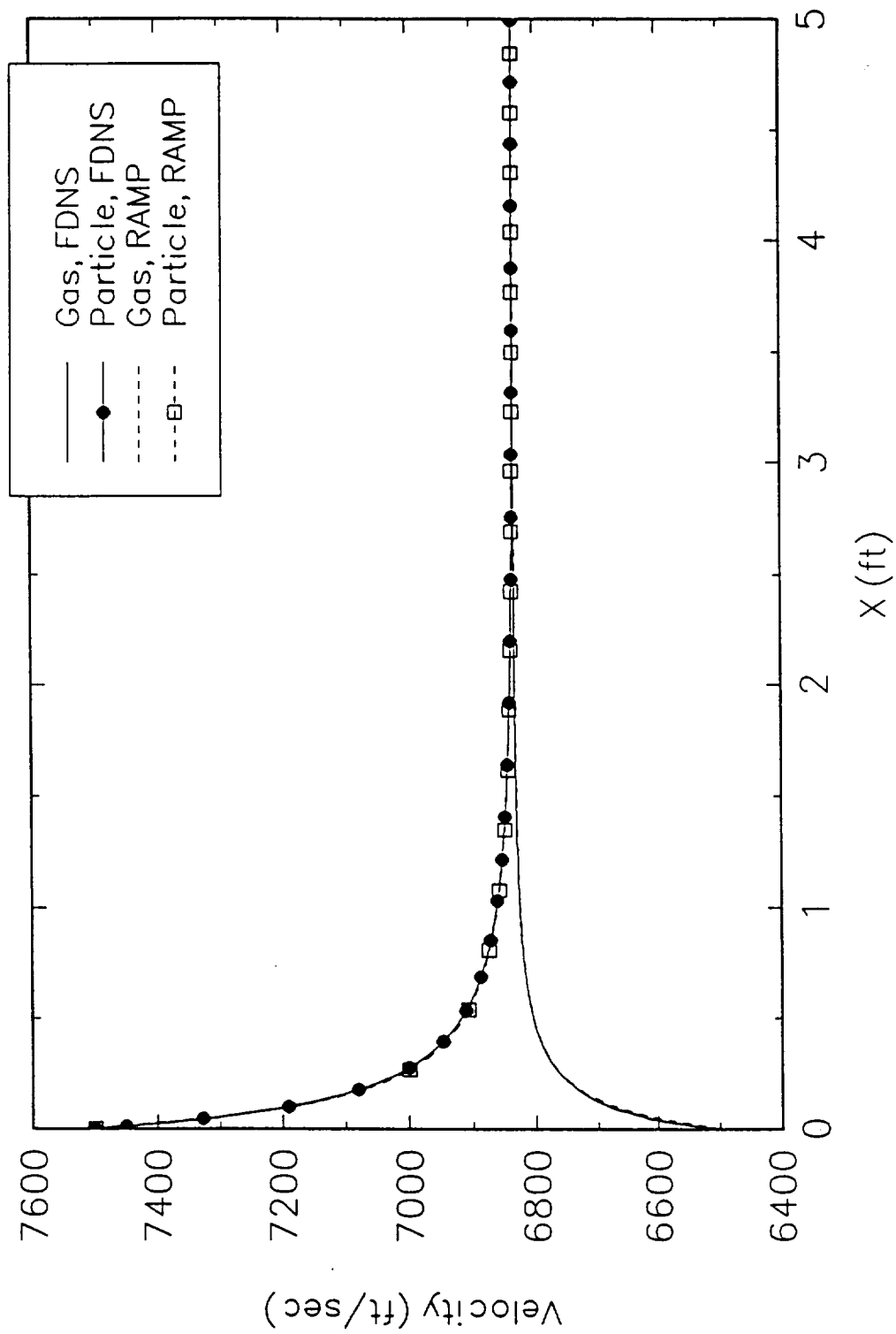
Fig. 3.12 Velocity Distribution Along a Two-Phase Supersonic Stream Tube
Test Case #3

grid system for ASRM nozzle (after burnback)

XMIN:-1.7100E+00
XMAX: 2.7734E+00
YMIN:-1.0681E+00
YMAX: 2.6681E+00
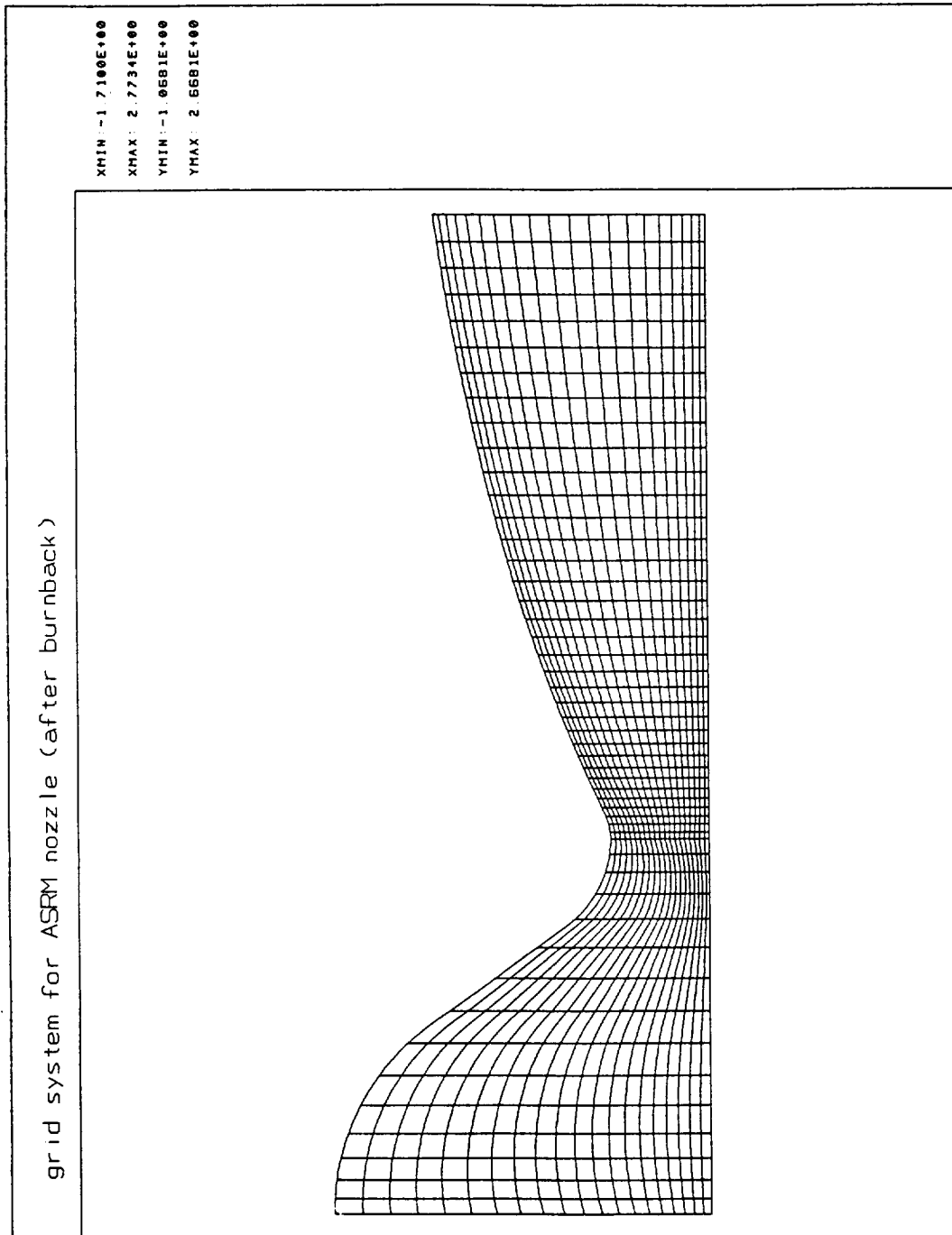
Fig. 3.13 FDNSEL MNASA08 ASRM Contoured Nozzle Grid (201 X 41) Simulating Late Burn Time
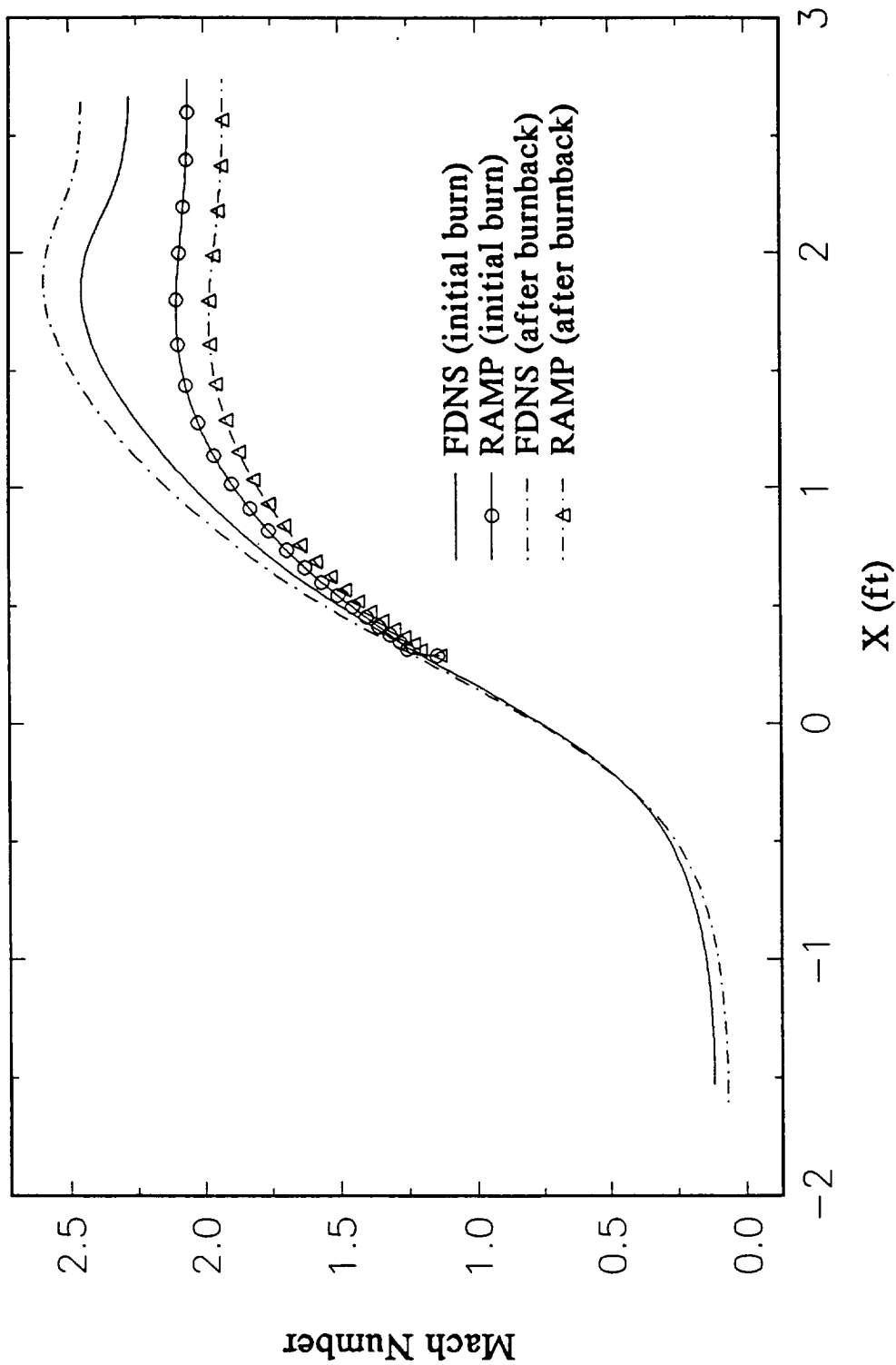
Fig. 3.14 Mach Number Distribution Along the Centerline of a Contoured Nozzle
(Two-Phase, Frozen Chemistry, Laminar)
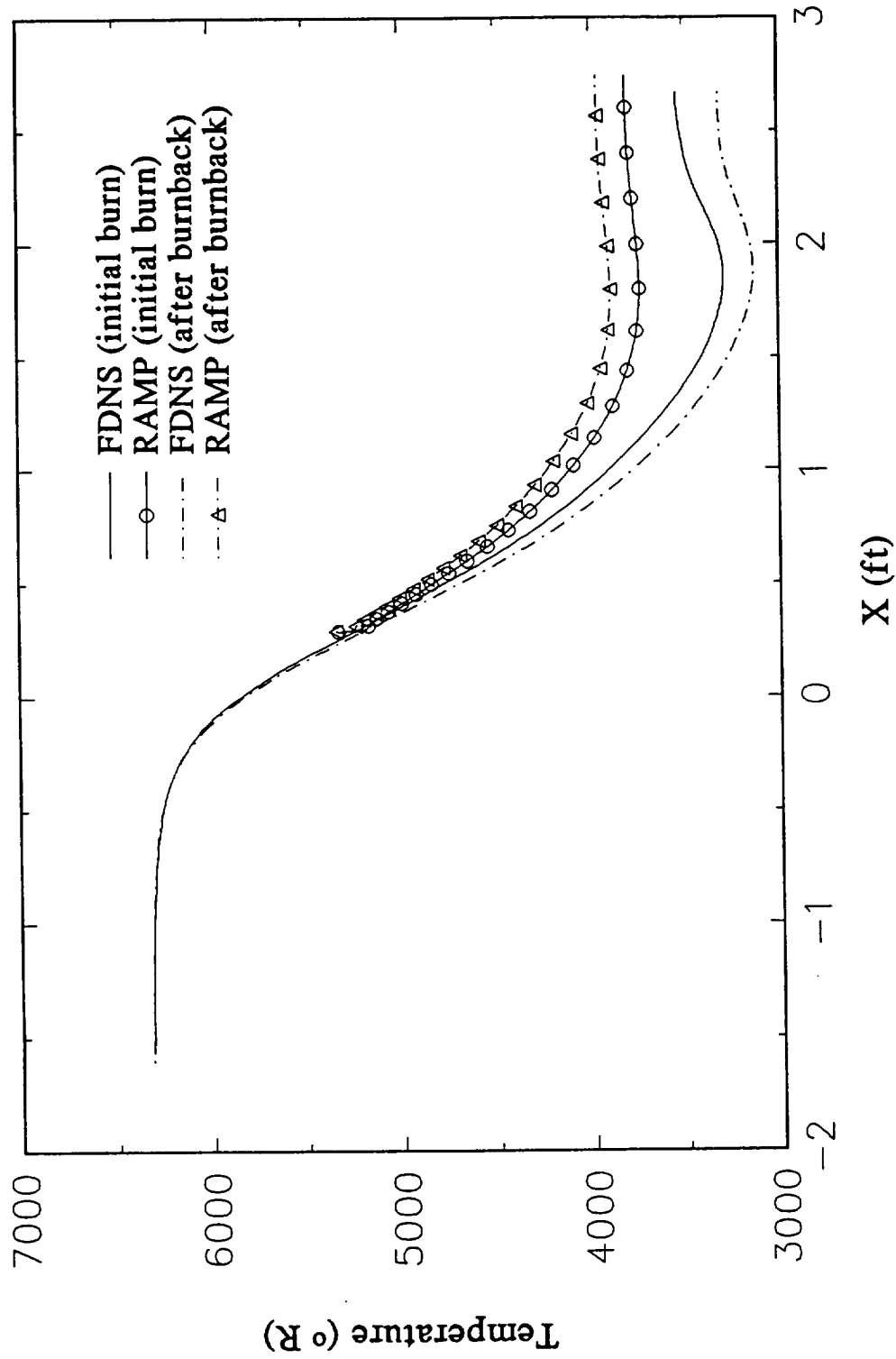
Fig. 3.15 Temperature Distribution Along the Centerline of a Contoured Nozzle
(Two-Phase, Frozen Chemistry, Laminar)
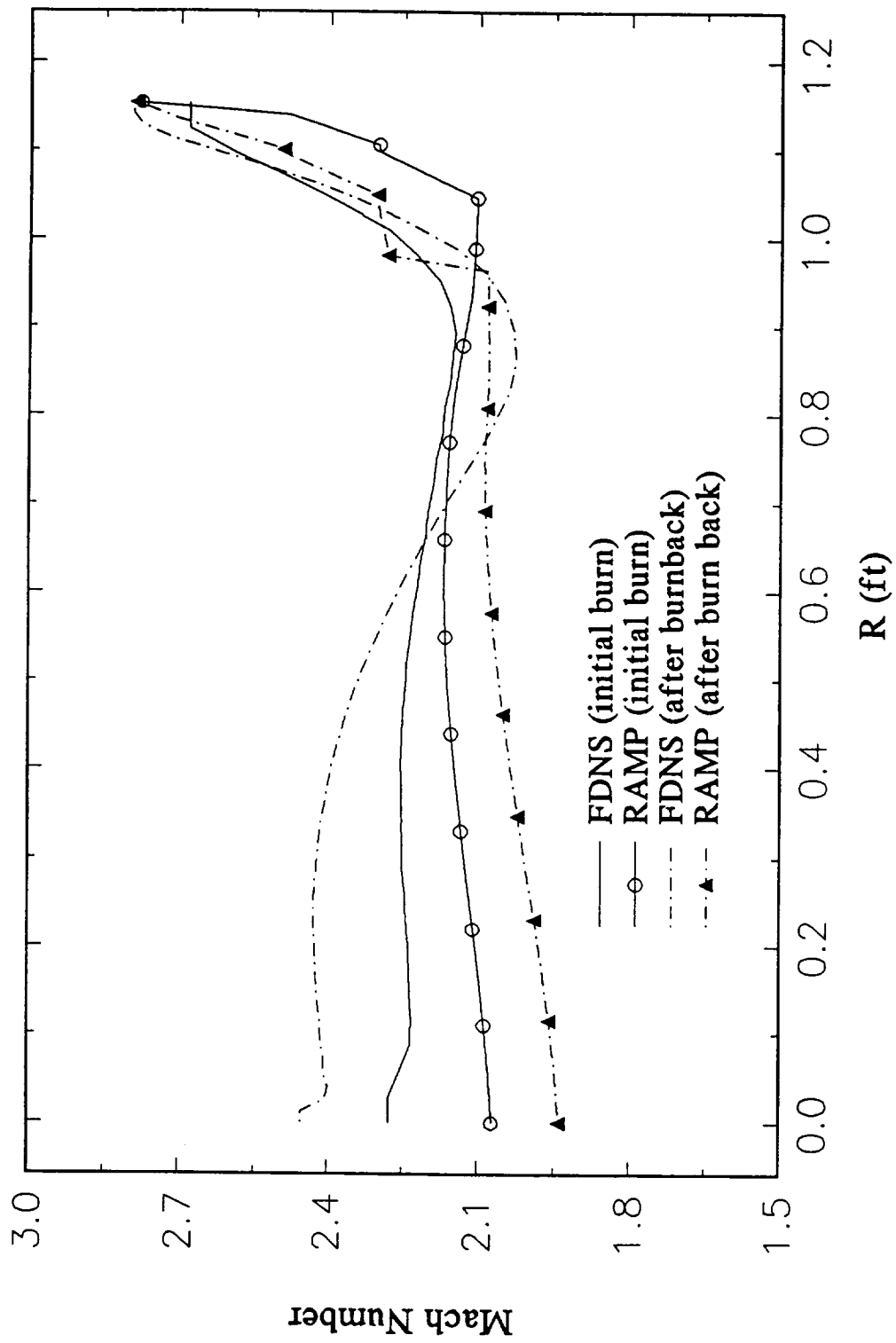
Fig. 3.16 Mach Number Profile at the Exit of a Contoured Nozzle
(Two-Phase, Frozen Chemistry, Laminar)
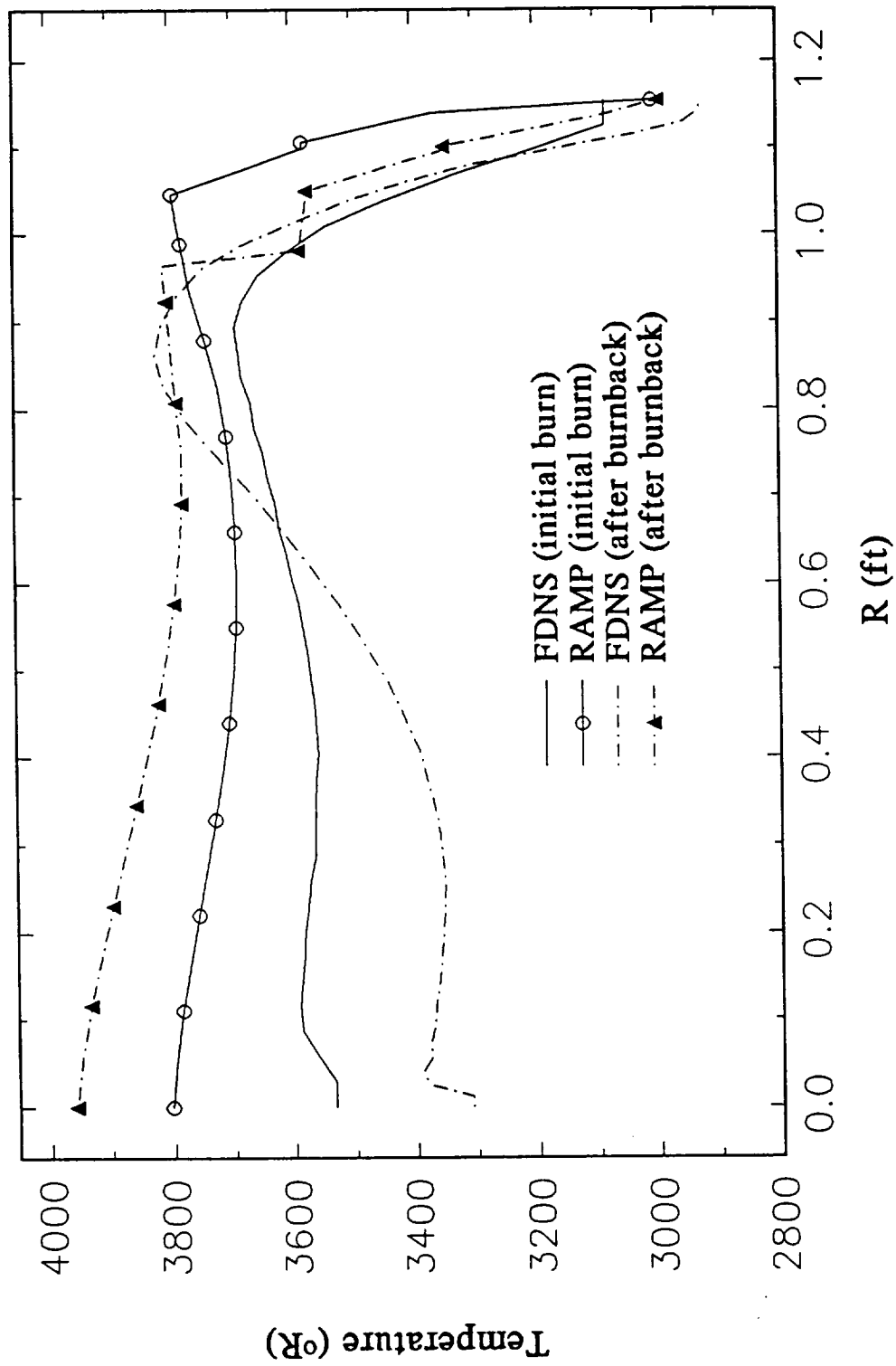
Fig. 3.17 Temperature Profile at the Exit of a Contoured Nozzle
(Two-Phase, Frozen Chemistry, Laminar)

as was previously shown for the centerline results. Figure 3.17 shows similar trends to the Mach number distributions with RAMP2 predicting overall higher temperature. The exit plane temperature distributions indicate that the steeper inlet angle results in containing a majority of the particles in a smaller area of the exit. This is apparent by observing the location in the exit where the temperature starts to rapidly drop off. For the RAMP cases, this occurs at approximately 1.05 feet for the burnback case and 0.95 feet for the initial burn case. FDNS shows this occurring at 0.9 feet for the burn back case and 0.85 feet for the initial burn case. The implications of the results presented in Figs. 3.14 thru 3.17 are that there should be significant differences in the particle density distributions between the RAMP and FDNS predictions.

Two possible explanations for the observed differences in the RAMP2 and FDNS results shown in Figs. 3.14 thru 3.15, that would influence the particle density distributions, are the Legrangian tracking method used by FDNS and combustion chamber geometry differences.

At the present time, FDNS assumes that the mass flux of the particles is constant along the initial data surface, although particulates need not be present at all points on this surface. The user may also specify how many particle trajectories may be initiated for each particle size at each cell on the initial data surface. The way the Lagrangian tracking method works is to use the trajectory information to effectively determine how many trajectories go through each cell and then allocate the mass associated with these trajectories to the particle terms in the forcing functions of the gas equations at each of the points that define any particular cell. Typically, FDNS is run with one trajectory for each cell. For uniformly expanding cases one particle trajectory provides enough accuracy to produce good results which is demonstrated by the source flow and duct cases presented earlier in the report. However, for the nozzle case where the flow is contracting and expanding, one trajectory may not be adequate. Figure 3.18 presents exit plane number density distributions for the smallest and largest particle size at the nozzle exit plane for the initial burn geometry nozzle case. Contained on this figure are results for RAMP and 3 FDNS cases. The FDNS results are for cases where 1, 5 and 20 particle trajectories were initiated in each cell. It is apparent from this figure that the particle number density becomes
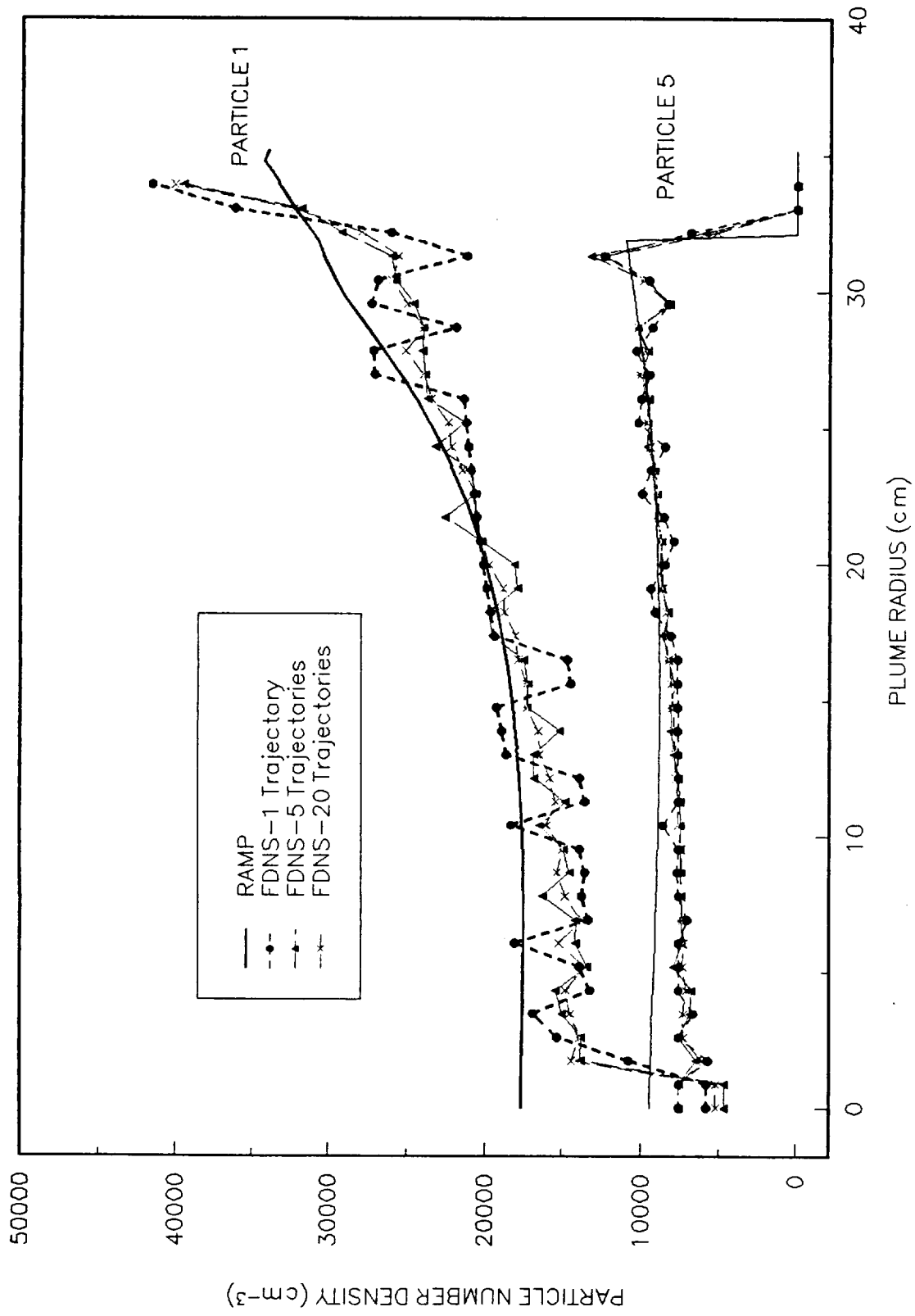
Fig. 3.18 MNASA ASRM Contoured Nozzle Exit Plane Number Density Distribution Using FDNS and RAMP2

better behaved as the number of trajectories increase, especially for particle 1 which is the smallest particle. This is to be expected since the smaller particles are more easily influenced by the gas. Also, of note in Fig. 3.18 is the large dip in number density near the axis for the smallest particle size. This is artificial, and is due to two factors. First, the FDNS code has a reflecting boundary condition at the axis of symmetry and walls. Thus, any particles that intersect the boundary are reflected, and in theory it is possible that FDNS could predict no particles at the centerline. Secondly, if the grid distribution is very fine near the axis, FDNS could also predict no particles at the axis. In reality this is not the case. The Lagrangian method needs to be improved near boundaries, perhaps with an extrapolation method. The dip in larger particle number density near the limiting streamline is caused by particles intersecting the nozzle wall and being reflected. More work needs to be done on FDNS in the treatment of particles near the boundaries. In spite of the improved number density distributions that resulted from using 20 particle trajectories per grid cell, there was little effect on the temperature of the flowfield. Two further calculations were made to help with the interpretation of the number density results. The number densities near the axis are approximately 20% below those predicted by RAMP. To verify that the gas results are consistent with the particle number density, RAMP2 was run for the same case but with the particle/gas flow rate ratio reduced by 20%. The predicted temperature at the exit plane was very close to that predicted by FDNS ($\sim 3600°R$ at the exit plane centerline). This further confirms that FDNS is properly handling the particle-gas interaction. As a final test of the calculation of particle number density, an additional check was made on the number density using another method.

As part of the Cycle 2 plume methodology (Ref. 3.5), a particle trajectory tracing code was developed. This code traces trajectories through a known gas flowfield and can be used to calculate number densities if one knows what the particle number density is at the point where the particle trajectory is initiated. The FDNS flowfield was mapped in a format that could be used by the trajectory program. Particle trajectories were initiated in this flowfield and tracked through the mapped flowfield. The predicted trajectories using the trajectory code were almost exactly what was predicted by FDNS. Using a streamtube/mass flow balance of the trajectory

code results gave number densities near the axis that were consistent with FDNS predictions. Therefore, by the process of elimination, the observed differences in RAMP2 and FDNS for the combustion chamber/nozzle case is most likely the result of geometric differences in combustion chamber treatment of the two codes.

The transonic module in the RAMP2 code assumes sink flow at the entrance angle to the throat (30° for the early burn case). FDNS was set up for the grid shown in Fig. 3.2 which has the flow entering a gentle contracting region followed by the 30° entrance to the throat. Both RAMP2 and FDNS assume that the particle mass flux is uniform across the inlet so that the initial values used by the two codes won't be responsible for the observed difference in the results. The only absolute confirmation that the differences in geometry is the reason for the difference in the results would be to rerun FDNS with the same source-like geometry. However, this was not done due to the stage in the study effort that deficiencies in the energy equation was discovered in FDNS. However, qualitatively the differences in the geometry can explain the differences in the results. One would expect the RAMP geometry to direct the particles toward the axis of the nozzle, since all particle trajectories and gas streamlines are focused toward the axis. On the other hand, in the entrance to the converging section of the chamber for the FDNS geometry, all particle trajectories (as well as gas flow) is parallel to the axis. One would expect that RAMP2 would predict higher number densities in the vicinity of the axis under these conditions.

RAMP2/SPF2 flowfields have been used extensively in the prediction of radiation environments. These calculations have shown excellent correlation with measured date. The only attempt at validating the FDNS methodology relative to radiation from the flowfield has been the study done under this contract. Until that time when more comparisons can be made to absolutely show the effects of combustion chamber nozzle geometry on radiation loads, FDNS modeling of the combustion chamber for radiation predictions should utilize the same sink flow geometry that RAMP2 uses. It is possible that future studies using FDNS modeling of the combustion chamber might explain some observed inconsistencies in radiation distributions

radially across the plume.

3.2.3 FDNS Input Instructions and Sample Case For Two-Phase Nozzle Analysis

The use and preparation of FDNS input files and common block lengths is described in detail in reference 3.11. However, some additional comments can be made for running two-phase flow cases. To initiate a two-phase flow case, two parameters must be set in the fdns01 include file. IJKPMX must be set to IIQMAX to invoke the two-phase Lagrangian tracking. The number of particle trajectories to track for each cell is set using the parameter NPMAX. For converging-diverging nozzle flows NPMAX should be set to at least 10. FDNS has two options for starting or restarting the calculations. If the start option (IDATA=2) is used, then the user must input flow and initial flowfield files using the include file fexmp01. The other option for starting FDNS is initiated by setting IDATA=1. In this case, the grid and flowfield files must be input to the code via the fort.12 (grid) and fort.13 (flowfield) files. The format of these files was previously specified in Tables 2.4 and 2.5 of Section 2.2.3. It is usually easier to write a code that will generate these files than it is using the IDATA=2 option.

Flowfield initialization can be very important in obtaining a converged solution for two-phase flow cases. For combustion chamber/nozzle cases the initial guess is not as important as for fixed upstream (supersonic) boundary cases. If the initial guess for a supersonic case is unrealistic, it is possible that a real solution will not be obtained. For combustion chamber/nozzle cases, a solution will be obtained, but if the initial guess is poor, excessive computer resources will be required for a solution. For these reasons, it is important that the initial flowfield (fort.13) file be as realistic as possible.

The other user supplied files is the fort.11 file that was previously described in Table 2.7. This file provides the overall control variables, boundary conditions, and reference properties for the FDNS solution.

The sample case that is described in this section is for the geometry previously shown in Fig. 3.2. The geometry corresponds to a simmulation of the MNASA48 contoured ASRM geometry at a chamber pressure of 590 psia. The fort.12 and fort.13 files for this case are contained on MS-DOS disks RAD3, RAD4 and RAD5. The fort.11 file is contained on disk RAD3. The source code for the version of FDNS that was used to run this case as well as the other cases presented in the report is found on disk RAD6.

This test case is an axisymmetric nozzle flowfield simulation with frozen gas phase chemistry at t=5 sec. motor burn time. The FDNS input required for this case is shown in Table 3.1. This table represents the complete FDNS input file for a 201 axial by 41 radial grid. The gaseous specie thermodynamic data (in JANNAF/CEC standard format) is for 12 gas species (NGAS=12). The particle input for 5 Al_2O_3 particle size classes (IDPTCL) of mass diameter (DDPTCL) 2.98 5.16, 7.04, 8.69, and 11.7 μm. Each of the particles has a mass density of 188 lbm/ft³ and a total enthalpy of .642149E+08 ft²/sec². This enthalpy corresponds to a temperature of 6321.6 °R which is the temperature of the gas at the inlet plane. This enthalpy is calculated assuming a specific heat of liquid Al_2O_3 of .34 BTU/lbm/°R, a solid specific heat of .32 BTU/lbm/°R, a melt temperature of 4172.4°R, and a heat of fusion of 499.74 BTU/lbm. The particles were assumed to be in thermal and dynamic equilibrium with the gas (UUPTL=U_{part}/U_{gas}=1.0). The particle mass flow for each particle class is calculated based on the particle to gas flowrate predicted by the RAMP2 code and the percentages for each particle class. RAMP2 calculates a gas flowrate of 194.66 and a particle flowrate of 97.666 lbm/sec. The distribution of flowrates amongst the particle sizes was selected based on the Cycle 2.0 methodology described in Ref. 3.5. Input to FDNS for each group is the particulate mass flow for that size group divided by 2π. The particles are assumed to be uniformly distributed from the nozzle axis to the nozzle wall thru MPTCL=1 (axis) and MPTCL2=41 (wall).

In the event that the user wants to consider reacting chemistry, NREACT can be set to 18 and the reaction set shown in Table 3.2 can be added after the reaction header record.

Table 3.1 Listing of fort.11 Input File For Two-Phase FDNS Sample Case

```
IDIM, (2-D axisy. nozzle test case, multi-phase flow)
   2,
 IZON,IZFACE,  IBND,    ID, ISNGL,
   1,     0,     4,     0,     0,
  IZT,   JZT,   KZT,  CBGX,  CBGY,  CBGZ,  CBVX,  CBVY,  CBVZ,
  201,    41,    1,   0.0,   0.0,    0.,    0.,    0.,    0.,
 NNBC,  IZB1,  IZF1,  IJZ1,  IJZ2,  JKZ1,  JKZ2, (2 LINES EACH)
        IZB2,  IZF2,  IJZ1,  IJZ2,  JKZ1,  JKZ2,
IBCZON,  IDBC, ITYBC,  IJBB,  IJBS,  IJBT,  IKBS,  IKBT,
   1,     2,     1,     1,     1,    41,     1,     1,
   1,     4,     3,     1,     1,   201,     1,     1,
   1,     3,     3,    41,     1,   201,     1,     1,
   1,     1,     2,   201,     1,    41,     1,     1,
IWBZON,  L1,   L2,   M1,   M2,   N1,   N2,  IWTM, HQDOX, IWALL, DENNX, VISWX,
ISNZON, ISNBC, ISNAX, ISNBS, ISNBT,
 IDATA,  IGEO,  6ITT, ITPNT, ICOUF, NLIMT,   IAX,  ICYC,
   1,    41,   201,   200,     3,     1,     2,     0,
-5.000E-01DTT,  IREC,   REC, THETA, BETAF,  IEXX,  PRAT,
  5.000E-01,     2,  1.00,   1.0,   1.0,     1,  -1.0,
  IPC,   JPC,  IPEX,  JPEX,   IMN,   JMN,
  202,     1,  4221,     1,   263,     1,
VISC(1/RE),IG,ITURB,   AMC,  GAMA,   CBE,   CBH, EREXT,
9.09960E-07, 1,     2, 0.089, 1.265,   0.0,   0.0,1.E-08,
 ISWU,  ISWP,  ISWK, ISKEW,
   1,     1,     1,     0,
INSO(IEQ): (VISCOSITY = 4.4228260E-07 SLUGS/FT-SEC)
 U, V, W,TM,DK,DE, 7, 8, 9,VS,FM,SF,
 1, 1, 0, 1, 0, 0, 0, 0, 0, 0, 1, 1,
----NGAS, NREA18, IUNIT, DREF(SLG), UREF(F/S), TREF(R), XREF  (FT),
   12,      0,     2,5.3000E-03,  411.2400, 6321.60, 1.00000E-0,
H2O                                  300.000  5000.000      18.01520
0.26340654E+01 0.31121899E-02-0.90278451E-06 0.12673054E-09-0.69164734E-14
-0.29876258E+05 0.70823874E+01 0.41675563E+01-0.18106868E-02 0.59450877E-05
-0.48670872E-08 0.15284144E-11-0.30289547E+05-0.73087996E+00
O2                                   300.000  5000.000      31.99880
0.36122139E+01 0.74853166E-03-0.19820646E-06 0.33749007E-10-0.23907374E-14
-0.11978151E+04 0.36703308E+01 0.37837136E+01-0.30233634E-02 0.99492754E-05
-0.98189101E-08 0.33031826E-11-0.10638107E+04 0.36416345E+01
H2                                   300.000  5000.000       2.01580
0.30558124E+01 0.59740403E-03-0.16747471E-06-0.21247544E-10 0.25195486E-14
-0.86168475E+03-0.17207073E+01 0.29432328E+01 0.34815508E-02-0.77713821E-05
0.74997493E-08-0.25203379E-11-0.97695410E+03-0.18186136E+01
O                                    300.000  5000.000      15.99940
0.25342960E+01-0.12478170E-04-0.12562724E-07 0.69029860E-11-0.63797098E-15
0.29231107E+05 0.49628592E+01 0.30309401E+01-0.22525853E-02 0.39824540E-05
-0.32604921E-08 0.10152035E-11 0.29136525E+05 0.26099341E+01
H                                    300.000  5000.000       1.00790
0.25000000E+01 0.00000000E+00 0.00000000E+00 0.00000000E+00 0.00000000E+00
0.25474391E+05-0.45989841E+00 0.25000000E+01 0.00000000E+00 0.00000000E+00
0.00000000E+00 0.00000000E+00 0.25474391E+05-0.45989841E+00
OH                                   300.000  5000.000      17.00730
0.28897815E+01 0.10005879E-02-0.22048808E-06 0.20191288E-10-0.39409830E-15
0.38857041E+04 0.55566425E+01 0.38737299E+01-0.13393773E-02 0.16348351E-05
-0.52133636E-09 0.41826975E-13 0.35802349E+04 0.34202406E+00
CO                                   300.000  5000.000      28.01040
0.29840696E+01 0.14891390E-02-0.57899683E-06 0.10364577E-09-0.69353550E-14
-0.14245228E+05 0.63479156E+01 0.37100928E+01-0.16190964E-02 0.36923593E-05
-0.20319675E-08 0.23953344E-12-0.14356310E+05 0.29555352E+01
CO2                                  300.000  5000.000      44.00980
0.44608040E+01 0.30981719E-02-0.12392571E-05 0.22741325E-09-0.15525955E-13
-0.48961441E+05-0.98635983E+00 0.24007797E+01 0.87350961E-02-0.66070879E-05
0.20021862E-08 0.63274039E-15-0.48377527E+05 0.96951456E+01
```

Table 3.1 Listing of fort.11 Input File For Two-Phase FDNS Sample Case (Cont.)

```
CL???                                            300.000   5000.000     35.45300
  0.29537796E+01-0.40792712E-03 0.15288342E-06-0.26384345E-10 0.17206581E-14
  0.13695677E+05 0.30667325E+01 0.20774281E+01 0.29487169E-02-0.43919732E-05
  0.24499776E-08-0.41007685E-12 0.13871928E+05 0.73136343E+01
CL2??                                            300.000   5000.000     70.90600
  0.43077814E+01 0.31182816E-03-0.16310807E-06 0.44511913E-10-0.43057753E-14
 -0.13458251E+04 0.20666684E+01 0.31316886E+01 0.48997877E-02-0.69411463E-05
  0.44785641E-08-0.10621859E-11-0.10979696E+04 0.77833424E+01
HCL??                                            300.000   5000.000     36.46100
  0.27665884E+01 0.14381883E-02-0.46993000E-06 0.73499408E-10-0.43731106E-14
 -0.11917468E+05 0.64583540E+01 0.35248171E+01 0.29984862E-04-0.86221891E-06
  0.20979721E-08-0.98658191E-12-0.12150509E+05 0.23957713E+01
N2                                               300.000   5000.000     28.01340
  0.28532898E+01 0.16022128E-02-0.62936891E-06 0.11441022E-09-0.78057466E-14
 -0.89008093E+03 0.63964896E+01 0.37044177E+01-0.14218753E-02 0.28670393E-05
 -0.12028385E-08-0.13954677E-13-0.10640795E+04 0.22336285E+01
IDPTCL,5*** PARTICLE INPUT CONTROL ****
    5,       0,
IPTZON,IDRCPT,LPTCL1,LPTCL2,MPTCL1,MPTCL2,NPTCL1,NPTCL2,(2 LINES EACH)
       ITPTCL,DDPTCL,DNPTCL,WDMASS,UUPTCL,HTPTCL,
    1,       1,      1,      2,      1,     41,      1,      1,
            5, 2.980,188.00,  0.307, 1.000,0.642149E+08,
    1,       1,      1,      2,      1,     41,      1,      1,
            5, 5.160,188.00,  1.808, 1.000,0.642149E+08,
    1,       1,      1,      2,      1,     41,      1,      1,
            5, 7.040,188.00,  4.310, 1.000,0.642149E+08,
    1,       1,      1,      2,      1,     41,      1,      1,
            5, 8.690,188.00,  3.662, 1.000,0.642149E+08,
    1,       1,      1,      2,      1,     41,      1,      1,
            5, 11.70,188.00,  5.457, 1.000,0.642149E+08,
***END******
```

Table 3.2 Listing of FDNS Finite Rate Chemistry Reaction Set For fort.11 Input File

```
REACTION:H2O,  O2,  H2,   O,   H,  OH,  CO,  CO2,  CL,  CL2, HCL,N2,
 1, 1.7000E13,  0.00,24070.,  0,  0,
          0., -1., -1.,  0.,  0.,  2.,  0.,  0.,  0.,  0.,  0.,0.,
 2, 2.1900E13,  0.00, 2590.,  0,  0,
          1.,  0., -1.,  0.,  1., -1.,  0.,  0.,  0.,  0.,  0.,0.,
 3, 6.0230E12,  0.00,  550.,  0,  0,
          1.,  0.,  0.,  1.,  0., -2.,  0.,  0.,  0.,  0.,  0.,0.,
 4, 1.8000E10, -1.00, 4480.,  0,  0,
          0.,  0., -1., -1.,  1.,  1.,  0.,  0.,  0.,  0.,  0.,0.,
 5, 1.2200E17,  0.91, 8369.,  0,  0,
          0., -1.,  0.,  1., -1.,  1.,  0.,  0.,  0.,  0.,  0.,0.,
 6, 4.0000E12,  0.00, 4030.,  0,  0,
          0.,  0.,  0.,  0.,  1., -1., -1.,  1.,  0.,  0.,  0.,0.,
 7, 3.0000E12,  0.00,25000.,  0,  0,
          0., -1.,  0.,  1.,  0.,  0., -1.,  1.,  0.,  0.,  0.,0.,
 8, 1.0000E16,  0.00,    0.,999,  0,
          0.,  0.,  0., -1., -1.,  1.,  0.,  0.,  0.,  0.,  0.,0.,
 9, 2.5500E18,  1.00,59390.,999,  0,
          0.,  1.,  0., -2.,  0.,  0.,  0.,  0.,  0.,  0.,  0.,0.,
10, 5.0000E15,  0.00,    0.,999,  0,
          0.,  0.,  1.,  0., -2.,  0.,  0.,  0.,  0.,  0.,  0.,0.,
11, 8.4000E21,  2.00,    0.,999,  0,
          1.,  0.,  0.,  0., -1., -1.,  0.,  0.,  0.,  0.,  0.,0.,
12, 6.0000E13,  0.00,    0.,999,  0,
          0.,  0.,  0., -1.,  0.,  0., -1.,  1.,  0.,  0.,  0.,0.,
13, 8.4300E13,  0.00, 2144.,  0,  0,
          0.,  0., -1.,  0.,  1.,  0.,  0.,  0., -1.,  0.,  1.,0.,
14, 3.0100E13,  0.00, 8858.,  0,  0,
         -1.,  0.,  0.,  0.,  0.,  1.,  0.,  0., -1.,  0.,  1.,0.,
15, 3.6100E12,  0.00, 3020.,  0,  0,
          0.,  0.,  0., -1.,  0.,  1.,  0.,  0.,  1.,  0., -1.,0.,
16, 9.0300E13,  0.00,  604.,  0,  0,
          0.,  0.,  0.,  0., -1.,  0.,  0.,  0.,  1., -1.,  1.,0.,
17, 3.6300E14,  0.00, -906.,999,  0,
          0.,  0.,  0.,  0.,  0.,  0.,  0.,  0., -2.,  1.,  0.,0.,
18, 1.4500E22,  2.00,    0.,999,  0,
          0.,  0.,  0.,  0., -1.,  0.,  0.,  0., -1.,  0.,  1.,0.,
```

3.2.4 Influence of Combustion Chamber Geometry on Flowfield Radiation Properties

One of the observations that has been made based on ground firings of solid rocket motors is that there is a tendency for measured radiation to increase with burn time, even if the chamber pressure is relatively constant. The MNASA series of tests showed 20-30% difference in radiation measurements at the same chamber pressure but at different times in the burn. Two possible reasons are carbon due to burning insulation or flowfield effects due to changes in the combustion chamber geometry as the grain burns back. Sambamuthi (Ref. 3.20) presented a good argument that burning insulation could account for increased radiation with time of burn. The results that were previously presented for the MNASA-ASRM combustion chamber/nozzle cases suggest that differences in the combustion chamber geometry could result in particle number density distribution changes within the nozzle, that in turn could result in different particle and gas temperature distributions in the plume. Figure 3.19 presents SIRRM (Ref. 3.21) single line-of-sight radiance calculations at the exit plane for two RAMP2 cases and one FDNS case. The two RAMP2 cases correspond to the 30 degree inlet (initial burn) and 54 degree inlet (burn back near the end of firing) MNASA contoured ASAM nozzle case. The FDNS results are for the 30 degree inlet case shown in Fig. 3.2. Examination of the RAMP2 results show that the integrated heat flux for the 54 degree inlet case is approximately 20% higher than the initial burn back case (30 degree inlet). These results are consistent with the observed differences in the measurements early and late in the burn. FDNS results for the initial burn back case are approximately 12% lower than the corresponding RAMP2 case. The absolute magnitude of the results shown in Fig. 3.19 are not important since the calculations were performed using a Cycle 1.0 methodology with frozen chemistry. The important finding is that combustion chamber geometry can influence predicted radiation. Further calculations need to be performed to validate and quantify combustion chamber effects.

3.3 Particle Size Distribution

One of the uncertainties in performing a two-phase flow calculation is the mean particle
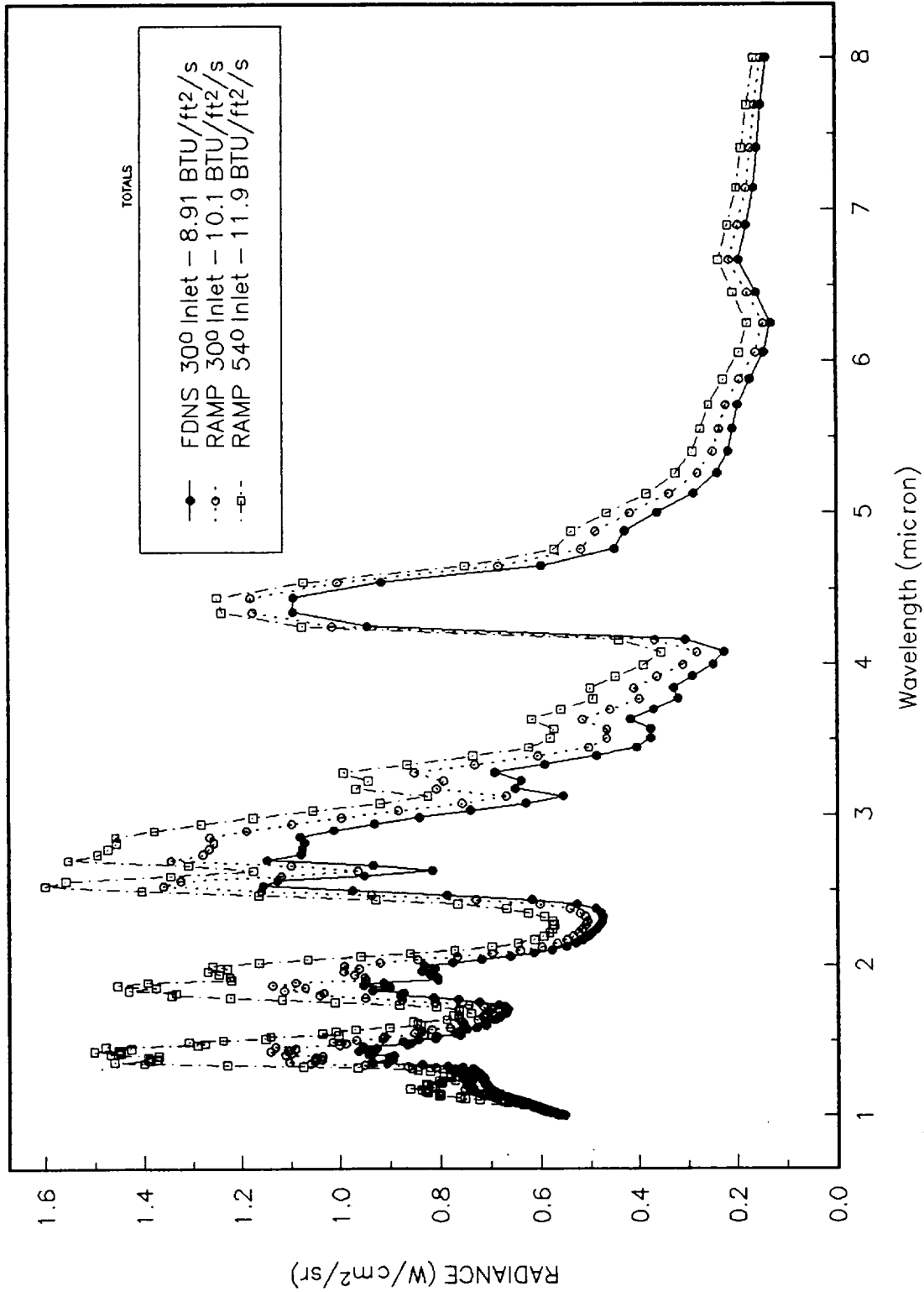
Fig. 3.19 MNASA ASRM (Cycle 1.0) Exit Plane Radiance Verses Wavelength Using RAMP2 and FDNS Flowfields with Combustion Chamber Geometry Variations

size and distribution of mass about the mean size. A majority of the mass of aluminum/aluminum oxide particulates that form at the propellant surface are comprised of very large particles (>100 μm) that subsequently break up in the transonic regions of the nozzle due to the large shear stresses that are present in this region. To investigate the validity of the existing particle size correlations, this portion of the overall study effort used the One-Dimensional Three-Phase Reacting Flow with Mass Transfer Between Phases code (OD3P) (Ref. 3.22). OD3P has been applied to the problem of predicting Al_2O_3 particle size measured during the NASA/MSFC 48 in. diameter ASRM/RSRM subscale solid motor MNASA test series. The particle size measurements taken during the MNASA test series are described in Ref. 3.23. In the following analysis the mass mean averaged particle diameter (D_{43}) for the MNASA9(RSRM48-3) test was predicted using a modified version of the OD3P program.

The MNASA9(RSRM48-3) test was chosen for analysis because in this test the largest number of samples were taken and reported (7 samples) during the test series. The operating characteristics at t=5 sec for the RSRM48-3 motor are shown in Table 3.3. The RSRM propellant contained: 69.7% Ammonium Perchlorate (AP), composed of 70% by mass of 200 μm and 30% by mass of 20 μm diameter AP particles; 16% Aluminum particles of 30 μm diameter; 14% PBAN Binder; and 0.30% Iron Oxide. The formulation of the RSRM propellant is reported Ref. 3.23.

Table 3.3. MNASA 09/RSRM48-3
Motor Operating Characteristics @ t = 5 sec

Propellant Binder Type	PBAN
Aluminum Loading (%)	16.
Nominal Chamber Pressure (psia)	680.
Calculated Gas Flowrate (lbm/sec)	241.52
Calculated Particle Flowrate (lbm/sec)	96.80
Throat Diameter, Initial (in)	9.950
Throat Diameter, Final (in)	10.399
Nozzle Exit Diameter, Initial (in)	24.104
Nozzle Type/Liner Material	Conical/CCP

The OD3P code as documented in Ref. 3.22 and obtained from the Air Force, Phillips Laboratory (AFSC), in Aug. 1991 has been reviewed and several improvements have been suggested by Mark Salita. The improvements to OD3P suggested by Salita are documented in Ref. 3.24, however an updated version of the code including the suggested improvements is not available from the Air Force. The work by Salita cited in Ref. 3.24 concluded that one of the major deficiencies in OD3P is the model for collision/ coalescence efficiency, particularly incomplete particle coalescence efficiency as large particles collide among themselves during the contraction/expansion process.

Based on the OD3P results presented in Ref. 3.24 for the full scale RSRM nozzle which indicate that large/large particle collisions have a low coalescence efficiency (approximately 3%), and assuming 3 particle sets with a combustion chamber mass median particle diameter of 100 μm which can be reduced in size by a factor of 2 upon breakup, the following OD3P particle size prediction was obtained for the RSRM48-3 motor. The initial combustion chamber particle mass mean diameter of 100 μm follows the full scale RSRM simulation of Salita in Ref. 3.24 (115 μm), and the work of Netzer in Ref. 3.25 (approximately 130 μm near the propellant surface).

The code was modified to assume a constant coalescence efficiency of 3%, and the input particle breakup radius ratio was set to 2.0. The OD3P calculation was initiated in the motor chamber at an area ratio of 6.62. The resulting axial particle size predictions are shown in Figs. 3.20 and 3.21. The OD3P prediction for the three particle group diameters in microns versus axial distance normalized by the throat radius (x/r*) is shown in Fig. 3.20. The OD3P code predicts that each of the three particle groups will break up three times and reach a final particle group diameter of 5.6, 10.8, and 9.9 μm; starting with initial diameters of 53.7, 100.0, and 186.1 μm, respectively. The OD3P prediction for particle mass mean diameter (D_{43}) for all three particle groups is compared to the industry standard Hermsen correlation (Ref. 3.26) and to the arithmetic average of the seven samples collected during the MNASA/RSRM48-3 test reported in Ref. 3.23 in Fig. 3.21. The nozzle exit plane D_{43} predicted by OD3P (8.96 μm)
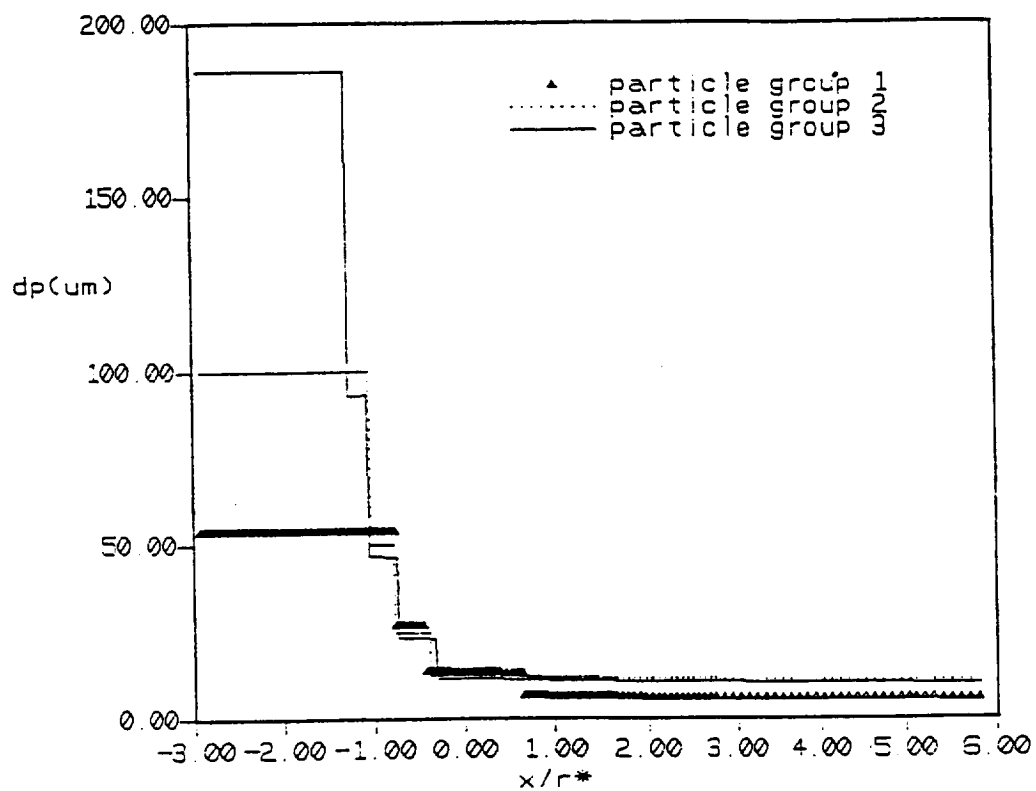
rsrm48-3 – od3p – dp=100um – 7/13/93 – seca
particle diameter(microns) vs. axial position

Fig. 3.20 OD3P RSRM48-3 Nozzle Particle Group Diameter vs. x/r*
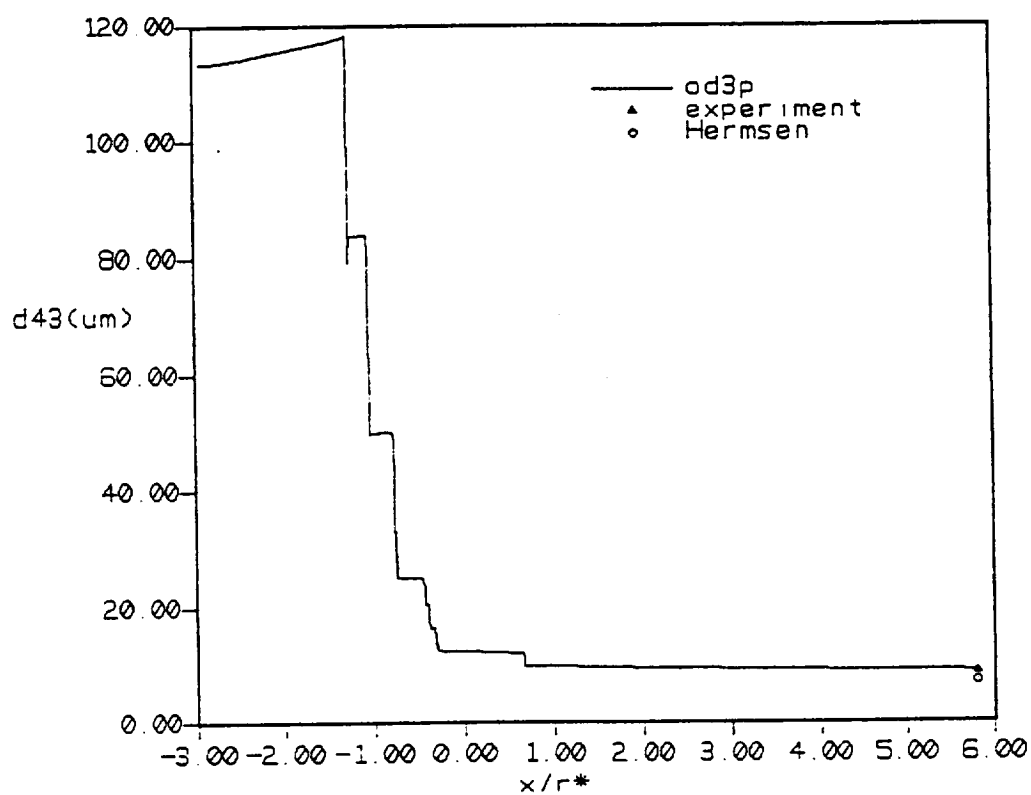
rsrm48-3 - od3p - dp=100um - 7/13/93 - seca
particle mass avg. dia.(microns) vs. axial position

Fig. 3.21 OD3P RSRM48-3 Nozzle Mass Mean Particle Diameter vs. x/r*

agrees well with the average of the test data for this test (8.64 μm), however both of these are slightly higher (24%) than the Hermsen correlation value of 7.12 μm, but within the accuracy of the correlation. The experimental particle collection technique sampled particles in the nozzle exhaust plume from approximately 150 to 620 nozzle exit radii downstream of the nozzle exit plane. The assumption is that once the particles have solidified near the nozzle exit plane there is no further particle size change downstream of the nozzle exit plane.

To test the assumption that the particle size does not significantly change beyond the nozzle exit plane, the previous analysis of the RSRM48-3 motor has been extended downstream beyond the nozzle exit plane in the near field plume to approximately 7 nozzle exit radii. In this analysis the one-dimensional, pressure defined, constant area streamtube flowfield option of the OD3P program was used to determine the exhaust plume gas and particle properties. The analysis was initiated at the nozzle exit plane with gas and particle properties as defined by the OD3P nozzle solution. The RSRM48-3 nozzle exit plane gas and particle starting conditions for the OD3P plume calculation are noted in Table 3.4. The plume centerline gas axial static pressure schedule required as input for the OD3P pressure defined option was determined from a typical SPF-II code (Ref. 3.1) plume sea level flowfield calculation for the RSRM48-3 motor. The SPF-II plume centerline axial pressure schedule was normalized by the SPF-II predicted centerline pressure at the nozzle exit plane and the result ratioed by the exit plane gas pressure as predicted by OD3P which is shown in Table 3.4. In other words the SPF-II code was used to determine the shape of the axial pressure schedule, and the initial pressure magnitude was determined by the OD3P nozzle solution exit plane pressure.

Table 3.4. MNASA09/RSRM48-3 OD3P Predicted Nozzle Exit Plane Gas and Particle Properties at = 5 sec	
Gas Pressure (psia)	18.73
Gas Temperature (°R)	3478.0
Gas Velocity (ft/sec)	7687.5
Gas Density (lbm/ft³)	0.01007
Particle Temperature/Phase	
• Particle Group 1 (°R)	3917.9 (subcooling)
• Particle Group 2 (°R)	4301.8 (liquid)
• Particle Group 3 (°R)	4249.5 (liquid)
Particle Velocity	
• Particle Group 1 (ft/sec)	7219.3
• Particle Group 2 (ft/sec)	6726.7
• Particle Group 3 (ft/sec)	6796.9
Particle Diameter	
• Particle Group 1 (microns)	5.63
• Particle Group 2 (microns)	10.78
• Particle Group 3 (microns)	9.96
Particle Mass Averaged Diameter, D_{43} (microns)	8.96

The RSRM48-3 plume centerline axial pressure schedule described above input to the OD3P code for this case is shown in Fig. 3.22. The key feature in the predicted plume centerline axial gas pressure distribution is the reflected shock which is shown in Fig. 3.22 to occur at approximately 4.0 nozzle exit radii. This is typical for a sea level conical nozzle expansion for a motor of this type. The plume centerline gas temperature predicted by OD3P for this case is shown in Fig. 3.23. The predicted plume particle size axial variation for each of the three particle size groups is shown in Fig. 3.24. Particle group 1, the smallest particle size group, begins to subcool within the nozzle at a nozzle area ratio of 4.0 (the nozzle exit plane is at an area ratio of 5.87); and has completed subcooling and begins to solidify at 2.0 nozzle exit radii, and has completed solidification at 4.0 nozzle exit radii downstream of the nozzle exit plane. Particle group 3, the next largest particle size group, begins to subcool at 0.2 nozzle exit radii and does not complete subcooling by 7.0 exit radii. Particle group 2, the largest particle size group, begins to subcool at 0.4 exit radii and does not complete subcooling by 7.0 exit radii.

The particle mass average diameter versus axial position predicted by OD3P for the RSRM48-3 plume is shown in Fig. 3.25. In Fig. 3.25 the OD3P prediction is compared with the NASA/MSFC measurements (Ref. 3.23) and the Hermsen correlation (Ref. 3.26) at the nozzle exit plane. The prediction is approximately 4% higher than the arithmetic average of the measurements for this motor. The most significant finding of this analysis is that once the particles reach the motor exit plane and have begun the process of subcooling and subsequently solidification, there is little further size change as the particles enter the plume at least to approximately 7 exit radii downstream. For this case the particle mass averaged diameter decreased from 8.96 μm at the nozzle exit plane to 8.63 μm at 6.9 exit radii or 3.7%, which is negligible.

The mean particle size (D_{43}) predicted by OD3P for the MNASA case is very close to that measured by Sambamurthi and reported in Ref. 3.23. It is recommended that the distribution of particles presented in Ref. 3.23 be used for motors of the size of the MNASA test
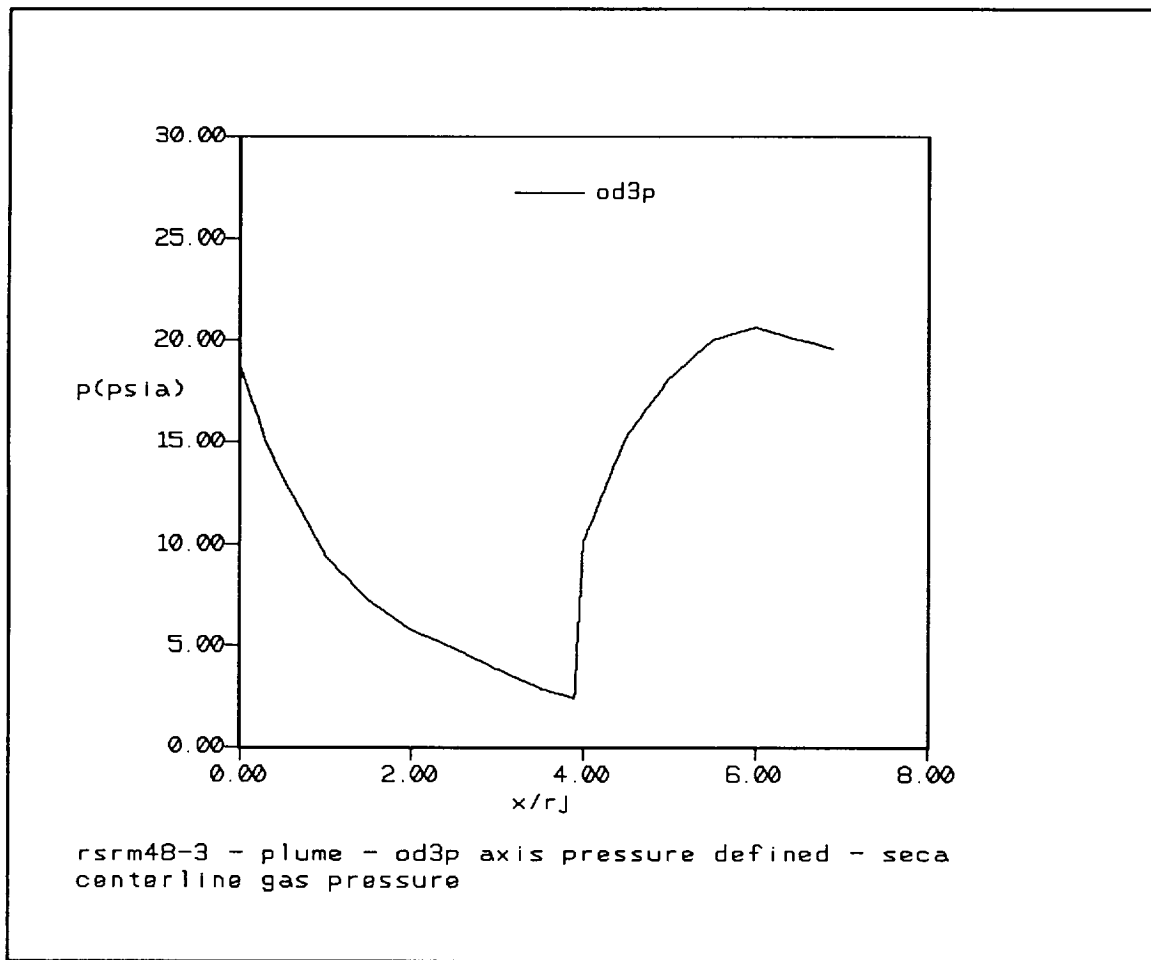
Fig. 3.22 OD3P RSRM48-3 Plume Centerline Gas Pressure
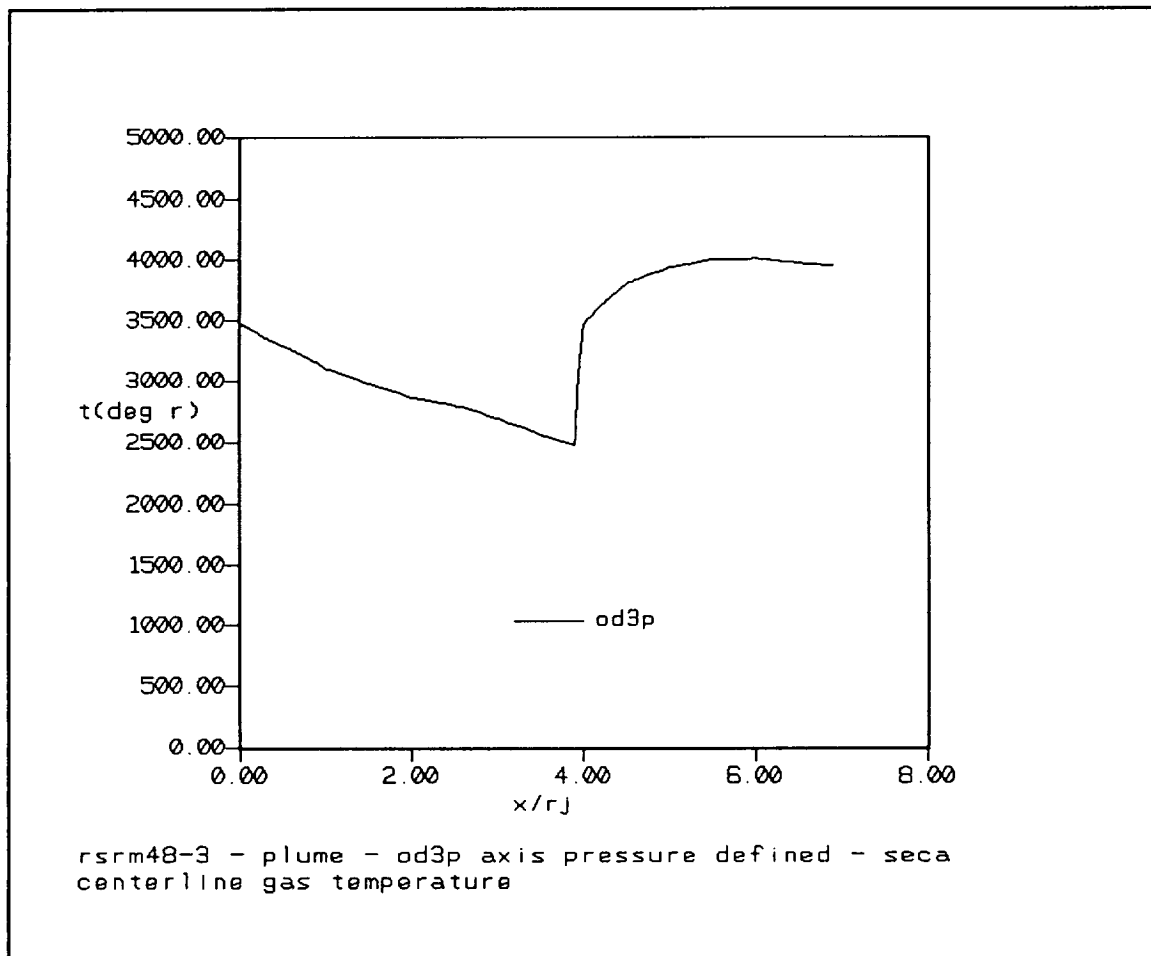
Fig. 3.23 OD3P RSRM48-3 Plume Centerline Gas Temperature
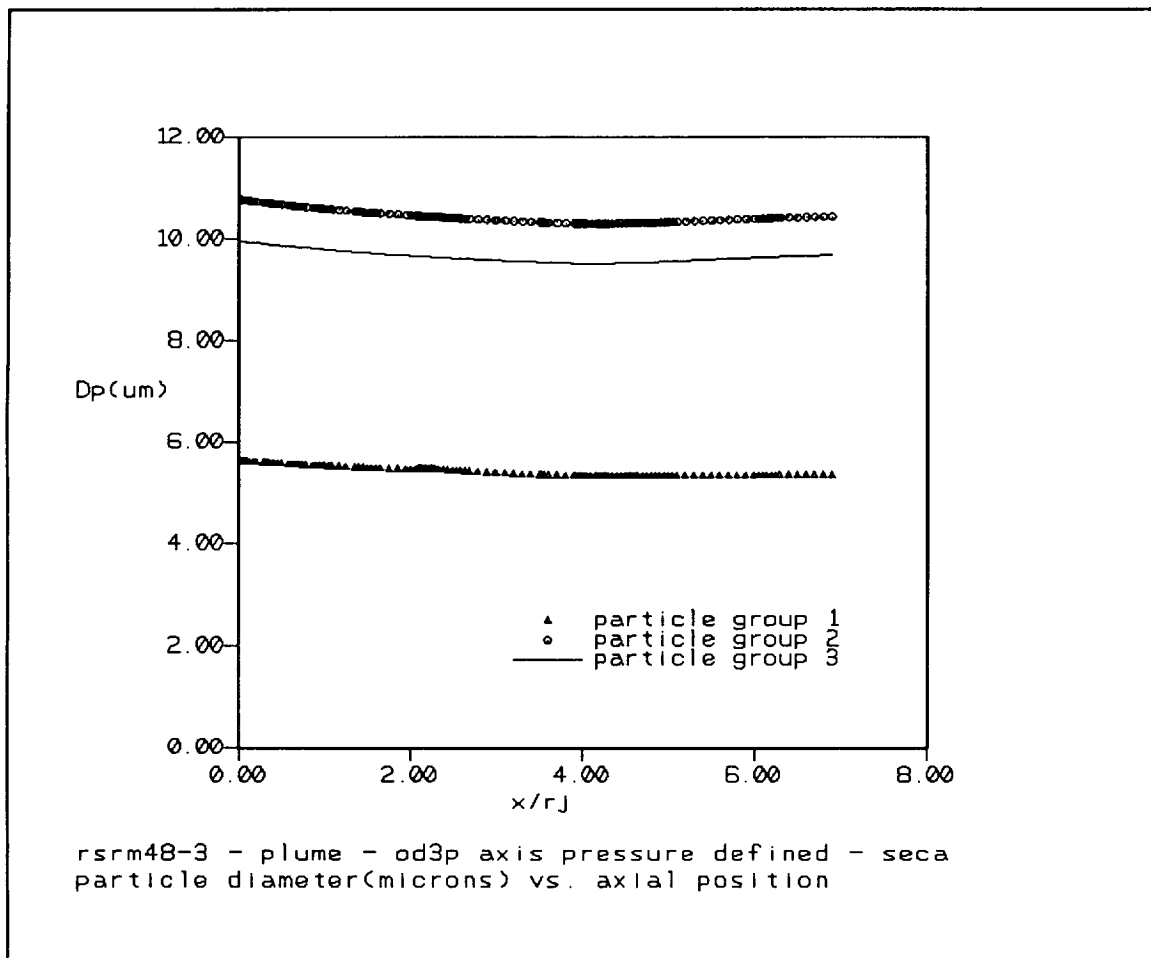
Fig. 3.24 OD3P RSRM48-3 Plume Particle Group Diameter vs. Axial Position
(X/R_j)
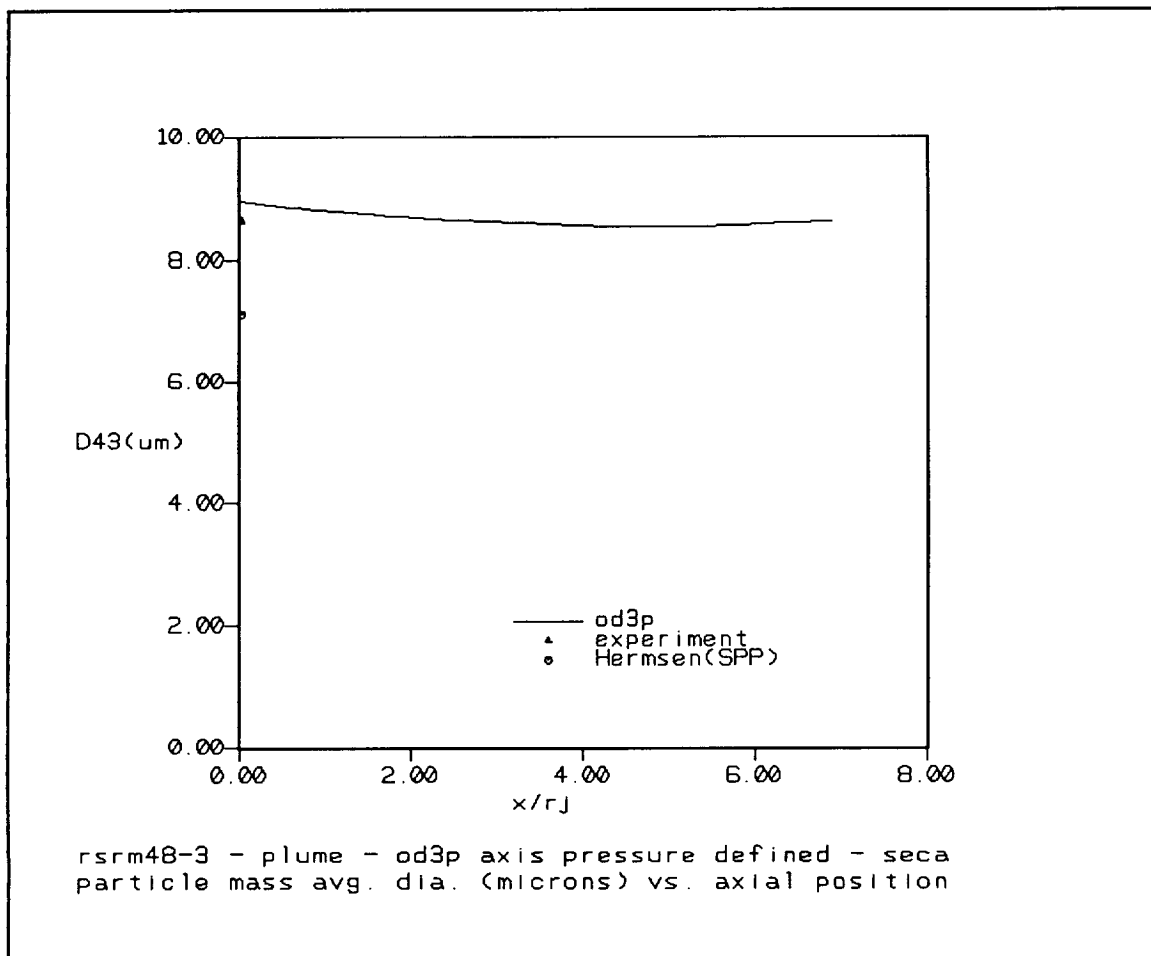
Fig. 3.25   OD3P RSRM48-3 Plume Particle Mass Average Diameter vs. Axial
Position (X/R$_j$)

series and smaller. This distribution was used for Cycle 2.0 predictions. Particle size measurements were also taken by Sambamurthi for the full scale RSRM motor (Ref. 3.27). These measurements are in very close agreement with the predictions made by Salita using OD3P (Ref. 3.24). The mean particle size measured and predicted are almost identical to those predicted using the Hermsen correlation. The measured and predicted size and mass fraction distributions are again almost identical. The measured mass distribution is best described as a monomodal log-normal distribution with a standard of deviation of .13. The results of OD3P calculations for the MNASA and full scale RSRM motors when compared with measured distributions show that OD3P can satisfactorily be used to make a prior prediction of particle sizes and distributions in the plume at least for these two classes of motors.

4.0 INTERPRETATION OF MNASA THERMAL IMAGE CAMERA DATA

The 48 in. diameter MNASA solid motor test series provided diverse and detailed measurements of the radiation properties of the exhaust plume that included: total radiometer, CVF spectrometer and thermal image camera data. The majority of previous studies used the radiometer and CVF spectrometer data to support flowfield and radiation model development. This section details the results of a study to investigate the thermal image data relative to the radiative properties of solid rocket motor exhaust plumes. The analyses of these additional thermal image data sets are required to provide insight into the continuing task of identifying the source and magnitude of discrepancies in the comparison of predicted solid motor radiance and radiant heat flux vs. measurements. In the discussion presented below, thermal image camera radiance data are compared to SIRRM-II code predictions made using both the FDNSEL and RAMP/SPF2 flowfield methodologies for various MNASA test series RSRM48 and ASRM48 subscale motor firings. The intent is to first identify the available MNASA thermal image test data, and second to compare radiance predictions to the available thermal image data, and lastly to critique the flowfield methodology and to identify shortcomings in the predictive methodology.

The results presented in this section were previously reported in a quarterly progress report (Ref. 4.1) and reflect flowfield calculations that were at various levels of maturity and validation. The RAMP/SPF2 flowfield solutions are referred to as Cycle 1.0, Cycle 1.5 and Cycle 2.0 plumes. These plume calculations refer to three levels of flowfield development that resulted from studies (Ref. 4.2) to predict the plume induced environments for the Space Shuttle Vehicle equipped with the Advanced Solid Rocket Boosters (ASRB's). These models are summarized in Ref. 4.2.

Early in the ASRM plume model development, it was found that the industry standard model under predicted the radiation data. One potential hypothesis was that small amounts of carbon particulates were present that could potentially result in radiation enhancement that might correlate the predictions with measurements. Early comparisons made assuming 2.5% carbon by weight in the plume resulted in excellent comparisons with the spectrometer data. Some of these comparisons have been included in this section for completeness. However, it was found during the ASRM plume studies that carbon was most probably not the factor that caused the discrepancy in theory and data. Cycle 2.0 model development identified deficiencies in the particle gas heat transfer model and the particle size model that would account for observed differences between Cycle 1.0 predictions and data. As a result, Cycle 2.0 plume model is recommended for use in predicting solid rocket motor plumes.

The FDNS results which are presented in this section were made prior to correcting the deficiencies in FDNS described in Section 3.2. The main problem with the calculation (i.e. the work loss term in the gas energy equation) results in FDNS calculations that simulate a reduced heat transfer between the gas and particles. FDNS calculations using the Cycle 2 methodology should result in plumes that are similar to those presented in this section for FDNS, albeit for different reasons. Due to the stage in the study that this deficiency was identified, it was not possible to recalculate the FDNS correlations that are presented in this section. It is recommended that these calculations be redone using the corrected version of FDNS.

4.1 MNASA Test Series Thermal Image Camera Data taken by Sverdrup, Inc.

Thermal Image Camera data was taken by Sverdrup, Inc. of Arnold Air Force Base, Tenn. by V. A. Zaccardi, et al (Ref. 4.3) during the MNASA test series. The data of interest to this investigation which have been requested from Sverdrup, Inc./AEDC, are identified in Table 4.1. In Table 4.1 the MNASA test number and test date, instrument description, bandwidth, and time frame are noted.

Table 4.1. MNASA Test Series Thermal Image Camera Data Taken by Sverdrup, Inc.

Test No. (Date)	Instrument Description	Bandwidth (μm)	Time Frame (sec)
MNASA03 ASRM48-1 (4/10/91)	Thermovision Infrared Raster Scanning Radiometers: • AGA 782-3 • AGA 782-2	2.11 to 2.46 3.14 to 4.08	5 sec ?
MNASA04 RSRM48-2	AGA 680 Thermovision Infrared Raster Scanning Radiometer	3.41 to 4.00	?
(7/2/91)	Mitsubishi IR-5120AII Thermal Image Camera	2.23 to 2.32	?
MNASA05 ASRM48-2 (8/27/91)	AGA 680 Thermovision Scanner	3.41 to 4.00	18.6
MNASA07 SPIP48-2	AGA 680 Thermovision Scanner	3.41 to 4.00	14.6 20.0 21.5 23.4
(11/6/91)	Mitsubishi IR-5120AII Thermal Image Camera	2.23 to 2.32	15.0

4.1.1 MNASA04/RSRM48-2 Thermovision Thermal Image Camera Data

The AGA 680 Thermovision Infrared Raster scanning radiometer was used to acquire plume thermal images in the 3.41 to 4.00 μm bandwidth. These data at an unknown time slice (but assumed to be between 1 and 27 sec) are shown in Fig. 4.1. The SIRRM-II predicted radiance contour plot in the 3.41 to 4.00 μm bandwidth for the RSRM48-2 test using an SPF2 flowfield plus 2.5% carbon is shown in Fig. 4.2. The resolution of the thermal image data shown in Fig. 4.1 is not sufficient to make a conclusive comparison with the radiance prediction except that the predicted radiance is qualitatively in the ball park, and the maximum predicted radiance near the plume centerline at the nozzle exit plane of 0.721 watts/cm^2/sr is approximately 42% of the maximum measured value of 1.2497 watts/cm^2/sr.

The Mitsubishi IR-5120AII thermal image camera was used to acquire plume thermal images in the 2.23 to 2.32 μm bandwidth. These data, also at an unknown time slice, are shown in Fig. 4.3. The SIRRM-II predicted radiance contour plot in the 2.23 to 2.32 μm bandwidth is shown in Fig. 4.4 for comparison with the measurement. In the comparison of this prediction to the measurement, the maximum predicted radiance of 0.350 watts/cm^2/sr near the plume centerline at the nozzle exit plane compares within 9.7% of the measured maximum value of 0.3875 watts/cm^2/sr at the same location. If the 2.5% carbon that was added to the SPF2 cycle 1 flowfield is removed, as would be the case in a standard SPF2 flowfield, the resulting SIRRM-II radiance contour prediction is shown in Fig. 4.5. In this case the maximum predicted radiance of 0.184 watts/cm^2/sr is a factor of 2.1 below the measured maximum. The comparison of the SIRRM-II predicted spectral radiance to the CVF spectrometer measurement for wavelengths from 0.7 to 5.7 μm at a plume centerline location of 0.686 m (or 2.24 nozzle exit radii) downstream of the nozzle exit plane for SPF2 cycle 1 flowfields with and without 2.5% carbon has been shown in Ref. 4.4. This figure, Fig. 4.6, is included here to demonstrate that if the flowfield used in the SIRRM-II plume radiance simulation produces a reasonable match with the spectrometer data for at least one axial position then the predicted magnitude of the maximum radiance will compare reasonably well with the maximum measured radiance as
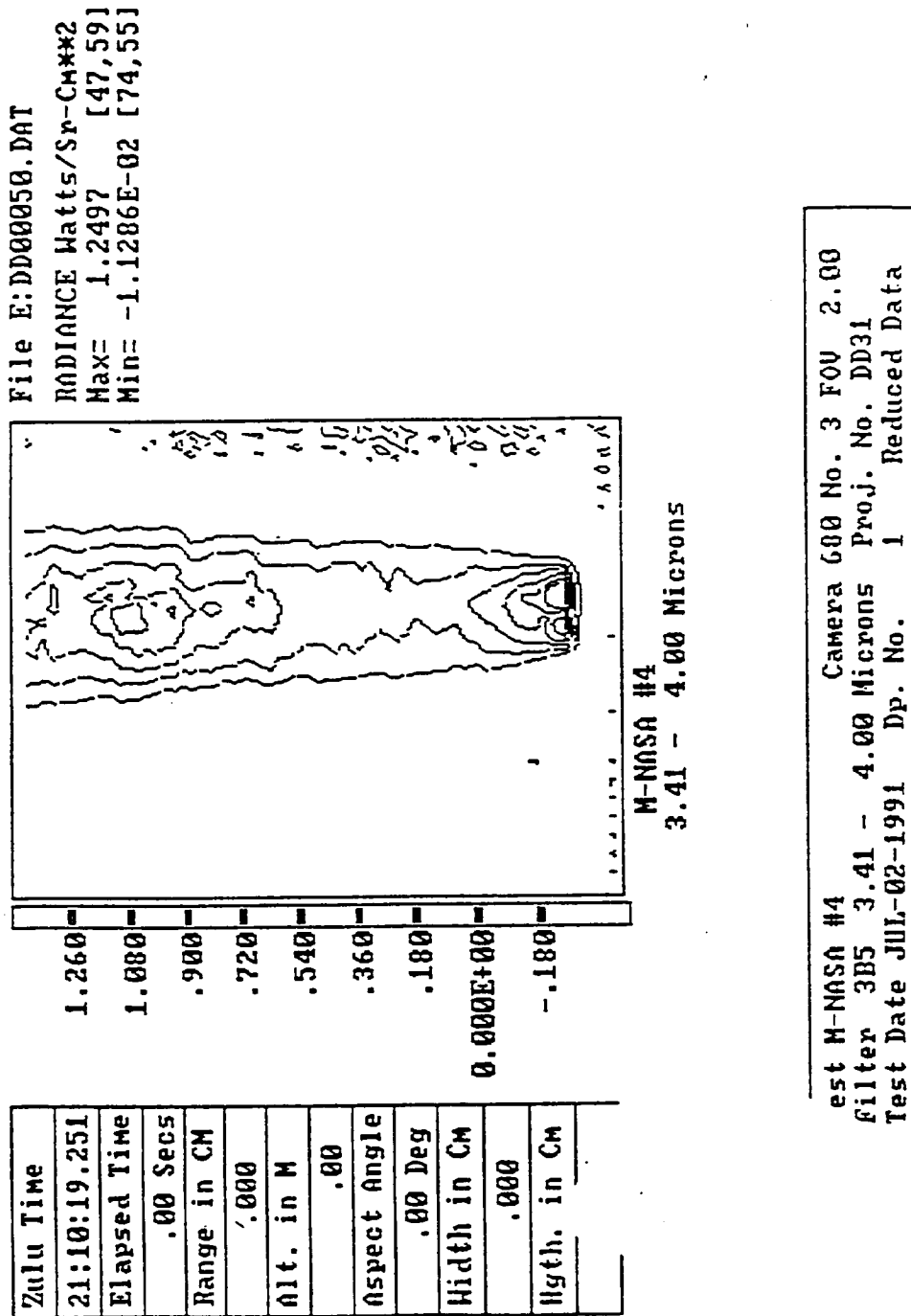
Fig. 4.1 MNASA04/RSRM48-2 Thermovision 680 Scanning Radiometer Data, 3.41 to 4.00 μm

SIRRM-II MOD 13   12-07-90   RUNID = 0.
RSRM48-2-3.4 to4.0um-SPF2MAP +2.5% carbon -ASPC=87
15 FEB 1994
APPARENT INBAND ISORADIANCE (W/SR/CM**2)
FILTER # 1

PROJECTED AXIAL POSITION X/RJ

R_j = 30.612 cm
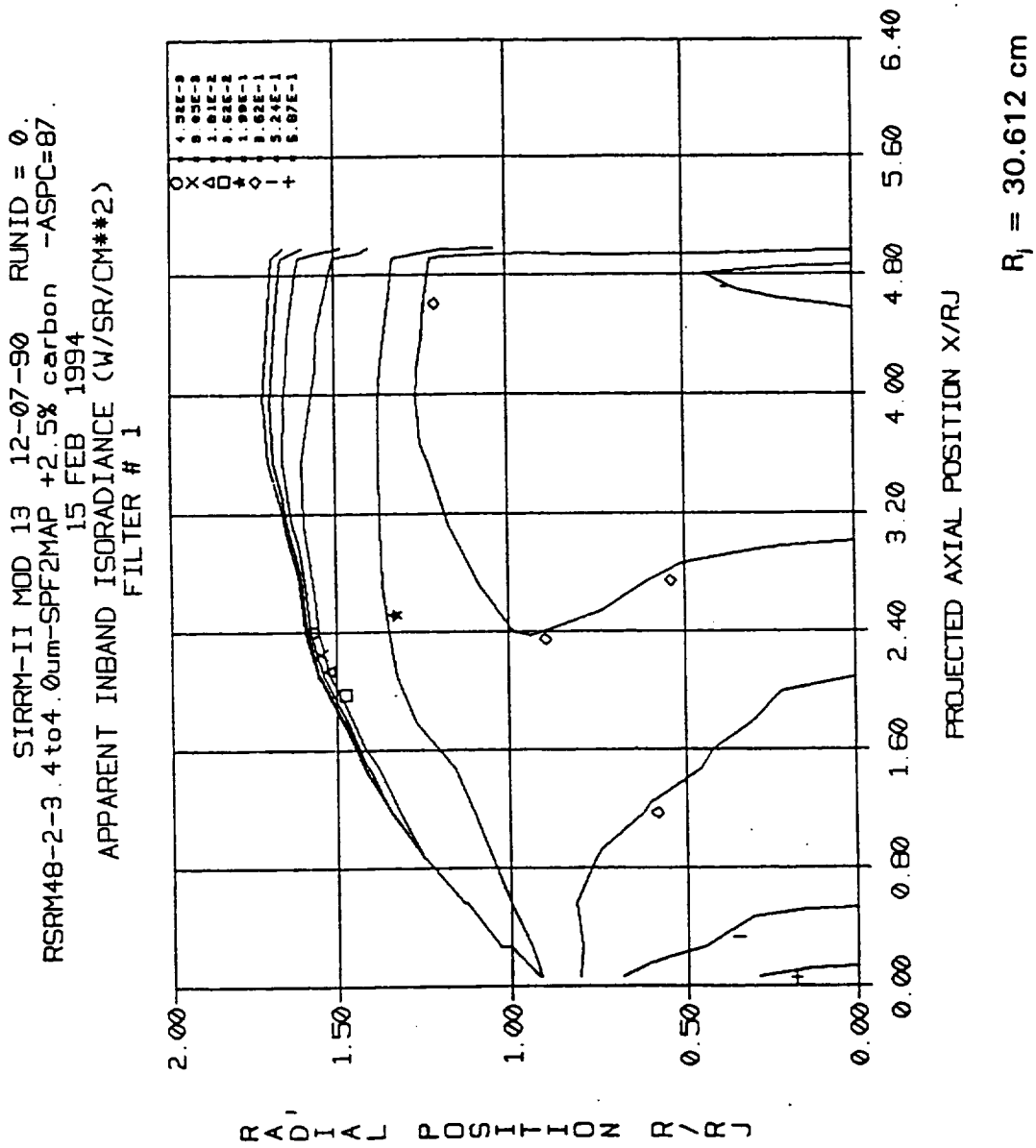
Fig. 4.2   MNASA/04/RSRM48-2 SIRRM-II Predicted Radiance Contours, 3.41 to 4.00 μm, SPF2 Flowfield plus 2.5% Carbon, at t=5 sec
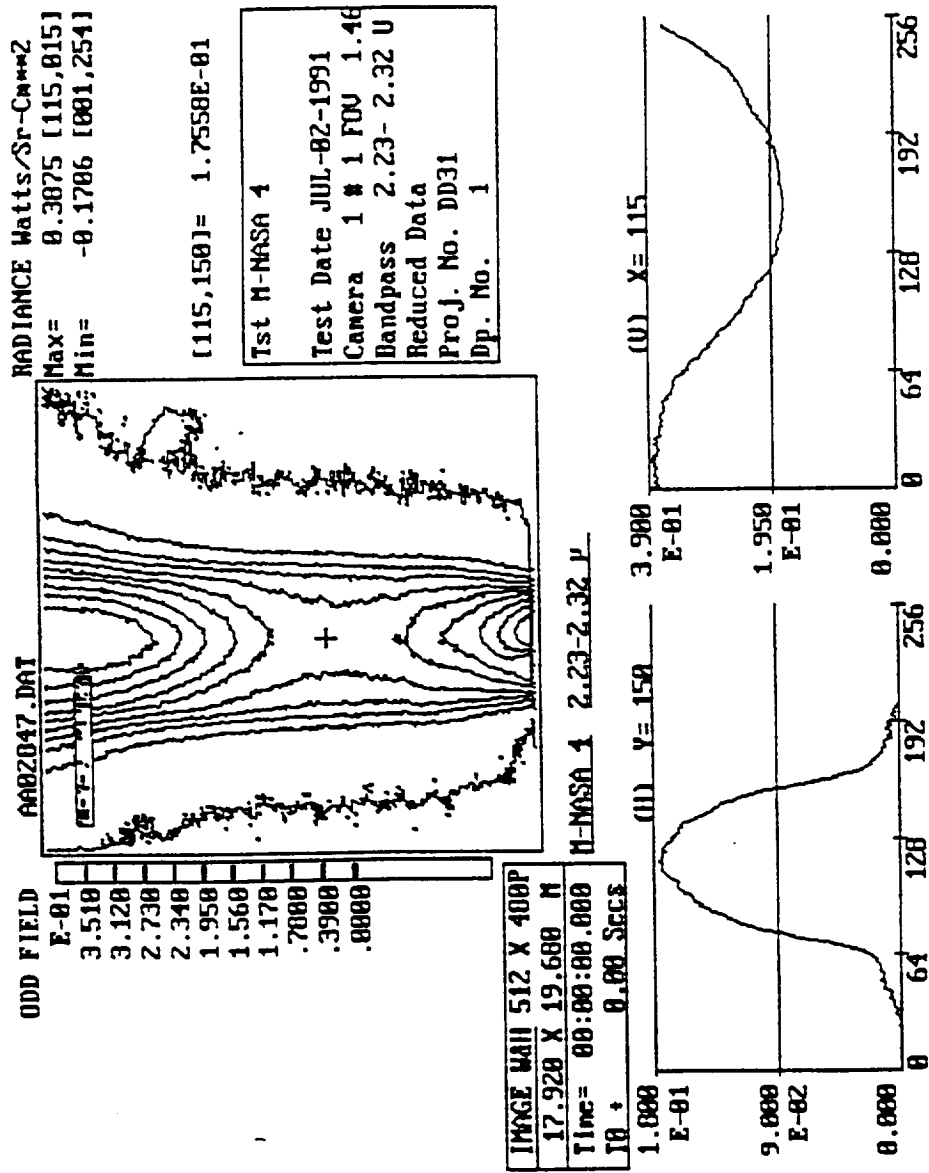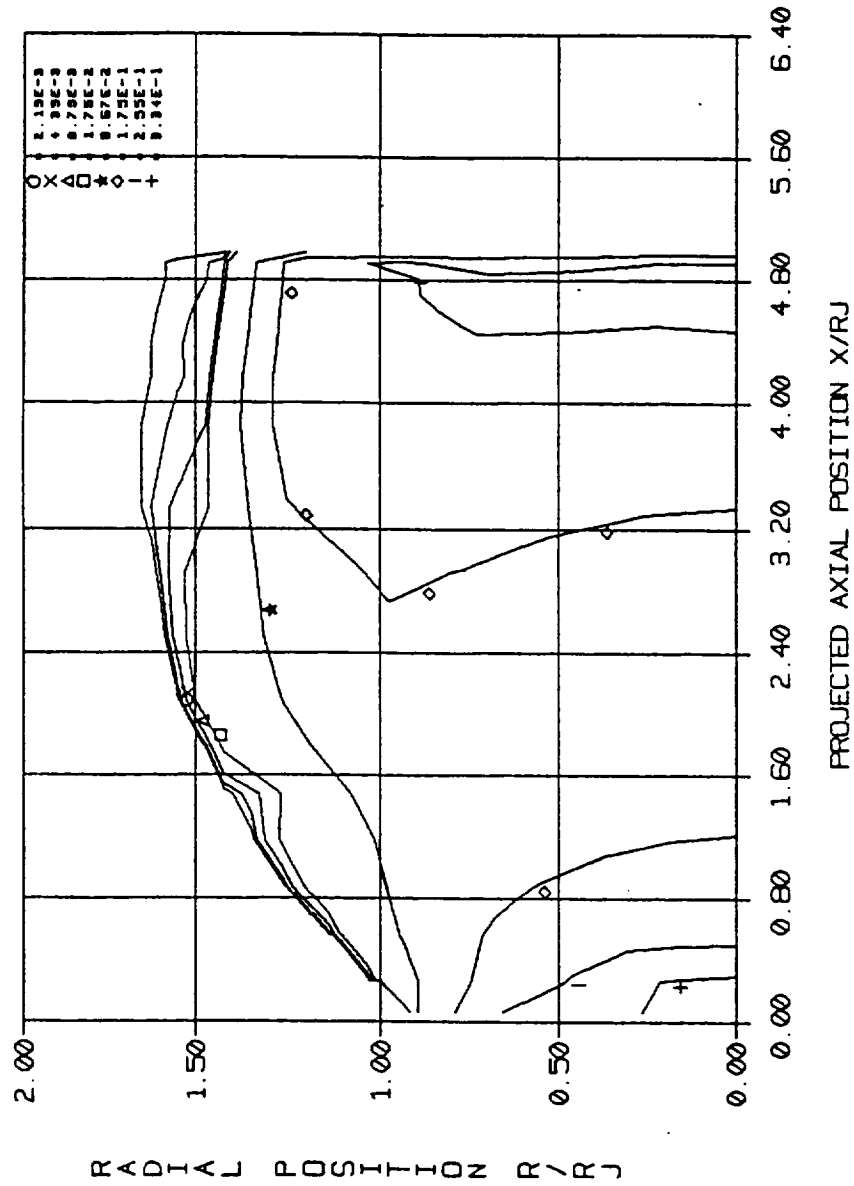
Fig. 4.3   MNASA4/RSRM48-2 Mitsubishi IR-5120AII Thermal Image Camera Data, 2.33 to 2.32 μm

Fig. 4.4   MNASA04/RSRM48-2 SIRRM-II Predicted Radiance Contours, 2.23 to 2.32 μm, SPF2 Flowfield plus 2.5% Carbon, at t=5 sec

SIRRM-II MOD 13   12-07-90   RUNID = 0.
RSRM48-2-2.2to2.3um-SPF2MAP +0.0% carbon -ASPC=87
15 FEB 1994
APPARENT INBAND ISORADIANCE (W/SR/CM**2)
FILTER # 1

PROJECTED AXIAL POSITION X/RJ
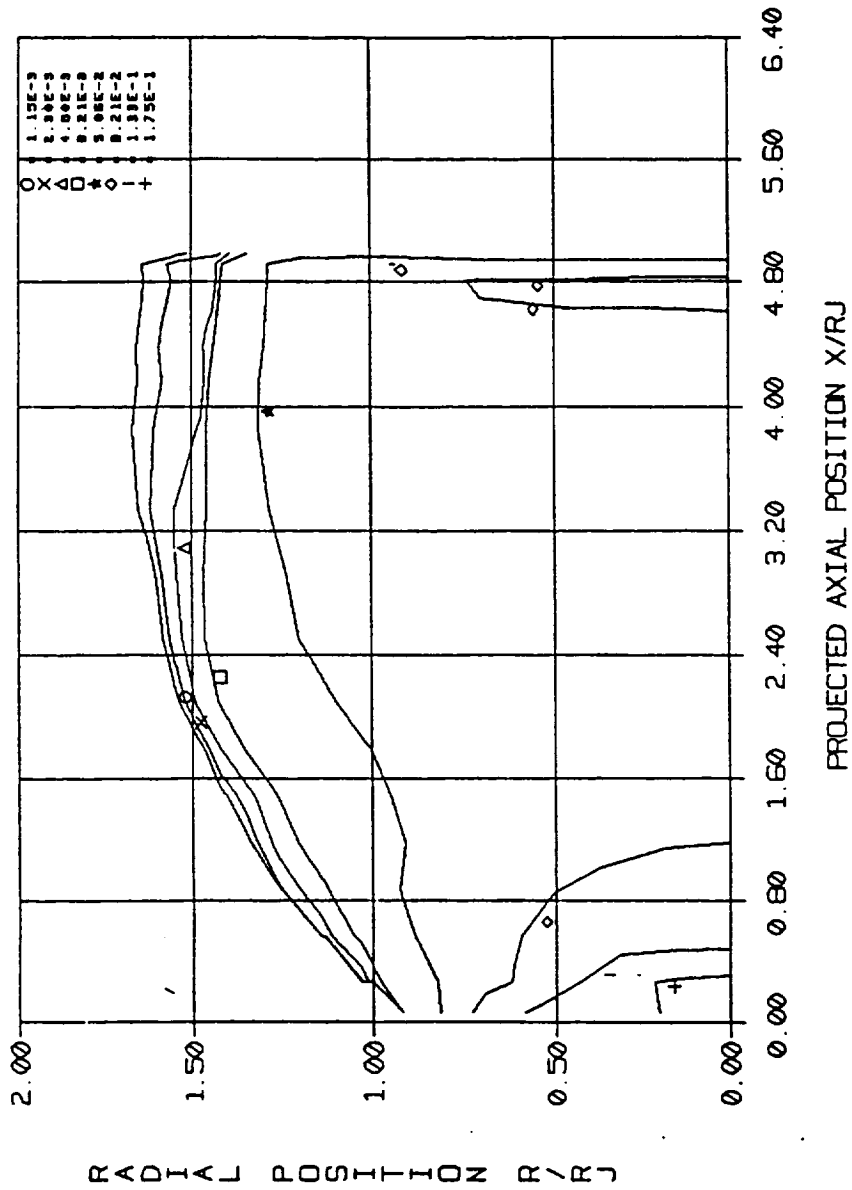
R_j = 30.612 cm

Fig. 4.5   MNASA04/RSRM48-2 SIRRM-II Predicted Radiance Contours, 2.23 to 2.32 μm, SPF2 Flowfield - No Carbon, at t=5 sec
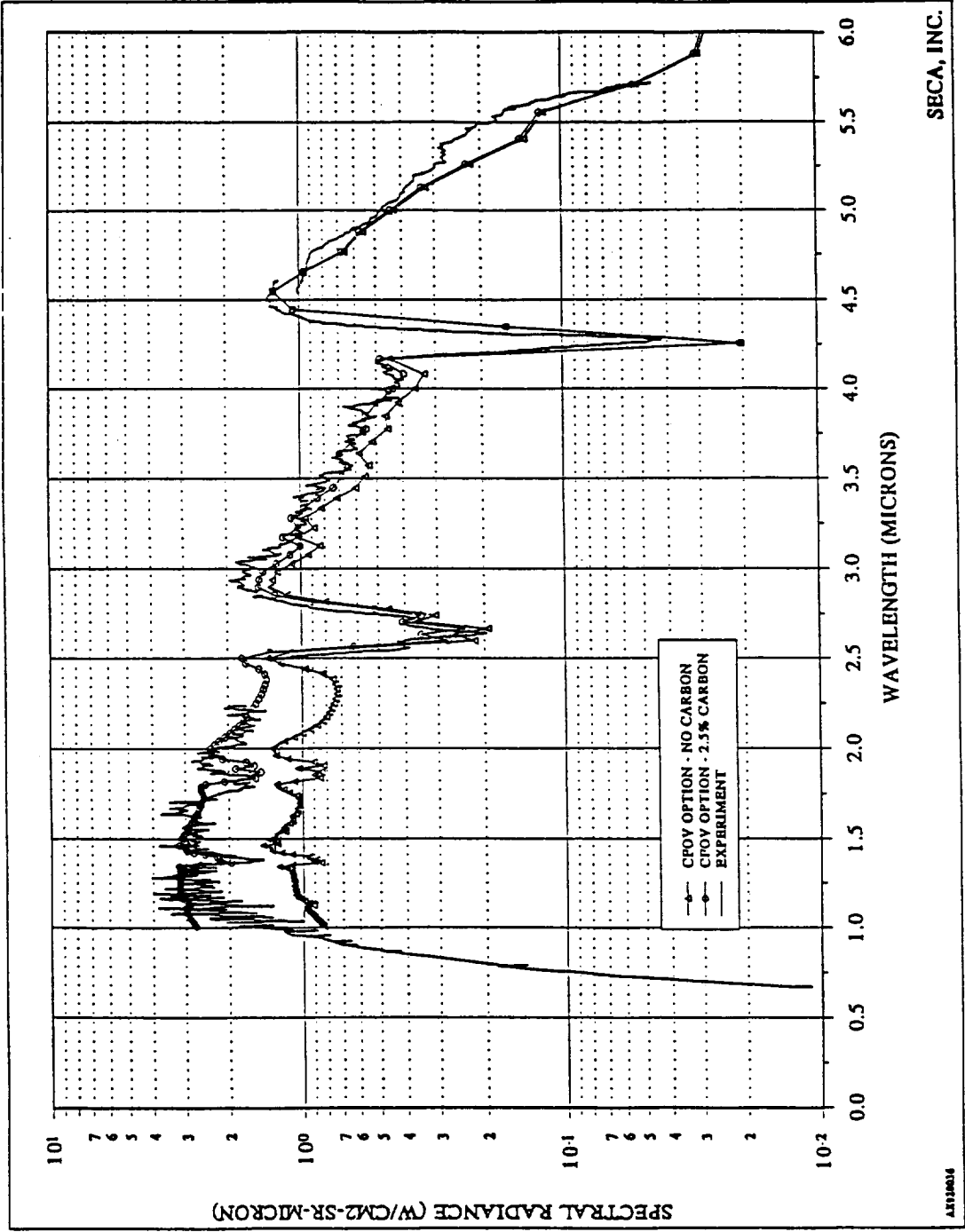
Fig. 4.6   MNASA02/RSRM48-1 SIRRM-II Predicted Plume Radiance and CVC Spectrometer Data, SPF2 Cycle 1 Flowfield, $x/r_j = 2.24$, at t=5 sec

shown in the comparison of Figs. 4.3 and 4.4.

4.1.2 MNASA03/ASRM48-1 Thermovision Thermal Image Camera Data

The AGA 782-3 and 782-2 Thermovision infrared raster scanning radiometers were used to acquire plume thermal images in the 2.11 to 2.46 μm and 3.14 to 4.08 μm bandwidths, respectively. The images from the AGA 782-2 scanning radiometer were saturated at motor ignition and therefore not usable for this analysis. The isoradiance data acquired by the AGA 782-3 scanning radiometer at t = 5.02 sec is shown in Fig. 4.7. In Fig. 4.7, which is a black and white representation of the radiance field, it is difficult to determine contour levels and the location of the maximum radiance level. However, the maximum measured radiance level appears to occur near the plume centerline at the nozzle exit plane and then the plume centerline radiance decreases roughly linearly downstream of the nozzle exit plane.

The SIRRM-II predicted radiance contour plot in the 2.11 to 2.46 μm bandwidth for the ASRM48-1 test at t = 5 sec is shown in Fig. 4.8. In this analysis of the ASRM48-1, the flowfield input to the SIRRM-II radiation code was generated using the FDNSEL two-phase Navier Stokes flow solver. The FDNSEL flowfield for the ASRM48 motors has been described previously in Ref. 4.5, and is used here in preference to an SPF2 flowfield because the FDNSEL flowfield best matches the CVF spectrometer data for the ASRM48 test series. Comparison of the measured and predicted radiance in Figs. 4.7 and 4.8, respectively, reveals that the predicted maximum radiance level of 2.55 watts/cm^2/sr is 12.1% higher than the measured maximum value of 2.275 watts/cm^2/sr on the plume centerline at the nozzle exit plane; but is located on the plume centerline between 1.60 and 2.00 m (5.1 nozzle exit radii) downstream of the nozzle exit plane. This characteristic of the ASRM48 motors will be demonstrated in the comparison of predicted to measured radiance for other ASRM48 motors presented later in this section.

4.2 MNASA Test Series Thermal Image Camera Data Taken by NASA/MSFC

Thermal image camera data was taken by Don Bryan(ED64) of NASA/MSFC using the Inframetrics 600 thermal image camera for tests MNASA04 through MNASA12, excluding MNASA09 (Ref. 7). These data for MNASA04 and MNASA06 and a bandwidth of 8 to 12 μm for a single image which is the average of frames from 5.0 to 5.5 sec in time are presented herein.

4.2.1 MNASA04/RSRM48-2 Inframetrics Thermal Image Camera Data

The Inframetrics 600 thermal image camera was used to obtain plume thermal images in the 8 to 12 μm bandwidth for the RSRM48-2 test. These data were taken by Don Bryan (ED64) of NASA/MSFC (Ref. 4.6) and provided to us in digital format. Good resolution of the visual images has been obtained by averaging several time slices of data together to produce a single composite time slice. In this case however, a single frame at the 5.0 sec time slice is used. Plume temperature (°F) and radiance (watts/cm^2/sr) contours from the Inframetrics 600 camera at the 5 sec single time frame for the RSRM48-2 test are shown in Figs. 4.9 and 4.10, respectively. The temperature contours shown in Fig. 4.9 assume an emissivity of 1.0 which is a questionable assumption for the assessment of the temperature field of two phase solid motor exhaust plumes. The radiance contours shown in Fig. 4.10 were reduced from the actual radiance measured by the Inframetrics 600 camera. The instrument was calibrated to a maximum temperature of 1345°C (2453°F) and a linear relationship is assumed above this temperature.

The SIRRM-II predicted plume radiance contour plot for the RSRM48-2 using an SPF2 flowfield plus 2.5% carbon is shown in Fig. 4.11. Comparing the predicted radiance contours in Fig. 4.11 with the thermal image measurements in Fig. 4.10 reveals that the predicted maximum plume centerline radiance at the nozzle exit plane of 0.557 watts/cm^2/sr is 7.1% higher than the measurement maximum of 0.52 watts/cm^2/sr at the same location.
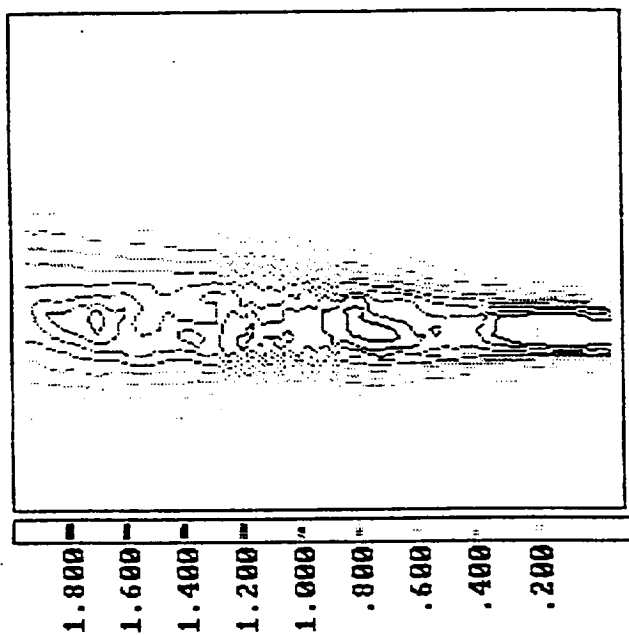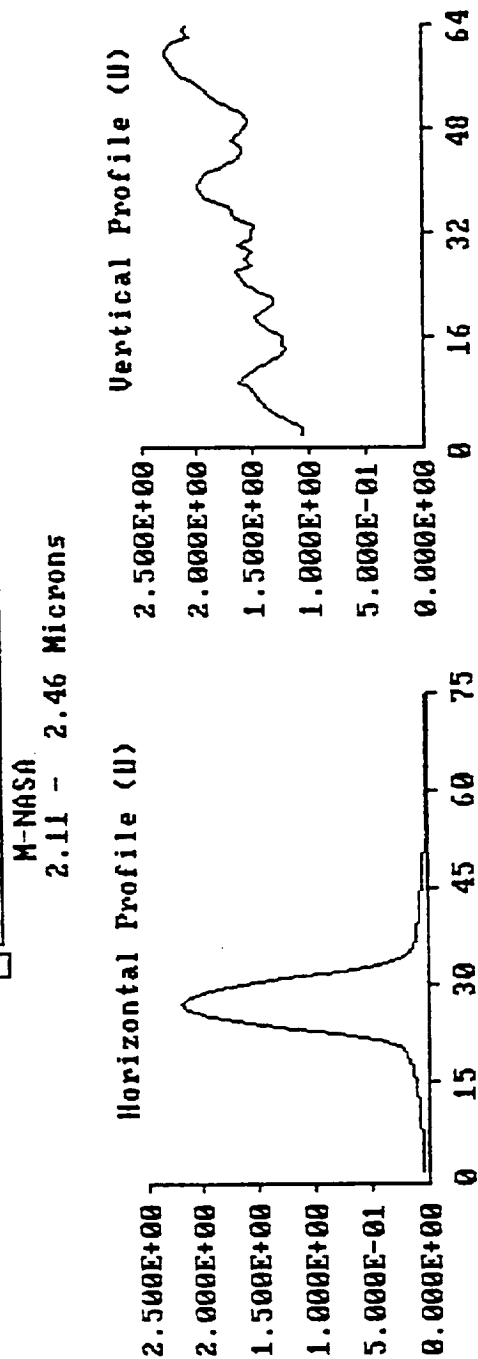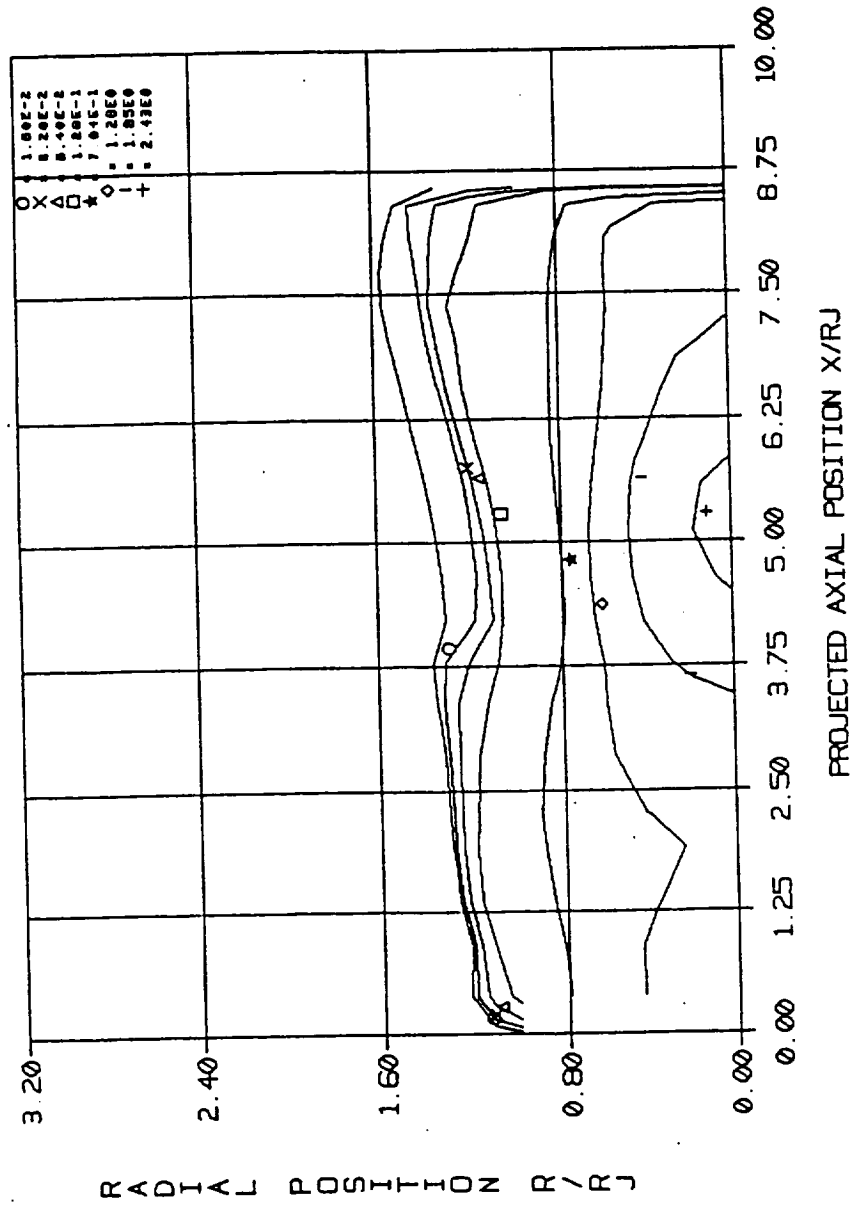
Fig. 4.7 MNASA03/ASRM48-1 Thermovision AGA 782-3 Scanning Radiometer Data, 2.11 to 2.46 µm, at t=5.02 sec

SIRRM-II MOD 13 12-07-90 RUNID = 0.
ASRM48-1-2.1 to 2.5um-FDNSMAP-no carbon-ASPC=87.
15 FEB 1994
APPARENT INBAND ISORADIANCE (W/SR/CM**2)
FILTER # 1

R$_j$ = 34.854 cm

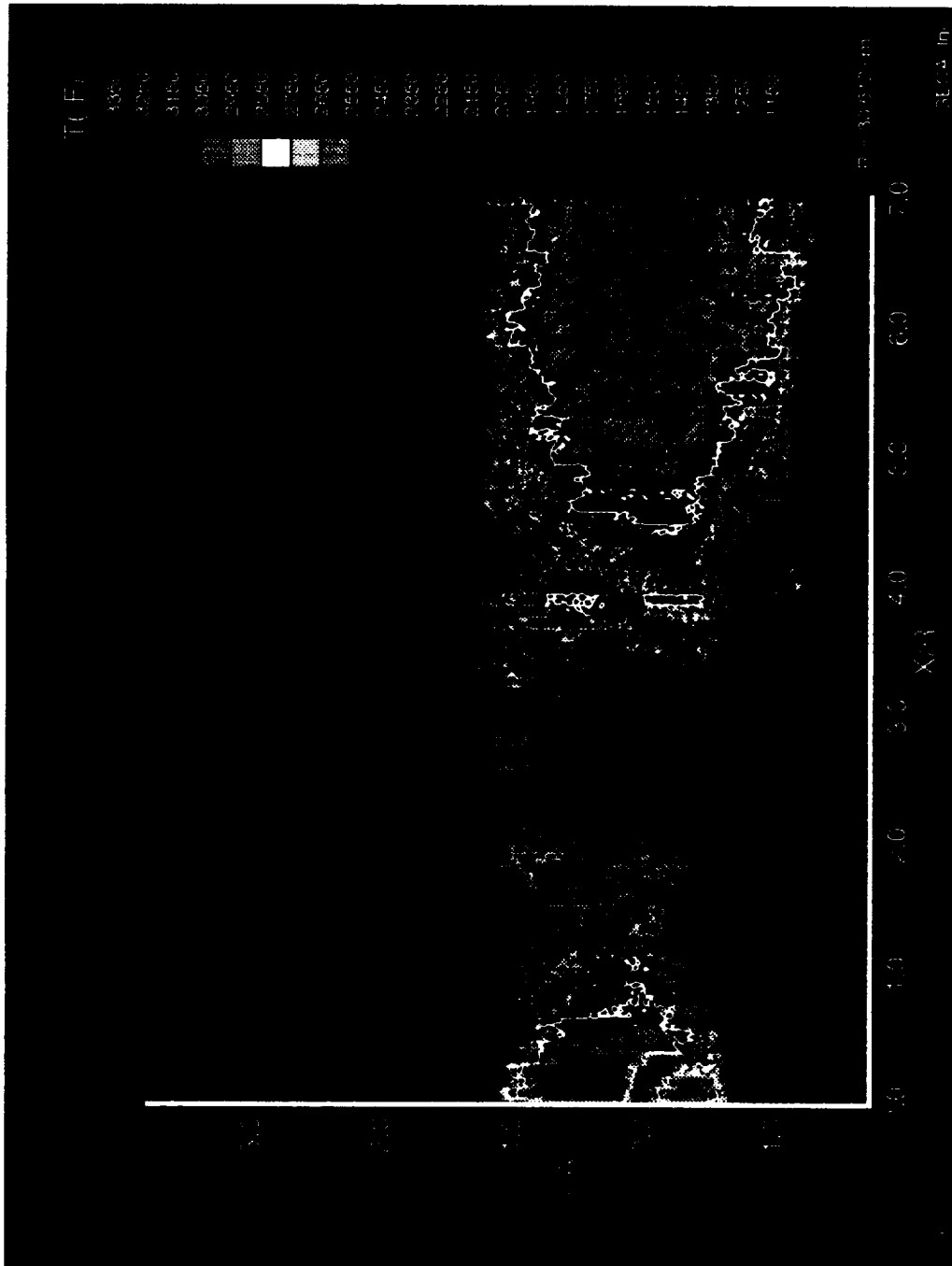Fig. 4.8 MNASA03/ASRM48-1 SIRRM-II Predicted Radiance Contours, 2.11 to 2.46 μm, FDNSEL Flowfield, at t=5 sec

Fig. 4.9   MNASA04/RSRM48-2 Inframetrics 600 Thermal Image Camera Temperature Contours (°F), 8 to 12 μm, Emissivity = 1.0, single frame at t=5.0 sec
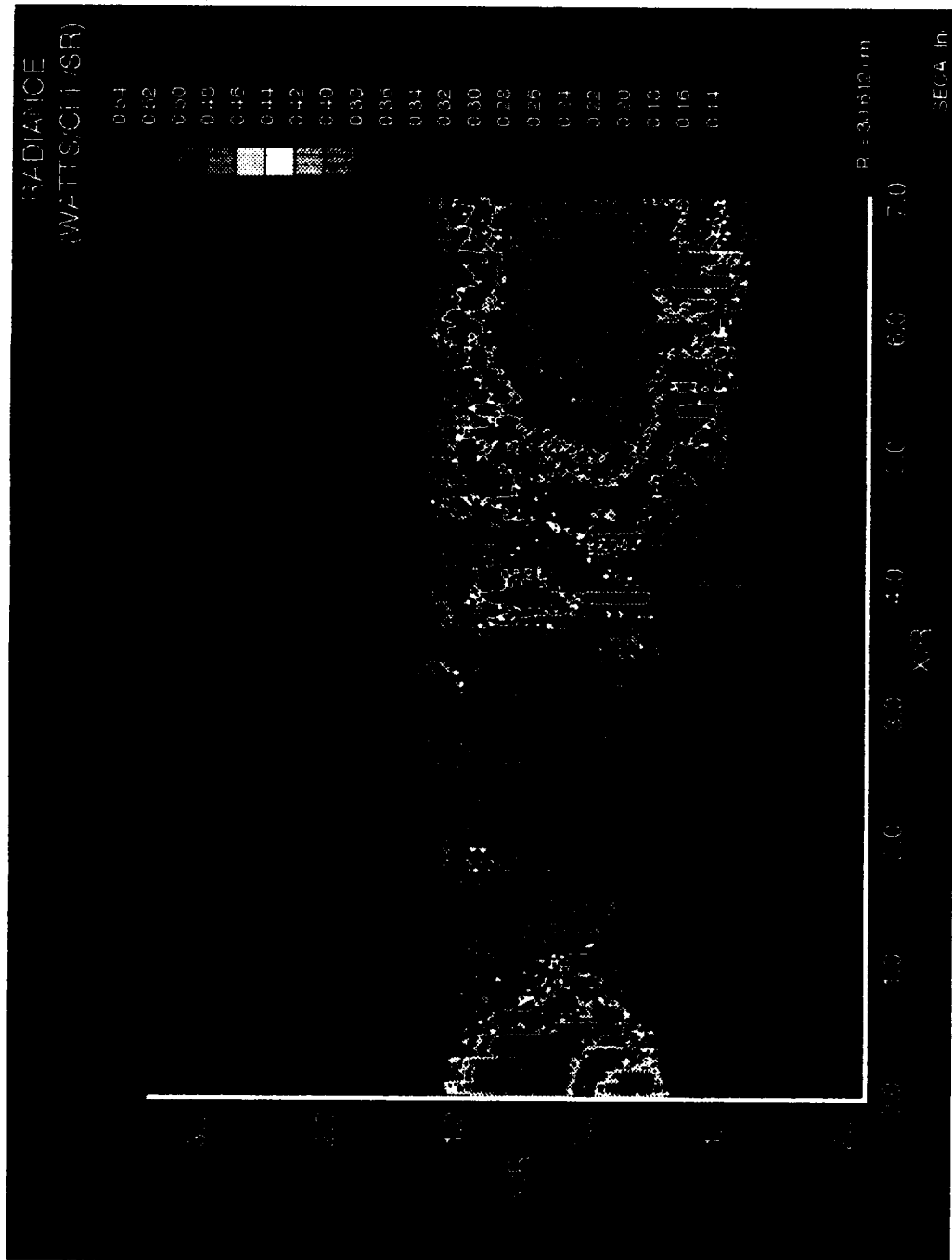
Fig. 4.10   NNASA04/RSRM48-2 Inframetrics 600 Thermal Image Camera Radiance
Contours (watts/cm²/sr), 8 to 12 μm, single frame at t=5.0 sec
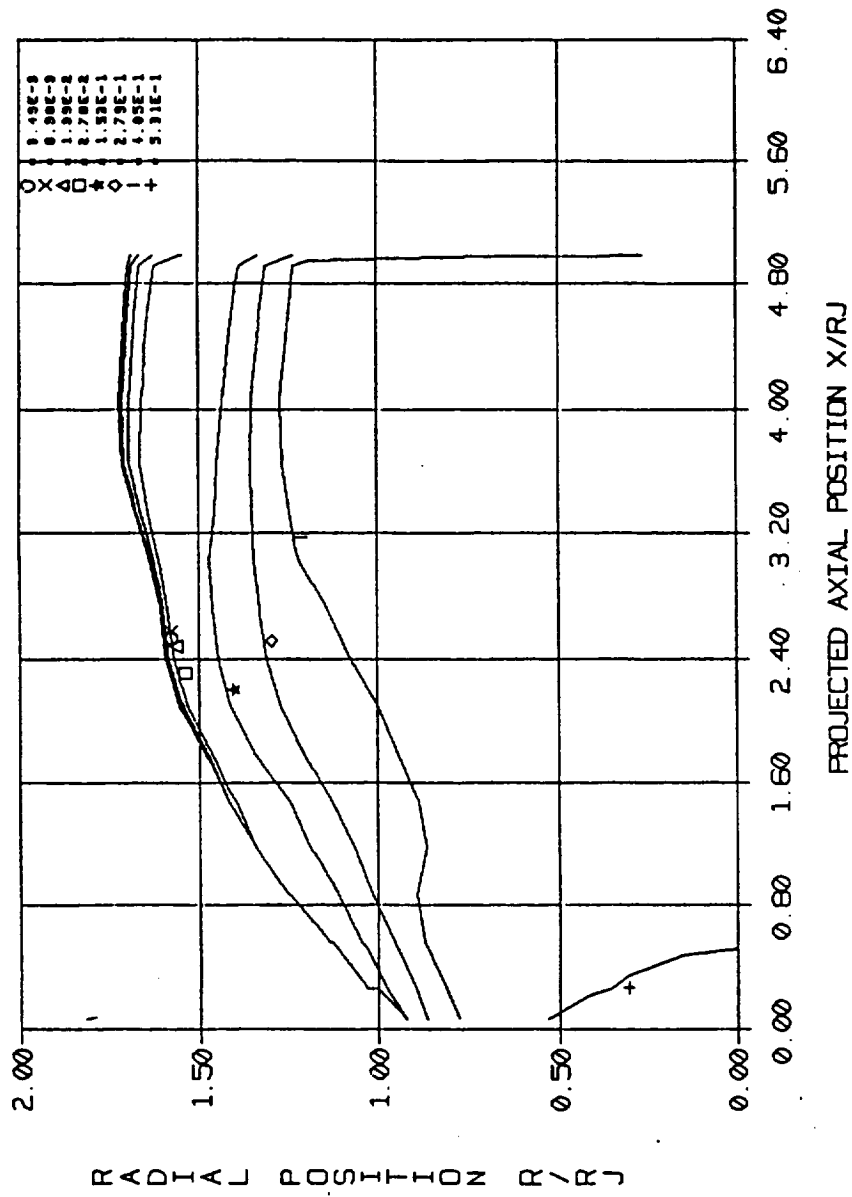
Fig. 4.11   MNASA04/RSRM48-2, SIRRM-II Predicted Radiance Contours, 8 to 12 μm, SPF2 Flowfield plus 2.5% Carbon, at t=5 sec

4.2.2 MNASA06/ASRM48-3 Inframetrics Thermal Image Camera Data

The inframetrics 600 thermal image camera was used to obtain plume thermal images in the 8 to 12 μm bandwidth for the ASRM48-3 test. These data were taken by Don Bryan (ED64) of NASA/MSFC and were digitized and provided to SECA, Inc. for this analysis (Ref. 4-6). The thermal image is the average of frames from 5.0 to 5.5 sec which provides a composite image at the 5.0 sec time frame. Plume temperature ($^{\circ}$F) and radiance (watts/cm^2/sr) contours from the Inframetrics 600 camera are shown in Figs. 4.12 and 4.13, respectively. The maximum measured radiance level of approximately 0.642 watts/cm^2/sr shown in Fig. 4.13 is clearly at the plume centerline at the nozzle exit plane and the centerline radiance decreases approximately linearly for the first two nozzle exit radii downstream of the nozzle exit plane.

The SIRRM-II predicted radiance contours for the ASRM48-3 test at t = 5 sec using a cycle 1.0 FDNS and cycle 2 SPF2 flowfields are shown in Figs. 4.14 and 4.15, respectively. Using the FDNS flowfield (Fig. 4.14), the predicted maximum plume centerline radiance of 0.621 watts/cm^2/sr occurs at approximately 5.1 nozzle exit radii, while the predicted nozzle exit plane centerline radiance is 0.599 watts/cm^2/sr which is 6.7% lower than the measurement maximum of 0.642 watts/cm^2/sr at the same location. Using the SPF2 cycle 2 flowfield the maximum predicted radiance (Fig. 4.15) of 0.633 watts/cm^2/sr occurs at the plume centerline at the nozzle exit plane and is 1.4% below the measured maximum value at the same location.

A comparison of predicted and measured ASRM48-3 plume centerline radiance at t = 5 sec is shown in Fig. 4.16. In this figure the SIRRM-II plume centerline radiance predictions using the FDNS, SPF2 cycle 2, and SPF2 cycle 1 flowfield methodologies are compared against the measured centerline radiance. The FDNSEL and SPF2 cycle 2 predictions are within 10% above the measurement from 0.5 to 7.5 nozzle exit radii downstream, and the SPF2 cycle 1 prediction is within 13% below the measurement for the first four nozzle exit radii. All of the centerline radiance predictions shown in Fig. 4.16 fall within the generally accepted measurement accuracy of $\pm$20% for thermal imaging systems of this type.
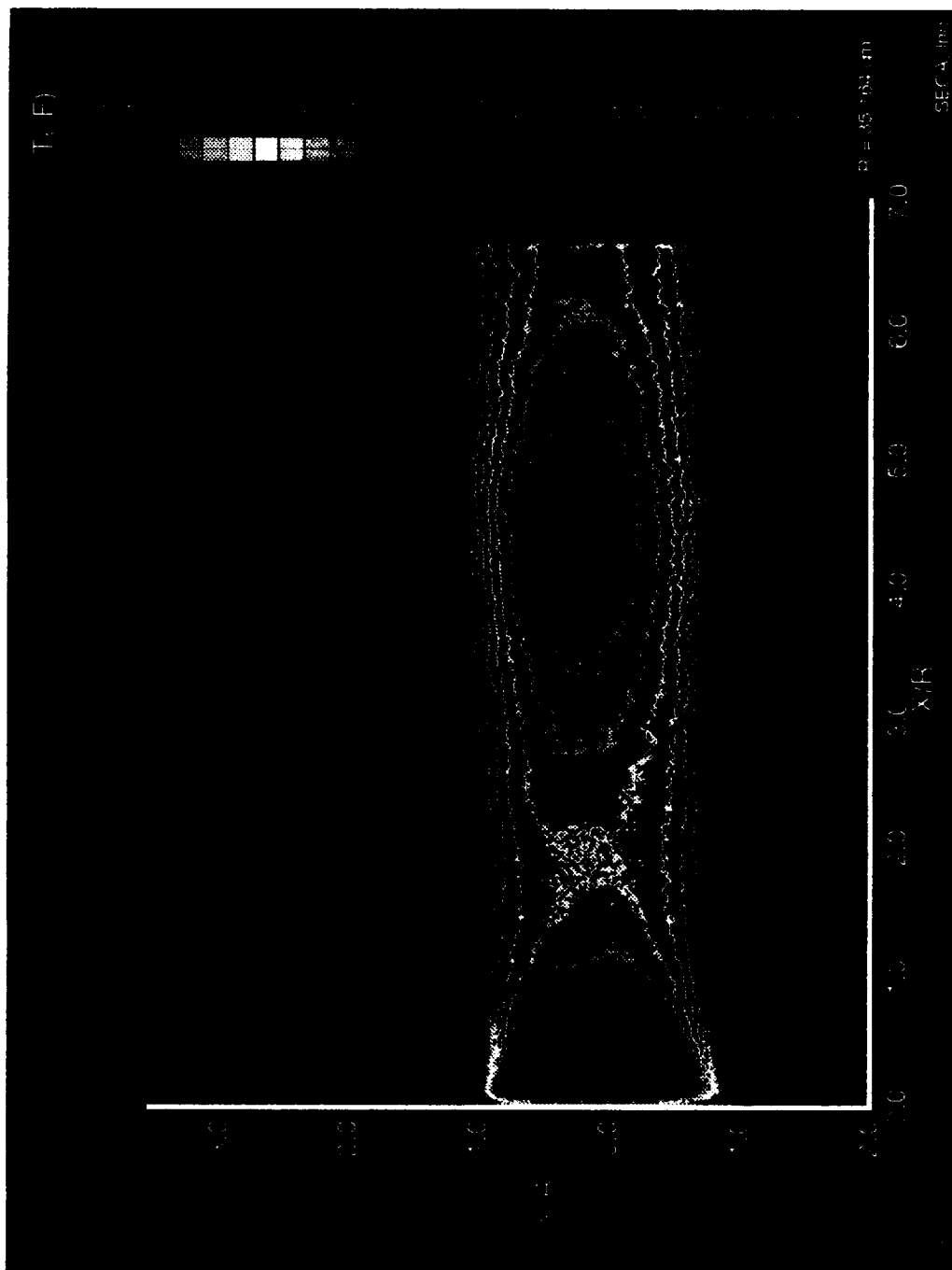
Fig. 4.12   MNASA06/ASRM48-3 Inframetrics 600 Thermal Image Camera Temperature Contours (°F), 8 to 12 μm, Emissivity = 1.0, at t = 5.0 to 5.5 sec
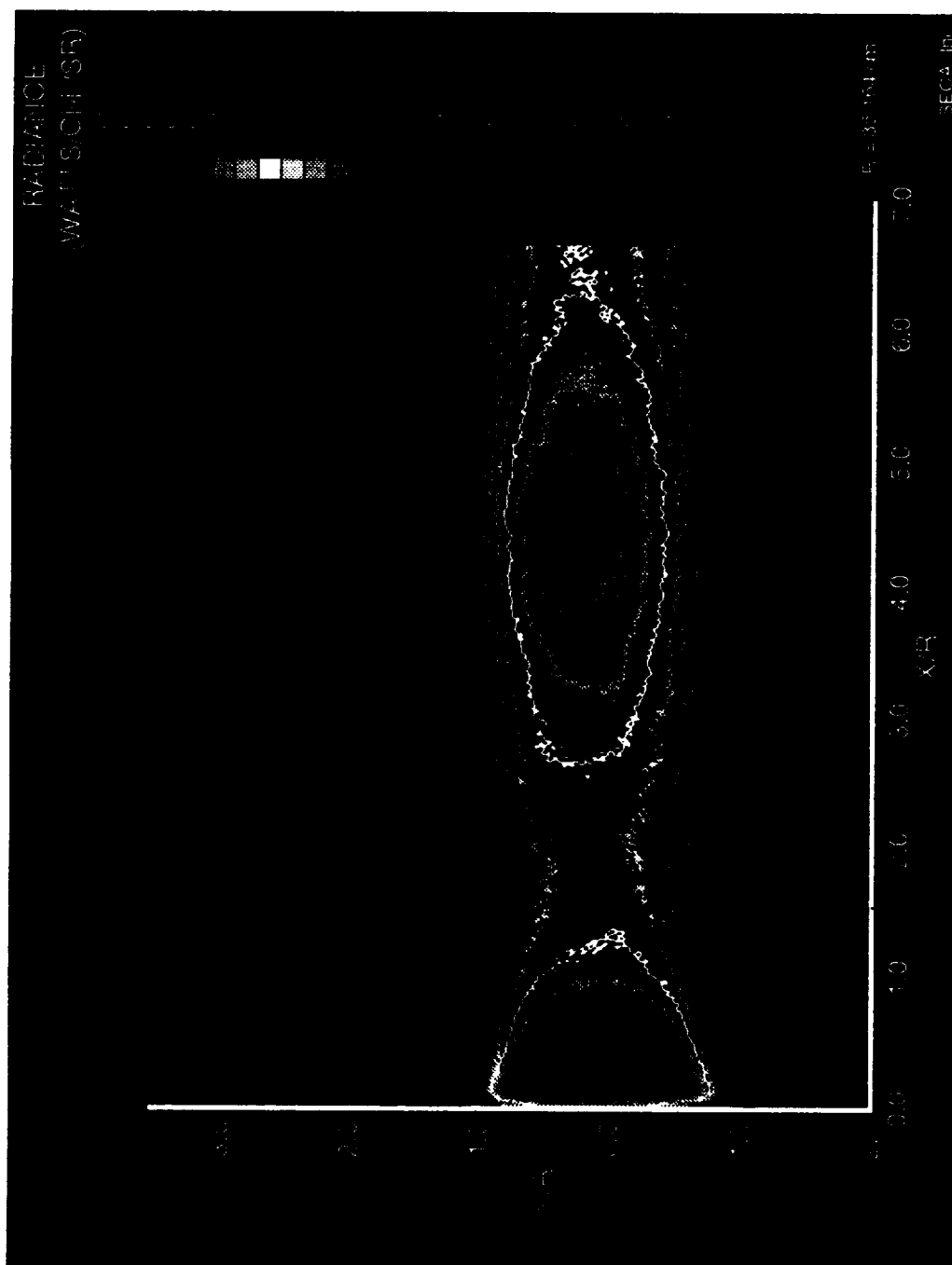
Fig. 4.13   MNASA06/ASRM48-3 Inframetrics 600 Thermal Image Camera Radiance
Contours (watts/cm^2/sr), 8 to 12 μm, at t = 5.0 to 5.5 sec

SIRRM-II MOD 13   12-07-90   RUNID = 0.
ASRM48-3-8.to 12.um-FDNSEL   map -no carbon-ASPC=87.
14 FEB 1994
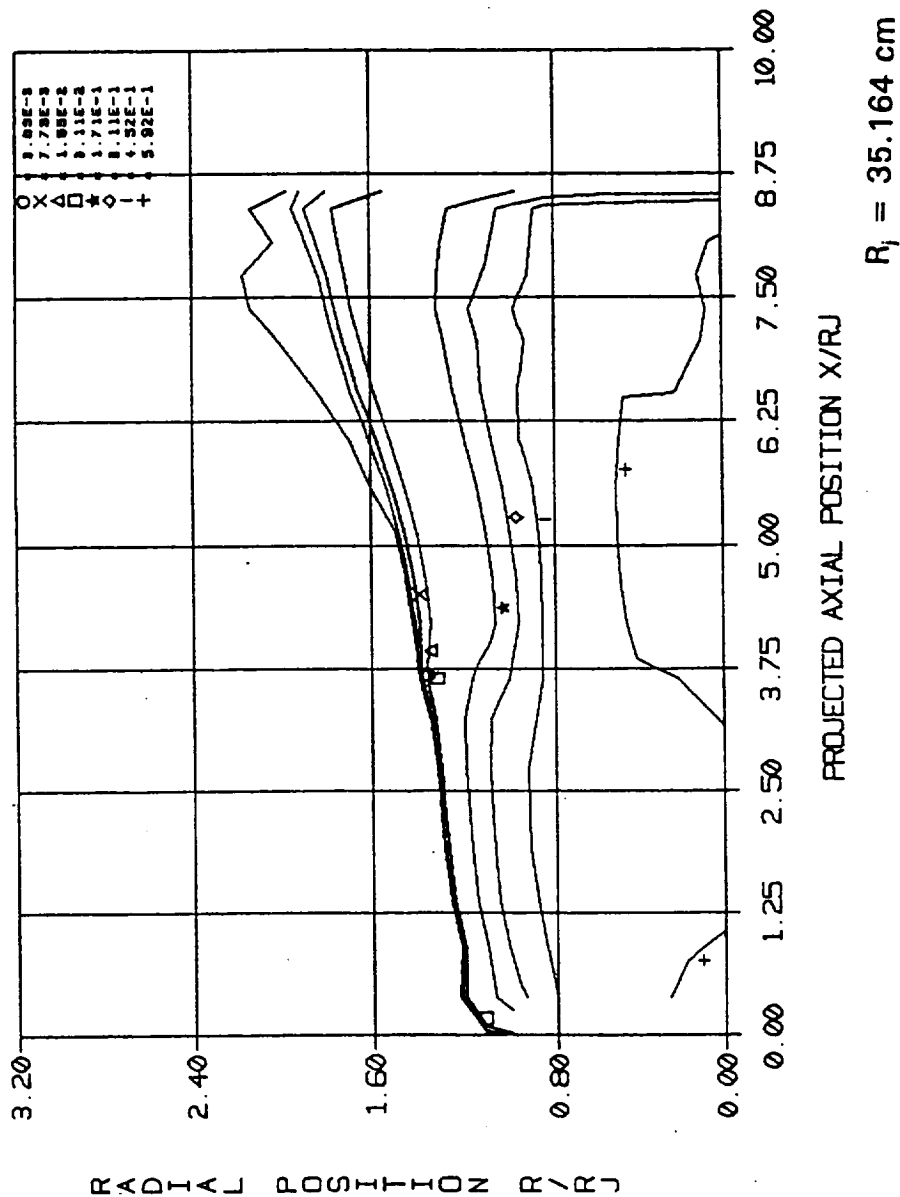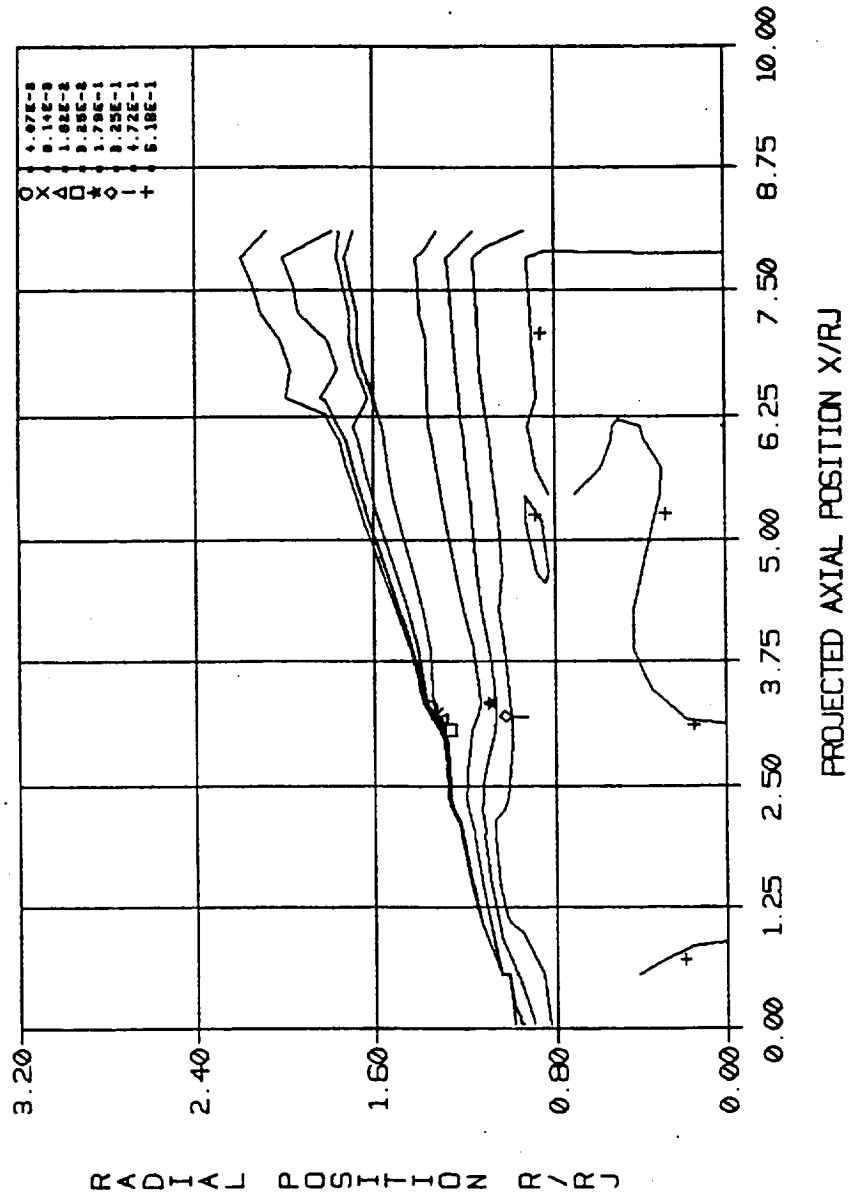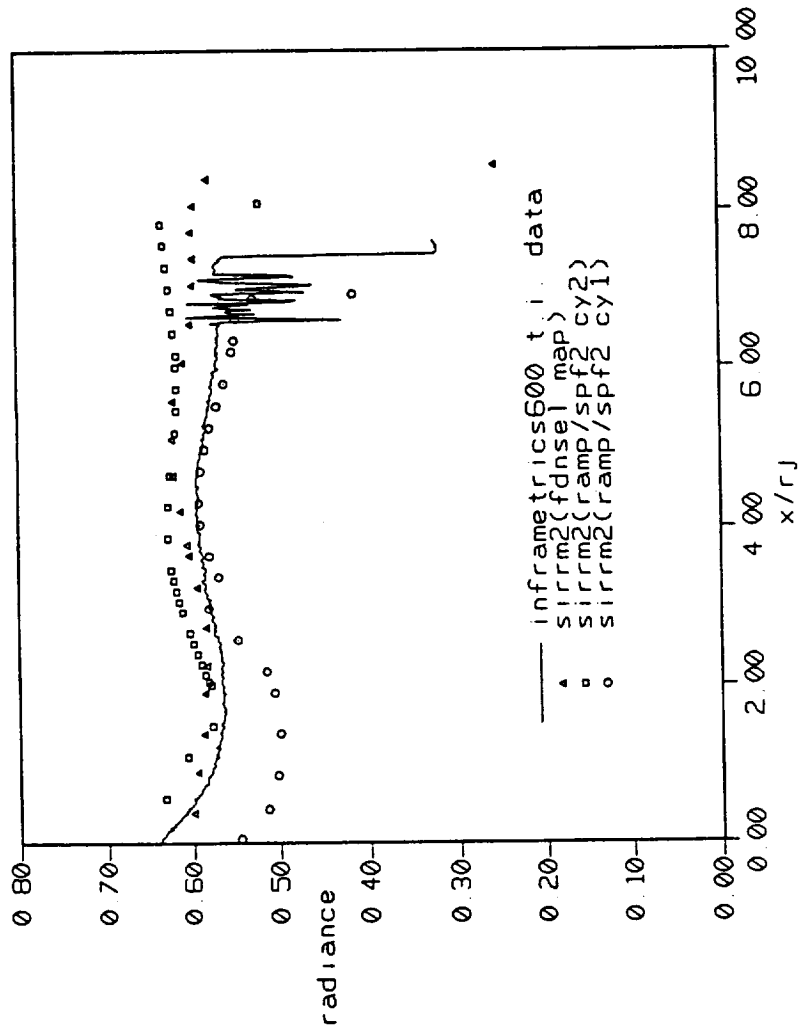APPARENT INBAND ISORADIANCE (W/SR/CM**2)
FILTER # 1

PROJECTED AXIAL POSITION X/RJ

$R_j = 35.164$ cm

Fig. 4.14   MNASA06/ASRM48-3 SIRRM-II Predicted Radiance Contours, 8 to 12 μm, FDNSEL Flowfield, at t = 5 sec

Fig. 4.15   MNASA06/ASRM48-3 SIRRM-II Predicted Radiance Contours, 8 to 12 μm, SPF2 Cycle 2 Flowfield, at t - 5 sec

$R_j = 35.164$ cm

asrm48-3 - 8 to 12 um - sirrm2 - no carbon - aspc= 87 deg
centerline radiance(w/cm2/sr) vs axial position

Fig. 4.16 MNASA06/ASRM48-3 Centerline Plume Radiance Comparison, 8 to 12 μm, at t = 5 sec

In the wavelength regions where MNASA thermal image data is available (2.1 to 2.5 μm, 3.4 to 4.0 μm, and 8 to 12 μm), these data provide another valuable method of evaluating the existing solid motor plume radiation prediction capability. However, the bandwidth where solid particulate radiation dominates (1.0 to 2.0 μm) has not been covered by the available thermal image measurements. Thermal image measurements in the 1.0 to 2.0 μm bandwidth could provide a better understanding of the complete picture of solid motor radiation.

5.0 CONCLUSIONS AND RECOMMENDATIONS

Based on the results of the research reported herein and on collateral work done by other investigators, the following conclusions and recommendations are offered.

Conclusions:

1.   The Cycle 2 flowfield and particulate properties predictions when used with current optical property data for Al_2O_3 provide acceptable estimates for SRM axisymmetric rocket plume base heating when used with a Monte Carlo radiation analysis.

2.   The generalized two-flux radiation model in the NOZZRAD code coupled with the view factor capability of the RAVFAC code provides a practical alternative to the Monte Carlo analysis and a convenient test vehicle for evaluating details of particulate/gas radiation analyses.

3.   The differences between the one-dimensional beam predictions made with the SIRRM and NOZZRAD codes requires further investigation. These differences are due to: (1) the method used for interpolation in Al_2O_3 optical data tables, and (2) the method of coupling the particulate and gaseous radiation in specified wavelength regions.

4.   The method of spherical harmonics as developed herein appears to offer a practical alternative to the Monte Carlo analysis, but much more verification needs to be performed with this code before it is mature enough to be used for design purposes.

5.   The FDNS code with particle tracking has been shown to give comparable predictions to the two-phase RAMP code for SRM nozzle flows. Boundary conditions for the particle/gas mixture entering the nozzle are currently specified arbitrarily. A more rigorous analysis of the interior ballistics of the SRM grain should be developed and validated to improve the accuracy and utility of both of these flowfield codes. Additional analyses of SRM plumes need to be made with the FDNS code to validate this code to the same level as the SPF/2 code. Since the FDNS code conceptually treats 3-dimensional rocket plumes for which essentially no validation data exists, the FDNS/SPF/2 plume comparisons are currently the only method of validating the two-phase FDNS code as a plume code.

6.   The thermo-vision camera offers the potential for providing useful validation data for axisymmetric SRM plumes. However, the wavelength interval used for making the thermo-vision measurements should be carefully chosen so that the data can be accurately interpreted. For viewing the internal structure of the plumes, wavelengths which make the plume optically thin, which avoids regions of gas/particle interaction, and which avoids spectral intervals in which the particle optical properties undergo rapid changes should be chosen for the measuring system. Spectral intervals of 5-6 and of 7-8 μm

should be considered for internal viewing of plumes. To verify radiation analyses, spectral intervals of maximum heating should be observed (1-2 μm). If the spectral intervals cannot be optimized because of instrumentation limitations, the thermo-vision camera data will be of limited value.

7. The OD3P code provides mean particle size predictions that are consistent with the measurements taken by Sambamurthi during the MNASA and TEM test series.

8. Preliminary exit plane radiation predictions for the MNASA motor indicate that the flowfield effects due to changes in combustion chamber geometry that occur during grain burnback can potentially explain the observed increase in measured radiation that occurs during a solid motor test firing.

Recommendations:

1. The Al$_2$O$_3$ optical property data (N$_1$ and N$_2$ values) files for the Mie theory conversion to radiation properties (σ_s, σ_b, and phase function parameters) should be optimized for radiation heating analysis. Gaseous/particle radiation interaction analysis should be further analyzed to include the recent improvements suggested by Reed (Ref. 5.1). These improvements should avoid the very narrow spectral interval and wide overall spectral region analyses required in the SIRRM code which were designed for plume signature analysis not base heating.

2. The NOZZRAD code should be used as a preliminary design tool for radiation analysis. The REMCAR code for Monte Carlo predictions should be used where more detailed analyses are required.

3. The method of spherical harmonics and extensions of the two-flux mode to make it a method of discrete coordinates should be further developed as alternative radiation analysis for future use.

4. Additional two-phase FDNS code plume predictions should be compared to SPF/2 predictions to obtain a validated CFD model for plume analyses.

5. More interaction between plume analysts and thermo-vision instrumentation specialists should be made before new test programs are instituted.

6.0 REFERENCES

1.1   Calia, V.S., et al, "Measurements of UV/VIS/LWIR Optical Properties of Al_2O_3 Particles," 18th JANNAF Exhaust Plume Mtg, Naval Postgraduate School, Monterey, CA, 1989, 14-16, November 1989.

1.2   Everson, J., and H.F. Nelson, "Development and Application of a Reverse Monte Carlo Radiative Transfer Code for Rocket Plume Base Heating," AIAA 93-0138, 31st Aerospace Sciences Meeting & Exhibit, Reno, VN, January 11-14, 1993.

1.4   Moylan, B., and P. Sulyma, "Investigation of Gas/Particle Heat Transfer Rates in Solid Rocket Motors," AIAA 92-3619, 1992.

1.5   Sambamurthi, J., "Plume Particle Collection and Sizing from MNASA Motor Tests in Support of Thermal Radiation Analysis," Memo ED33-100-92, NASA/MSFC, August 20, 1992.

1.6   Anfimov, N.A., et al, "Analysis of Mechanisms and Nature of Radiation from Aluminum Oxide in Different Phase States in Solid Rocket Exhaust Plumes," AIAA 93-2818, 1993.

1.7   Smith, S.D., "Flowfield Modeling to Support Solid Rocket Motor Base Heating," SECA-FR-94-01, SECA, Inc., Huntsville, AL, February 1994.

2.1   Moyers, R.L., et al, Memorandum: ASRM/Nozzle Test MNASA-5, Sverdrup Technology, Inc., Arnold Air Force Base, TN, September 27, 1991.

2.2   Reed, R.A., et al, "New Measurements of Liquid Aluminum Oxide," 1993 JANNAF Exhaust Plumes Subcommittee Meeting, Phillips Laboratory, Kirtland AFB, NM, 1993.

2.3   Konopka, W.L., et al, "Measurements of Infrared Optical Properties of Al_2O_3 Rocket Exhaust Particles," AIAA-83-1568, AIAA Thermophysics Conf., Montreal, Canada, 1-3 June 1983.

2.4   Calia, V.S., Grumman Aerospace Corp., Bethpage, NY, personal communication, August 1991.

2.5   Bohren, C.F. and Huffman, D.R., Absorption and Scattering of Light by Small Particles, Wiley and Sons, 1983.

2.6   Markarian, P., and R. Kosson, "Standardized Infrared Radiation Model (SIRRM-II)," AFAL-87-098, Grumman Aerospace Corp., Bethpage, NY, March 1988.

2.7   Anfimov, N.A., et al, "Analysis of Mechanisms and Nature of Radiation from Aluminum Oxide in Different Phase States in Solid Rocket Exhaust Plumes," AIAA 93-2818, 1993.

2.8 Rawlins, W.T., et al, "Effects of Supercooling and Melt Phenomena on Particulate Radiation in Plumes," PSI-2153/TR-1136, Physical Sciences, Inc., Andover, MA, 1991.

2.9 Oliver, S.M., and B.E. Moylan, "An Analytical Approach for the Prediction of Gamma-to-Alpha Phase Transformation of Aluminum Oxide (Al_2O_3) Particles in the Space Shuttle ASRM and RSRM Experiments," AIAA-92-2915, 1992.

2.10 Propellant Exhausts," J. of Prop. and Power, 6, pp. 668-671, 1990.

2.11 Ludwig, C.B., et al, "Handbook of Infrared Radiation from Combustion Gases," NASA SP-3080, 1973.

2.12 Edwards, D.K., "Molecular Gas Band Radiation," in Advances in Heat Transfer, 12, T.F. Irvine, Jr. and J.P. Hartnett, eds., Academic Press, NY, pp. 115-193, 1976.

2.13 Tien, C.L., "Thermal Radiation Properties of Gases," in Advances in Heat Transfer, 5, T.F. Irvine, Jr. and J.P. Hartnett, eds., Academic Press, NY, pp. 153-324, 1968.

2.14 Hottel, H.C., and A.F. Sarofim, Radiative Transfer, McGraw-Hill, NY, 1967.

2.15 Everson, J., and H.F. Nelson, "Development and Application of a Reverse Monte Carlo Radiative Transfer Code for Rocket Plume Base Heating," AIAA 93-0138, 31st Aerospace Sciences Meeting & Exhibit, Reno, VN, January 11-14, 1993.

2.16 Reardon, J.E., and Y.C. Lee, " A Computer Program for Thermal Radiation from Gaseous Rocket Plumes (GASRAD)," RTR 014, Remtech, Inc., Huntsville, AL, December 1979.

2.17 Markarian, P., presentation on the Six-Flux Radiation Model in SIRRM, 1993 JANNAF Exhaust Plume Technology Subcommittee Meeting, Phillips Laboratory, Kirtland AFB, NM, 1993.

2.18 Baladrishnan, A., and D.K. Edwards, "Molecular Gas Radiation in the Thermal Entrance Region of a Duct," Trans. of the ASME, J. of Heat Trans., 101, pp. 489-495, 1979.

2.19 Modest, M.F., Radiative Heat Transfer, McGraw-Hill, 1993.

2.20 Tan, Z., "Radiative Heat Transfer in Multidimensional Emitting, Absorbing, and Anisotropic Scattering Media/-mathematical Formulation and Numerical Methoc," J. of Heat Transfer, III, pp. 141-147, 1989.

2.21 Tan, Z., and J.R. Howell, "New Numerical/Method for Radiation Heat Transfer in Nonhomogeneous Participating Media," J. of Thermophysics and Heat Transfer, 4, pp. 419-424, 1990.

2.22 Ou, Szu-Cheng S., and Kuo-Nan Lion, "Generalization of the Spherical Harmonic Method to Radiative Transfer in Multi-Dimensional Space," J. Quant. Spectrosc. Radiat. Transfer, 28, pp. 271-288, 1982.

2.23 Lovin, J.K. and A.W. Lubkowitz, "User's Manual for 'RAVFAC' A Radiation View Factor Digital Computer Program," NASA CR-61321, Lockheed Missiles & Space Co., Huntsville, AL, November 1969.

2.24 Kostamis, P., et al, "Numerical Modeling of Radiation Phenomena in Two-Phase Flows," Numerical Simulation of Fluid Flow and Heat/Mass Transfer Processes, Ed. by N.C. Markatos, et al, Springer-Verlag, 18, 1986, pp. 386-396.

2.25 Chen, Y.S., and R.C. Farmer, "Adaption of the Multidimensional Group Particle Tracking and Particle Wall-Boundary Condition Model to the FDNS Code," SECA-TR-92-06, SECA, Inc., Huntsville, AL, March 1992.

2.26 Saladino, A.J., and R.C. Farmer, "Radiation/Convection Coupling in Rocket Motor & Plume Analysis," SECA-FR-93-10, SECA, Inc., Huntsville, AL, July 1993.

2.27 Smith, S.D., et al, "Model Development for Exhaust Plume Effects on Launch Stand Design - PLIMP/LSD," SECA-93-FR-9, SECA, Inc., Huntsville, AL, June 1993.

2.28 Laderman, A.J., et al, "Study of Thermal Radiation, Particle Impingement Heating, and Flow Field Analysis of Solid Propellant Rocket Exhausts," Report No. V-4045, Aeronutronic Div., Philco-Ford Corp., Newport Beach, CA, 1967.

2.29 Dash, S.M., et al, "The JANNAF Standard Plume Flowfield Model (SPF/2), Vol. 11, Program User's Manual," SAI/PR TR-16-11, SAIC, Princeton, NJ, May 1984.

2.30 Sulyma, P., NASA/MSFC, Personal communication, 2 December 1994.

3.1 Dash, S.M., et al, "The JANNAF Standardized Plume Flowfield Code Version II (SPF-II," Volume I and II, CR-RD-SS-90-4, U.S. Army Missile Command, Huntsville, AL, July 1990.

3.2 Smith, S.D., "High Altitude Supersonic Flow of Chemically Reacting Gas-Particle Mixtures - Volume I - A Theoretical Analysis and Development of the Numerical Solution," LMSC-HREC TR D8674001, Lockheed Missiles & Space Co., Huntsville, AL, October 1984.

3.3 Svehla, R.A., and B.J. McBride, "FORTRAN IV Computer Program for Calculation of Thermodynamics and Transport Properties of Complex Chemical Systems," NASA TN D-70456, January 1976.

3.4 Evans, R.M., "Boundary Layer Integral Matrix Procedure BLIMPJ User's Manual," Aerotherm UM-75-64, July 1975.

3.5 Smith, S.D., "Flowfield Modeling to Support Rocket Motor Base Heating," SECA-FR-94-01," SECA, Inc., Huntsville, AL, February 1994.

3.6 Everson, J. and H.F. Nelson, "Development and Application of a Reverse Monte Carlo Radiative Transfer Code for Rocket Plume Base Heating," Presented at the AIAA 31st Aerospace Sciences Meeting, Reno, NV, January 1993.

3.7 Smith, S.D., et al, "Model Development for Exhaust Plume Effects on Launch Stand Design - PLIMP/LSD," SECA-FR-93-9, SECA, Inc., Huntsville, AL., June 1993.

3.8 Chen, Y.S., AIAA Paper 88-0417, January 1988.

3.9 Chen, Y.S., AIAA Paper 89-0286, January 1989.

3.10 Wang, T.S., and Y.S. Chen, AIAA Paper 90-2494, July 1990.

3.11 Chen, Y.S., "FDNS-General Purpose CFD Code - User's Guide," ESI-TR-93-01, Engineering Sciences, Inc., Huntsville, AL, May 1993.

3.12 Sanford, M.D., AIAA Paper 91-1789, June 1991.

3.13 Lauder, B.E., and D.B. Spalding, Comp. Meth. Appli. Mech. Engr., 3, pp. 169-289, 1974.

3.14 Chen, Y.S. and R.C. Farmer, AIAA Paper 91-1967, June 1991.

3.15 Wang, T.S., Y.S. Chen, and R.C. Farmer, "Numerical Investigation of Transient SSME Fuel Preburner Flowfield with a Pressure Based Reactive CFD Method," 7th SSME CFD Working Group Meeting, MSFC, April 1989.

3.16 Carson, D.J., and R.F. Hoglund, AIAA J., 2, November 1964.

3.17 Henderson, C.B., AIAA J., 14, p. 707, June 1976.

3.18 Drake, R.W., Journal of Heat Transfer, 83, American Society of Mechanical Engineers, 1961.

3.19 Moylan B., and P. Sulyma, "Investigation of Gas/Particle Heat Transfer Rates in Solid Rocket Motors," AIAA 92-3619, AIAA/SAE/ASME/ASEE 28th Joint Propulsion Conference and Exhibit, Nashville, TN, July 1992.

3.20 Sambamurthi, J.E., "An Explanation for Lack of Steady State Radiation Measurements in Plume Environment Subscale Solid Rocket Motor Test Series (PESSTS) Test Program," ED33-24-94, NASA/MSFC, Huntsville, AL, 10 May 1994.

3.21 Markarian P., and R. Kosson, "Standardized Infrared Radiation Model (SIRRM-II), Volume II: User's Manual," AFAL-TR-87-098, Grumman Corporation, Bethpage, NY, March 1988.

3.22 Hunter, S.C., et al, "One Dimensional Reacting Three-Phase Flow with Mass Transfer Between Phases," AFRPL-TR-81-103, April 1982.

3.23 Sambamurthi, J., "Plume Particle Collection and Sizing from MNASA Motor Tests in Support of Thermal Radiation Analysis," ED33-100-92, Marshall Space Flight Center, AL, 20 August 1992.

3.24 Salita, M., "Implementation and Validation of the One-Dimensional Gas/Flow Code OD3P," CPIA pub. 529, Vol. II, 26th JANNAF Combustion Meeting, pp. 69-81, October 1989.

3.25 Netzer, D., et al, "Plume Particle Size Distribution and Optical Properties," Ibid.

3.26 Hermsen, R.W., "Aluminum Oxide Particle Size for Solid Rocket Motor Performance Prediction," Journal of Spacecraft and Rockets, 18, November-December 1981.

3.27 Sambamurthi, J.E., "Plume Particle Collection and Sizing from the Static Firing of the Full-scale Redesigned Solid Rocket Motor (RSRM) Test in Support of Thermal Radiation Analysis," ED33-28-94, NASA/MSFC, Huntsville, AL, 8 August 1994.

4.1 Saladino, A.J., et al, "Radiation from Advanced Solid Rocket Motor Plumes," NAS8-39370, SECA QPR-94-02, SECA, Inc., Huntsville, AL, February, 1994.

4.2 Smith, S.D., "Final Report - Flowfield Modeling to Support Solid Rocket Motor Base Heating," SECA FR-94-01, SECA, Inc., Huntsville, AL, February 1994.

4.3 Zaccardi, V.A., MNASA Test Series Thermal Image Data, personal communication, Sverdrup Technology, Inc., Arnold Air Force Base, TN, December 17, 1993.

4.4 Saladino, A.J., J.A., Freeman and R.C. Farmer, "Radiation from Advanced Solid Rocket Motor Plumes," NAS8-39370, SECA-QPR-92-18, SECA, Inc., Huntsville, AL, November 1993.

4.5 Saladino, A.J., J.A. Freeman and R.C. Farmer, "Radiation from Advanced Solid Rocket Motor Plumes," NAS8-39370, SECA-QPR-93-02, SECA, Inc., Huntsville, AL, February 1993.

4.6   Bryan, D.M., ASRM48-3, Thermal Image Plume Temperature Data, personal communication, NASA/MSFC ED64, February 1993.

5.1   Reed, R.A., et al, "Compatibility of Infrared Band Models with Scattering," AIAA-92-2891, 1992.

Report Documentation Page

1. Report No.	2. Government Accession No.	3. Recipient's Catalog No.

4. Title and Subtitle	5. Report Date
Radiation from Advanced Solid Rocket Motor Plumes	December, 1994
	6. Performing Organization Code

7. Author(s)	8. Performing Organization Report No.
Richard C. Farmer, Sheldon D. Smith and Brian L. Myruski	SECA-FR-94-18
	10. Work Unit No.

9. Performing Organization Name and Address	11. Contract or Grant No.
SECA, Inc. 3313 Bob Wallace Avenue, Suite 202 Huntsville, AL 35805	
	13. Type of Report and Period Covered

12. Sponsoring Agency Name and Address	14. Sponsoring Agency Code
George C. Marshall Space Flight Center Marshall Space Flight Center, AL 35812	

15. Supplementary Notes

Peter R. Sulyma, Technical Monitor

16. Abstract

The overall objective of this study was to develop an understanding of solid rocket motor (SRM) plumes in sufficient detail to accurately explain the majority of plume radiation test data. Improved flowfield and radiation analysis codes were developed to accurately and efficiently account for all the factors which effect radiation heating from rocket plumes. These codes were verified by comparing predicted plume behavior with measured NASA/MSFC ASRM test data.

Upon conducting a thorough review of the current state-of-the-art of SRM plume flowfield and radiation prediction methodology and the pertainent experimental data base, the following analyses were developed for future design use.

● The NOZZRAD code was developed for preliminary base heating design and Al_2O_3 particle optical property data evaluation using a generalized two-flux solution to the radiative transfer equation.

● The IDARAD code was developed for rapid evaluation of plume radiation effects using the spherical harmonics method of differential approximation to the radiative transfer equation.

● The FDNS CFD code with fully coupled Euler-Lagrange particle tracking was validated by comparison to predictions made with the industry standard RAMP code for SRM nozzle flowfield analysis. The FDNS code provides the ability to analyze not only rocket nozzle flow, but also axisymmetric and three-dimensional plume flowfields with state-of-the-art CFD methodology.

● Procedures for conducting meaningful thermo-vision camera studies were developed.

17. Key Words (Suggested by Author(s))	18. Distribution Statement
Rocket Propulsion, Rocket Plume/Radiation Solid Rocket Motors, CFD	unclassified – unlimited

19. Security Classif. (of this report)	20. Security Classif. (of this page)	21. No. of pages	22. Price
unclassified	unclassified	185	